

The wear studies of boron suboxide based cutting tool materials in machining applications

Christopher Stuart Freemantle

A dissertation submitted to the Faculty of Engineering and the Built Environment, University of the Witwatersrand, Johannesburg, in fulfilment of the requirements for the degree of Master of Science in Engineering.

February 2010

DECLARATION

I declare that this dissertation is my own unaided work. It is being submitted for the degree of Master of Science in Engineering to the University of the Witwatersrand, Johannesburg. It has not been submitted before for any degree or examination to any other university.

Signed:

Christopher Stuart Freemantle

Date:

ABSTRACT

The wear characteristics of the first generation of boron suboxide (B_6O) based cutting tool materials fabricated from spark plasma sintered $B_6O/Y_2O_3/Al_2O_3$ material have been investigated in terms of chemical and abrasive wear when machining compacted graphite cast iron (CGI).

Static interaction diffusion couple experiments were conducted at temperatures ranging from 700 °C to 1300 °C in order to simulate the chemical interaction between the tool material (B_6O) and the workpiece material (CGI). The samples were studied using optical microscopy, scanning electron microscopy (SEM) and energy dispersive x-ray spectrometry (EDS) as well as x-ray diffraction (XRD) in order to identify the microstructural and compositional changes as well as determine resulting phases. Interactions observed below 900 °C were found to be minimal, with significant chemical interactions occurring at 1100 °C and above. Iron boride phases were seen to evolve at the interface of the tool and workpiece materials. Silicon diffusion has been identified as a rapidly diffusing constituent with a tendency to diffuse towards the interface. Due to the formation of various chemical products during the experiments, chemical wear is expected to affect B_6O tools at expected machining temperatures.

Resistance to oxidation of B_6O based materials was examined at 1000 °C, revealing a tendency for formation of boric acids on the surface of the material in response to B_2O_3 formation and reaction with atmospheric moisture. Evaporation of boric acids has been observed to result in a mass loss of the material along with boric acid product crystal formation upon cooling.

Turning tests have revealed that the first generation of B_6O based cutting tools perform comparably with PcBN at very low cutting speeds, but suffer severe abrasive wear as the cutting speed is increased, due to the need for improvements in tool fabrication and the reduction of material damage and a heat affected zone resulting from laser cutting.

Ultrahigh pressure sintered B_6O based material was produced but was found to possess a poor microstructure.

Computational thermodynamics and phase diagram generation has been successfully compared to experimental results in predicting reaction products and chemical behaviour of the tool materials at machining temperatures.

ACKNOWLEDGEMENTS

The author would like to express sincere appreciation to all those who assisted in this work, in particular:

- Dr. Herrmann, for his assistance and patience during the completion of this project
- Prof. I. Sigalas, for the opportunity, guidance and funding provided
- Colleagues K. Katuku, A. Andrews, O.T. Johnson and E. Ofunguyiwa for their assistance especially during the early days of this project
- O.T. Johnson, for the patience and late nights spent at the SEM unit
- Element 6, especially Dr. Tina Heiligers for her assistance in SEM work
- Wayne Leahy of Element 6 Ireland, for assistance with cutting tool fabrication
- The IKTS team, for assistance with spark plasma sintering and characterisation
- The support and workshop staff of Chemical and Metallurgical Engineering for their kind assistance
- The Centre of Excellence in Strong Materials for their financial assistance
- The XRD team at Gate House, run by Dr. David Billing, for their efforts and advice
- My friends and family for the support during this period

TABLE OF CONTENTS

	Page
ABSTRACT	i
ACKNOWLEDGEMENTS	ii
1 INTRODUCTION.....	16
1.1 Subject of the dissertation	16
1.2 Background to the project	16
1.2.1 Collaborative nature of the project.....	16
1.2.2 Motivation for research covered by the project	16
1.3 Objectives of the dissertation.....	17
1.4 Scope and limitations	18
1.5 Plan of development	18
2 LITERATURE REVIEW	20
2.1 Hard materials and boron.....	20
2.2 Synthesis of boron suboxide (B_6O).....	20
2.3 Super-hard boron rich materials:	21
2.3.1 High pressure and high temperature synthesis:.....	24
2.3.2 Mackay Packing.....	29
2.4 The hardness of boron suboxide relative to cubic boron nitride	30
2.4.1 Hard and tough boron suboxide based materials.....	31
2.5 The use of boron suboxide in drag cutters and drill bits	35
2.6 Cutting tools and materials.....	35
2.7 Properties and classes of tool materials:.....	38

2.7.1	Wear modes / processes typical to ceramic cutting tools:	39
2.8	Static interaction diffusion couples	42
2.8.1	PcBN / Fe interaction:	43
2.8.2	PCD and WC-Co interactions:	44
2.9	Machining of ferrous metals with ceramic tool materials.....	47
2.9.1	Introduction to machinability of ferrous metals:.....	47
2.10	Machining of Compacted Graphite Cast Iron (CGI).....	47
2.10.1	Mixed ceramics.....	51
2.10.2	Polycrystalline cubic boron nitride.....	52
2.10.3	Polycrystalline diamond	53
2.11	Thermal stability of boron suboxide	55
2.12	Thermochemical / thermodynamic studies of B ₆ O.....	61
3.	METHODOLOGY	64
3.1	Powder preparation for hot press and high pressure compacts..	64
3.1.1	Milling	64
3.1.2	Washing	65
3.1.3	Chemical analysis	66
3.1.4	Planetary ball milling	66
3.1.5	Particle size analysis	68
3.2	Sintering	68
3.2.1	Hot press runs	68
3.2.2	Containment of material during sintering	69
3.2.3	IKTS SPS production	71
3.2.4	High pressure sintering	72

3.2.4.1	Pre-compaction (formation of a green compact)	72
3.2.4.2	Sintering.....	72
3.3	Hardness and fracture toughness.....	72
3.4	Cutting tool fabrication.....	73
3.4.1	SPS low pressure compacts	73
3.4.2	High pressure compacts	75
3.5	Static Interaction diffusion couples	75
3.5.1	Sample preparation	75
3.5.2	Diffusion couple heat treatment profile.....	77
3.5.3	Cross sectional preparation	78
3.6	Optical microscopy	78
3.7	Scanning electron microscopy.....	78
3.8	X-ray diffraction	79
3.9	Density and open porosity determination	79
3.10	Oxidation resistance testing	80
3.10.1	Sample preparation	81
3.10.2	Heat treatment regimen	81
3.10.3	Mass change measurements	82
3.11	Machining and wear studies	82
3.11.1	Lathe operation and machining characteristics.....	82
3.11.2	Tool failure analysis.....	85
4	RESULTS.....	87
4.1	Powder for hot pressing and high pressure compacts	87
4.1.1	Particle size analysis	87

4.1.2	Chemical analysis	90
4.2	Hardness and fracture toughness characteristics of produced materials.....	91
4.2.1	Hot pressed samples	91
4.2.2	IKTS SPS samples.....	92
4.2.3	High pressure sintering	93
4.3	Static interaction diffusion couples	103
4.3.1	Starting microstructures and compositions.....	103
4.3.2	Diffusion couple analysis - introduction	107
4.3.3	The 700 °C diffusion couple	107
4.3.4	The 900 °C diffusion couple	116
4.3.5	The 1100 °C diffusion couple	122
4.4	Oxidation Resistance.....	140
4.4.1	Characterization of the starting materials	140
4.4.1.1	X-ray diffraction	140
4.4.2	Mass change observations	143
4.4.2.1	Optical microscopy	145
4.4.3	Characterization of post heat treatment surface changes using optical microscopy	146
4.4.3.1	1 hour at temperature	146
4.4.3.2	2 hours at temperature	147
4.4.3.3	4 hours at temperature	149
4.4.3.4	10 hours at temperature	151
4.4.3.5	20 hours at temperature	153
4.4.3.6	50 hours at temperature	155

4.4.4	X-ray diffraction of the oxidised samples	157
4.4.4.1	Runs to monitor phase changes.....	157
4.4.4.2	Runs to monitor mass changes	159
4.4.4.3	SEM of oxidation tested surfaces after 50 hours of heat treatment	161
4.5	Machining and wear studies	164
4.5.1	Cutting tool fabrication results	164
4.5.1.1	X-ray diffraction studies of laser cut surface	166
4.5.2	Turning test results	167
4.5.2.1	50m/min cutting speed	167
4.5.2.2	100m/min cutting speed	168
4.5.3	Tool failure analysis.....	169
4.5.3.1	Optical microscopy of surface effects	171
4.5.3.2	Scanning electron microscopy investigation of chamfer and surface finish.....	172
4.5.3.3	SEM investigation of wear scars	173
5	DISCUSSION	178
5.1	Powder preparation.....	178
5.1.1	Pure B ₆ O powders	178
5.1.2	Co and CoO additive powders	178
5.2	Properties of the sintered materials.....	179
5.2.1	Lower pressure samples	179
5.2.2	Ultrahigh pressure sintered compacts.....	179
5.3	Static Interaction diffusion couples	184
5.3.1	The 700 °C couple demonstrated minimal interaction.....	184

5.3.2	Interaction was observed at 900 °C	186
5.3.3	Substantial interaction took place at 1100 °C.....	190
5.3.4	The 1300 °C couple can only reveal limited useful information	196
5.4	Oxidation resistance	198
5.5	Machining and wear studies	201
5.5.1	SEM tool investigation.....	203
5.5.1.1	100m/min wear scar forms quickly	203
5.5.1.2	50 m/min wear scar minimal after 1min of cutting time.....	203
6	CONCLUSIONS.....	205
7	REFERENCES	209
	APPENDIX.....	217

LIST OF FIGURES

FIGURE 2.1: THE CRYSTAL STRUCTURE OF BORON SUBOXIDE (B_6O).....	23
FIGURE 2.2: OPTICAL IMAGES OF ORANGE – RED COLOURED B_6O GRAINS.....	26
FIGURE 2.3: TEM PHOTOGRAPHS OF BORON SUBOXIDE CRYSTALS AT (A) LOWER MAGNIFICATION DISPLAYING EUHEDRAL MORPHOLOGIES WITH SOME FAULTED CRYSTALS AND ICOSAHEDRAL TWINS.....	26
FIGURE 2.4: (A) SEM MICROGRAPH OF B_6O PARTICLES (MULTIPLY-TWINNED) (B) TWO ICOSAHEDRA LIBERATED FROM THE PREVIOUSLY SURROUNDING MATRIX MATERIAL. (C) THE IDEAL STRUCTURE OF STOICHIOMETRIC B_6O AS DESCRIBED PREVIOUSLY. (D) AN OUTLINE OF THE RHOMBOHEDRAL UNIT CELL WITH RHOMBOHEDRAL AXES AND HEXAGONAL AXES SHOWN.	28
FIGURE 2.5: (A) TEM IMAGE (LOW MAGNIFICATION) OF MTP'S OF B_6O SHOWING INDIVIDUALS IN BRAGG ORIENTATION	29
FIGURE 2.6: THE DEVELOPMENT OF THE SUPER-ICOSAHEDRAL STRUCTURE FORMED BY B_6O	30
FIGURE 2.7: AN ICOSAHEDRAL STRUCTURE FORMED FROM MACKAY PACKING (A) SEM IMAGE OF AN ISOLATED B_6O ICOSAHEDRON. (B) AN ILLUSTRATION OF THE RELATIONSHIP BETWEEN THE ICOSAHEDRON SHAPE AND THE TETRAHEDRAL UNIT CELL. (C) SEM IMAGE OF AN MTP SHOWING CLEAR RE-ENTRANT ANGLES INDICATIVE OF TWINNING.	31
FIGURE 2.8: WEAR MAP OF 85VOL. % PCBN CUTTING TOOL PERFORMANCE WHEN MACHINING AISI 420 STAINLESS STEEL AT VARIOUS DEPTHS OF CUT AND CUTTING SPEEDS	37
FIGURE 2.9: GRAPHS DISPLAYING THE VARIATION OF FLANK WEAR WITH CUTTING TIME AS DESCRIBED BY B. MILLS.....	38
FIGURE 2.10: GRAPH SHOWING THE FRACTURE TOUGHNESS VERSUS STRENGTH FOR VARIOUS CUTTING TOOL MATERIALS.....	39
FIGURE 2.11: SKETCH SHOWING WEAR, THERMAL SHOCK CRACKING AND EDGE CHIPPING FOR CERAMIC CUTTING TOOLS	40
FIGURE 2.12: VARIOUS WEAR MODES DISPLAYED ON A TYPICAL PCBN CUTTING TOOL AS DESCRIBED BY SECO.	41
FIGURE 2.13: INTERACTION COUPLES FOR PCBN (GRADE '50') AT A: 1100°C B: 1300°C (OVERVIEW OF THE MATERIAL INTERFACES) C: 1300°C SHOWING DETAILED INTERFACIAL REGION AND D: EDS COMPOSITIONAL PROFILE AT 1300 °C.	43
FIGURE 2.14: INTERACTION COUPLES FOR PCBN (GRADE '85') AT A: 1100°C – NOTE THE ABSENCE OF ANY SIGNIFICANT INTERACTION B: 1300°C (OVERVIEW OF THE MATERIAL INTERFACES) C: 1300°C SHOWING INTERFACIAL REGION AND D: EDS COMPOSITIONAL PROFILE AT 1300 °C.....	44
FIGURE 2.15: INTERACTION COUPLES FOR PCD, A: 700°C, B: 900°C, C&D: 1100°C AND DETAIL OF THE INTERFACE AT HIGHER MAGNIFICATION, E: COMPOSITIONAL PROFILE AT THE INTERFACE.	45
FIGURE 2.16: TAYLOR CURVE FOR THE THREE INVESTIGATED MATERIALS.....	46
FIGURE 2.17: DEEP ETCHED SCANNING ELECTRON MICROGRAPHS OF THE GRAPHITE STRUCTURE IN GREY IRON, CGI AND SPHEROIDAL GRAPHITE IRON (SGI).....	48
FIGURE 2.18: WEAR MAP AND WEAR SCARS PRODUCED AS THE RESULT OF MACHINING CGI WITH ALUMINA / TITANIUM CARBIDE MIXED CERAMIC CUTTING TOOL MATERIALS.....	51
FIGURE 2.19: A) PCBN 1 (50% CBN) MACHINING WEAR MAP SHOWING BETTER OVERALL PERFORMANCE OF THIS MATERIAL, B) PCBN 2 (85% CBN) MACHINING WEAR MAP DEMONSTRATING POOR WEAR CHARACTERISTICS AT HIGHER CUTTING SPEED AND FEED RATES.	52
FIGURE 2.20: WEAR SCARS PHOTOGRAPHED OF THE PCBN GRADES, THE CODE ABOVE EACH IMAGE IS INDICATIVE OF THE SAMPLE I.E. PCBN 1 OR 2, THEN THE CUTTING SPEED E.G. S100 = 100M/MIN AND THE FEED RATE OF 0.1MM PER REVOLUTION.	53

FIGURE 2.21: WEAR MAP GENERATED FROM THE MACHINING OF CGI WITH PCD DISPLAYING FAVOURABLE WEAR BEHAVIOUR COMPARED TO THE OTHER TOOL MATERIALS..	54
FIGURE 2.22: COMPARISON OF TOOL LIFE AND NUMBER OF BORES ACHIEVED AGAINST CGI AND GRAY CAST IRON FOR DIFFERENT CUTTING TOOL MATERIALS.	55
FIGURE 2.23: OPTICAL IMAGE OF A HOT PRESSED B_6O SAMPLE ANNEALED AT 1900 °C.....	56
FIGURE 2.24: SEM IMAGES SHOWING HOW A B_6O COMPOSITE (HP19CB ₆ O5.6WT%AL) DECOMPOSED AFTER ANNEALING AT 1900 °C:	56
FIGURE 2.25: BACKSCATTER IMAGE OF AN ANNEALED (AT 1800 °C) HOT PRESSED B_6O COMPOSITE, HP19CB ₆ O5.6WT%ALHT18.....	57
FIGURE 2.26: OPTICAL IMAGES OF SAMPLES ANNEALED AT 1900 °C, SHOWING DECOMPOSITION A: HP19B ₆ OHT19 AND B) HP19CB ₆ O5.6WT%ALHT19	58
FIGURE 2.27: TGA AND DTA ANALYSES OF SINGLE PHASE COMPACTS A) B_4C AND B_6O PREPARED AT 5GPA, 1700°C FOR 20 MINUTES. HEATING RATE: 3°C/MIN, ATMOSPHERE: AIR.....	60
FIGURE 2.28: B_2O_3 FILM THICKNESS AFTER OXIDATION IN AIR FOR 4 HOURS AS A FUNCTION OF HEAT TREATMENT TEMPERATURE.	60
FIGURE 2.29 GRAPH OF TEMPERATURE VERSUS HEAT CAPACITY AS DESCRIBED BY ANDREWS FOR B_6Si & B_6O (EXTRAPOLATED EXPERIMENTAL VALUES) AND B_6O AFTER CORRECTION B_6O DATA WAS MEASURED IN THE RANGE 298.15K TO 800K.....	61
FIGURE 2.30: FRACTURE TOUGHNESS AGAINST HARDNESS OF MOST OF THE BORON SUBOXIDE BASED MATERIALS PRODUCED BY THE CERAMICS GROUP MEMBERS IN RECENT YEARS	62
FIGURE 3.1 PHOTOGRAPH OF THE ATTRITION BALL MILL	65
FIGURE 3.2: PLANETARY BALL MILL	67
FIGURE 3.3 THE UNIAXIAL HOT PRESS AND ASSOCIATED COMPONENTS.	69
FIGURE 3.4: CROSS SECTIONAL DIAGRAM OF THE HEXAGONAL BORON NITRIDE (hBN) POT, PILL AND ACCOMPANYING GRAPHITE PISTON USED.	70
FIGURE 3.5: SCHEMATIC REPRESENTATION OF THE SETUP OF SPARK PLASMA SINTERING TECHNOLOGY AS DESCRIBED BY THE IKTS FRAUNHOFER INSTITUTE.	71
FIGURE 3.6: CUTTING TOOL SPECIFICATIONS USED FOR THE INSERTS PRODUCED AND TESTED DURING THIS PROJECT.	74
FIGURE 3.7: PHOTOGRAPHS OF CUTTING TOOL INSERTS PRODUCED FOR THIS PROJECT AND THE CORRESPONDING TOOL HOLDER SHOWN SECURED WITHIN THE TURRET OF THE LATHE.	74
FIGURE 3.8: PHOTOGRAPHS OF THE HIGH PRESSURE CUTTING TOOLS PRODUCED	75
FIGURE 3.9: STATIC INTERACTION DIFFUSION COUPLE POT ARRANGEMENT PRIOR TO HOT PRESSING.	77
FIGURE 3.10: CROSS SECTION OF THE ARRANGEMENT OF THE SAMPLES SUPPORTED ON NICHROME THERMOCOUPLE WIRE DURING THE OXIDATION RESISTANCE TESTING.	82
FIGURE 3.11: PHOTOGRAPH OF THE CNC TURN MASTER LATHE.	84
FIGURE 3.12: CGI WORKPIECE HELD WITHIN THE CHUCK JAWS AS WELL AS TOOL HOLDER IN THE SETUP USED FOR TURNING TESTS.	84
FIGURE 4.1: RESULTS OF THE STARTING PARTICLE SIZE ANALYSIS OF THE PURCHASED B_6O POWDER PRIOR TO 20 HOURS OF MILLING AT 400 RPM.	88
FIGURE 4.2: RESULTS OF THE PARTICLE SIZE ANALYSIS CURVE OF VOLUME PERCENT AGAINST PARTICLE SIZE OF THE MILLED POWDER AFTER MILLING FOR 20 HOURS AT 400RPM.	88
FIGURE 4.3: PARTICLE SIZE OF THE STARTING POWDER BEFORE BATCH 3 WAS MILLED.....	89
FIGURE 4.4: PARTICLE SIZE OF BATCH 3 AFTER MILLING FOR 20 HOURS AT 200RPM.	89
FIGURE 4.5: IN-LENS DETECTOR SEM IMAGE OF THE PURE B_6O ULTRA HIGH PRESSURE SINTERED COMPACT	95

FIGURE 4.6: VERY HIGH MAGNIFICATION SEM IMAGE (WITH IN-LENS DETECTOR) SHOWING FINE DETAILS IN THE GRAIN STRUCTURE OF PURE B ₆ O SINTERED AT ULTRAHIGH PRESSURE.	95
FIGURE 4.7: SEM MICROGRAPHS SHOWING DISTRIBUTION OF ADDITIVE MATERIAL.....	97
FIGURE 4.8: HIGH MAGNIFICATION SEM MICROGRAPH SHOWING AN AGGLOMERATE OF ADDITIVE MATERIAL	97
FIGURE 4.9: EXTENSIVE OPEN POROSITY AND INHOMOGENEITY IS VISIBLE ON THE UHP B ₆ O/CoO SAMPLE.	98
FIGURE 4.10: XRD SCAN OF THE UHP B ₆ O/CoO MATERIAL SHOWING THE EXPECTED CoB PHASE AS WELL AS ALONG WITH B ₆ O.....	99
FIGURE 4.11: LOW MAGNIFICATION (100x) SEM IMAGE SHOWING THE DISTRIBUTION OF COBALT ADDITIVE IN THE B ₆ O BULK. HIGHER MAGNIFICATION (500x) SEM MICROGRAPH SHOWING TWO Co ADDITIVES IN THE B ₆ O BULK.	100
FIGURE 4.12: SEM MICROGRAPH OF A Co ADDITIVE AND IT'S ASSOCIATED 'HALO EFFECT' SHOWING BORIDE DIFFUSION INTO THE B ₆ O MATRIX.	101
FIGURE 4.13: SEM MICROGRAPH SHOWING THE DIFFUSION OF COBALT BORIDES FROM THE AGGLOMERATE INTO THE B ₆ O BULK IN THE UHP B ₆ O/Co SAMPLE.	101
FIGURE 4.14: IN-LENS DETECTOR SEM IMAGE SHOWING B ₆ O GRAINS ALMOST FREE OF ADDITIVE MATERIAL	102
FIGURE 4.15: XRD OF THE B ₆ O/Co MATERIAL SHOWING THE EXPECTED B ₆ O AND CoB PHASE.....	102
FIGURE 4.16: LOW MAGNIFICATION OF POLISHED CGI MICROSTRUCTURE SHOWING THE ABUNDANCE OF VERMICULAR GRAPHITE, HIGHER MAGNIFICATION IMAGE SHOWING GRAPHITE FLAKES CLEARLY AND SOME PEARLITE, VERY HIGH MAGNIFICATION IMAGE SHOWING THE VERY FINE PEARLITE (LAYERED) MORPHOLOGY THAT IS TYPICAL IN THIS CLASS OF CAST IRONS.....	104
FIGURE 4.17: XRD TRACE OF THE POLISHED SURFACE OF A COMPACTED GRAPHITE CAST IRON PILL USED FOR STATIC INTERACTION DIFFUSION COUPLE EXPERIMENTS.	105
FIGURE 4.18: SCANNING ELECTRON MICROGRAPH AND CORRESPONDING EDS ANALYSIS OF THE SURFACE COMPOSITION OF POLISHED CGI.	105
FIGURE 4.19: OPTICAL MICROGRAPH OF PURE B ₆ O WITH POLISHED SURFACE TO BE IN CONTACT WITH CGI DURING THE COUPLE EXPERIMENTS.....	106
FIGURE 4.20: OPTICAL MICROGRAPH AT LOW MAGNIFICATION SHOWING THE B ₆ O (BOTTOM) AND CGI (TOP) PILLS AS SEEN FROM THE SIDE.	108
FIGURE 4.21: B ₆ O SURFACE AFTER THE 700°C TREATMENT; CGI SURFACE AS SEEN AT HIGH MAGNIFICATION	109
FIGURE 4.22: SEM MICROGRAPH SHOWING THE PEARLITE MORPHOLOGY THAT RESULTED AFTER THE 700°C EXPERIMENT; THE ELEMENTAL COMPOSITION OF THIS REGION DISPLAYS THE EXPECTED IRON AND CARBON CONSTITUENTS AS WELL AS SOME IMPURITIES.	110
FIGURE 4.23: SEM IMAGE AND CORRESPONDING EDS TRACE FOR THE IRON SURFACE AT 700°C	111
FIGURE 4.24: SEM MICROGRAPH AND EDS SCAN OF THE ENTIRE PHOTOGRAPHED REGION OF THE B ₆ O SIDE OF THE 700°C DIFFUSION COUPLE.	112
FIGURE 4.25: HIGHER MAGNIFICATION SEM MICROGRAPHS OF THE WHITE SPOTTED REGION OF THE B ₆ O SURFACE.	113
FIGURE 4.26: EDS LINE SCANS AND CORRESPONDING SCANNED REGIONS ON THE IMAGES SHOWN AND PLOT OF THE DIFFUSION PROFILE FOR THE CONSTITUENT ELEMENTS.....	115
FIGURE 4.27: B ₆ O SURFACE RESULTING FROM THE 900°C DIFFUSION COUPLE TREATMENT.; THE PULLED OUT B ₆ O HAS ADHERED TO THE CGI.....	116

FIGURE 4.28: MICROGRAPH SHOWING THE CHANGE IN THE IRON MICROSTRUCTURE AS A RESULT OF THE HEAT TREATMENT AT 900°C	117
FIGURE 4.29: THE SURFACE OF THE CGI PILL AFTER THE DIFFUSION COUPLE EXPERIMENT AT 900°C...	117
FIGURE 4.30: LINE SCAN IMAGES AND CORRESPONDING EDS PLOT OF THE VARIOUS DETECTED ELEMENTS ACROSS THE 900°C DIFFUSION COUPLE INTERFACE.	121
FIGURE 4.31: B ₆ O SURFACE SHOWING NO REMARKABLE FEATURES AFTER THE 1100°C COUPLE EXPERIMENT; CGI SURFACE SHOWING NO EVIDENCE OF GRAPHITE FLAKES, BUT DARKER REGIONS COULD INDICATE THEIR PRIOR PRESENCE; LARGE B ₆ O ADHERENT ISLANDS EMBEDDED IN THE CGI PILLS.	122
FIGURE 4.32: SEM MICROGRAPH OF THE B ₆ O SIDE OF THE 1100°C DIFFUSION COUPLE.	123
FIGURE 4.35: LOW MAGNIFICATION IMAGE OF THE B ₆ O/CGI INTERFACE; HIGHER MAGNIFICATION IMAGE SHOWING INTERFACIAL DETAIL.	129
FIGURE 4.36: CROSS SECTION OF THE INTERFACIAL AREA OF THE ADHERENT B ₆ O ON THE CGI HALF OF THE COUPLE SHOWING ELEMENTS DETECTED BY EDS IN EACH REGION.	130
FIGURE 4.37: SEM MICROGRAPH SHOWING DETAIL OF THE INTERFACE BETWEEN IRON AND B ₆ O.....	130
FIGURE 4.39: HIGH MAGNIFICATION SEM MICROGRAPH OF THE WHITE REGION NOTICED NEAR THE INTERFACE OF THE 1100°C CGI/B ₆ O DIFFUSION COUPLE.....	132
FIGURE 4.40: CROSS SECTIONAL DIFFUSION PROFILES SHOWING THE RELATIVE ABUNDANCES OF ELEMENTS AT OR NEAR THE CGI/B ₆ O 1100°C DIFFUSION COUPLE INTERFACE.....	133
FIGURE 4.41: THE SEPARATED 1300°C DIFFUSION COUPLE	134
FIGURE 4.42: LOW MAGNIFICATION SEM MICROGRAPH SHOWING THE UNUSUAL FEATURES ACCOMPANYING THE CGI/B ₆ O DIFFUSION COUPLE AT 1300°C.....	136
FIGURE 4.43: HIGH MAGNIFICATION SEM IMAGES OF THE INTERFACIAL REGION OF THE 1300°C COUPLE SHOWING A CREVICE THAT LIKELY CORRESPONDS TO REMOVED SOFT PHASES AS THE RESULT OF POLISHING.	137
FIGURE 4.44: EDS LINE SCAN SHOWING THE REGION SCANNED ON THE SEM MICROGRAPH (RED LINE LEFT TO RIGHT) AND THE CORRESPONDING PLOT OF THE SCAN RESULTS OF THE 1300°C DIFFUSION COUPLE EXPERIMENT BETWEEN CGI AND B ₆ O	138
FIGURE 4.45: XRD PATTERN CORRESPONDING TO THE (PURE B ₆ O) PHASE MONITORING SAMPLE 1.	141
FIGURE 4.46: XRD PATTERN CORRESPONDING TO THE PURE B ₆ O OXIDATION RESISTANCE SAMPLE 1 SHOWING ONLY THE EXPECTED PURE B ₆ O FINGERPRINT.	142
FIGURE 4.47: PEAK LIST SHOWING THE CORRESPONDENCE OF THE MEASURED B ₆ O PEAKS	142
FIGURE 4.48: XRD PATTERN OF THE B ₆ O/Y ₂ O ₃ /AL ₂ O ₃ OXIDATION RESISTANCE SAMPLE 1.....	143
FIGURE 4.49: TIME DEPENDENCE OF THE AVERAGE MASS LOSS PER UNIT SURFACE AREA OF THE SAMPLES WITH A SIGNIFICANT OVERALL MASS LOSS OF THE PURE B ₆ O MATERIAL	144
FIGURE 4.50: THE STARTING MICROSTRUCTURE OF PURE B ₆ O OXIDATION RESISTANCE SAMPLE 1 AFTER POLISHING; THE STARTING MICROSTRUCTURE OF PURE B ₆ O OXIDATION RESISTANCE SAMPLE 3 AFTER POLISHING.....	145
FIGURE 4.51: THE STARTING MICROSTRUCTURE OF THE B ₆ O/Y ₂ O ₃ /AL ₂ O ₃ OXIDATION RESISTANCE SAMPLE 1 AFTER POLISHING; THE STARTING MICROSTRUCTURE THE B ₆ O/Y ₂ O ₃ /AL ₂ O ₃ OXIDATION RESISTANCE SAMPLE 2 AFTER POLISHING. SAMPLE 3 IS OMITTED BECAUSE THE IMAGES ARE UNREMARKABLY DIFFERENT.	145
FIGURE 4.52: B ₆ O SURFACE AFTER HEAT TREATMENT AT 1000°C FOR ONE HOUR.	146
FIGURE 4.53: VARIOUS MICROGRAPHS OF THE B ₆ O/Y ₂ O ₃ /AL ₂ O ₃ SAMPLES HEAT TREATED IN AIR AT 1000°C FOR ONE HOUR.	147

FIGURE 4.54: RELATIVELY LOW MAGNIFICATION IMAGES SHOWING THE SIGNIFICANT CHANGES IN SURFACE FEATURES AFTER THE 2 HOUR HEAT TREATMENT OF THE PURE B_6O SAMPLES; HIGH MAGNIFICATION IMAGES OF THE CRYSTALS FORMED ALL OVER THE SAMPLE SURFACES.	148
FIGURE 4.55: OPTICAL MICROGRAPHS THAT ARE REPRESENTATIVE OF THE OBSERVATIONS MADE DURING THE $B_6O/Y_2O_3/AL_2O_3$ OXIDATION RESISTANCE INVESTIGATION AFTER HEATING AT $1000^{\circ}C$ FOR TWO HOURS IN AIR.	149
FIGURE 4.56: REPRESENTATIVE OPTICAL MICROGRAPHS OF THE PURE B_6O HEAT TREATED SAMPLES AT $1000^{\circ}C$ FOR FOUR HOURS IN AIR	150
FIGURE 4.57: REPRESENTATIVE OPTICAL MICROGRAPHS OF THE CRYSTAL FORMATIONS OBSERVED ON ALL OF THE $B_6O/Y_2O_3/AL_2O_3$ SAMPLES AFTER HEAT TREATING FOR 4 HOURS AT $1000^{\circ}C$ IN AIR. THE CRYSTALS APPEAR TO BE IN EXCESS OF 200 MICRONS IN DIAMETER	151
FIGURE 4.58: REPRESENTATIVE MICROGRAPHS OF THE RESULTING PURE B_6O SAMPLE SURFACES AFTER THE TEN HOUR HEAT TREATMENT IN AIR AT $1000^{\circ}C$	152
FIGURE 4.59: OPTICAL MICROGRAPHS RESULTING FROM THE TEN HOUR HEAT TREATMENT AT $1000^{\circ}C$ IN AIR	153
FIGURE 4.60: MICROGRAPHS DEPICTING THE SURFACE FEATURES AND MICROSTRUCTURE OF THE PURE B_6O SAMPLES HEAT TREATED AT $1000^{\circ}C$ FOR 20 HOURS IN AIR.	154
FIGURE 4.61: REPRESENTATIVE OPTICAL MICROGRAPHS OF THE CRYSTAL FORMATIONS OBSERVED ON THE $B_6O/Y_2O_3/AL_2O_3$ SAMPLES AFTER HEAT TREATING FOR 20 HOURS AT $1000^{\circ}C$ IN AIR.....	155
FIGURE 4.62: MICROGRAPHS OF THE SURFACES SHOWING GLASSY PHASE AND LARGE SINGLE CRYSTALS ON THE PURE B_6O SURFACES AFTER 50 HOURS AT $1000^{\circ}C$	156
FIGURE 4.63: UNREMARKABLE DIFFERENT FEATURES OBSERVED ON THE 50 HOUR SURFACES AS COMPARED TO THE TWENTY HOUR SURFACE.....	156
FIGURE 4.64: OVERLAID PEAK EVOLUTION AFTER THE SUCCESSIVE HEAT TREATMENT AND SUBSEQUENT XRD SCAN OF THE PURE B_6O SAMPLE 3 HEAT TREATED AT $1000^{\circ}C$ IN AIR.	157
FIGURE 4.65: OVERLAID PEAK EVOLUTION AFTER THE SUCCESSIVE HEAT TREATMENT AND SUBSEQUENT XRD SCAN OF THE PURE B_6O SAMPLE 2 HEAT TREATED AT $1000^{\circ}C$ IN AIR.	158
FIGURE 4.66: XRD PATTERN SHOWING THE DETECTED PHASES FOUND ON THE PURE B_6O SAMPLE AFTER THE 50 HOUR HEAT TREATMENT.	159
FIGURE 4.67: XRD PATTERN CORRESPONDING TO THE $B_6O/Y_2O_3/AL_2O_3$ SAMPLE SURFACES SHOWING AN ABUNDANCE OF EVOLVED PHASES AFTER 50 HOURS OF HEAT TREATMENT.....	160
FIGURE 4.68: SEM MICROGRAPHS AND EDS TRACES OF THE REGIONS A AND B SHOWING ELEMENTS PRESENT IN EACH REGION.	161
FIGURE 4.69: SINGLE CRYSTAL FORMATION AND EDS TRACE OF THE CRYSTAL ITSELF SHOWING ITS ELEMENTAL COMPOSITION.	162
FIGURE 4.70: SEM MICROGRAPH SHOWING THE LAYERED ROSETTE SHAPED CRYSTALS THAT WERE OBSERVED ON THE YTTRIA ALUMINA SAMPLES; THE EDS TRACE OF THE REGION SHOWN IN THE MICROGRAPH; SEM MICROGRAPH OF SOME REMOVED POWDER FROM THE SAMPLE SURFACE WITH EDS OF THE INDICATED REGION.....	163
FIGURE 4.71: LASER CUT BLANK VIEWED FROM ABOVE SHOWING EDGE CHIPPING AND BRITTLE FRACTURE; THE SAME BLANK SHOWING THE MELT LAYER SIMILAR TO THAT OBSERVED IN THE THERMAL STABILITY TESTS; CLOSE UP IMAGE OF THE MELT LAYER THAT STRONGLY RESEMBLES THERMAL STABILITY TESTING RESULTS; ZOOMED IN IMAGES OF THE REGIONS INDICATED BY THE ARROWS SHOWING CRYSTALLITE FORMATION	164

FIGURE 4.72: DBC50 RAKE FACE AND FLANK RESPECTIVELY SHOWING GOOD CHAMFERING AND HONING WITH INSIGNIFICANT SURFACE IMPERFECTIONS; $B_6O/Y_2O_3/Al_2O_3$ RAKE FACE AND FLANK RESPECTIVELY SHOWING A HIGH DEGREE OF DEFECTS.	165
FIGURE 4.73: XRD TRACE OF THE LASER CUT MELT SURFACE OF A BLANK	166
FIGURE 4.74: WEAR MAP OF THE TOOL PERFORMANCE OF DBC50 VS. B_6O FOR 50M/MIN, DEPTH OF CUT 0.25MM AND FEED RATE OF 0.1MM PER REVOLUTION.....	168
FIGURE 4.75: THE BEST FLANK OF THE TOOL SELECTED FOR 100M/MIN CUTTING TRIALS; AFTER A CUTTING TIME OF 106.50 SECONDS, A FLANK WEAR SCAR IN EXCESS OF $100\mu m$ RESULTED; AFTER A CUTTING TIME OF 213.00 SECONDS, A FLANK WEAR SCAR IN EXCESS OF $250\mu m$ RESULTED.....	169
FIGURE 4.77: LASER CUT SIDE OF THE MATERIAL; UNCUT (NORMAL) SIDE OF THE MATERIAL; LASER CUT SIDE OF THE MATERIAL; UNCUT (NORMAL) SIDE OF THE MATERIAL.....	171
FIGURE 4.78: HIGH MAGNIFICATION OPTICAL MICROGRAPH OF A B_6O CUTTING TOOL SURFACE. SIMILARLY; THE SAME EFFECT ON ANOTHER, SEPARATE TOOL.....	172
FIGURE 4.79: SEM MICROGRAPHS OF THE CHAMFER AND RAKE FACES OF TWO $B_6O/Y_2O_3/Al_2O_3$ CUTTING TOOLS SHOWING SURFACE POROSITY.	173
FIGURE 4.81: SEM MICROGRAPH OF THE 100M/MIN AFTER 1 MINUTE OF CUTTING TIME AGAINST CGI. MAGNIFIED IMAGE OF THE WEAR SCAR.	174
FIGURE 4.83: 50M/MIN WEAR SCAR AND CORRESPONDING EDS TRACES.	176
FIGURE 5.1: SEM MICROGRAPH OF THE B_6O/Co SINTERED COMPACT, THE SIZE OF THE FORMED COBALT BORIDE PHASE (WHITE) CAN BE SEEN TO BE APPROXIMATELY 4 TO 5 MICRONS: THE SAME APPROXIMATE SIZE AS THE STARTING POWDER (5 MICRONS). B_6O/CoO MATERIAL WITH CoB PHASES APPROXIMATELY 30 MICRONS IN SIZE: THE STARTING POWDER POSSESSED AN AVERAGE PARTICLE SIZE OF 34 MICRONS.	180
FIGURE 5.2: THE COBALT-BORON PHASE DIAGRAM SHOWING THAT THE CoB PHASE IS MOLTEN ABOVE $1460^{\circ}C$ AT 50AT. % OF COBALT AND BORON (AT AMBIENT PRESSURE).....	182
FIGURE 5.3: COBALT-OXYGEN PHASE DIAGRAM UP TO 60AT. % OXYGEN.....	183
FIGURE 5.4: PHASE DIAGRAM OF THE B- B_2O_3 SYSTEM AT 5 GPa	183
FIGURE 5.5: Fe-O-B TERNARY PHASE DIAGRAM GENERATED FOR A TEMPERATURE OF $700^{\circ}C$	185
FIGURE 5.6: DIAGRAM SHOWING EXPECTED FeB, Fe_2B LAYERING	187
FIGURE 5.7: Fe-B PHASE DIAGRAM	188
FIGURE 5.8: GAMMA-Fe AND ALPHA-Fe SOLVUS CURVES	188
FIGURE 5.9: Fe-O-B TERNARY PHASE DIAGRAM GENERATED FOR A TEMPERATURE OF $900^{\circ}C$	189
FIGURE 5.10: Fe-O-B TERNARY PHASE DIAGRAM GENERATED FOR A TEMPERATURE OF $1100^{\circ}C$	191
FIGURE 5.11: LINE SCAN OF THE $1100^{\circ}C$ DIFFUSION COUPLE ON THE CGI SIDE SHOWING REGIONS AND FEATURES OF INTEREST	192
FIGURE 5.12: BINARY PHASE DIAGRAM OF THE C-Fe SYSTEM SHOWING THE COMPOSITION OF THE CGI USED IN THIS PROJECT (VERTICAL LINE) AND THE TEMPERATURE OF $1100^{\circ}C$ AS THE HORIZONTAL LINE INDICATED	193
FIGURE 5.13: C-Fe-Si PHASE DIAGRAM: STABLE VERTICAL SECTION AT 2.08 MASS PERCENT SILICON.	195
FIGURE 5.14: Fe-O-B TERNARY PHASE DIAGRAM PREDICTED FOR $1300^{\circ}C$	197
FIGURE 5.15: PARTIAL PRESSURE VS. TEMPERATURE CURVES OF THE GASEOUS PHASES PREDICTED TO EXIST AT 80% RELATIVE HUMIDITY.	200

LIST OF TABLES

TABLE 2-1: STRUCTURAL DATA FOR SOME PHASES CRYSTALLIZING IN THE B_4C -TYPE STRUCTURE I.E. SPACE GROUP $R\bar{3}m$ NO. 166, HEXAGONAL AXES.	23
TABLE 2-2: SUMMARY OF RUNS PERFORMED BETWEEN AMBIENT PRESSURE AND 10 GPa IN THE TEMPERATURE RANGE OF 1200 TO 1800°C BY HUBERT ET AL.	25
TABLE 2-3: SUMMARY OF THE MECHANICAL PROPERTIES OF B_6O COMPOSITE MATERIALS PRIOR TO ANDREWS.	34
TABLE 2-4: MATERIAL PROPERTIES OF THE CERAMIC CUTTING TOOLS USED IN THE WORK OF PRETORIUS ET AL.	50
TABLE 2-5: PROPERTIES BEFORE AND AFTER HEAT TREATMENT OF $B_6O/Y/Al$ SELECTED MATERIALS....	58
TABLE 3-1: COMPOSITION OF CGI USED	83
TABLE 4-1: DURATION OF MILLING, SPEED, AND SPREAD OF THE PARTICLE SIZES RESULTING FROM THE MILLING PROCESS.	87
TABLE 4-2: AVERAGE PARTICLE SIZES OF THE STARTING POWDERS FOR THE ADDITIVES USED IN THE ULTRAHIGH PRESSURE SINTERING POWDER PREPARATION	90
TABLE 4-3: IRON AND CHROMIUM WEIGHT PERCENTAGES IN THE B_6O POWDER BATCHES AFTER WASHING AND ICP ANALYSIS.	90
TABLE 4-4: PROPERTIES OF HOT PRESSED PURE B_6O MATERIALS USED IN THIS PROJECT	92
TABLE 4-5: PROPERTIES OF SPS $B_6O/Y_2O_3/Al_2O_3$ MATERIALS USED IN THIS WORK.....	93
TABLE 4-6: DENSITY AND OPEN POROSITY RESULTS OF THE SINTERED COMPACTS.....	94
TABLE 4-7: HARDNESS MEASUREMENTS PERFORMED BY THE IKTS TEAM.....	94
TABLE 4-8: DETECTED PHASES ON EITHER SIDE OF THE 700°C DIFFUSION COUPLE IN ORDER OF ABUNDANCE.....	113
TABLE 4-9: DETECTED PHASES ON EITHER SIDE OF THE 900°C DIFFUSION COUPLE IN ORDER OF ABUNDANCE.....	119
TABLE 4-10: SUMMARY OF THE ATOMIC PERCENTAGES REPORTED BY EDS SCANS OF THE B_6O SURFACE OF THE 1100°C DIFFUSION COUPLE.	124
TABLE 4-11: SUMMARY OF THE ATOMIC PERCENTAGES REPORTED BY EDS SCANS OF THE CGI SURFACE (HIGHER MAGNIFICATION REGION) OF FIGURE 4.33 OF THE 1100°C DIFFUSION COUPLE.....	125
TABLE 4-12: DETECTED PHASES ON EITHER SIDE OF THE 1100°C DIFFUSION COUPLE RANKED ACCORDING TO ABUNDANCE	128
TABLE 4-13: DETECTED PHASES ON EITHER SIDE OF THE 1300°C SEPARATED DIFFUSION COUPLE RANKED ACCORDING TO ABUNDANCE	135
TABLE 4-14: THE DETECTED PHASES BY XRD ON THE YTTRIA-ALUMINA B_6O SAMPLE IN DECREASING ORDER OF ABUNDANCE.....	160
TABLE 5-1: WETTING OF HOT-PRESSED BORON SUBOXIDE SAMPLES.....	186

1 INTRODUCTION

1.1 Subject of the dissertation

The dissertation concerns the work performed during the Masters program of the author in the field of advanced boron suboxide (B_6O) ceramic materials as potential cutting tool materials intended for the machining of hard to machine ferrous metals, specifically compacted graphite cast iron (CGI). The dissertation evaluates the thermodynamic, thermochemical and diffusion properties and characteristics of such materials at expected machining temperatures, examines wear (tribological) behaviour of the materials concerned as well as oxidation resistance and ultrahigh pressure sintering characteristics of such materials. Failure analyses and thermodynamic predictions regarding performance of these materials are also investigated.

1.2 Background to the project

1.2.1 Collaborative nature of the project

This project has been a collaborative effort between the IKTS team based in Dresden Germany who performed various analytical procedures and produced cutting tool materials and the Ceramics group based at the University of the Witwatersrand Johannesburg. Cutting tool fabrication was performed in collaboration with Element 6 Ireland and SEM and ultrahigh pressure work (UHP) was performed at Element 6 Springs, South Africa.

1.2.2 Motivation for research covered by the project

A number of ferrous metals such as compacted graphite cast iron (CGI) and austempered ductile cast iron (ADI) possess very good properties in terms of strength and toughness and could find extensive use in the motor industry for the creation of high power diesel engines among other potential applications^{1, 2}. The problems with using such materials has been the inability to effectively and cheaply machine these materials because of the high degree of wear (abrasive and chemical) that is experienced by the cutting tools during machining these materials and the

poor tool life experienced by most cutting tools used to machine them. Boron suboxide, being a superhard material comparable to the hardness of cubic boron nitride and polycrystalline diamond, could be a potential candidate for the machining of difficult to machine ferrous metals. Recent work^{3, 4, 5} has greatly improved the fracture toughness of boron suboxide based materials to the point where the fracture toughness is believed to be comparable to that of polycrystalline cubic boron nitride tools typically used to machine such metals. Because of this, the wear performance of boron suboxide based cutting tool materials is required knowledge if this material is to find use as an industrial cutting tool. An understanding of the thermodynamic and thermochemical stability and behaviour of these materials both individually and in contact with the workpiece material is relevant to machining because machining (dry turning) without a lubricant requires a tool that can tolerate high cutting temperatures (up to 1100°C typically) and possesses both high hardness and fracture toughness. Furthermore, machining (especially in atmospheric conditions) can result in a host of chemical wear mechanisms between tool and workpiece and the atmosphere that require an in-depth understanding before proceeding with the launch of the material as industrial cutting tool material.

In essence, this project represents the logical step forward from theoretical and experimental improvement and optimization of B₆O, which has been investigated in detail in recent years, into an evaluation of its practical potential industrial applications.

1.3 Objectives of the dissertation

The objectives of the dissertation are to:

- Provide an insight into the thermodynamic behaviour of B₆O based materials at expected machining temperatures and conditions
- Describe the fabrication of cutting tools from selected cutting tool materials of choice (B₆O composites)
- Evaluate the performance of turning tests on CGI and perform wear scar and failure analyses on the tools in order to evaluate the material and compare it to its closest rival, polycrystalline cubic boron nitride
- Produce ultrahigh pressure materials with superior properties for potential future evaluation as industrial cutting tool materials

- Perform static interaction diffusion couple experiments in order to evaluate the chemical reactivity of tool and workpiece materials across a range of expected machining temperatures
- Investigate the oxidation resistance of B_6O in an attempt to predict reactions at machining temperatures in air.

1.4 Scope and limitations

This project concerns the abovementioned objectives and the evaluation of the first batch of produced B_6O cutting tool materials. It investigates the cutting performance of one specific cutting tool geometry between B_6O material and polycrystalline cubic boron nitride based material. The objectives as outlined above were addressed in such a way as to provide an initial insight into the potential problems and performance facing B_6O based cutting tool materials in machining applications of hard to machine ferrous metals, specifically CGI. Ultrahigh pressure results while reported here in terms of characterisation are not reported in terms of turning tests because these were not completed by the completion of the volume of work required for this degree and the work is an ongoing process.

1.5 Plan of development

An in depth literature review of superhard and related boron rich materials is initially presented in Chapter 2 followed by a review of machining operations, wear modes and mechanisms and previous turning tests on tool materials that could compete with B_6O based cutting tools. The concept of static interaction diffusion couples is explained, followed by high temperature studies on B_6O based materials.

The methodology section (Chapter 3) covers the various procedures undertaken during the project, ranging from powder preparation to sintering and characterisation of the sintered compacts. Tool preparation and turning tests are described as well as diffusion couples and oxidation resistance experiments.

The results section (Chapter 4) begins with powder preparation results and characterisation of sintered compacts, followed by static interaction diffusion couple

results, turning test results and oxidation resistance testing as well as a tool failure analysis investigation, followed by a detailed discussion (Chapter 5) and conclusions (Chapter 6) that can be drawn from the work covered in this project.

2 LITERATURE REVIEW

2.1 Hard materials and boron

Materials formed between light elements (typically these belong to the ceramic class of materials) exhibit a wide range of properties such as high hardness, low density, interesting electrical characteristics, heat refractive properties, as well as inertness and good wear resistance. These materials frequently contain boron as a component for example cubic boron nitride, boron carbides and boron suboxides⁶. In terms of structure, these materials generally belong to one of the two following groups: tetrahedrally coordinated diamond-like structures e.g. sphalerite and wurtzite types of structure, and icosahedral boron rich structures comprised of icosahedra (20 sided polyhedra) comprising twelve atoms.

Because boron possesses three valence electrons, it can bond covalently to a wide variety of other atoms, opening up a range of possibilities in terms of product phases. It is also possible for boron, with its unpaired electrons, to form bonding functions that provide the possibility of forming a great many electronic and ultimately molecular configurations⁷. Boron itself occurs in three phases, two of which are crystalline (α and β -rhombohedral) as well as a third amorphous phase. The most reactive phase of boron is amorphous boron (no crystalline characteristics) which leads to the increasingly more stable α and then β crystalline phases as temperature (and pressure) increases⁷.

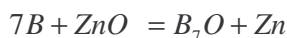
2.2 Synthesis of boron suboxide (B_6O)

Boron rich compounds and their chemistry is an active subject in the sciences today because of their abundance of interesting physical and chemical properties^{8, 9, 10 and 11}.

B_6O was first thought to exist by Wientraub in 1909. From then on, B_2O , B_6O and $B_{13}O_2$ were successfully synthesized by chemists but lacked defined structures and chemical formulae⁸. Badzian was the first to point out that boron suboxide is a super-hard material⁸ and since then, scientists have paid the material more attention. Various methods of synthesis of boron suboxide have been used to date; these

include the reduction of B_2O_3 with B, Mg or Si at high temperature or the oxidation of B with various oxidizing agents such as MgO , CrO_3 , $KClO_3$ etc at very high temperature for long periods of time. Later in this review, more recent efforts will be discussed, which have proven less difficult at synthesising B_6O ⁷.

A method of synthesis of B_6O was devised in the early 1990's by Liu and Zhao which makes use of the oxidation of boron with an excess of zinc oxide under a pressure of 3.5 GPa and a temperature of 1200 °C according to the following formula⁸:



In this formula B_7O is effectively the same as B_6O_{1-x} where $x < 1$; in that B_6O is usually oxygen deficient. In some literature, B_6O_{1-x} is referred to as B_7O ⁸.

The method in question, although effective at producing non-stoichiometric B_6O , is more expensive and complex than is necessary due to the use of such high temperatures and pressures. The authors also comment on the problems associated with the methods of the oxidation of boron to produce boron suboxides this way, especially contamination of the final product with metal borides, problems with effective containment of the highly reactive contents as well as 'high pressure shooting' (loss of material through a loss in containment) at high pressures. The method of producing boron suboxide by using ZnO reduction of boron does not produce gases and does not produce stable zinc borides, but still requires high pressures and temperatures and is thus expensive.

A pure and well crystallized product was reported containing a single phase of B_6O and was not contaminated by boron or metal borides⁸.

2.3 Super-hard boron rich materials:

Torsten Lundström in his comprehensive paper on superhard materials¹² explains that the hardness of a material is dependent on various types of defect (dislocations, grain boundaries and point defects) and that is generally agreed within the materials community that the hardest materials are to be found under certain members of the group of light elements (e.g. boron and carbon) due to the high bond strengths that occur between such materials characteristically. Hard materials can also be found in compounds between such materials e.g. cubic boron nitride (cBN) as mentioned

earlier in this review. The materials comprised of such elements also possess characteristically high bulk moduli¹².

B₆O of the α -rhombohedral type has been investigated by several researchers over the years due to its ceramic nature and as a potential new structural material. Many higher borides comprising B₁₂ sub-structural units have also been investigated. These borides have unique bonding properties not easily explainable by the usual valence theory¹³. Early work on B₆O was directed towards determination of the probable parameter range for the stoichiometry of B₆O before the study on Rietveld refinement conducted by Kobayashi et al¹³. The correct oxygen position in the crystal structure of B₆O remained an open question until this study was conducted.

Oxygen deficient structures of boron suboxide samples were revealed using the Rietveld refinement method. It was found that the crystal structure of B₆O belongs to the $R\bar{3}m$ space group (i.e. rhombohedral or trigonal space group), number 166 in the list of three dimensional crystallographic space groups¹³. The abovementioned technique revealed that the oxygen occupation factor is around 0.76 and the unit cell dimensions were found to be $a_{\text{hex}} = 0.5367\text{nm}$, and $c_{\text{hex}} = 1.2328\text{nm}$ in the hexagonal unit cell.

Using the data obtained from the analysis, the structure of B₆O was proposed as displayed later in figure 2.4^{14, 15}.

The structure of boron suboxide is built of eight icosahedra at the apexes of a rhombohedral unit cell. Oxygen atoms are triply coordinated to boron atoms in separate icosahedra in the (001) plane¹⁵.

Investigations into boron suboxide have revealed that it can possess a Vickers hardness as high as 45 GPa (100g load) for a single crystal and a fracture toughness¹⁶ of up to 4.5 MPa.m^{1/2} compared to cubic boron nitride which has a hardness of up to 60 GPa and a fracture toughness¹⁷ of 2.8 MPa.m^{1/2} while diamond itself possesses a single crystal fracture toughness of 5 MPa.m^{1/2} a hardness of 10 to 100GPa^{18, 19}. It can thus be seen that boron suboxide possesses properties comparable to diamond and cubic boron nitride.

Lundström also iterates that the borderline between hard and super-hard materials is not always clear due to the complex nature of hardness and the difficulty in measuring it with reasonable accuracy. SiC and TiC with microhardness values of around 30 GPa can be considered borderline materials. If this choice is accepted,

then it would place further compounds in the super-hard group including most of the compounds between the light elements Be to O and some further compounds. It is noted in his paper that a number of boron-rich materials belong to the same space group as boron suboxide as illustrated in table 2-1 below.

Table 2-1: Structural data for some phases crystallizing in the B_4C -type structure i.e. space group $R\bar{3}m$ no. 166, hexagonal axes¹².

Atom	Position	x	z	Occupancy
$B_{12}S_{2-y}$ ($y \approx 1$)				
B(1)	18h	0.1714(4)	0.6387(3)	1.0
B(2)	18h	0.1078(2)	0.8845(3)	1.0
S	6c	0	0.4087(2)	0.485(6)
$B_{12}Se_{2-y}B_y$ ($y \approx 1$)				
B(1)	18h	0.1707(2)	0.6370(3)	1.0
B(2)	18h	0.1059(3)	0.8828(2)	1.0
B(3)	6c	0	0.382(1)	0.531(2)
Se	6c	0	0.4192(1)	0.469(2)
$B_6O_{0.83}$				
B(1)	18h	0.1571(3)	0.6389(2)	1.0
B(2)	18h	0.1125(2)	0.8870(2)	1.0
O	6c	0	0.3773(2)	0.831(5)

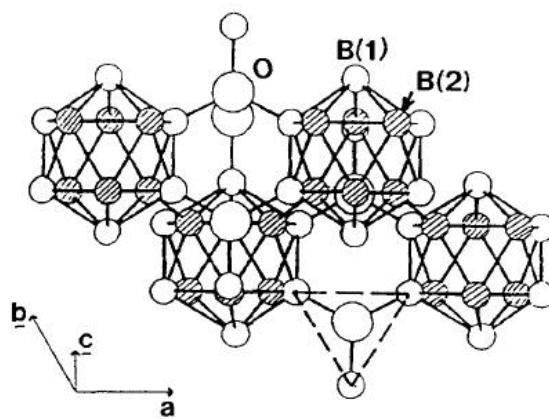


Figure 2.1: The crystal structure of boron suboxide (B_6O)¹⁴

The oxygen atoms can be seen (according to the table and figure 2.1 above) to occupy position 6c (hexagonal axes) and are situated 3.03 Å from each other. According to Lundström, such a distance is too great to allow direct bonding between these atoms. As such, each oxygen atom is bonded to three equatorial boron atoms

belonging to different boron icosahedra¹². Lundström also observed that there are no more than two oxygen atoms per icosahedron¹⁴.

Only partial occupancy of the oxygen atoms in boron suboxide has been observed in several investigations into its structure^{8, 12, 13 and 14}. A vacancy concentration of 17 – 22% has been found to be the general range in which it occurs at room temperature and pressure¹². As mentioned above, there is a relation between the temperature of the material and the oxygen occupancy factor; this can be summarized by the formula B_6O_{1-x} where x decreases with pressure and increases with temperature⁶.

Lundström mentions in one of his later papers, that boron suboxide may possess semiconductivity and that it possesses a higher hardness than boron carbides, hence the attention it has received in potential industrial applications¹⁴.

2.3.1 High pressure and high temperature synthesis:

Hubert et al¹⁵ successfully synthesized micrometer sized boron suboxide crystals using high pressures and high temperatures when sintering. The results of their investigation are pertinent to this literature review because they are representative of a significant leap in the observation and understanding of boron suboxide and its structure as well as the formation of larger crystals than ever before.

Hubert et al mention that the development of B_6O in industrial applications has been impeded by the difficulty associated with synthesizing material of a high degree of crystallinity¹⁵.

Prior to the work performed by Hubert et al¹⁵, no single crystals of boron suboxide were obtained. Sintered ceramics via hot-pressing and fine powders were, however, produced previously, as mentioned above. In their work, Hubert et al¹⁵ synthesized B_6O by the reduction of B_2O_3 with Boron under a pressure of 10GPa using a multi-anvil press at temperatures between 1200 and 1800 °C. Characterization of the resulting samples was performed by utilizing x-ray diffraction (XRD), scanning and transmission electron microscopy as well as parallel electron energy-loss spectrometry (PEELS).

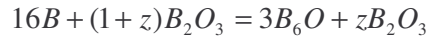
The team was very thorough in their investigation and table 2-2 below illustrates their various methods of producing densified boron suboxide products.

Table 2-2: Summary of runs performed between ambient pressure and 10 GPa in the temperature range of 1200 to 1800 °C by Hubert et al¹⁵.

run	initial mixture B ₂ O ₃ :16B	P (GPa)	T (°C)	time (min)	products	particles morphologies		optical microscopy ^f
						SEM ^{c,e}	TEM ^{d,e}	
RP1	2	1 atm	1400	480	B ₆ O + B ₂ O ₃ (s) + am	fine irregular euh	euh (to 1 μm)	Br powder
642	1	2	1700	30	B ₆ O + aph	sintered fine grains	euh < 1 μm	R-Br
679	1.5	2	1700	30	B ₆ O + B ₂ O ₃ (s) + am	sintered fine grains	euh >> icos	R-Br
656	1.2	3	1700	30	B ₆ O + B ₂ O ₃ (s) + am	sintered fine grains	euh >> icos	R-Br
667	1.1	4	1700	30	B ₆ O + B ₂ O ₃ (s)	icos in sintered fine grained matrix	euh > icos	dark R icos
672	2	4	1700	120	B ₆ O + B ₂ O ₃ (s)	icos (to 30 μm) >> euh crystals (to 40 μm)	euh > icos	dark R icos >> O-R euh
423	4	5	1800	30	B ₆ O + B ₂ O ₃ (s)	icos (0.1–5 μm)	icos. (to 1 μm)	O-R icos >> dark R icos
558	1	5.5	1700	30	B ₆ O + B ₂ O ₃ (s) + am	icos (to 20 μm)	euh > icos	O-R icos >> dark R icos
620	1.05	5.5	1700	30	B ₆ O + B ₂ O ₃ (s)	icos (to 20 μm)	icos >> euh	O-R icos >> dark R icos
653	1.2	5.5	1700	30	B ₆ O + B ₂ O ₃ (s)	icos (to 10 μm)	icos >> euh	O-R icos >> dark R icos
451	2	5.5	1800	5	B ₆ O + B ₂ O ₃ (s)	euh > icos (to 1 μm)	icos > euh	O-R powder
555	1	7.5	1700	30	B ₆ O + am	sintered fine grains > icos	euh > icos	O-R powder
488	4	7.5	1700	30	B ₆ O + B ₂ O ₃ ^b	icos (1–3 μm)	icos (to 1 μm)	O-R icos
396	4	10	1200	180	B ₂ O ₃ ^b + B ₆ O	sintered fine grains	euh	O-R powder
404	1	10	1600	20	B ₆ O + am	sintered fine grains	euh	O-R powder
401	4	10	1800	5	B ₆ O + B ₂ O ₃ ^b	sintered fine grains > euh (1–10 μm)	μm-sized euh	O-R powder

^a The products determined using XRD and PEELS are listed in order of decreasing abundance. ^b B₂O₃ polymorphs; am, amorphous phase (minor amounts); (s), water-soluble boron oxide(s). ^c SEM observation of the coarse part of the sample. ^d TEM observation of the fine part of the sample. ^e >, abundance; euh, euhedral grains; icos, icosahedral grains. ^f Br, brown; R, red; R-Br, reddish-brown; O-R, orange-red.

The team combined amorphous boron powder and B₂O₃ according to the following reaction in order to produce their B₆O:



Powder XRD showed that boron suboxide was successfully formed over the entire temperature and pressure range as well as other products including amorphous material. The boron to oxygen ratio was determined using PEELS which revealed that the XRD results could indeed be confirmed as accurate.

It was important for the team to note, however, that well crystallized boron suboxide was observed to be formed between 4 and 5.5 GPa of pressure at elevated temperatures of 1700 °C and especially in mixtures where the B:B₂O₃ ratio is less than one i.e. when B₂O₃ is in excess¹⁵.

It was also noted that good crystals were formed when even higher pressures of 7.5 to 10 GPa were used, but these pressures had the disadvantage of producing insoluble B₂O₃ (polymorphs) which hindered the removal of the amorphous material from the crystalline B₆O.

The morphology of the grains of boron suboxide produced at the different pressures and temperatures are summarized in table 2-1. It was noted that grains larger than one micron can be divided into several categories. These categories include multiply twinned icosahedral particles, euhedral (trigonal grains), intergrown subhedral to anhedral icosahedral grains and rounded anhedral sintered masses formed by submicron grains, as can be seen in figure 2.2 and 2.3 ¹⁵.

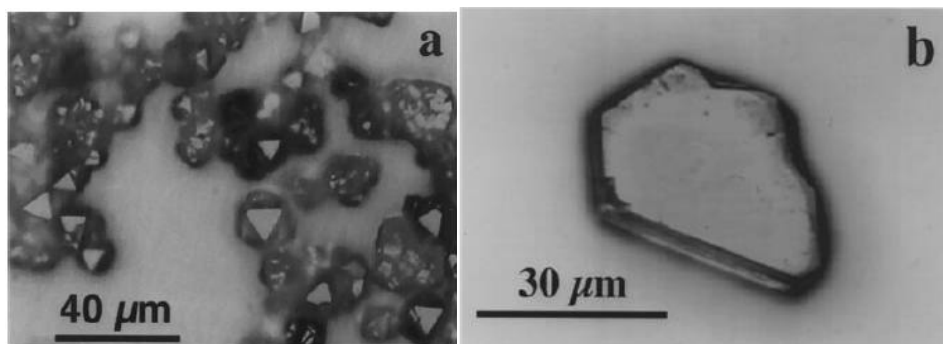


Figure 2.2: Optical images of orange – red coloured B_6O grains showing triangular faces of reflected light in (a) and a euhedral crystal in (b) ¹⁵.

It was noticed by Hubert et al that high pressure – high temperature techniques produced B_6O closer to the ideal composition and stoichiometry ¹⁵.

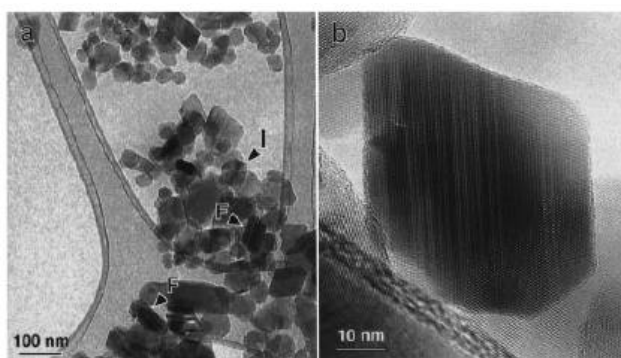


Figure 2.3: TEM photographs of boron suboxide crystals at (a) lower magnification displaying euhedral morphologies with some faulted crystals (F) and icosahedral twins (I); (b) A high resolution photograph showing stacking faults and twin lamellae ¹⁵.

The group concluded that samples prepared under high pressure and at high temperatures are less oxygen deficient and are closer to the nominal B_6O composition. They also recognize that the shape and rigidity of the icosahedral B_6O particles formed in such a synthesis could have very useful wear and abrasive properties¹⁵.

McMillan et al²⁰ synthesized B_6O as described previously¹⁵ using multi-anvil apparatus pressing mixtures of B and B_2O_3 in various ratios at pressures ranging from 1 to 10 GPa and within the temperature range of 1200 to 1800 °C for times ranging from several minutes to several hours. The same methods of analysis were used as described above. Figure 2.4 shows SEM micrographs of the produced B_6O crystals and the unit cell of B_6O . Figure 2.5 shows TEM micrographs and diffraction patterns of the material respectively.

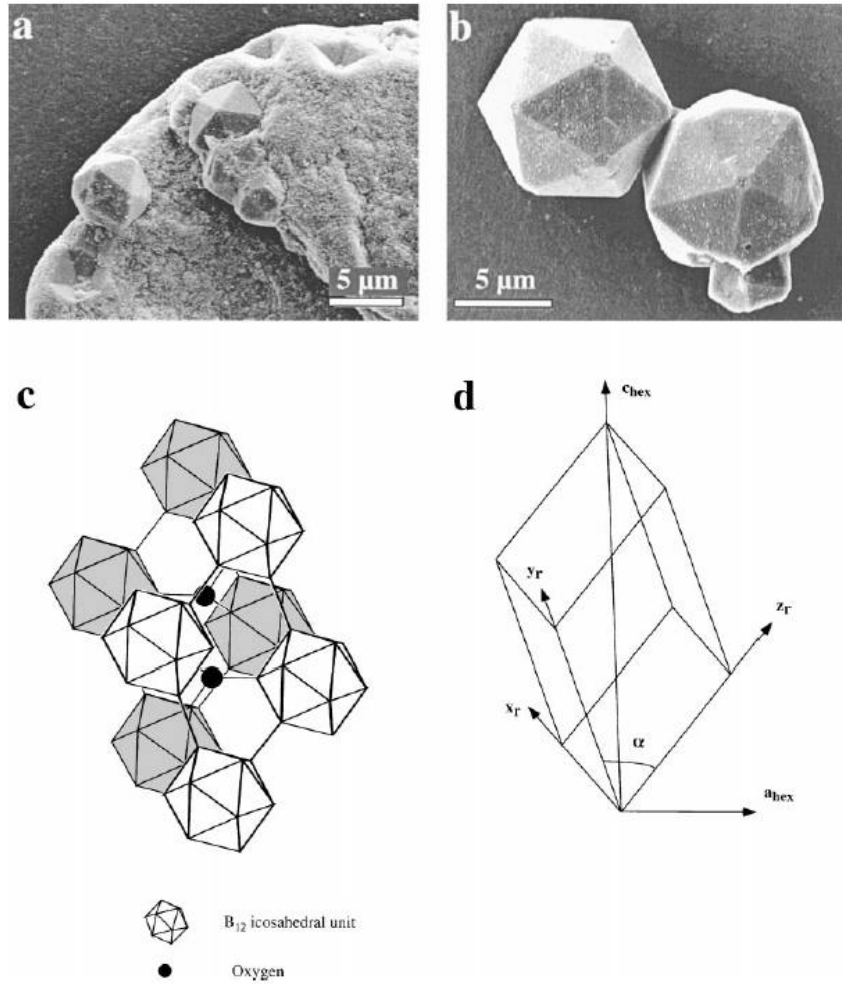


Figure 2.4: (a) SEM micrograph of B₆O particles (multiply-twinned) in a fine-grained matrix derived from the high pressure synthesis experiments. (b) Two icosahedra liberated from the previously surrounding matrix material, one is orientated along a three-fold axis (i.e. a triangular face) and the other is orientated along a five-fold axis (pentagonal structure). The re-entrant impressions visible on the crystals are indications of multiple twinning. (c) The ideal structure of stoichiometric B₆O as described previously. (d) An outline of the rhombohedral unit cell with rhombohedral axes (x_r , y_r , z_r) and hexagonal axes (c_{hex} , a_{hex}) shown. The angle α can distort from its ideal 70.5° (tetrahedral angle) depending on the ratio of $c_{hex} : a_{hex}$.²⁰

The presence of re-entrant faces that can be seen in figure 2.4b are indicative of multiply-twinned particles rather than simply a quasi-crystalline material²⁰. The group theorized that the particles of boron suboxide had grown from within the melt via Mackay packing. Mackay packing operates by means of successive shells of

icosahedral boron units (B_{12}) forming and orientating themselves around a central nucleus²⁰.

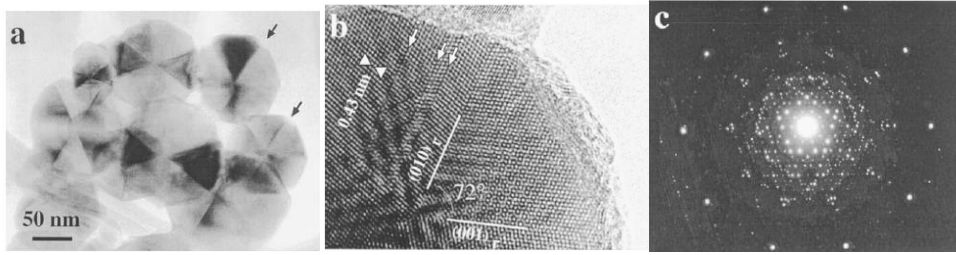


Figure 2.5: (a) TEM image (low magnification) of MTP's of B₆O showing individuals in Bragg orientation, these are visible as the darker regions. (b) High resolution TEM image of boron suboxide in the [100] zone axis orientation (rhombohedral) along a five-fold axis of an icosahedron. Stacking faults are indicated by the arrows and the Moiré effect (optical interference pattern) is visible in the central region of the icosahedron due to the superposition of other twin individuals. (c) Electron diffraction pattern of a selected area of a B₆O icosahedral MTP showing five-fold symmetry²⁰.

2.3.2 Mackay Packing

It is stated by McMillan et al²⁰ that Mackay packing is responsible for the structure of boron suboxide. Mackay packing (first described by A. Mackay in 1962) is a non-crystallographic packing scheme for identical spheres by assembling successive shells of these spheres around a central icosahedron. It has been observed that the cubic close packed arrangement of spheres forms a cuboctahedral figure which can be distorted into an icosahedron with little difficulty²⁰. Radiating spheres orient themselves on each of the triangular faces of the central icosahedron, this can be clearly seen in the schematic shown in figure 2.6 and is further demonstrated with relevance to B₆O in figure 2.7.

The group also identified that multiply twinned particles experience difficulty in growing at lower pressures as well as at pressures above 7.5GPa due to cubic close packing being more favourable than Mackay packing at such enormous pressures²⁰.

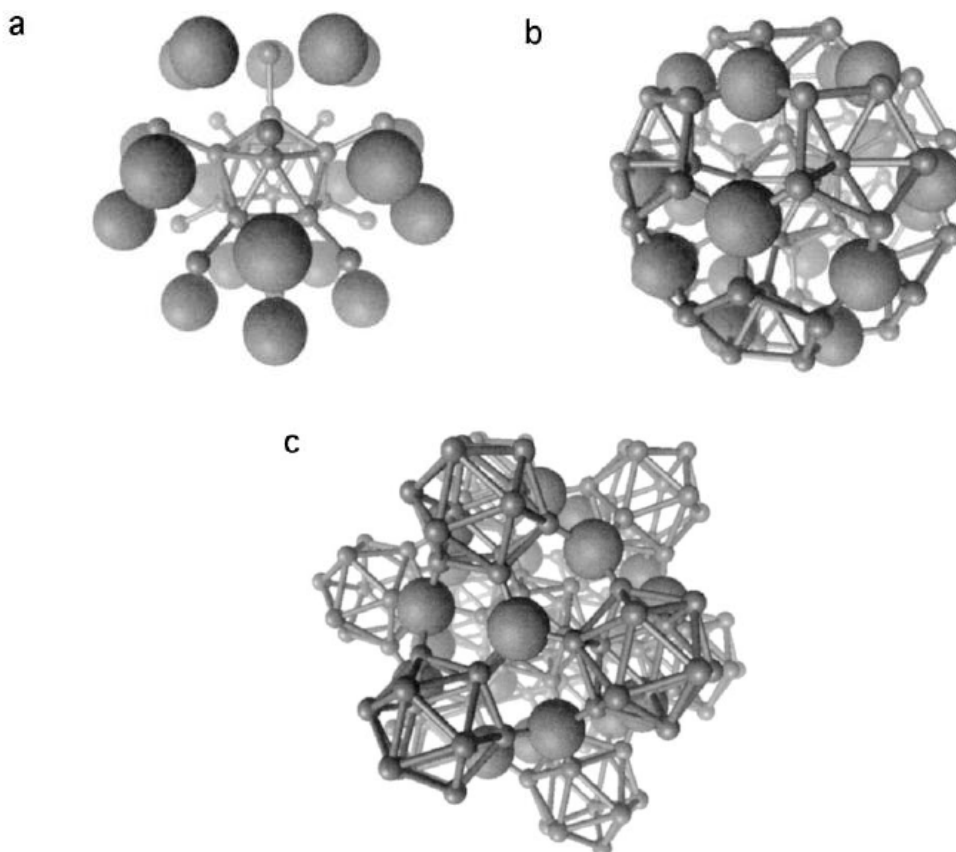


Figure 2.6: The development of the super-icosahedral structure formed by B₆O. This structural progression was developed by McMillan et al²⁰ by using energetics calculations. (a) The central boron icosahedron surrounded by 20 oxygen atoms orientating themselves with the triangular faces of the icosahedron. (b) Oxygen-boron bonds can be seen in this image with the next 'layer' of boron icosahedra orientating around the forming structure. (c) The completed icosahedral 'cage' comprising thirteen boron icosahedra (B₁₂) and 20 oxygen atoms leading to the stoichiometry B₁₅₆O₂₀ i.e. not quite nominal B₆O.

2.4 The hardness of boron suboxide relative to cubic boron nitride

The Vickers hardness of boron suboxide was measured using the diamond indentation method under a loading force of 0.98N (microhardness) by He and Zhao¹⁶. It was found that the hardness was 45GPa and the fracture toughness was 4.5 MPa.m^{1/2} as mentioned earlier. Typically cBN has a hardness of between 45 and 50 GPa under similar conditions, depending on the quality of the material¹⁶. The hardness of single crystals of boron suboxide were tested by He and Zhao as

mentioned above, thus showing that boron suboxide could have great potential as a new ultrahard material. Typically, ultrahard materials have hardness greater than 40 GPa^{16, 21}. It was noted by these scientists was that Vickers hardness tends to decrease with increasing load and a wide variety of hardness values have so far been reported for boron suboxide, ranging from 32 to 38 GPa.

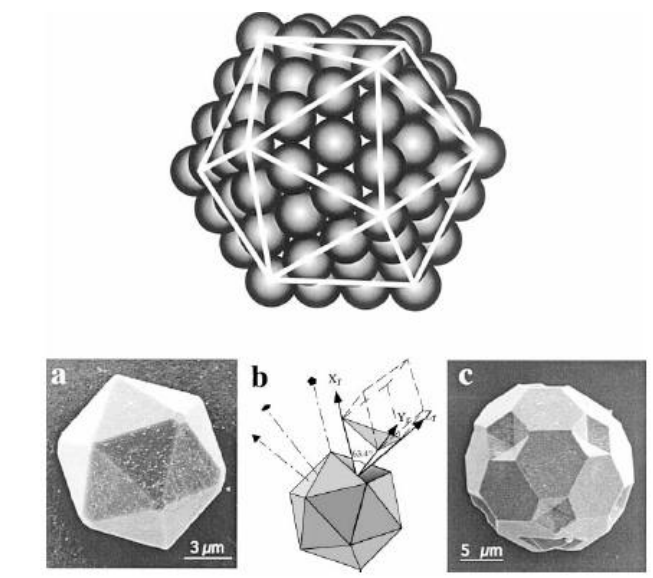


Figure 2.7: (Top) An icosahedral structure formed from Mackay packing in which the central sphere is surrounded by 12 others arranged at the corners of an icosahedron. Additional layers are added by placing spheres above the interstices of the lower layer in a ccp arrangement. (a) SEM image of an isolated B₆O icosahedron. (b) An illustration of the relationship between the icosahedron shape and the tetrahedral unit cell. (c) SEM image of an MTP showing clear re-entrant angles indicative of twinning. This grain displays the same morphology as the C₆₀ molecule²⁰.

2.4.1 Hard and tough boron suboxide based materials

Recently, boron suboxide has been synthesized at temperatures of around 1400 °C from the reaction of amorphous boron powder and boric acid⁷. Additives of aluminium were incorporated and the powder mixture was sintered at 1900 ° at pressures of 50 MPa for 20 minutes. Various weight percentages of Aluminium additives produced varying hardness and fracture toughness values for the sintered compacts. The hardness (30 GPa) was observed to marginally decrease from that of the pure B₆O

compact, yet fracture toughness was substantially improved. The hardest of the composite materials was B_6O with 2.2 wt.% Al additive and this material was also observed to possess the lowest Al_2O_3 content. Its hardness was measured to be 29.3 GPa with a fracture toughness of $3 \text{ MPa}\cdot\text{m}^{1/2}$.

Dense materials with hardness higher than 30GPa and fracture toughness exceeding $3 \text{ MPa}\cdot\text{m}^{1/2}$ were subsequently produced²² by liquid phase sintering techniques and this work was pioneered by Shabalala⁵. He produced boron suboxide composites by firstly synthesizing the starting powder from the reaction of amorphous boron powder and boric acid in the laboratory. Specific additives namely Al and Al_2O_3 were deposited onto the powder by using the chemical vapour deposition technique. In addition, these additives were mixed with the starting material and the CVD and mixing results were compared and contrasted. The resulting materials were then sintered at pressures of 50MPa in a uniaxial hot press for 20 minutes in a temperature range from 1600 to 1900 °C.

An in depth investigation into the phase composition of the resulting microstructures of the sintered compacts was performed. Density and hardness determination was also carried out which revealed measured densities of greater than 97% of the expected theoretical density. It was found that alumina addition via both methods (CVD and mixing) resulted in better mechanical properties than pure B_6O itself, especially in terms of fracture toughness. Furthermore a slight decrease in hardness was observed with the addition of Al_2O_3 , but a corresponding increase in fracture toughness. A secondary phase, namely alumina borate, $Al_{18}B_4O_{33}$, was found to be present in the grain boundaries. This phase is believed to be responsible for the increase in fracture toughness in these materials by means of a mismatching thermal expansion coefficient of this material with the boron suboxide, resulting in residual stresses that are thus capable of influencing crack propagation and hence fracture toughness values. This is not conclusive, however, as secondary phase pockets typically contain residual porosity. It is therefore more likely that the porosity acts as a crack arresting site upon crack propagation, rather than generating residual stresses that result in crack deflection and consequently increased fracture toughness.

It was also noted by Shabalala⁵ that composites produced from carbon addition displayed a marked decrease in hardness values and a substantial increase in fracture toughness.

It has been noted by several researchers including Johnson⁴ (most recently) and Shabalala that the presence of secondary phases in the sintered compacts allows for the presence of toughening mechanisms for example crack bridging and crack deflection. This is assumed to occur because of mismatch in thermal expansion between the grain boundary phases and the B₆O phases, which places the grain boundary and the grains under residual stress^{45, 46}.

The work was further driven forward subsequently to Shabalala's work by the efforts of Andrews in his PhD thesis³ in which he expanded on prior work and explored the properties of new boron suboxide based composites. In his thesis, Andrews discusses the methods used and composites produced by a wide range of authors. Since the focus of the current literature survey is to produce an overview of these properties, table 2-3 has been included for brevity. As a result of the need for brevity, not every paper discussing B₆O can be included, should great detail be required by the reader, the theses of Andrews³ and Shabalala⁵ can be used to this end. Note, though the original of this table is referenced from Andrews³, the reference numbering has been updated to correspond with that of this literature survey as the overlap with the current work is extensive and relevant.

Andrews studied an extensive range of weight percentages of additives specifically Y, Al and Si additions. A broad range of fracture toughness and strength values were obtained ranging from as low as 16.6 GPa and a corresponding toughness of 7.2 MPa.m^{1/2} to the hard and brittle pure B₆O compacts with a hardness of around 35 GPa. In addition, a few composites of TiB₂, TiC and Pd additions were produced but the properties of these were comparable to the Yttria/Alumina additions. In general, good densities were obtained especially with the Yttria/Alumina additives.

Table 2-3: Summary of the mechanical properties of B₆O composite materials prior to Andrews³.

Composite materials	Microhardness, (GPa) 100g load	Fracture toughness, K _{IC} (MPam ^{1/2})	Sintering conditions	Elastic modulus (GPa)	Ref.
B ₆ O crystal	45	4.5	5.5GPa, 2100 °C, 60min	-	16
B ₆ O sintered compact	31-38	<1.5	~21 to 28MPa, 1900 to 2100 °C, unspecified time	470	23
B ₆ O-30 vol.% B ₄ C	~46 (200g load)	Very low	4GPa, 1700 °C, 20min	-	18
B ₆ O-40 vol.% cBN	~46 (200g load)	<1.8	6GPa, 1800 °C, 20min	-	18
B ₆ O-60 vol.% diamond	~57 (200g load)	<1	5GPa , 1700 °C, 20min	-	24
B ₆ O infiltrated with Al	41	8.7	Explosive consolidation followed by 40MPa, 1600 °C, 4h	-	25
B ₆ O coated with Al ₂ O ₃ (Al = 2.2wt %)	31.1 (500g load)	3.1	50MPa, 1900 °C, 20min	514	7
B ₆ O-10 wt% C	22.8 (500g load)	5.5	50MPa, 1900 °C, 20min	-	5

2.5 The use of boron suboxide in drag cutters and drill bits

Aluminium infiltrated boron suboxide based composites were consolidated by two methods by Kayhan²⁵. After sintering for 12 hours at 1450 °C and crushing and grinding of the material to form a powder, explosive consolidation and hot pressing were used to re-compact the samples and observe the results. The introduction of metallic elements, as mentioned above, improves fracture toughness, hence the choice of aluminium infiltrated boron suboxide in this study. Following consolidation, the samples were re-sintered at 1800 °C for two hours under vacuum.

The explosive consolidation and the hot pressing techniques were seen to be successful in consolidating the material. The same average hardness values of 38 – 40 GPa were reported for both compacts. The toughness of the compacts was reported to be between 5 and 6 MPa.m^{1/2}. This high value of fracture toughness has been thought to be unrealistic by other authors because despite the fact that fracture toughness was calculated using three point bend testing, the 'pure' B₆O material produced by the researchers was found to have a toughness of 6.23 MPa.m^{1/2} which is far in excess of the typically brittle pure phase that other authors have confirmed³. Furthermore, the notch radius used was 0.5mm, which is too high to give reliable fracture toughness values.

Temperature stabilities of the boron suboxide based composites were also reported to exceed 1800 °C that is far greater than that of diamond cutters that become less stable around 750 °C. The potential use of this material was thus appreciated by the researchers in terms of its usage as drag cutters, drill bits and in cutting applications²⁵.

2.6 Cutting tools and materials

Ceramic cutting tools have found increasing uses for high speed finishing and high material removal rate during machining operations because of their favourable mechanical properties²⁶. Such properties include high hardness, high abrasion resistance, good strength, high hot hardness, good thermal shock resistance as well as corrosion and wettability resistance²⁷ when cutting metallic materials. Because metal cutting is a complicated process, such properties are required in order for a cutting tool to perform adequately. Unfortunately many ceramic cutting material

candidates possess low toughness and are prone to fracture during machining operations. This is one of the chief reasons why ceramic cutting tools are not more widely used in industry today.

One of the main causes of cutting tool failure and replacement is tool wear. The impact of tool wear on a nation's economy can be very significant. Productivity could be greatly increased by the use of cutting tools less prone to wear and which could consequently be used longer in machining operations. A further result would be the reduction of time wastage while replacing and setting up of the new tool component after a prior failure has occurred, hence further improving efficiency of manufacture.

A possible way to achieve the goal of improved tool life is to make the tools more resistant to wear and to optimize the conditions under which machining is performed in order to prolong tool life. The ideal situation would be one where desirable levels of productivity were attained at an acceptable rate of tool wear²⁸.

In order to diminish tool wear and fracture it is necessary to employ tools in appropriate conditions which can be determined through investigations into the relationships between wear mechanisms taking place, the cutting temperatures and the cutting conditions²⁶. A worthwhile method of achieving this goal is the use of wear maps (or diagrams) that describe the wear of the cutting tool in question during machining operations as a function of machining conditions employed²⁸.

Turning is the operation of rotating the work material (held in the chuck of a lathe) while a tool is held rigidly in a tool post and moved at a constant rate along the axis of the work piece (usually a bar) while removing a layer of material from the surface of the work piece. The cutting speed is the rate at which the uncut surface of the work piece passes the cutting tool (measured in metres per minute) while the feed is the distance moved by the tool in an axial direction at each revolution of work (mm per revolution.)²⁹

Wear maps typically plot the wear modes as a function of cutting conditions. From such maps, it is possible to determine the regions where various wear rates occur, allowing for optimization of the machining operation. Wear maps of several different ceramic cutting tools frequently include regions corresponding to the formation of a built up edge, a safety zone (in which the tool can operate effectively without excessive wear) and a region of plastic deformation or crater wear initiation in which the tool fails to perform satisfactorily²⁸. Wear maps can also include regions showing

abrasion and adhesion wear processes as well regions corresponding to fracture. The wear map depicted in Figure 2.8 below is that of an 85 vol. % cubic boron nitride with TiN binder and a $3\mu\text{m}$ grain size ceramic tool when machining AISI 420 stainless steel.

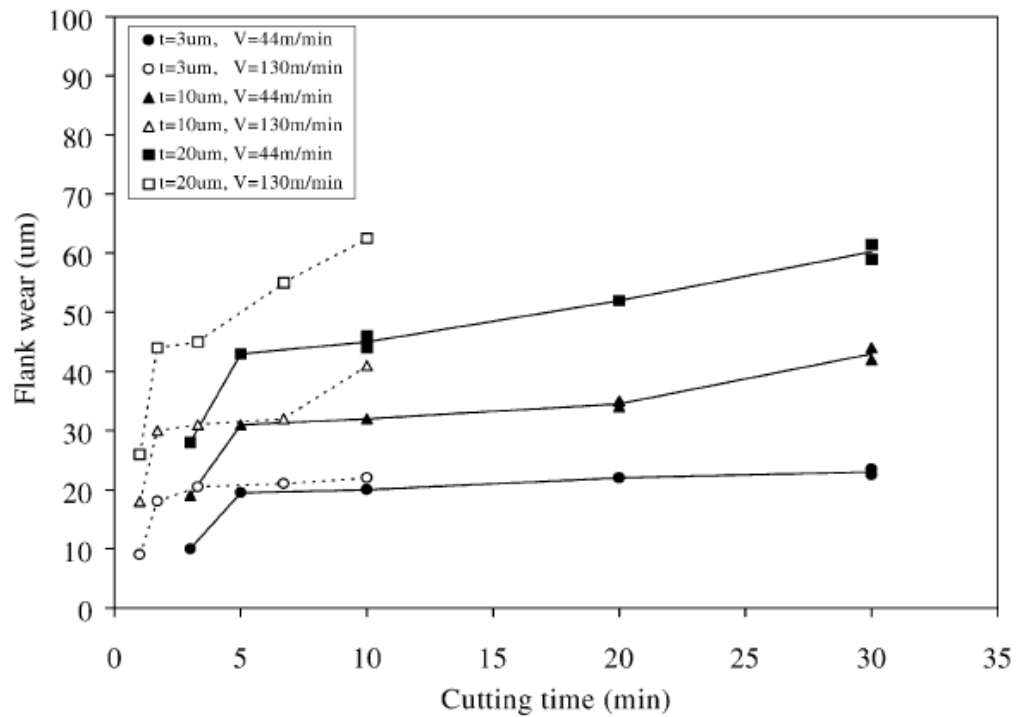


Figure 2.8: Wear map of 85vol. % PcBN cutting tool performance when machining AISI 420 stainless steel at various depths of cut (t) and cutting speeds (v)³⁰.

Other useful graphs of experimental data can also yield useful results as can be seen in figure 2.9. Examples of these include plots of tool life against cutting speed, flank wear against cutting time and flank wear vs. surface roughness at different cutting speeds, feed rates and depths of cut as well as flank wear vs. cutting length, among many others^{31, 32}.

2.7 Properties and classes of tool materials:

Cutting tool materials can be divided into three main categories namely:

- 1) High speed steels
- 2) Cemented carbides
- 3) Ceramic and superhard materials

The third category includes diamond and cubic boron nitride, sialons as well as alumina based composites to date²⁸. Should boron suboxide prove to be a worthwhile cutting tool material, it will also fall into this category in future.

Other methods of improving cutting tool performance include those modified by surface engineering using coating techniques²⁸.

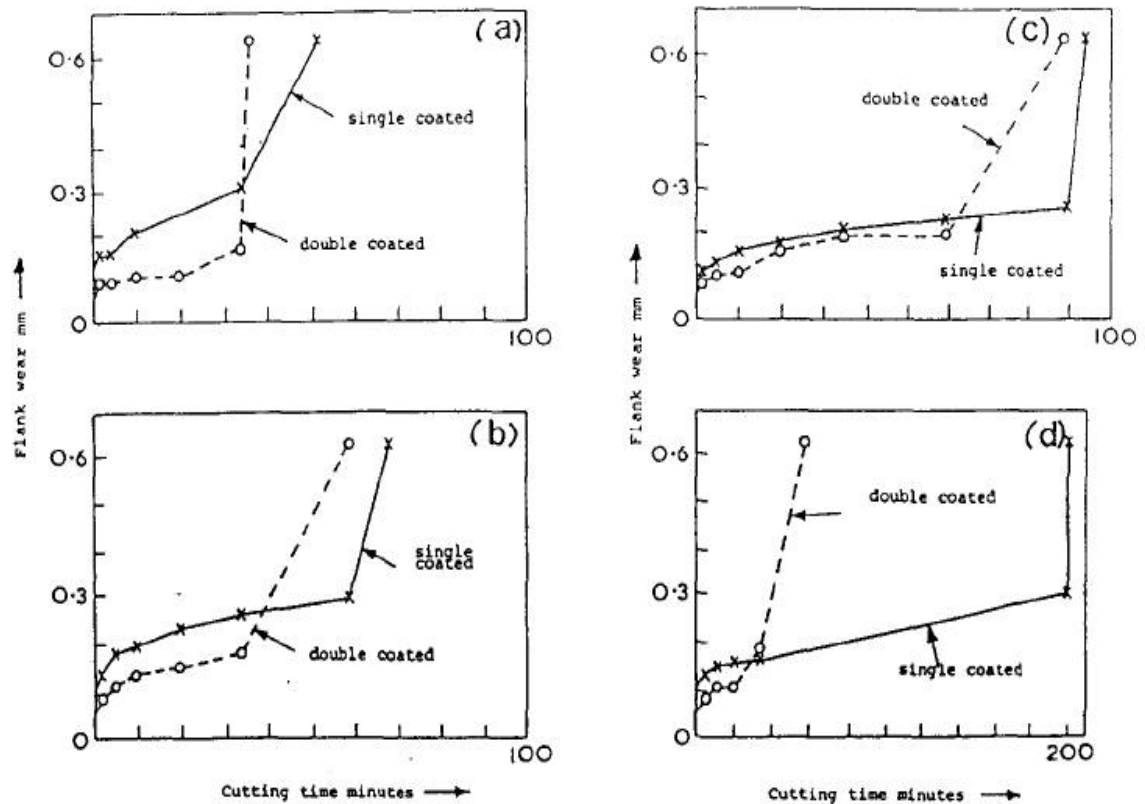


Figure 2.9: Graphs displaying the variation of flank wear with cutting time as described by B. Mills³³ on the cutting properties of high speed steels when machining grey cast iron. (a) M1 HSS (b) M2 HSS (c) M15 HSS (d) T4 HSS type cutting tool at cutting speeds of 65m/min and a feed of 0.035mm/rev.

Cutting tool performance is a complex subject and is dependent on a number of factors that are generally described by the term machinability. Machinability can be measured in terms of surface quality of the finished product, but it is more usual to consider machinability in terms of economic tool life, especially with ceramic tool materials²⁸.

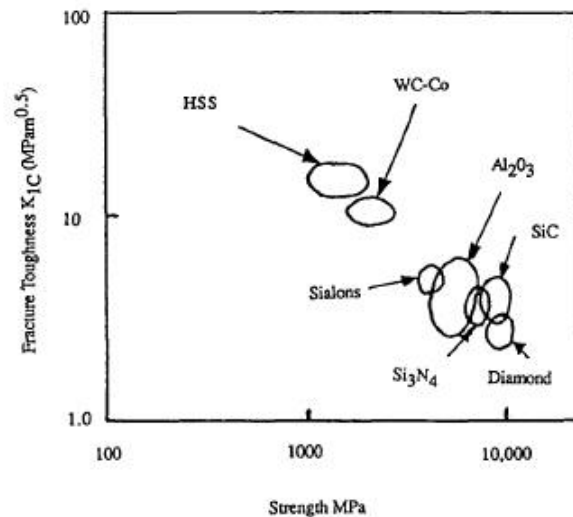


Figure 2.10: Graph showing the fracture toughness versus compressive strength for various cutting tool materials. Note, compressive strength is plotted for all but HSS and WC-Co in this figure. It will be interesting to observe where boron suboxide based cutting tool materials fit on such a graph³³.

2.7.1 Wear modes / processes typical to ceramic cutting tools:

A cutting tool is considered to have failed when sufficient wear has occurred to allow surface finish and dimensional tolerance to be impaired or when catastrophic tool failure occurs or is imminent. Figure 2.11 below shows the wear processes that typically occur on cutting tools during machining²⁸. The fracture toughness and strength of ceramics (which largely determine the nature of tool failure) can vary greatly as illustrated in figure 2.10.

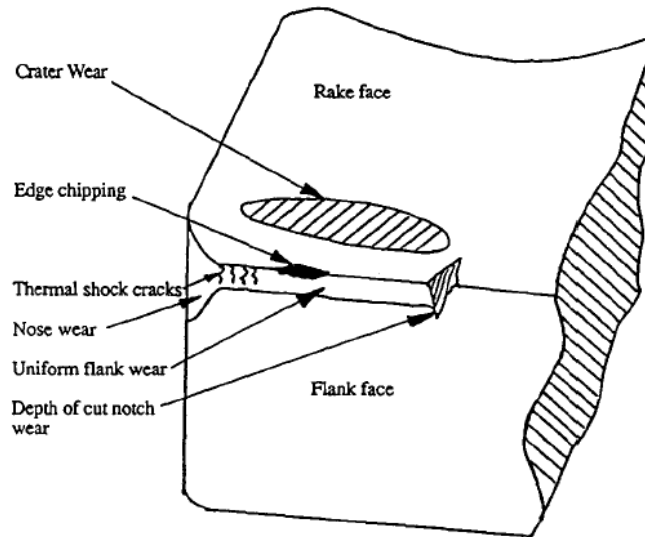


Figure 2.11: Sketch showing wear, thermal shock cracking and edge chipping for ceramic cutting tools²⁸.

The rake face is the face along which the chip of work piece material flows off the work piece during the cutting operation. Crater wear, caused by chemical interaction between the rake face and the hot chip, occurs by diffusion processes between the tool and the chip and also by adhesion between the tool and the chip. Fracture below the adhered surface then leads to the 'crater' phenomenon occurring. This form of wear can be reduced by decreasing the potential solubility of the tool and the chip in each other as well as increasing the chemical stability of the tool²⁸. Diffusion wear typically causes cratering at high cutting speeds and is dependent not only on high temperatures (typical for diffusional processes) but also on the flow rate of the material close to the seized surface²⁹. This form of wear (as well as oxidation) has been documented to occur between cBN cutting tools and ADI / CGI work pieces at higher cutting speeds (further discussed later).

The visible thermal shock cracks in figure 2.11 above are caused by large thermal gradients at the cutting edge and are normally found at the tool nose (cutting edge) and the flank face. Thermally shock resistant materials with high toughness and thermal conductivity as well as a low thermal expansion coefficient can minimize this effect. . Figure 2.12 shows the typical wear modes that can be experienced by ceramic cutting tools in machining.

Other wear modes specific to the ceramic machining of ADI, CGI and hardened steel include adhesion wear and abrasive wear along with the diffusion-oxidation wear described above.

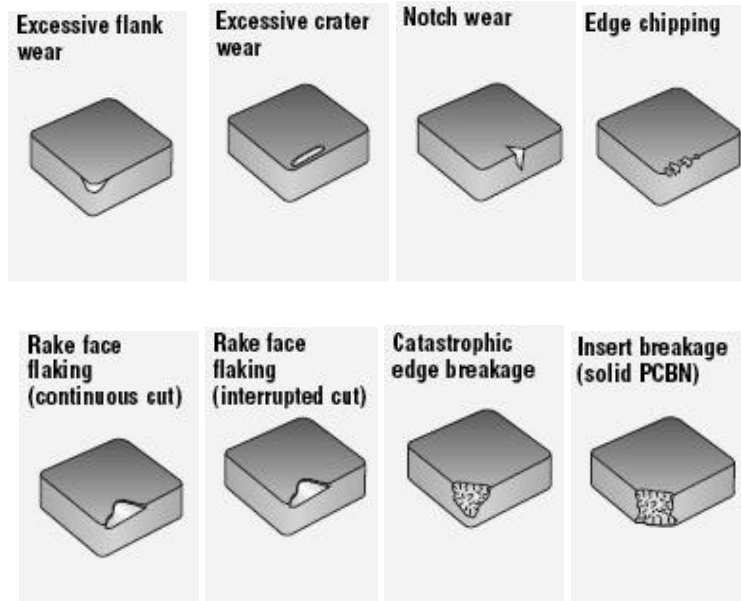


Figure 2.12: Various wear modes displayed on a typical PcBN cutting tool as described by Seco (Sweden) ³⁴.

In general, the classes of ceramic cutting tools can be characterized as; alumina based ceramics, alumina based composites, sialon ceramics as well as the superhard materials which include diamond and cubic boron nitride based composites³³. It has been noted that there is a tendency for fine grained alumina to retain its hardness and compressive strength at higher temperatures when compared to cemented carbides, unfortunately alumina based materials tend to possess lower toughness and hardness values than cemented carbides. Alumina based cutting tools find limited application in industry due to lower fracture toughness and thus a tendency for variable performance under industrial machining conditions.

2.8 Static interaction diffusion couples

The chemical compatibility of tool and work piece materials can be assessed by means of static interaction diffusion couple experiments performed at expected machining temperatures. This has not been done previously for B₆O materials, but has been investigated by a number of authors in relation to ferrous workpiece materials and polycrystalline diamond, cubic boron nitride and sialon ceramic tool materials. In this section, the static interaction diffusion couple investigations of these authors are discussed to act as a base of comparison with the results of B₆O couple experiments. In the view of Vleugels and Van Der Biest³⁵, the results obtained by this type of experiment, although only approximate replicas of machining situations, can yield useful insights into the machining process. If diffusion and dissolution occur during machining, or an interaction layer is formed, these phenomena are most likely reproduced in a static interaction couple and the much longer contact times permit a more accurate analysis and therefore a better understanding of the chemical wear process³⁶.

S. Giménez et al³⁷ investigated the chemical compatibility of polycrystalline diamond (PCD) and polycrystalline cubic boron nitride (PcBN) in contact with iron. It was noted that the use of PCD is not recommended when machining ferrous alloys because of the poor chemical compatibility of the tool and workpiece materials. This phenomenon leads to high chemical wear (an exception exists when machining certain cast iron types between 200 and 500m/min)³⁷.

PcBN tools are primarily used to machine hard ferrous materials because of their good thermal compatibility with iron (this is generally believed however the literature does show some contradictory results in this regard³⁷), some investigations have lead to the conclusion the PcBN is inert with respect to iron, while others propose that chemical wear is an important mechanism.

Machining is a dynamic situation far from thermodynamic equilibrium, however an assessment of chemical interaction behaviour by using diffusion couple experiments can reveal the potential for chemical interactions to take place during the machining process and thus reveal as to whether diffusion is possible under such conditions.

Tool materials (PcBN and PCD) were placed in contact with iron and pressed together under a low load (2.5 MPa) for one hour in a vacuum (<0.1 Pa) and at

temperatures of 700, 900, 1100 and 1300 °C at a heating and cooling rate of 50 degrees per minute. The samples were polished prior to the pressing procedure.

The chemical reactivity and the extent of the interdiffusion of the tool-workpiece combinations were carried out by subsequent cutting of the couples and polishing of the interfacial / cross sectional area.

Turning tests were also undertaken with a feed and depth of cut of 0.1mm and 0.2mm respectively. PCD cutting speeds were 35, 45, 50 and 100 m/min and those for PcBN were 200, 400, 600 and 800 m/min.

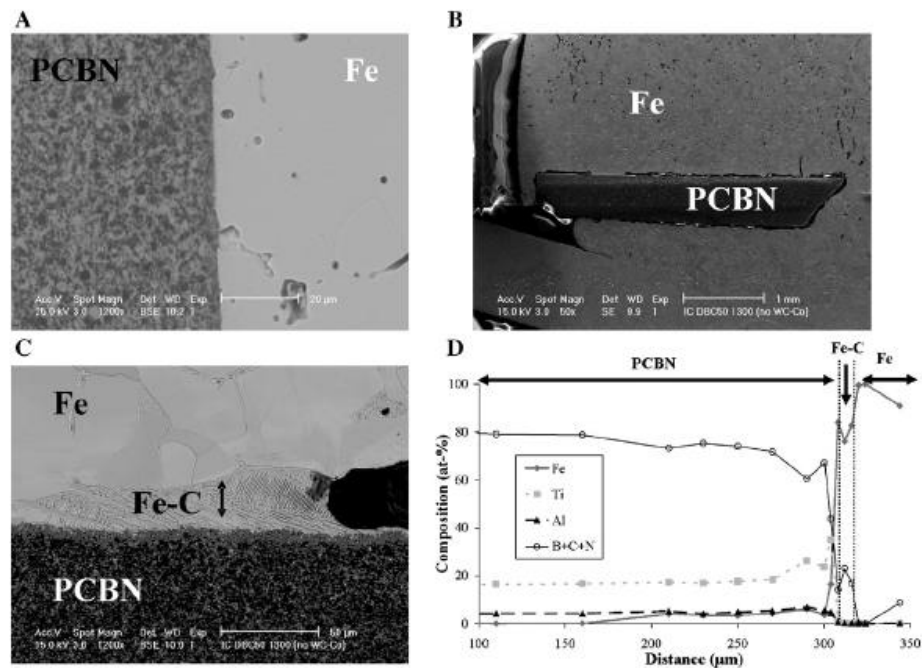


Figure 2.13: Interaction couples for PcBN (grade '50') at A: 1100°C B: 1300°C (overview of the material interfaces) C: 1300°C showing detailed interfacial region and D: EDS compositional profile at 1300 °C³⁷.

2.8.1 PcBN / Fe interaction:

No interaction was detected below 1300 °C and this is visible in figure 2.13 above. A high degree of interaction was observed at 1300 °C and evidence of iron penetration into the tool is provided by the light contrasted area of the tool adjacent to the interface (in Fig. 12B) The iron side of the interface appears decorated by an Fe-C rich structure which is thought to have originated from the eutectic reaction³⁷.

Diffusion of C into the iron and of iron into the tool material is evident when viewing the composition profile.

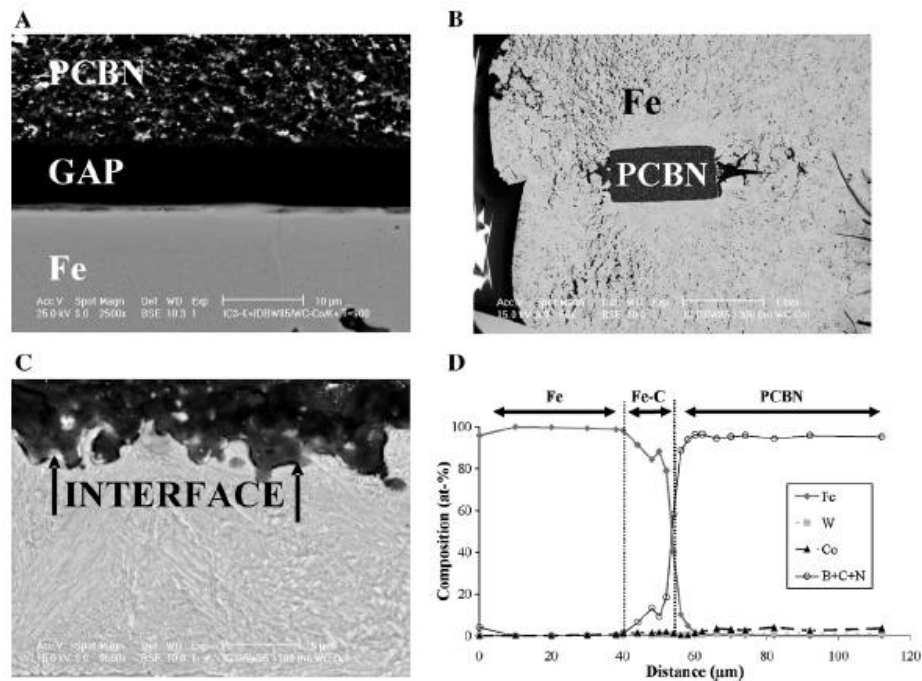


Figure 2.14: Interaction couples for PcBN (grade '85') at A: 1100°C – note the absence of any significant interaction B: 1300°C (overview of the material interfaces) C: 1300°C showing detailed interfacial region and D: EDS compositional profile at 1300 °C³⁷.

The micrographs shown in figure 2.14 above showed no significant reaction below 1300 °C whilst at 1100 °C the tool-workpiece interface displayed a distinct continuous gap. Interaction is evident at 1300 °C with an interaction product containing Fe and C and with a morphological structure similar to pearlite when viewed at higher magnification³⁷.

2.8.2 PCD and WC-Co interactions:

Polycrystalline diamond (~90 vol.%) was also used in interaction couple experiments. The presence of pearlite on the iron side of the couple at 900 °C is evidence of interaction taking place (fig. 2.16 B). After testing at 1100 °C the pearlitic nature becomes even more evident (fig. 2.16 C). A higher magnification image shows a 20 micrometer deep layer near the interface with similar contrast as iron, but without a

pearlitic structure. It is important to note that the tool material completely dissolved in iron at 1300°C at which the morphological stability of the couple was lost and characterization became impossible.

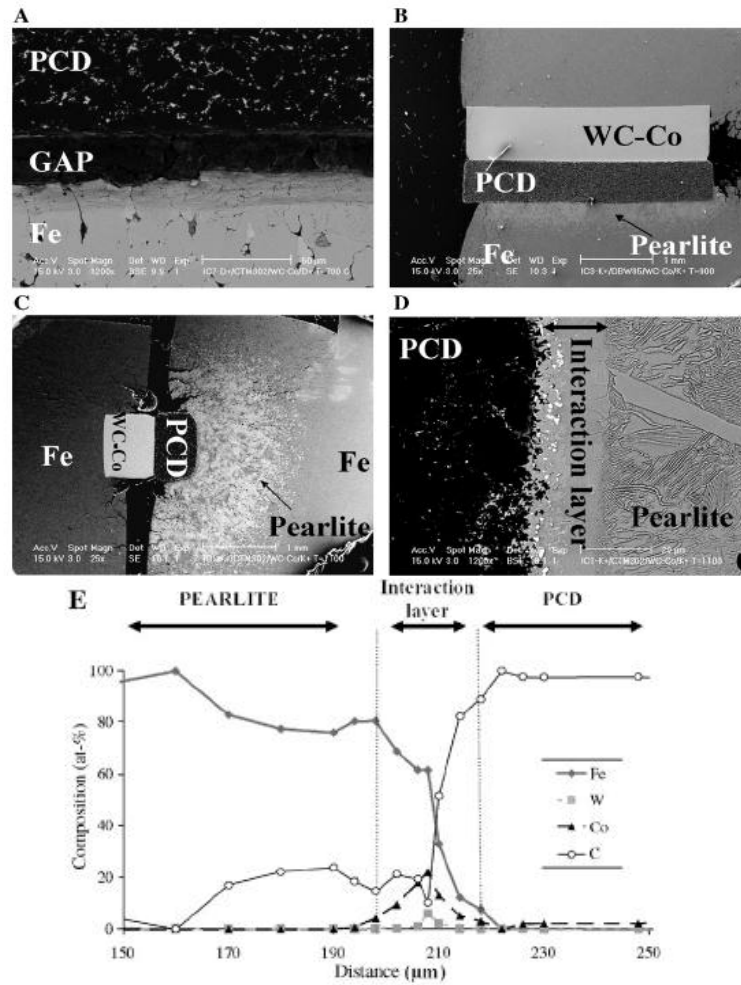


Figure 2.15: Interaction couples for PCD, A: 700 °C, B: 900 °C, C&D: 1100 °C and detail of the interface at higher magnification, E: Compositional profile at the interface³⁷.

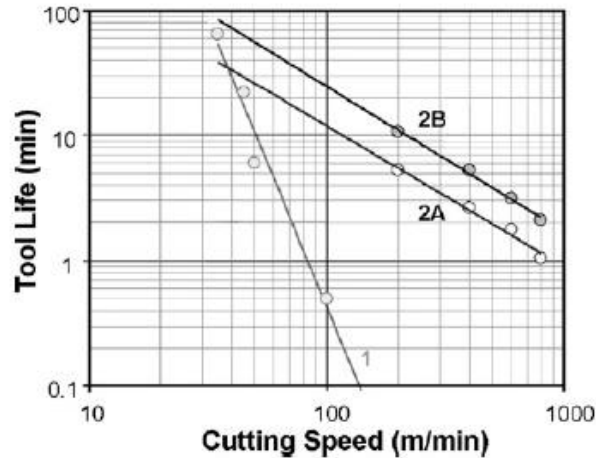


Figure 2.16: Taylor curve for the three investigated materials (2B = PcBN '85', 2A = PcBN '50' and 1 = PCD)³⁷

The interaction couples as well as the machining tests demonstrate that the main wear mechanism operating in these materials is chemical in nature. The chemical compatibility of these materials with iron can be ranked as:

$$\text{Wc-Co} < \text{PCD} < \text{PCBN-2A} < \text{PCBN-2B}.$$

Equilibrium solubility calculations were also performed and were found to be in good agreement with the observations made as a result of the diffusion couple experiments.

Similarly, static interaction couples were utilized by other authors in their studies of tool materials intended to machine ferrous metals^{35, 36}.

When steels are machined with Si_3N_4 based cutting tools, it has been found that chemical wear is the dominant wear mechanism³⁵. The wear rate of these ceramic tools has been observed to be two orders of magnitude lower when machining grey cast iron than when machining AISI 1045 steel. Interdiffusion of the constituent species has been observed to be lower when machining cast iron than when machining steel. Wear due to chemical instability is usually associated with the formation of a crater on the rake face of cutting tools however it can also be a principle mechanism in terms of flank wear³⁵.

2.9 Machining of ferrous metals with ceramic tool materials

2.9.1 Introduction to machinability of ferrous metals:

Hardened steel, compacted graphite iron (CGI) and austempered ductile iron (ADI) have excellent properties for applications in the automotive industry due to their high strength, relatively low cost, good toughness and wear resistance properties as well as high freedom in terms of shape fabrication³⁸. CGI could be the material for the upcoming new generation high power diesel engines because it allows for an increase in cylinder pressures and therefore an increase in fuel economy and a higher power output compared to grey cast iron². ADI finds uses in high performance transmission parts and chassis components^{1,2}. The reason these materials are not used more extensively is because they are very difficult to machine and cause poor tool life.

In many industries, increasing demands regarding cost and weight efficiency require the development of new materials. Materials of similar or greater strength are required for the task at hand, but preferably possessing lower density to meet the demand. As mentioned above, ADI and CGI could result in an improvement of efficiency within the automobile industry, provided that they can be cost-effectively machined.

Because of the abovementioned factors, it would be greatly beneficial to investigate alternative materials to the machining of these classes of cast iron and hardened steel; as such the machinability of these materials by ceramic tools is discussed in detail in the following sections. The industrial driving force for better machinability of these materials substantiates investigations into their machinability and understanding of the wear modes and mechanisms that result from machining of these materials.

2.10 Machining of Compacted Graphite Cast Iron (CGI)

As mentioned earlier, CGI is a candidate material for use in the automobile industry because of its good combination of mechanical and elastic properties. It has been noted that the cBN tool lifespan is twenty times longer for the machining of regular

cast iron than compacted graphite cast iron⁴⁰. Various PcBN grades have been investigated when machining CGI and many contain different binders^{38, 39 and 40}.

Figure 2.17 shows the microstructures of some cast iron grades.



Figure 2.17: Deep etched scanning electron micrographs of the graphite structure in grey iron, CGI and spheroidal graphite iron (SGI)⁴¹.

Perhaps the most extensive and comprehensive ‘across the board’ study of CGI machining with various ceramic cutting tools that the author has come across is the work of Neels Pretorius et al^{42 and 43}. The team used various cutting tool materials but focused primarily on polycrystalline diamond (PCD), PcBN, cermets and coated carbide tools as well as several other ceramics. Optimum machining parameters were of primary interest and as such machining wear maps (as described earlier) as a function of speed and feed rate were generated⁴³.

Subsequently, the best performing tools were tested in more detail in order to establish the tool life that they exhibit.

According to their review of CGI in industry, Pretorius et al^{42 and 43} note that manufacturers generally specify one shift (i.e. in terms of workers on the factory floor) as a minimum tool life criterion together with a certain cycle time which depends on the speed and required output of the production line. Cast iron machining (grey cast iron) with PcBN has led to 20-25km of cutting length at a cutting speed of 800m/min while other ceramics can only achieve 10km at 400m/min. Fewer inserts are consequently required which saves time and expense of having to remove and install a new, expensive insert.

Interrupted cutting operations result in a 30-50% decrease in tool life of PcBN inserts however, while the most disastrous reduction in tool life occurs in continuous operations such as cylinder boring. In such instances, tool life can be reduced to 10% of the usual tool life when turning grey cast iron⁴³.

As a consequence of such poor performance in terms of continuous operations, PcBN is superseded in terms of use by carbide inserts and coated carbide tools which are run at lower cutting speeds and are used for this sort of rough boring operation. Multiple inserts and an increased feed rate are used in this case to compensate for lower cutting speeds. It is important to note, however, that carbide inserts do not perform anywhere near as well as PcBN in less aggressive operations e.g. finishing operations where surface quality of PcBN machining is superior to carbides.

PCD has been recently evaluated in addition to PcBN because of the abovementioned problems with other materials especially with boring operations⁴³. Darmstadt University, Ford and Audi ran a collaborative evaluation of PCD inserts in their use as a boring tool. A single PCD insert was found to give a tool life of 1900 bores under standard boring conditions and was able to machine cylinder bores at 50% higher cutting speeds than carbide tools while achieving a seven fold increase in tool life⁴³.

Wear maps (as shown along with wear scars in figures 2.18 to 2.21) were constructed in order to better understand the wear behaviour and relative merits of the different cutting tool materials constructed as a function of speed and feed rate. Machining parameters such as depth of cut, cutting speed, feed rate etc are used as the axis variables when producing wear maps. The use of wear maps to describe flank and crater wear, wear modes and mechanisms over a wide range of machining conditions make them a valuable tool indeed. This type of wear map is produced from actual turning tests / machining operations as opposed to other types of wear maps which are qualitative in nature. This means that the optimization of the tool material can be carried out with respect to actual, observed behaviour and this, combined with a qualitative understanding, leads to better diagnostic methods for tool failure. Ultimately the hope of such an understanding is to improve tool life and quality by finding ways of countering the wear characteristics uncovered by this type of investigation.

In their paper, Pretorius et al used a full factorial experimental design comprising a comprehensive regimen for each tool investigated as described by the following criteria:

- Cutting speed: 100 - 350 m/min
- Feed rate: 0.1 - 0.35 mm/rev
- Depth of cut: 0.25 mm
- Coolant: Compressed air (5 bar)
- Time: 5 min

The CGI workpiece used was a grade containing >95% pearlite and a 10%

nodularity, which is typical for engine blocks. The tool materials are shown in table 5 below.

Table 2-4: Material properties of the ceramic cutting tools used in the work of Pretorius et al⁴² and 43.

Material group	Description
PCD	Coarse grain ($\approx 20 \mu\text{m}$) multimodal [9]
PCBN 1	50% CBN, TiC binder, $\approx 2 \mu\text{m}$ grain size [9]
PCBN 2	85% CBN, Al,W,Co binder, $\approx 2 \mu\text{m}$ grain size [9]
Ceramic	Al_2O_3
Mixed Ceramic	$\text{Al}_2\text{O}_3 + \text{TiC}$
Cermets 1	Ti(C,N) with W & Co
Cermets 2	TiN-based
Coated Carbide	TiCN + Al_2O_3 Coating

2.10.1 Mixed ceramics

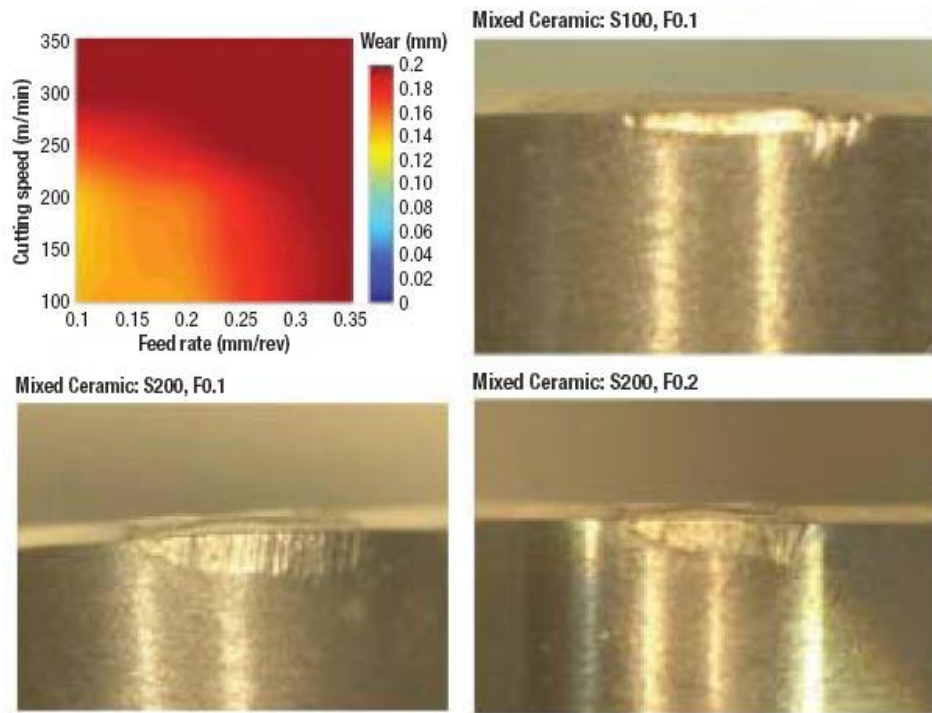


Figure 2.18: Wear map and wear scars produced as the result of machining CGI with alumina / titanium carbide mixed ceramic cutting tool materials⁴³.

It was observed by the authors that the mixed ceramic has a higher hardness than that of pure alumina, but nevertheless does not perform adequately as a cutting tool for use in high speed production lines because the wear on the tool was already higher than 0.1mm after five minutes of cutting time. The material in question is believed to possess a higher 'hot hardness' compared to the cermet grades that were also tested, however notch wear is evident on the wear scars of the ceramic as a result of the brittleness relative to cermets. Evidence of a heat affected zone around the wear scars was also observed on the cermets, which is believed to have reduced tool life and eliminated these materials from further consideration when machining CGI. The cermets' wear scars did not exhibit notch wear behaviour; nevertheless, the cermets did not perform as well as the ceramic materials in terms of cutting performance and as such are not reviewed here any further. Similarly, because of a large extent of wear after only five minutes of machining, the coated carbide tools are disqualified from the class of suitable cutting tool materials when machining CGI.

2.10.2 Polycrystalline cubic boron nitride

Polycrystalline cubic boron nitride (PcBN) materials can be classified according to microstructure, the cBN content, the quantity of binder phase used and the relative hardness and toughness of the resulting materials. In their study, Pretorius et al⁴⁵ used two grades of PcBN as described in table 2-9. The first was 50% cBN material with a titanium carbide binder and a 2 μ m grain size, while the second was an 85% cBN material with Al, W, and Co containing binder phase material and the same grain size as before.

Interestingly, at cutting speeds of 100m/min, the high cBN content material (PcBN 2 in table 2-9) have a lower wear for the same cutting time compared to the lower cBN containing material. Although the authors of this article did not mention this fact, which is hardly surprising due to the decreased amount of the softer binder phase, presenting a consequently harder cutting tool than one comprising only 50% cBN. Accelerated wear was, however, observed at much lower cutting speeds and feed rates compared to the low cBN containing material. This behaviour is indicative of chemical wear mechanisms potentially coming into play under more severe machining conditions (high speed) and a mechanical wear mechanism at much lower speeds and less severe conditions. Overall, the 50% cBN material appears to be the best material in terms of performance but the maximum viable cutting speed is only 300m/min and consequently no high speed machining solution for CGI⁴³. The wear maps and wear scars can be seen in figure 2.19 and 2.20 respectively.

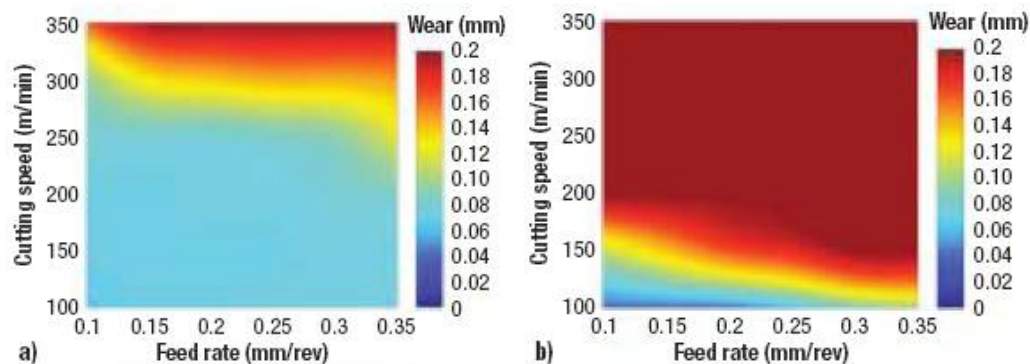


Figure 2.19: a) PcBN 1 (50% cBN) machining wear map showing better overall performance of this material, b) PcBN 2 (85% cBN) machining wear map demonstrating poor wear characteristics at higher cutting speed and feed rates⁴³.

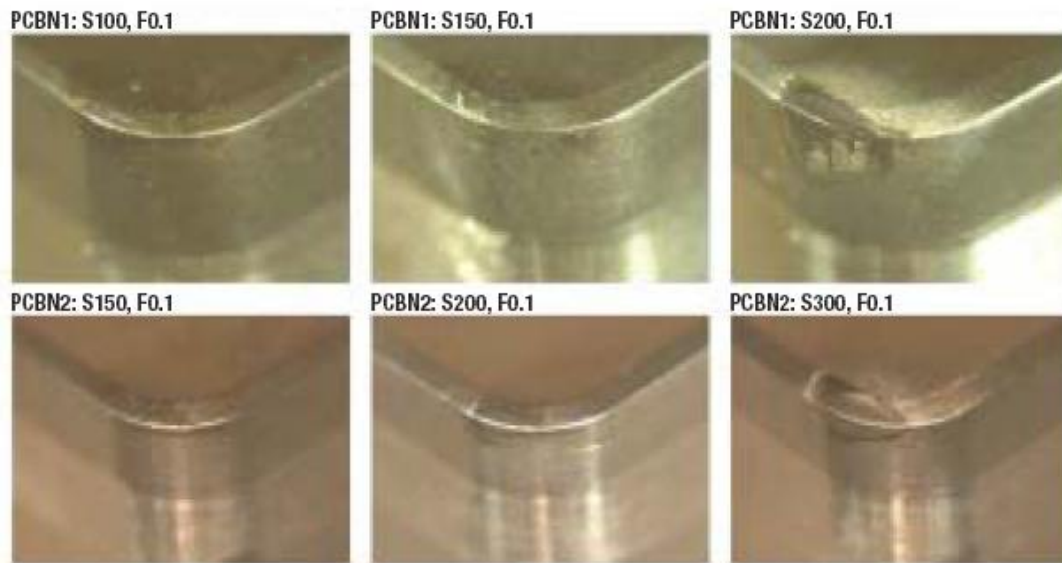


Figure 2.20: Wear scars photographed of the PcBN grades, the code above each image is indicative of the sample i.e. PcBN 1 or 2, then the cutting speed e.g. S100 = 100m/min and the feed rate of 0.1mm per revolution⁴³.

2.10.3 Polycrystalline diamond

Polycrystalline diamond (PCD) materials are comprised of an intergrown collection of randomly oriented diamond particles and a metallic catalyst material (e.g. Cobalt) that acts as a binder. The thermal conductivity and hardness of such materials are high as a consequence of the diamond composition, while toughness is provided by the metallic binder. PCD exhibits a sufficiently low wear after five minutes that enables it to be a potential material for machining CGI in that it achieves a comparable tool life to that achieved by machining of grey cast iron with PcBN. At lower machining speeds with PCD, the wear mode appears to be mechanical in nature (blue area on wear map below) and it can be seen that very little wear occurs in this range. Thermally accelerated wear occurs resulting in the loss of the nose radius of the cutting tool at higher machining speeds⁴³.

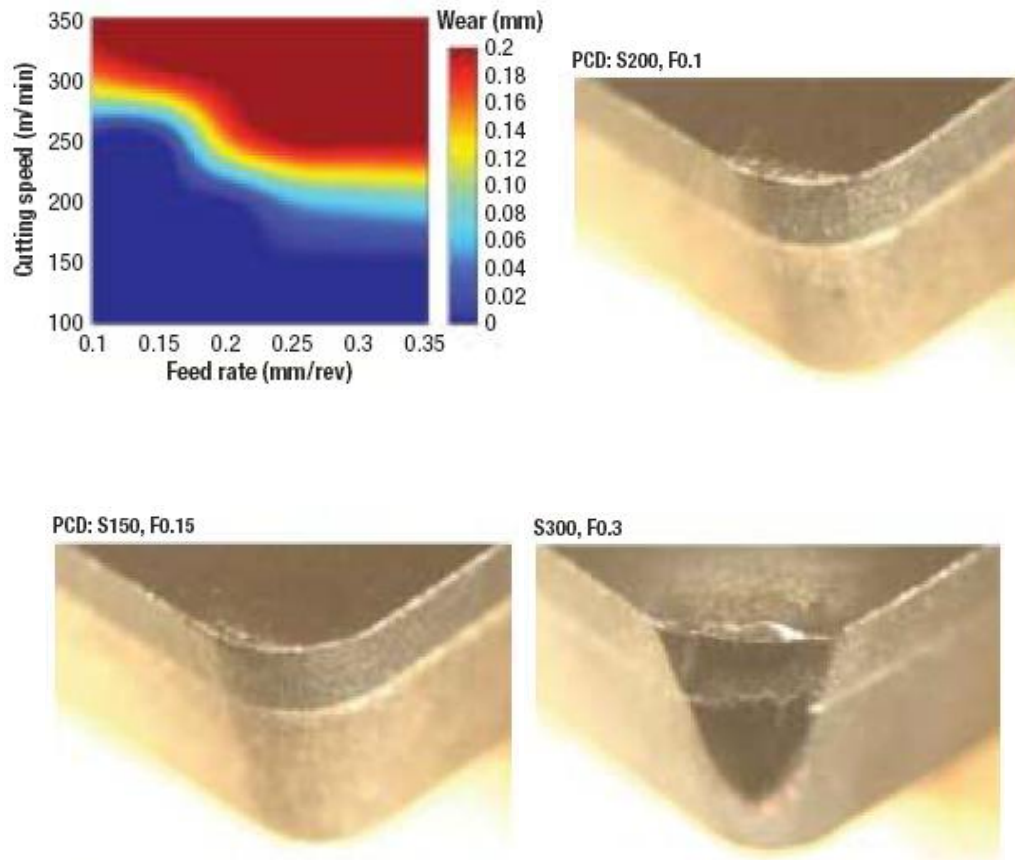


Figure 2.21: Wear map generated from the machining of CGI with PCD displaying favourable wear behaviour compared to the other tool materials. Again, the other images are micrographs of the cutting edge of the cutting tool displaying no significant wear scars until higher speed (300m.min) and a deeper feed rate (0.3mm/rev) showing the loss of the nose radius of the tool⁴³.

Use of coolant, the PCD type and the type of machining operation determine when thermal degradation begins to set in, in such a machining operation. Results of the current B₆O study will be compared with the work of Pretorius in order to assess the performance of this new class of cutting tool. Figure 2.22 shows the comparison of tool life across the tested tool materials in terms of boring operations.

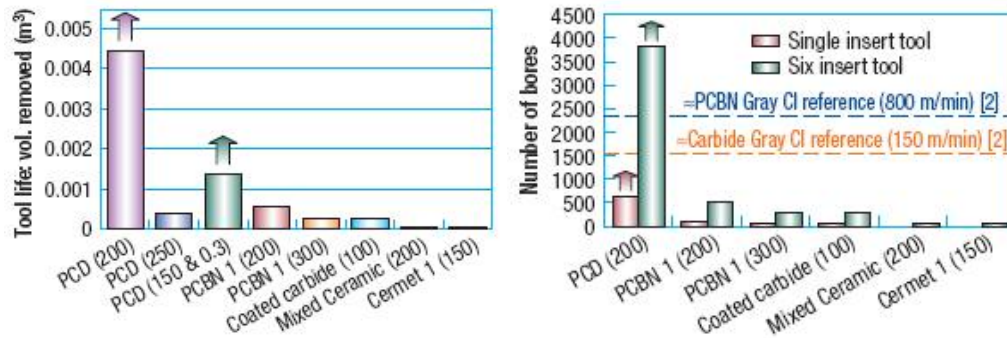


Figure 2.22: Comparison of tool life and number of bores achieved against CGI and gray cast iron for different cutting tool materials⁴³.

2.11 Thermal stability of boron suboxide

Shabalala⁵ noticed that stacking faults and localized plastic deformation were present in sintered B_6O materials, and as such these materials, namely, $HP19B_6O$ and $HP19cB_6O5.6wt\%Al$ (HP = hot pressed with 19 indicating 1900°C sintering temperature followed by a weight percentage of additive) were annealed in a hot press under argon atmosphere at 1800 and 1900°C for 3 hours. The composite sample was further annealed at 1450°C for 6 hours.

Analysis of the heat treated samples revealed that the pure material could be considered stable under argon at 1900°C and only a slight decomposition was observed and a 3.5% mass loss was recorded over the entire heat treatment. The composite sample was observed to be relatively stable up to 1800°C and underwent a significant mass loss of 11% when treated at 1900°C. The decomposition was observed to start from the surfaces and progress toward the centre in the form of visible porosity. SEM comparisons before and after the heat treatments revealed the amount of secondary phase ($Al_{18}B_4O_{33}$) had decreased, especially in the near surface area. A complete depletion of Al-based phases was found in the outermost regions of the sample. Figures 2.23 shows an optical micrograph of annealed material at 1900°C, and figure 2.24 shows pre and post annealed states of the material taken at different points on the sample.

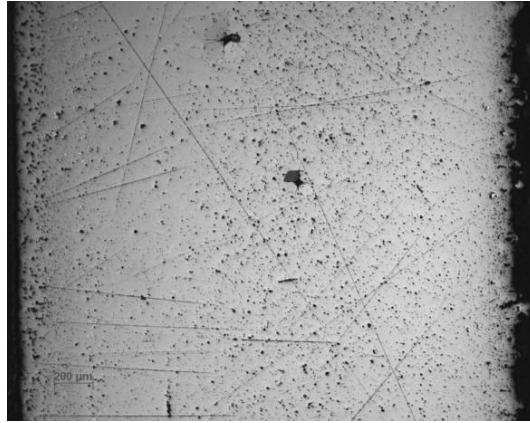


Figure 2.23: Optical image of a hot pressed B_6O sample annealed at 1900 °C, HP19B₆OHT19, showing slight decomposition⁵

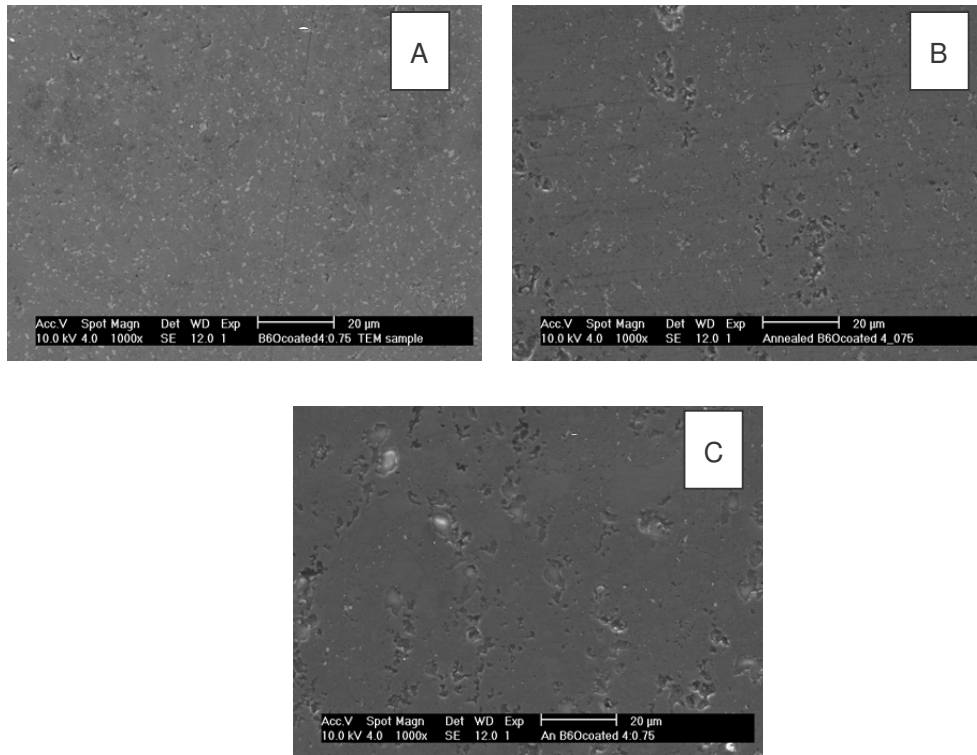


Figure 2.24: SEM images showing how a B_6O composite (HP19cB₆O5.6wt%Al) decomposed after annealing at 1900 °C⁵:

- A: Image of a B_6O composite before annealing
- B: Image of a B_6O composite after annealing, taken at the centre
- C: Image of a B_6O composite after annealing, taken on the edge

The expected phases were observed in XRD analysis namely B_6O and $Al_{18}B_4O_{33}$ ^{5, 7}.

Both micrographs of the B₆O and composite material (figure 2.25) reveal that the decomposition during heat treatment, at 1800 °C, is strongly reduced as opposed to that at 1900 °C.

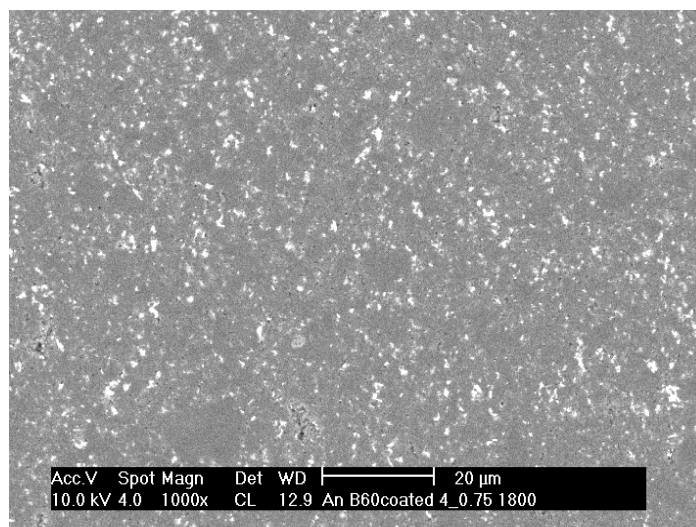


Figure 2.25: Backscatter image of an annealed (at 1800 °C) hot pressed B₆O composite, HP19cB₆O5.6wt%AlHT18⁵.

Shabalala⁵ observed that at 1900 °C, a slight decomposition was observed for pure B₆O sample resulting in an annealed sample (HP19B₆OHT19) with a density of 2.47 g/cm³, while a major decomposition was observed for composites containing Al⁵. It was noted that the decomposition started at the surface and progressed inwards as shown in figure 2.26. A small density change was observed and it was concluded that Al containing samples (and of course the resultant phases mentioned earlier) decompose more strongly than B₆O reducing the density of the sample.

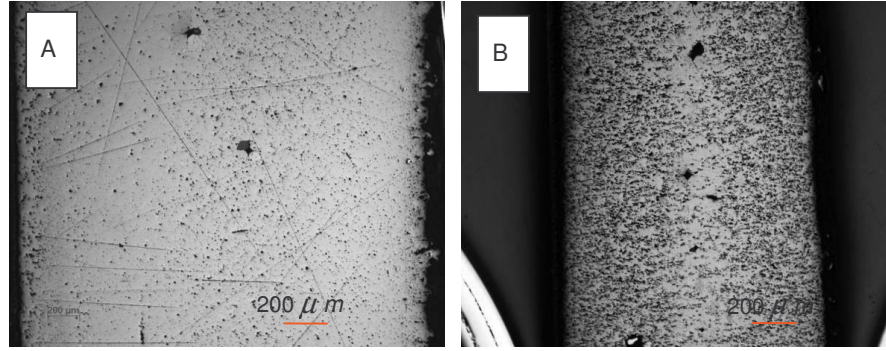


Figure 2.26: Optical images of samples annealed at 1900 °C, showing decomposition A: HP19B₆OHT19 and B) HP19cB₆O5.6wt%AlHT19⁵

Andrews³ carried out heat treatment regimens on hot pressed B₆O composites at a temperature of 1250 °C for 10 hours in an argon atmosphere. He tested materials of the following compositions: **1wt. % Al₂O₃ / 1.32wt. % Y₂O₃**; **2wt. % Al₂O₃ / 2.65wt. % Y₂O₃**; **2.87wt. % Al₂O₃ / 1.58wt. % Y₂O₃** and **2wt. % Al₂O₃ and 2.65wt. % Y₂O₃**. The table below shows the measured properties for these materials.

Table 2-5: Properties before and after heat treatment of B₆O/Y/Al selected materials³.

Material	Weight loss (wt %)	Density (g/cm ³)	Open porosity (%)	Hv ₅ (GPa)	K _{IC} (MPam ^{1/2})
18B₆O1Al1.32Yb-2	-	2.54	0.9	29.7±0.6	4.1±0.3
18B₆O1Al1.32Yb-2HT	0	2.54	0.8	30.0±0.8	3.5±0.4
18B₆O2Al2.65Yb-2	-	2.56	1.2	29.2±0.7	4.4±0.1
18B₆O2Al2.65Yb-2HT	0.4	2.52	1.6	31.5±1.2	3.6±0.6
18B₆O2.87Al1.58Yb	-	2.53	0.8	28.3±0.9	3.8±0.9
18B₆O2.87Al1.58YbHT	0.2	2.50	1.1	30.2±0.5	3.6±0.6
18B₆O2Al2.65Y1Sib	-	2.55	1.2	27.6±0.6	3.2±0.5
18B₆O2Al2.65Y1SibHT	0.3	2.56	2.3	28.5±1.0	3.7±0.3

It was observed that the 1wt.% Al / 1.32wt.% Y material was stable under the heat treatment conditions specified as indicated by the table. Note that the codes all represent firstly the sintering temperature i.e. 18 = 1800 °C; the material i.e. B₆O with following weight percentages of Al and Y and the b is indicative of the batch name of the material he produced. HT indicates that the sample underwent a heat treatment process.

It can be seen that some of the materials show a slight decrease in density but Andrews reported that this phenomenon could exist within the margin of experimental error.

No crystallization of other phases was observed. Optical microscopy was also conducted on the samples and no decomposition had taken place during the heat treatment. Andrews contended that such materials are stable under heat treatment conditions such as those tested³.

Scanning electron microscopy was also used to analyze the surfaces of the samples. It is noted by Andrews that the SEM is not substantially different from the SEM images of the compacts before heat treatment²².

Itoh et al¹⁸ studied the oxidation resistance of boron suboxide and found that B₆O compacts displayed oxidation resistance in air up to 600 °C. Some minor oxidation behaviour occurred in the temperature range of 700-1000 °C, resulting in the formation of a liquid film of B₂O₃. It was noted that these compacts exhibited superior oxidation resistance in air at elevated temperatures compared to B₄C compacts, sintered under the same conditions. The B₆O compacts were reported to have densities higher than 95% of the theoretical maximum while the open porosity was not mentioned. DTA / TGA analyses were also performed on both B₄C and B₆O in order to establish the oxidation behaviour in air as shown in figure 2.27 and 2.28 below.

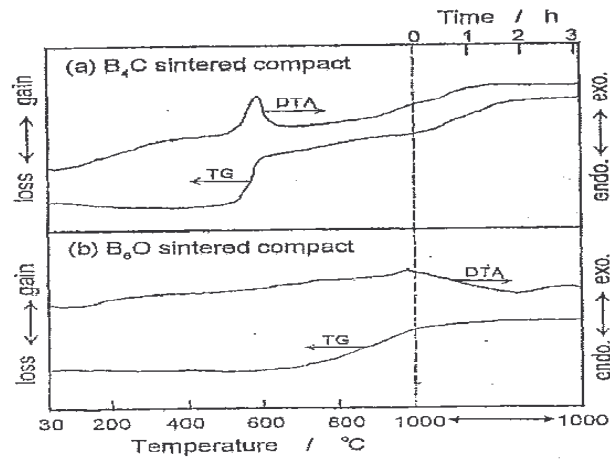


Figure 2.27: TGA and DTA analyses of single phase compacts a) B_4C and B_6O prepared at 5GPa, 1700°C for 20 minutes. Heating rate: 3°C/min, atmosphere: air.¹⁸

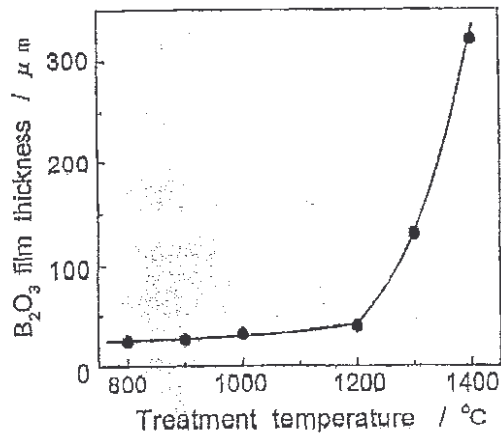


Figure 2.28: B_2O_3 film thickness after oxidation in air for 4 hours as a function of heat treatment temperature¹⁸.

As is visible from the above graph (figure 2.28) displaying B_2O_3 film thickness versus temperature, the B_2O_3 layer does not exceed 50 microns until a temperature in excess of 1200°C is achieved, after which the B_6O is rapidly oxidized and the B_2O_3 film thickness drastically increases with temperature¹⁸.

2.12 Thermochemical / thermodynamic studies of B₆O

In his PhD thesis, Andrews used the prior work of Makarov and Ugai⁴⁶ to calculate and predict required thermodynamic data for phase equilibria calculations on B₆O.

Andrews described how the thermodynamic properties (volume, entropy, enthalpy, internal energy, heat capacity and chemical potential) are related to the Gibbs energy.

Andrews used the integral functions to plot a graph of Cp versus temperature (figure 2.29) but he noted that the extrapolation of the heat capacity (Cp) values to higher temperatures was not useable at lower temperatures due to a lack of available thermodynamic data at elevated temperatures. A linear Cp function was introduced to act as a correction factor between the heat capacities of B₆O and B₆Si in the temperature range of 800K to 2300K³ as can be seen below.

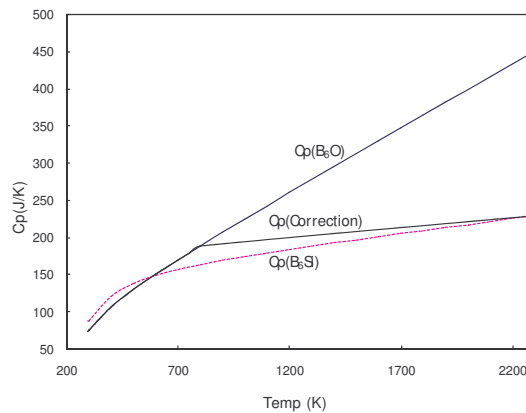


Figure 2.29 Graph of temperature versus heat capacity as described by Andrews³ for B₆Si & B₆O (extrapolated experimental values) and B₆O after correction (the data of B₆Si taken from Makarov⁴⁴) B₆O data was measured in the range 298.15K to 800K and was taken from Tsagareishvili et al⁴⁵.

Andrews used the thermodynamic data ($\Delta H_{298.15}$, $S_{298.15}$ and $C_{p(\text{correction})}$) obtained to calculate the needed phase equilibria using FactSageTM 5.4.1. He used this data to predict stable phases and to help in the search for better sintering aids that paved the way for the work of O.T. Johnson and his colleagues.

Using the approach described by He and Zhao¹⁶, hardness and fracture toughness value for a wide range of composites were investigated by several members of the

ceramics group at the University of the Witwatersrand over the past few years. The work of many group members was collated into a graph displaying hardness against fracture toughness for many of the boron suboxide based materials that have been produced. The fracture toughness equation used for the research represented in figure 2.30 is as follows:

$$K_{IC} = \xi \left(\frac{E}{H_v} \right)^{0.5} \left(\frac{P}{c^{3/2}} \right)$$

Where: K_{IC} refers to the fracture toughness in $\text{MPa}\cdot\text{m}^{1/2}$, E is the elastic modulus of the material, H_v is the Vickers hardness, P is the applied force and c refers to the average radial crack length for that indentation. The constant ξ is usually taken as 0.016 for B_6O as in previous work^{3, 4, 5, and 16} but is a material dependent property.

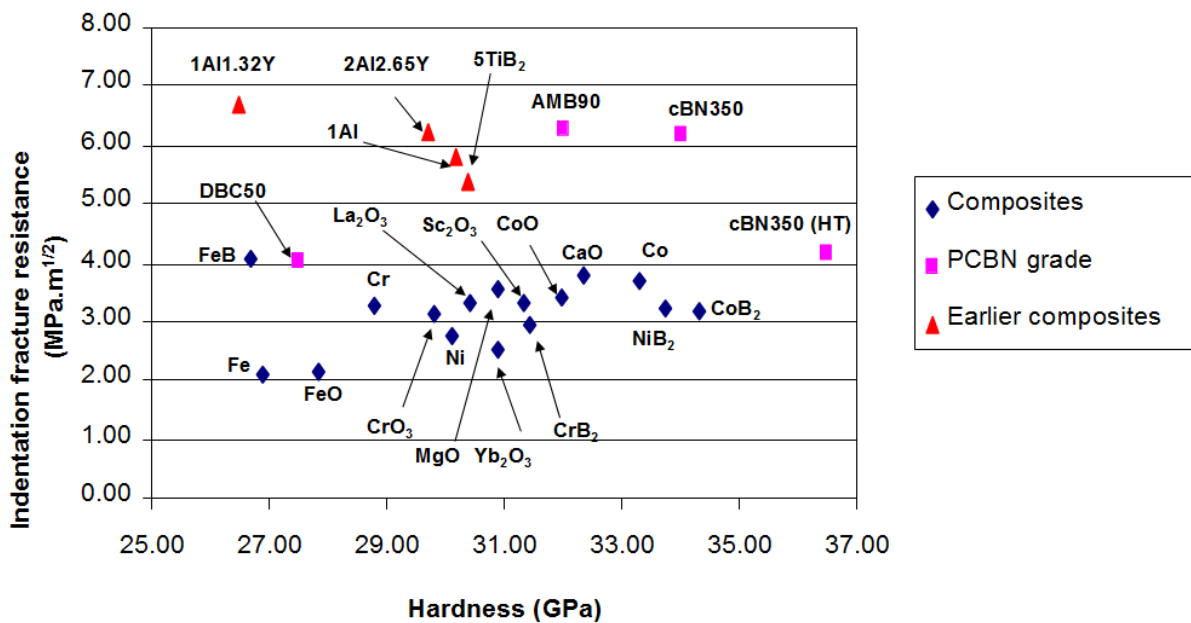


Figure 2.30: Fracture toughness against hardness of most of the boron suboxide based materials produced by the ceramics group members in recent years. Each labelled point is indicative of the additive that was present to make up the secondary phase in each case. The exact weight percentages of additives can be found in Appendix A. Element 6 PcBN grades can be seen as labelled. Note: 'Al' refers to alumina (Al_2O_3) and 'Y' refers to Yttria (Y_2O_3), the full chemical formula is omitted to allow for a clearer graph.

From this graph, it was decided that the high pressure tools would be produced from the cobalt additives, while the first set of low pressure SPS produced cutting tools would be produced from the well characterized $B_6O/Al_2O_3/Y_2O_3$ (called alumina-yttria) materials for the simple reason that the research team at the IKTS and the work of Andrews and Shabalala has resulted in more extensive knowledge of this material than the other newer composite materials. Furthermore some questions were raised regarding the reliability of Vickers fracture toughness determination described by He and Zhao¹⁶, due to the large scatter and difficulty associated with reproducing the results, hence the choice of a well characterized material for cutting tool fabrication.

The literature review has covered prior work on the major topics relating to the current research. The connection between material characteristics and properties such as hardness and fracture toughness, chemical reactivity, thermal stability and tool-workpiece chemical and abrasive interactions during machining operations as a function of machining parameters is greatly relevant in a comprehensive study of machinability of a workpiece by a chosen tool material. In the rest of this report the interconnection between all of these techniques is presented and explored in order to evaluate the first ever produced boron suboxide based cutting tool materials. Graphs, wear maps, photomicrographs and other material similar to that already presented in the literature survey will follow and will ultimately relate back and be compared to this literature survey in order to place this study as a comparison with prior related work.

3. METHODOLOGY

This section of the dissertation contains experimental details, methods and apparatus used during the course of the project beginning with powder preparation and characterization followed by sintering methodology and hardness and toughness determination. Cutting tool fabrication is then discussed followed by static interaction diffusion couple experiments after which microscopy, x-ray diffraction studies, thermal stability experiments and finally cutting experiments and determination of cutting tool performance is described.

3.1 Powder preparation for hot press and high pressure compacts

The starting material (powder) used in the production of all B_6O compacts in this work was produced previously by the reaction of boric acid and amorphous boron powder as described in the previous work of Andrews³ and Johnson⁴. This particular batch of powder was produced by Dr. Matthias Herrmann's team based in the IKTS Dresden, Germany, and was purchased by the ceramics group at the University of the Witwatersrand for use in the B_6O projects. The average particle size of this powder was approximately $3\mu m$ - too large for successful sintering which is achieved by minimization of grain size. As such, further milling of this starting powder was required.

3.1.1 Milling

The first stage of milling was performed using an attrition ball mill as shown in figure 3.1 below.



Figure 3.1 Photograph of the attrition ball mill used in the first stage of milling. The container houses the powder and the correct proportion of steel balls which is then milled for a set time and speed.

Steel balls of 2.5mm in diameter were placed in the mill in a 1:10 (e.g. 10g B_6O powder to 100g steel balls) mass ratio with the B_6O powder to be milled. An appropriate milling medium for lubrication (and to prevent reactions with air) was required, and as such, isopropanol was used for this purpose. A milling speed of 200 rpm was utilized for a milling time of twenty hours. After this process had been completed, a significant amount of iron contaminants existed within the milled suspension because of the erosive action of the powder on the balls and of the balls on each other. As such, washing was required to remove contaminants that were introduced by this process. Another problem with the milling process is that the formation of B_2O_3 is a possibility.

3.1.2 Washing

Washing with dilute hydrochloric acid solution removes the iron contaminants which can then be decanted off of the washed medium and the process is repeated until the acid solution is clear. 50ml of 90% HCl was added to 450ml of distilled water into a

1 litre glass beaker. The acid solution was used to wash the powder and allowed it to settle, followed by decanting and repeated as many times as necessary.

Typically, the iron contaminants can be seen to visibly bubble and react when the acid is introduced as well as changing the liquid colour to a semi-transparent dirty yellow. Once the washing has been repeated multiple times (ten times in this case), this becomes clearer and clearer. Once the solution is clear enough, it is washed firstly with some more water and subsequently decanted to reduce HCl concentration, followed by washing with ethanol.

After completing this stage, the powder was dried in a rotary evaporator, crushed as finely as possible and removed for chemical analysis.

3.1.3 Chemical analysis

After washing was performed, it was necessary to send a sample of powder for chemical analysis in order to verify composition. Inductively coupled plasma analysis was used in order to perform this task and to determine the amount of remaining iron and chromium within the powder to ensure an adequate level of purity. The analysis was performed using an end on plasma and coupled charge detector attached to a Spectrociros CCD IPCP analyser with plasma operated at 1200W. 0.1g of sample was digested in a 55% HNO_3 and a 40% HF containing solution by microwave digestion in a Multiwave 3000 SOLV sample preparatory microwave. The digestion process was allowed to proceed for 65 minutes after which the scan was performed.

The results of the chemical analyses performed are discussed in the results section later in this report. Three separate powder batches were used for the samples produced in this work.

3.1.4 Planetary ball milling

In the cases where composite materials were produced during the course of this work, a planetary ball mill was used in order to mix the additive with the bulk of the B_6O powder. Most of the work in this project attempts to characterize pure B_6O compacts in the context of machining, following the logic that the bulk of the composite materials produced are composed of boron suboxide and thus by

quantifying the behaviour of pure B_6O , the dominant processes relevant to machining can be appreciated. Nevertheless work was performed during this project that helped in the choices of composite cutting tool materials and as such, the process is reported here. In the case of the high pressure experiments conducted, the additives with which the B_6O powder was sintered were Co and CoO.

0.133g of Co powder was measured and added to 9.867g of B_6O powder (making a total of 10g) in order to obtain 1.33wt% (0.39 vol. %) of Co.

Similarly 0.961g of CoO powder was measured and added to 9.039g of B_6O powder (9.61wt%, 4.06 vol. % CoO). Relevant calculations for this work can be viewed in the appendix section.

Isopropanol was added to the mixture as well as a number of 2.5mm diameter steel balls to assist in the mixing process. The mixture was milled using the planetary ball mill (figure 3.2) for 2 hours in order to ensure a homogeneous distribution of the additive within the bulk powder. The milled mixtures were dried and crushed in order to break the agglomerates and produce a fine powder for sintering. A photograph of the planetary mill is included below.



Figure 3.2: Planetary ball mill used for mixing of the pure B_6O powder with additives

The particle size of the Co and CoO powders which were used was analysed using a Malvern Mastersizer 2000 particle size analyzer in order to better quantify the final distribution and microstructure resulting from these additives in the sintered compacts. This is described further in the following section.

3.1.5 Particle size analysis

In order to ensure that a particle size of sufficiently small magnitude was obtained, particle size analysis using a Mastersizer 2000 Malvern particle size analyser was performed on the batches of milled powder. A small amount of powder was suspended in distilled water with sodium hexa-meta-phosphate as the dispersive medium. The machine was calibrated before use in order to ensure that the results are accurate. Calibration involved ensuring the apparatus was properly cleaned and set up prior to the testing, followed by checking the measured particle size distribution against a known size distribution of glass beads provided by the manufacturer. The results of the batches that were measured can be found in the following results chapter.

3.2 Sintering

Sintering is the process of producing a solid compact from a volume of starting powder usually at a temperature below the melting point of the material being compacted. The driving force of this process is the reduction of surface energy. Sometimes a liquid phase can be formed in the process which can act as a lubricant and can assist densification by acting as a material transport medium.

3.2.1 Hot press runs

This project made use of a uniaxial hot press (HP20 thermal technology) that was manufactured by Thermal Technology Industries.

In this instance, the hot press concerned comprised a heating chamber which is composed primarily of graphite components and a water cooling system. The chamber is capable of reaching 2200 °C if necessary and the hydraulic press can

apply a load of up to 10000kg. Such large loads are seldom used because it is above the maximum load tolerance of the graphite punch and die set which is 100MPa of pressure. The pressure applied is of course dependent on the dimensions of the crucible that is utilized during the compaction process. The load is applied uniaxially from the lower punch (the hydraulic compartment is below the furnace chamber mechanism) and a pump is used to evacuate the furnace chamber down to as low as 10millitor. After evacuation of the chamber has been completed, inert argon gas is fed through the system and into the heating chamber and the viewing window. Typically, the load is applied once a required temperature has been reached after which sintering commences fully. In Figure 3.3, a photograph of the uniaxial hot press used in this investigation is shown.



Figure 3.3 The uniaxial hot press and associated components.

3.2.2 Containment of material during sintering

Although the main components within the furnace are composed of graphite, the pot itself used to contain boron suboxide powder cannot be graphite for the reason that

at the temperatures used for sintering, carbon diffusion is very rapid and thus would result in an impure sample containing carbide products. It is for this reason that hexagonal boron nitride pots are utilized when sintering boron suboxide. The pots are of approximately 18mm diameter into which B_2O_3 powder is placed and slightly compacted. Following this step, an hBN piston of 3mm in thickness is placed between the starting powder and a graphite piston that has been prepared to fit into the hBN pot housing. The reason a graphite piston has been utilized is because the original hBN pistons that were used could not tolerate the high pressures applied (up to 80MPa) and used to crack and ruin the run. As such, stronger graphite pistons were introduced with the hBN protective pill to prevent carbon contamination of the sintered compact. A schematic of the pot and piston setup used for hot pressing is shown in figure 3.4.

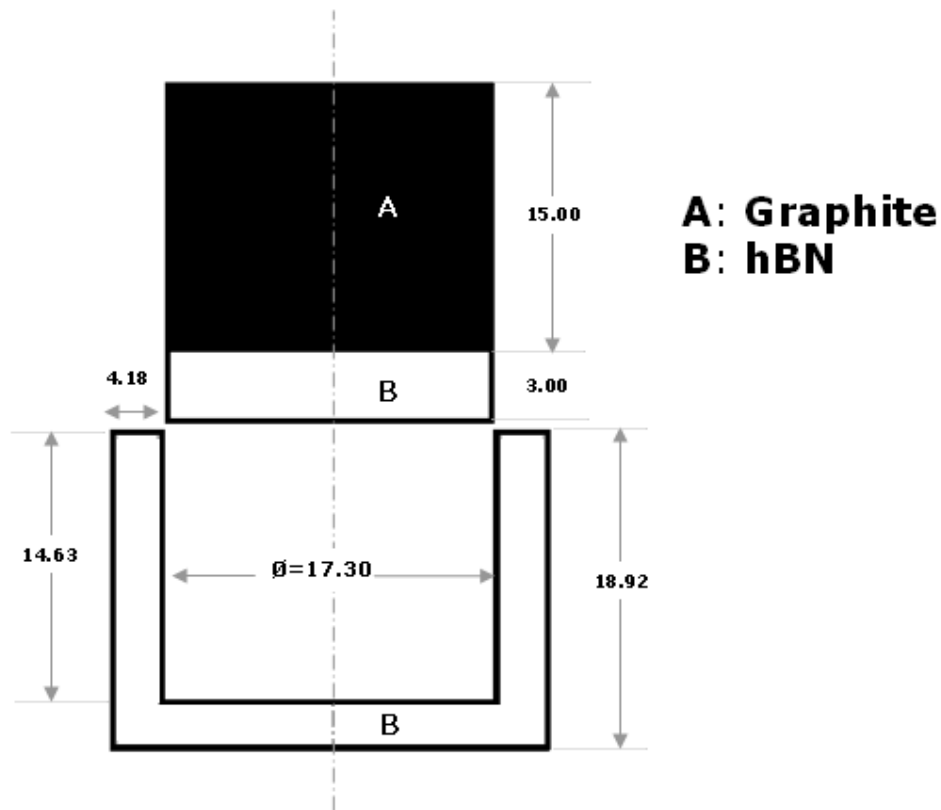


Figure 3.4: Cross sectional diagram of the hexagonal boron nitride (hBN) pot, pill and accompanying graphite piston used to hot press the compacts used in this project.

3.2.3 IKTS SPS production

Spark plasma sintering technology was used at the IKTS Fraunhofer Institute in Dresden Germany to produce boron suboxide based composite plates that could be used to fabricate cutting tools. This method of sintering employs a pulsed electric current to heat the sample⁴⁶. A high current and low voltage is employed to allow for current flow through the punch and die assembly which heats and sinters the sample. Very high heating rates ($> 300^{\circ}\text{C}/\text{min}$) can be achieved with SPS thus drastically reducing sintering time. This technique allows for minimization of grain growth due to short sintering times and is thus a very powerful technique for creating nanostructured ceramics⁴⁶. Figure 3.5 shows a schematic of an SPS machine.

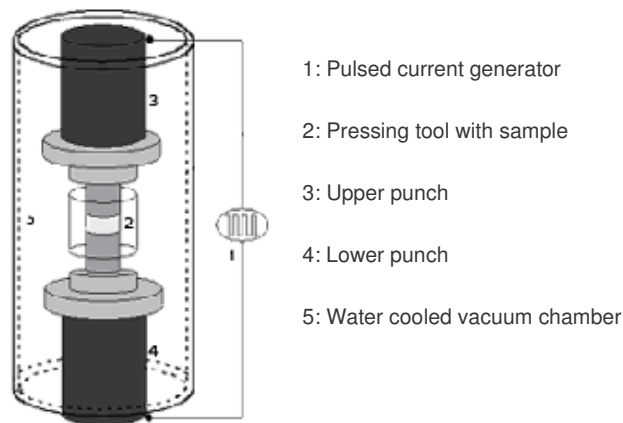


Figure 3.5: Schematic representation of the setup of spark plasma sintering technology as described by the IKTS Fraunhofer Institute⁴⁶.

Ceramic plates were produced using this technique. The material was sintered at 1800°C under 50 MPa of pressure for 5 minutes. The cutting tools produced during the course of this project from this material will be discussed further later. However, the boron suboxide based cutting tools produced in this work were those of the alumina/yttria boron suboxide composite type and thus powder preparation techniques would have followed similar methods to that mentioned earlier. The starting powders and the sintered plates were all produced by the IKTS team. The sintered material resulting in the cutting tool materials used in this project possess a composition of boron suboxide with 2 Wt.% Al_2O_3 (alumina) and 2.65 Wt.% Y_2O_3 (yttria). The choice of cutting tool materials is discussed later in this chapter.

3.2.4 High pressure sintering

High pressure sintering was performed as a part of this project in an attempt to create high pressure sintered composite materials for comparison with the relatively low pressure compacts produced using the uniaxial hot press or by SPS. The goal was to use the resulting material to produce cutting tools and ultimately compare the performance of such cutting tools with the performance of the tools prepared at lower pressures. Two additives were selected for this part of the work namely cobalt and cobalt oxide since it had been previously found by the ceramics group that these additives exhibit favourable properties when added as secondary phases with B_6O .

As mentioned earlier in this report, the selected weight / volume percentages were added to the milled B_6O powder and dried and crushed before pre-compaction.

3.2.4.1 Pre-compaction (formation of a green compact)

Before high pressure sintering could commence, 4.89g of each powder (pure B_6O , $B_6O + Co$ and $B_6O + CoO$) were weighed and transferred to a pre-compaction capsule. A tungsten carbide material was placed on top of the powder filled container in order to prevent contamination of the powder as a result of contact with the die. 18MPa of pressure was applied for 15 seconds in order to form a green compact.

3.2.4.2 Sintering

A total of six samples were prepared, two from each type of powder produced. The samples were sintered under a pressure of 7GPa for 10 minutes at a temperature of 1500 °C. This was accomplished using an industrial hot press at Element 6, Springs.

3.3 Hardness and fracture toughness

In preparation for the selection of tool materials, hardness and fracture toughness measurements were performed on low pressure (80MPa) compacts produced by the ceramics group, as well as the high pressure compacts that were produced at Element 6. Hardness and fracture toughness testing was performed on bakelite

mounted and subsequently polished samples. The polishing procedure involved the use of progressive grinding pads from 80 to 120, 240, 600 and 1200 grit followed by fine grinding with 9µm diamond paste followed by 3 and finally 1µm paste. Grinding / polishing time was approximately doubled from each subsequent step, for example, 30 seconds on an 80 grit pad to 60 seconds on the 120 grit pad and so on. Optical microscopy was used to ensure that the introduced scratches at each stage were uniformly directional and of the same size, after which the next step of grinding commenced. Similar methods were used in the final polishing steps, although time spent on each pad varied according to the requirements of the sample. Some samples can be more difficult to polish effectively and may require more time for fine grinding and polishing than others. For this reason, microscopy was used to monitor the quality of each stage in the process.

After polishing, a LECO V-100-A2 Vickers hardness tester equipped with a diamond indenter was used to indent the sample surfaces. All but the pure B₆O samples were indented with a 5kg load, while the pure B₆O was indented with a 1kg load due to its brittle nature. The lengths of the diagonals of the indentations were measured as well as the crack lengths that proceed from the corners of the indentation. These measurements can then be used to calculate Vickers hardness and a corresponding (approximate) fracture toughness value.

$$H_v = 1854.4 \frac{P}{d^2}$$

Where: Hv refers to the Vickers hardness value (in GPa usually for hard or superhard materials), P is the applied force (N) and d is the average of the diagonals (m) of the indentation that was measured.

3.4 Cutting tool fabrication

3.4.1 SPS low pressure compacts

Spark plasma sintered compacts (plates) produced at the IKTS (Dresden, Germany) of 2 Wt.% Al₂O₃ (alumina) and 2.65 Wt.% Y₂O₃ were sent to Element 6 Ireland for cutting tool fabrication. The samples were first cut into blanks using a laser cutting technique after which they were chamfered and honed to produce a finished cutting tool. The selected square cutting tool geometry possessed a nose radius of 0.8mm

and a chamfer of 0.1mm in thickness. The cutting tools themselves were 3.18mm thick. PcBN (DBC50 Element 6 grade) cutting tools were prepared of the same geometry as the B_6O tools in order to provide a basis for comparison. The tolerances of the cutting tools give an idea of the error in measurement that can be expected when producing cutting tools e.g. the size can vary slightly as a result of the fabrication process. The tolerances on these cutting tools were $\pm 0.025\text{mm}$ for the length, $\pm 0.1\text{mm}$ for the nose radius and $\pm 0.13\text{mm}$ for the thickness. An illustration of the exact cutting tool specifications used for both the DBC50 and B_6O tools can be seen in figure 3.6. Amborite DBC50 is a fine grained PcBN material supported on a tungsten carbide (WC) base with a cBN content of 50% by volume and a TiC binder phase with an average cubic boron nitride grain size of $2\mu\text{m}^{49}$. Photographs of the cutting tools produced during this project and their tool holder are shown in figure 3.7.

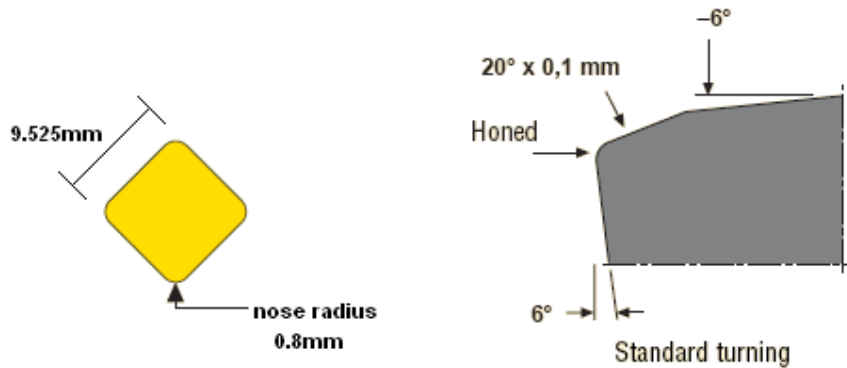


Figure 3.6: Cutting tool specifications used for the inserts produced and tested during this project.

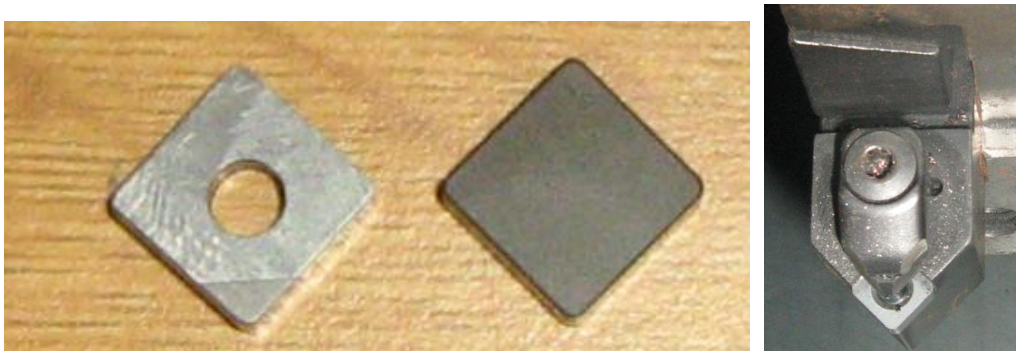


Figure 3.7: Photographs of cutting tool inserts produced for this project, left: the DBC 50 cutting tool and right: the B_6O cutting tool. Alongside right is the corresponding tool holder shown secured within the turret of the lathe.

3.4.2 High pressure compacts

The high pressure compacts that resulted from the high pressure sintering work were also sent to Element 6 Ireland for cutting tool fabrication. It was decided that round cutting tools would prove a better cutting tool for potential evaluation of the B_6O material as problems were encountered with the square inserts (as will be described in detail later). Similar preparation methods as those mentioned above were used except that the tool geometry had been changed to round instead of square. 13.7mm diameter round cutting tools with a 20 degree and 200 micron deep chamfer were produced with a 5 micron edge hone. The thickness of the samples was not generalized and as such corresponding shims were produced to ensure that the tools maintain relative heights with respect to the tool holder. Figure 3.8 shows the cutting tools fabricated from the high pressure material. The change in geometry from square to round is evident. The chamfering and honing of this material resulted in less edge chipping and surface flaws than the lower pressure yttria alumina composite material.

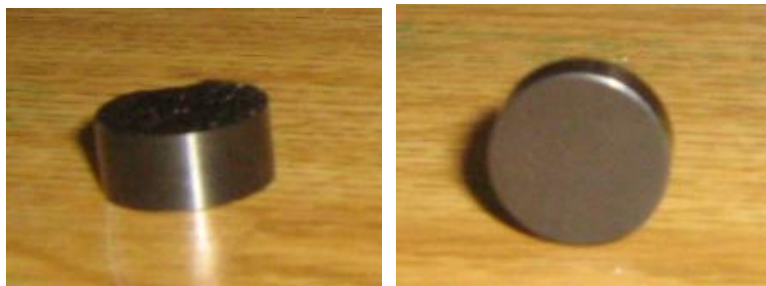


Figure 3.8: Photographs of the high pressure cutting tools produced for this project. Left: the B_6O/Co cutting tool and right: the pure B_6O cutting tool.

3.5 Static Interaction diffusion couples

3.5.1 Sample preparation

As mentioned in the literature review, static interaction diffusion couple experiments can provide a wealth of knowledge in terms of the diffusion and chemical processes and reactions that can occur during machining. Because couples allow for sufficient time to pass, the chemical reactions can be observed in detail and these reactions

can be expected to occur in a similar way when it comes to machining under similar pressures and temperatures. To achieve this goal, pure B_6O compacts were sintered as described above using the uniaxial hot press. The compacts were removed from their hBN pots and had to be ground down to size to reduce the radius of the compact. This was necessary because some radial expansion occurs under the pressures and temperatures experienced during sintering resulting in a compact that possesses a diameter slightly larger than that of the original hBN pot. After grinding the sample to size and ensuring its ability to fit into a second hBN pot, the two disc surfaces were polished in the same way described above. Polishing of these surfaces was performed in order to maximize the surface contact area between the B_6O pill and the cast iron surfaces.

Similarly, compacted graphite cast iron (CGI) pills of the same diameter (~17mm) were produced by cutting a piece off one of the cast iron work pieces to be used in machining tests. This piece was then machined down into a cylinder of the correct diameter after which pills of 3mm thickness were cut off. The CGI pills were polished down to 0.05 μm diamond paste grit size to ensure a smooth contact surface and to similarly maximize surface contact area. Micrographs of the CGI material were taken firstly in an unetched and then in an etched state by using 5% Nital solution for 20 seconds. Once both the B_6O and CGI pills had been prepared, XRD scans of the surfaces of the pills were conducted in order to verify the starting composition and to act as a basis for comparison for the resulting products after heat treatment.

Before the interaction was allowed to begin, the samples were washed in ethanol to remove any surface contaminants and were thoroughly dried with hot air.

The samples were then placed in a new hBN pot in the configuration as shown in figure 3.9.

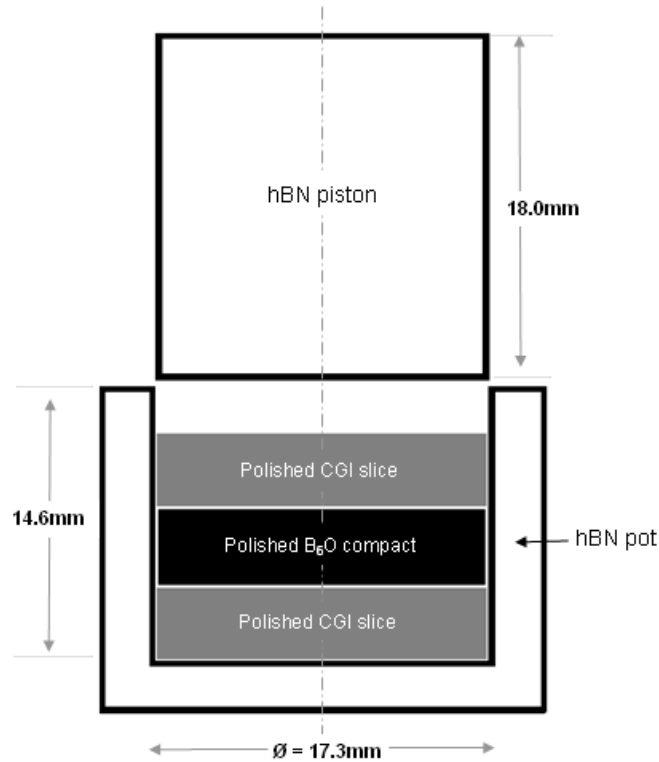


Figure 3.9: Static interaction diffusion couple pot arrangement prior to hot pressing.

3.5.2 Diffusion couple heat treatment profile

Once the pot had been prepared, it was placed within a graphite punch and die set used for hot press operation. The hot press was run under an argon atmosphere at temperatures of 700 °C, 900 °C, 1100 °C and 1300 °C for one hour under a load of 10MPa. The reason for these temperatures and pressures being chosen is because a comparison between this work and the prior work involving PcBN and other couples by Giménez³⁷ et al could provide a useful insight into how boron suboxide couples compare with competitor materials. These temperatures are within the lower and upper bounds of expected machining temperatures and the pressure of 10MPa is as close to the pressure that Giménez³⁷ used (2.5 MPa) as is possible with the hot press. The hot press is incapable of producing a lower pressure than 10MPa using a pot and piston of this diameter and configuration. The couples were heat treated at their respective temperatures for one hour with a heating and cooling rate of 20 °C per minute.

3.5.3 Cross sectional preparation

Once the heating treatment process was complete, the couple-containing hBN pot was removed from the hot press and gently opened. Optical microscopy was performed to examine the interaction surfaces where possible following which the couples were cross sectioned using a diamond cut-off blade on a rotary cutter. Half of the diffusion couple was polished using the regimen described above, while the second half was retained for XRD and further examination.

3.6 Optical microscopy

Optical microscopy was extensively used in this project in many different ways. The primary areas where optical microscopy was used was the examination of wear scars produced from turning tests, but the same microscope technology was used for the examination of the static interaction diffusion couple surfaces, Vickers indentations and crack lengths as well as visual assessment of the surfaces of the thermal stability samples. The microscope used was an Olympus BX41M optical microscope coupled to an Olympus Camedia camera connected via USB to an adjacent computer equipped with Analysis 5 software. The software in question allows for multiple images to be taken in succession at slightly different focal lengths, the sequence of images is then collated into one single image by the extended focal imaging (EFI) function of the software. An EFI map is produced which provides topographical data on the surface in question i.e. it displays the highest and lowest points of the image in shades of gray, black and white depending on the height of the region. The composite image contains the focused regions of the previous sequence of images and thus yields a final image that contains all this focused information and hence allows for three dimensional (non-planar) surfaces to be examined with the microscope when they would otherwise be obscured and out of focus. The EFI technique is powerful because it can allow for a better appreciation of surface effects and features that would otherwise be difficult to observe using optical microscopy.

3.7 Scanning electron microscopy

Scanning electron microscopy (SEM) was performed at Element 6 Springs in order to better characterise the examined surfaces and samples. A Philips XL 30 ESEM-FEG

XL series scanning electron microscope equipped with energy dispersive x-ray spectrometry (EDS) facilities was used to produce all of the SEM micrographs and EDS profiles during the course of this project.

3.8 X-ray diffraction

X-ray diffraction was used to verify the phase composition of the various materials produced during the course of the project. A Philips PW1710 powder x-ray diffractometer utilizing copper K α radiation set at a potential of 40kV and current of 20mA was used for the majority of the XRD work. The scanning range (2θ) was 10° to 80° with a step size of 0.02° per step. Philips X'Pert Highscore® software along with the International Centre for Diffraction Data (ICSD) database was used to identify the phases present in the tested materials.

A Bruker D8 diffractometer using Cu K α radiation equipped with a Goebel Mirror and VANTEC high speed detector was used for high resolution XRD work that was performed during the course of this project. Traces were collected over a period of 20 minutes with an incremental step size of 0.021 degrees over the range of 5 - 90 degrees (2θ). The x-ray diffraction code used in all XRD traces for B₆O in this project is the 00-050-1505 code from the international XRD database.

3.9 Density and open porosity determination

Density and open porosity were calculated according to the Archimedes method. This method requires that the sample first be boiled in distilled water for three hours in order to dislodge any gaseous bubbles that may adhere to the sample and to ensure that the surface pores of the sample are filled with water. It has been standard practise by the ceramics group to boil samples produced (typically 3 to 4mm thick and no more than 15mm wide or in diameter) for three hours rather than the ASTM method of five hours because the results are much the same⁴.

To perform the calculation, the suspended mass (in grams) of the sample is measured by placing it upon a small suspended support in a beaker of distilled water

on a 4 decimal point accuracy balance. The measured mass in this instance is designated the suspended mass (M_s). The saturated or wet mass is then measured by removing excess water from the sample by lightly dabbing the sample with paper towel in order to remove excess water, but retain a wet surface with surface pores still filled with water. The resulting mass from this measurement is called the wet mass (M_w). The sample is then dried in an oven at 120°C for twenty minutes to dry off the surface, after which the dry mass (M_d) is measured. Each measurement should be repeated to ensure reproducibility, and in this work, each measurement was taken five times and the average of the five values in each case was taken and used in the following equations:

$$\rho_s = \frac{M_d \rho_w}{(M_s - M_w)} \text{ and } P_o = \left(\frac{M_w - M_d}{M_s - M_w} \right)$$

Where: ρ_s is the sample density; M_d is the dry mass; M_s is the suspended mass and M_w is the 'wet' mass. P_o is the open porosity and ρ_w is the density of water (1g/cm³).

3.10 Oxidation resistance testing

Oxidation tests were performed during the course of this project in order to assess the chemical reactivity of boron suboxide based sintered compacts in the range of expected machining temperatures namely 1000°C. The reactivity in air has been assessed by holding the samples at temperature for different holding times and by monitoring mass changes and new phases formed as a result of the heat treatment. It is hoped that the results of this work will indicate potential reactions that can occur while machining with B₂O₃ based cutting tools. Oxidation studies using high resolution XRD as the main phase evolution detecting mechanism were performed for 1, 2, 3, 4 and 5 hours at temperature. The mass changes of these results were pointless as the mounting polymer used to support the samples after each heat treatment can change the mass. However phase composition and evolution after each step was analyzed using high resolution XRD. A second oxidation resistance run on different samples (pure B₂O₃ and yttria alumina tool material samples) were conducted in order to measure the mass changes and observe microstructural changes by utilizing optical microscopy.

3.10.1 Sample preparation

Pure B₂O₃ sintered compacts were hot pressed in the manner described earlier in this section and were cut into rectangular shapes in order to ensure a measurable surface area. SPS produced yttria/alumina samples (of the same composition and plate used to produce the cutting tools for this work) were also cut into rectangular shapes in a similar way using a diamond cut-off wheel.

The samples were then ground and polished in the usual way until 0.5 micron diamond paste was used as the final polishing step. Density and open porosity measurements as well as optical microscopy were performed on the samples in order to quantify the starting density and appearance (microstructure) of the materials. XRD was performed on each sample in order to characterise the starting phases present in the materials. The samples were cleaned with ethanol and dried in a 120°C oven in order to ensure that the surfaces were as clean and dry as possible. After this drying process, the samples were kept at all times (except heat treatments of course) in a sealed desiccator equipped with silica gel as the humidity maintaining medium. The samples were weighed using a 0.01mg accuracy scale before heat treatments began.

3.10.2 Heat treatment regimen

At the start of the heat treatments, the samples were gently placed on coiled thermocouple wire gauze that was constructed for the task. Nichrome thermocouple wire was used because of its high temperature melting point and thermal stability up to temperatures far in excess of the testing temperature of 1000°C. The samples themselves were placed onto the constructed support by using cleaned tongs / tweezers (to avoid contamination by contact with fingers) and the contact area between the samples and the wire was minimized as much as possible. The wire support was then placed between two alumina-based ceramic furnace tiles capable of withstanding a heating / cooling rate of 15°C per minute without risk of fracture. Sufficient air flow was allowed to occur between the tiles which were open on all sides, and were placed approximately 2cm apart supported by support struts (legs) that were cut from the same tiling material and a cross sectional view of the experimental setup can be seen in figure 3.10.

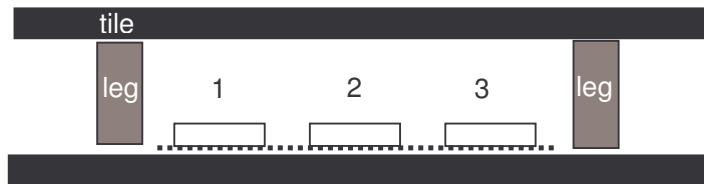


Figure 3.10: Cross section of the arrangement of the samples supported on nichrome thermocouple wire during the oxidation resistance testing. Two legs and three samples are obscured but there were 6 samples in total and four supporting legs.

The first heat treatment was to the required temperature of 1000 °C at a heating rate of 10 °C/min and a holding time of one hour followed by a 10 °C cooling rate down to room temperature. The same procedure was used for all of the samples and heat treatments except that the holding time was increased from 1 hour to 2, 4, 10, 20 and finally 50 hours. After each step, the samples were gently removed from the support taking care not to dislodge material from the surfaces and with the use of tweezers were placed onto a microscope slide and optical microscopy was performed in order to investigate the microstructural changes after each heat treatment.

3.10.3 Mass change measurements

The change in mass that the samples experienced as a result of the heat treatments were measured by using a five decimal point accuracy scale measuring in grams after heat treatment and optical microscopy had been performed. Samples were only exposed to air (room temperature) during transportation to the scale as well as during measurement and optical microscopy. The rest of the time they were kept in the desiccator.

3.11 Machining and wear studies

3.11.1 Lathe operation and machining characteristics

As described earlier in this section, cutting tools composed of boron suboxide and yttria/alumina additives were produced in order to evaluate the machining performance of this material against typically 'difficult to machine' materials.

Compacted graphite cast iron (henceforth referred to as CGI) was chosen as the workpiece material because of the high wear rate typically demonstrated by machining this material with most other ceramic cutting tools, such as PcBN. CGI workpieces were obtained from Sintercast Sweden and possessed the following chemical composition as seen in table 3-1.

Table 3-1: Composition of CGI used

%C	%Si	%Mn	%S	%Cr	%Cu	%Mg	%Sn
3.75	2.19	0.41	0.014	0.03	0.86	0.009	0.110

Optical and scanning electron micrographs of the starting CGI material were taken in order to verify the expected starting microstructure of the material.

Dry finish turning tests were performed on the CGI workpieces using the cutting tools described in the cutting tool fabrication section above. A CNC Turn Master LA200 L Liouya-Hsing lathe with a 14.72kW power output was used to conduct the turning tests. Photographs of the lathe and the workpiece setup can be seen in figures 3.11 and 3.12. Cutting speeds of 50 and 100 metres per minute were used to test the cutting tools and higher cutting speeds would have been attempted if the cutting tool performance on lower speeds had been satisfactory. The flank wear failure criterion for cutting tool wear scars was used which states that a 300 micron wear scar on the flank face of the cutting tool can be considered the point at which the cutting tool has failed and can no longer provide a good surface finish.



Figure 3.11: Photograph of the CNC Turn Master lathe used to perform turning tests during this project. A CGI workpiece can be seen in the chuck as well as the turret containing the tool holder.

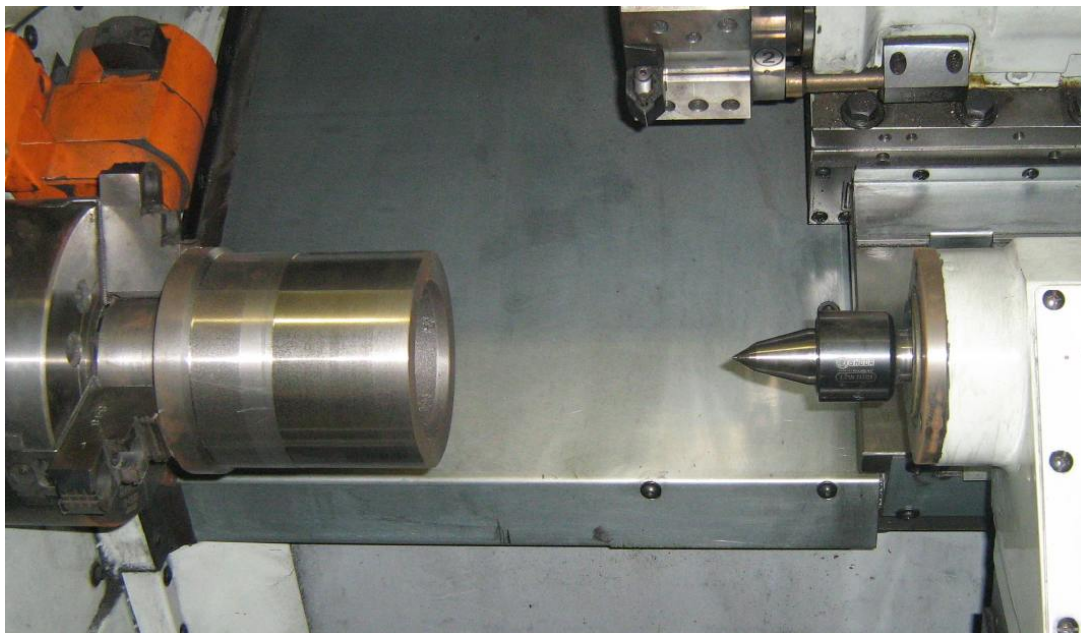


Figure 3.12: CGI workpiece (left) held within the chuck jaws as well as tool holder (top) in the setup used for turning tests.

The depth of cut was taken as 0.25mm and the feed rate was set to 0.1mm per revolution. The cutting tool inserts were secured onto a tool holder with the combination of tool holder and cutting tool insert resulting in a rake angle of -6° , a clearance angle of 6° and a lead angle of 45° . Pass lengths were incrementally increased and the cutting time corresponding with this pass length was calculated in order to plot graphs of flank wear against cutting time and flank wear against cutting distance for each cutting speed investigated.

$$t_c = 0.06 \frac{\pi d_1 l}{v_s f}$$

Where: t_c refers to the cutting time in seconds, d_1 refers to the diameter of the workpiece in mm at the start of the cut, l refers to the pass length (mm) and v_s refers to the surface speed of the workpiece in m/min. The conversion factor of 0.06 allows for unit conversion to time in seconds by compensating for the set parameters with different base units i.e. m/min as opposed to mm per second. It is standard machining practise to use the units as they have been presented in the above equation.

After each pass was performed, the cutting tool was removed from the tool holder and examined for progression of the flank and crater wear scars. The flank wear scar was measured using the optical microscopy techniques described earlier and the average of ten wear scar measurements was taken as the corresponding wear scar width for that particular cutting length, time and speed. The tool was re-inserted into the tool holder and another pass length cut and so on, until the flank wear failure criterion of 300 microns was reached or the cutting tool failed (fractured). Each cutting length was performed at least twice in order to ensure reproducibility and consistency of the results. The B₆O cutting tools were pitted against the DBC 50 cutting tools (described earlier) in order to compare the viability of the B₆O based tools as a competitor material for DBC 50.

3.11.2 Tool failure analysis

As a result of observations made during the course of the turning tests, a brief tool failure analysis was undertaken in order to better understand the observations made.

Scanning electron microscopy and EDS scans of the B₆O cutting tools were performed in order to assess tool quality. XRD scans of the same tools were performed to verify phase composition. Optical microscopy of the tool cutting surfaces and surface morphology was performed in order to view microstructural features. Density and open porosity was determined of several B₆O cutting tools to evaluate the effectiveness and results of the tool fabrication process against the original values obtained for the starting materials.

4 RESULTS

4.1 Powder for hot pressing and high pressure compacts

As described in the methodology, three powder batches were used to sinter the various materials for this project. The batches shall be designated batch 1, batch 2 and batch 3. Batch 1 was used to produce the oxidation resistance samples used for progressive XRD analysis as well as the static interaction diffusion couple B₆O pieces. Batch 2 was used to produce the remaining oxidation resistance samples and finally batch 3 was used to produce the high pressure compacts.

4.1.1 Particle size analysis

Batch 1:

This batch comprised particles of 0.635 microns making up to 50% (d50) of the material, while 90% of the particles were less than 1.309µm in size (d90). The measured particle sizes can be seen in table 4-1.

Table 4-1: Table showing duration of milling, speed, and spread of the particle sizes resulting from the milling process.

	Duration (hrs)	Speed (Rpm)	d0.1(µm)	d0.5 (µm)	d0.9 (µm)
	5	400	0.46	1.17	2.81
			0.45	1.18	3.71
			0.44	1.13	2.83
Average			0.45 ± 0.01	1.16 ± 0.03	2.99 ± 0.51
	12	400	0.37	0.79	1.64
			0.37	0.79	1.61
			0.37	0.76	1.57
Average			0.37 ± 0.01	0.78 ± 0.02	1.61 ± 0.04
	15	400	0.38	0.82	1.84
			0.36	0.75	1.67
			0.36	0.75	1.70
Average			0.37 ± 0.02	0.77 ± 0.05	1.74 ± 0.09
	20	400	0.318	0.655	1.39
			0.308	0.622	1.30
			0.325	0.631	1.24
Average			0.32 ± 0.01	0.64 ± 0.02	1.31 ± 0.08

Batch 2:

In this batch, the main focus was not to monitor the effects of milling, but rather to ensure that the average particle size was below one micron. It can be seen from the average curve shown below (from measurements using the Malvern particle size analyser) that this is indeed the case. Figures 4.1 and 4.2 show the starting and finishing particle size distributions.

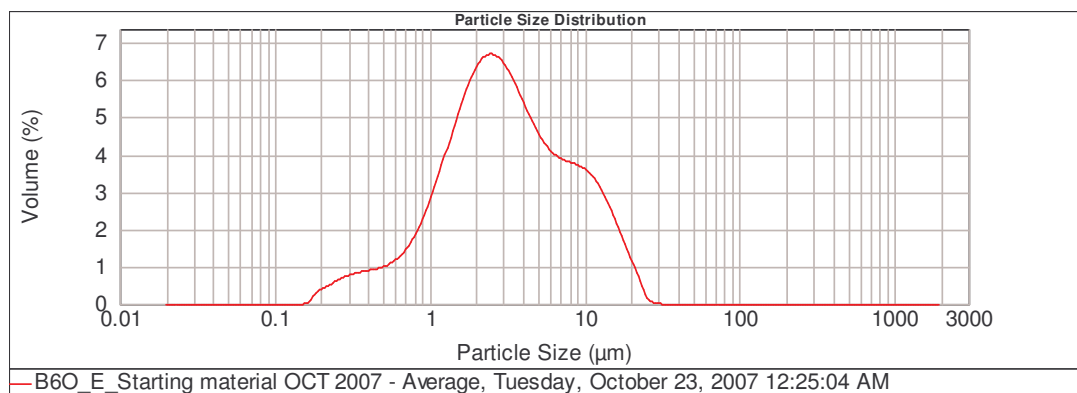


Figure 4.1: Results of the starting particle size analysis of the purchased B₆O powder prior to 20 hours of milling at 400 rpm.

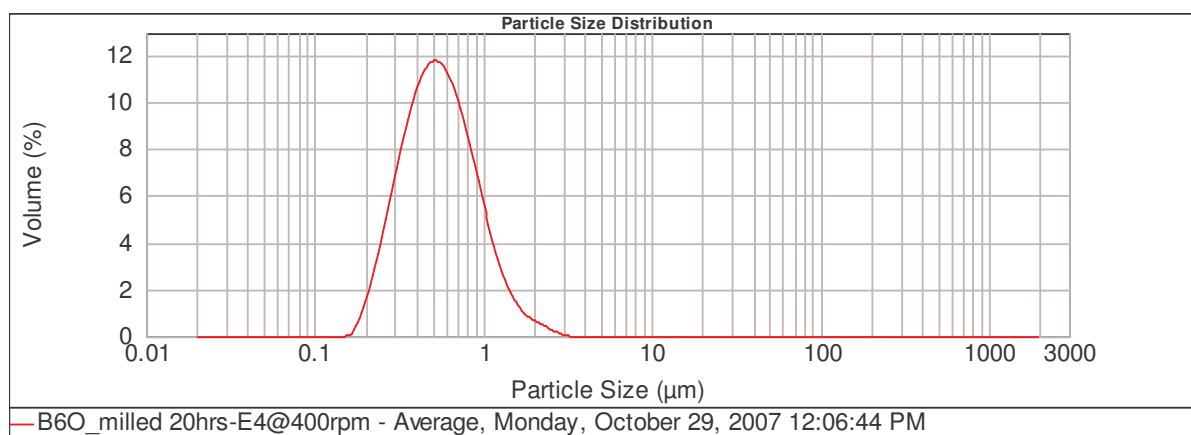


Figure 4.2: Results of the particle size analysis curve of volume percent against particle size of the milled powder after milling for 20 hours at 400rpm. It is clear that the average particle size is well below 1 micron.

Batch 3:

This powder batch was milled at 200rpm as it was found during the course of the project and through collaboration with other ceramic group members that higher speed milling did not appear to reduce particle size more efficiently. The evidence indicating this can be found in the appendix. After 20 hours of milling at this speed, the d50 value was found to be 0.112 μm , which is well below the 1 micron requirement. No change in particle size distribution was observed after milling for 20 hours at this speed. Batch 3's particle size profiles before and after milling can be seen in figures 4.3 and 4.4.

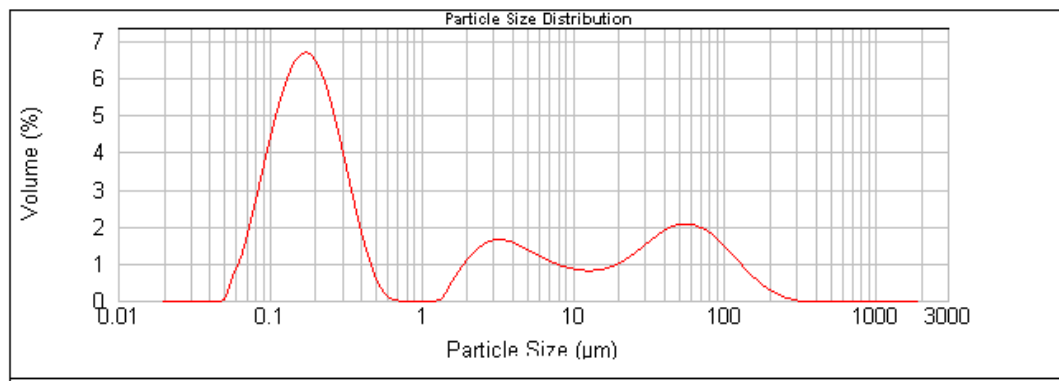


Figure 4.3: Particle size of the starting powder before batch 3 was milled.

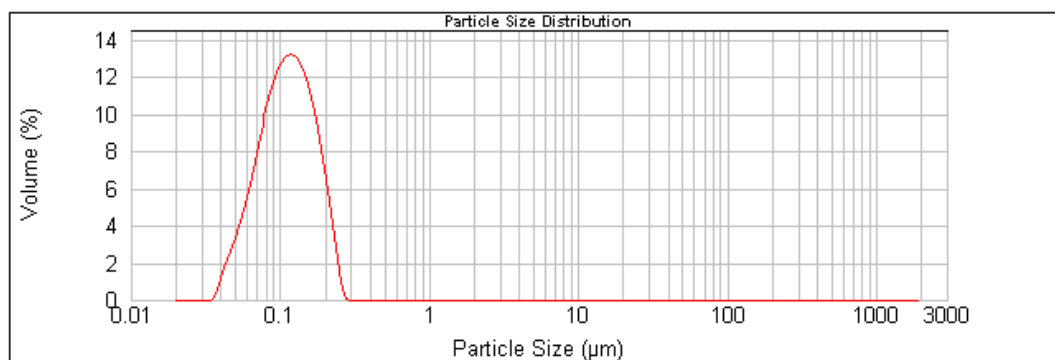


Figure 4.4: Particle size of batch 3 after milling for 20 hours at 200rpm.

The particle size distribution of the starting Co and CoO powders was also analyzed as shown in table 4-2.

Table 4-2: Average particle sizes of the starting powders for the additives used in the ultrahigh pressure sintering powder preparation

	CoO Powder	Co Powder
Average particle size:	5 μm	34 μm

4.1.2 Chemical analysis

Inductively coupled plasma analysis was used to identify the degree of residual contamination introduced from the milling procedure with steel balls after washing had been completed. Table 4-3 shows the weight percentage of contamination of iron and chromium remaining after washing.

Table 4-3: Iron and chromium weight percentages in the B₆O powder batches after washing and ICP analysis.

Batch	Fe (wt. %)	Cr (wt. %)
1	0.052 \pm 0.001	0.054 \pm 0.001
2	0.039 \pm 0.001	0.057 \pm 0.001
3	0.058 \pm 0.001	0.024 \pm 0.001

4.2 Hardness and fracture toughness characteristics of produced materials

4.2.1 Hot pressed samples

Samples of pure boron suboxide were hot pressed as described in the methodology. It was generally found that these samples possessed a density in excess of 95% of the theoretical density. Hardness and fracture toughness measurements were performed in collaboration with O.T. Johnson⁴ and E. Ofunguyiwa⁴⁸ in order to obtain comparative hardness values for the potential tool materials during the selection process at the beginning of this project. At each stage of this report, as the material in each section is used, its density and open porosity are described, but the overall hardness values are the same as those of Johnson⁴ for hot pressed B₆O. Generally, the characterization work in this project has centred around pure B₆O for the simple reason that any tool material based on B₆O will comprise mostly of this material, thus there is the need to first characterize its behaviour before moving on to the behaviour of composite materials. The applied load corresponded to a 5kg mass by using the Vickers hardness indenter caused fracturing on the surface of the sample and as such a 1kg load was substituted in its place. The sample exhibited a tendency to crack rapidly and thus using diagonal crack paths to determine fracture toughness is not practical in this instance due to the material's brittle nature and the difficulty of measuring the said crack lengths accurately.

Table 4-4: Properties of hot pressed pure B₆O materials used in this project

Hot pressing conditions	Density (g/cm ³)	Open Porosity (%)	Vickers hardness (GPa)	Sample
1900 °C, 50 MPa, 20 minutes	2.46	3.7	30.2 ± 1.0 (1 kg) ⁴	Reported by Johnson ⁴
Same as above	2.51 ± 0.01	2.86 ± 0.09	–	700 °C couple
Same as above	2.48 ± 0.02	3.25 ± 0.15	–	900 °C couple
Same as above	2.52 ± 0.01	3.46 ± 0.27	–	1100 °C couple
Same as above	2.48 ± 0.04	2.41 ± 0.15	–	1300 °C couple
Same as above	2.46 ± 0.01	1.59 ± 0.09	–	Phase monitoring 1
Same as above	2.49 ± 0.01	2.44 ± 0.04	–	Phase monitoring 2
Same as above	2.48 ± 0.08	5.32 ± 0.28	–	Phase monitoring 3
Same as above	2.51 ± 0.05	3.54 ± 0.11	–	Oxidation stability 1
Same as above	2.46 ± 0.07	3.52 ± 0.18	–	Oxidation stability 2
Same as above	2.46 ± 0.16	1.27 ± 0.55	–	Oxidation stability 3

4.2.2 IKTS SPS samples

Previously, samples of yttria / alumina boron suboxide materials of the composition described in the methodology were produced by Anthony Andrews³ as part of his PhD thesis. The hardness and fracture toughness of 2 wt. % Al₂O₃ and 2.65 wt. % Y₂O₃ relative to other composites produced by the ceramics group can be viewed in

figure 3.8 in the methodology section. The hardness and fracture toughness of this specific material was measured as 29.7GPa and 6.2 MPa.m^{1/2}.

Table 4-5: Properties of SPS B₆O/Y₂O₃/Al₂O₃ materials used in this work

Hot pressing conditions	Average Density (g/cm ³)	Average Open Porosity (%)	Hv ₅ (GPa) ³	Sample
1800 °C, 50 MPa, 5 minutes	2.58 ± 0.01	0.16 ± 0.03	29.7 ± 1.4	SPS B ₆ O/Y ₂ O ₃ /Al ₂ O ₃ plate cut into oxidation samples 1-3

4.2.3 High pressure sintering

High pressure sintering of B₆O based materials was investigated in order to determine the viability of the product material for potential cutting tool applications. Pure B₆O, B₆O/Co and B₆O/CoO based materials were produced in order to compare the properties of these materials to those sintered at lower pressures. The ultrahigh pressure sintering operation was performed at 7GPa and a temperature of 1500 °C for ten minutes.

Different loads were used for indenting the samples because of pure B₆O's characteristically low fracture toughness. During the hardness test of the pure B₆O sample, flaking out of the sample in the vicinity of the indentation was observed.

Pure B₆O is very brittle; therefore it was difficult to determine the fracture toughness of the pure B₆O sample by measuring the crack lengths. Crack lengths were measured using optical microscopy to focus the crack and measure the diagonal crack length by using the associated Analysis software. Because of the high hardness values obtained and in order to verify the measurements taken at the University of the Witwatersrand, the same samples were sent to the IKTS Dresden Germany for scanning electron microscopy and hardness measurements.

Table 4-6: Density and open porosity results of the sintered compacts*

Sample	Wt. % of additive	Theoretical density	Measured density	Measured % porosity	Percentage of Theoretical Density
Pure B ₆ O	0	2.60	2.55	0.046	98.18
B ₆ O + Co	1.33	2.63	2.58	0.026	98.39
B ₆ O + CoO	9.61	2.76	2.67	0.158	96.83

* Results obtained by Moropeng⁴⁹, unfortunately no error values were provided by the author in her final 4th year report

Table 4-7: Hardness measurements performed by the IKTS team

Sample	Load [g]	Hardness (Hv _{0.4}) [GPa]
B ₆ O+CoO UHP	400	35,9 ± 0.9
B ₆ O+Co UHP	400	35,6 ± 0.5
B ₆ O (pure) UHP	400	35,1 ± 0.5

Pure B₆O:

The following pages contain SEM micrographs taken at the IKTS with the aid of an in-lens detector capable of acquiring better surface imagery in scanning electron microscopy by using secondary electrons only.

Figure 4.5 shows very clearly the grain size of the resulting compact. Some open porosity is visible, but the pores themselves are significantly less than half a micron in diameter. Sub-grain features are also visible with small fracture-like lines appearing in many of the grains as indicated in the arrowed regions. Some of these could be said to be microfractures resulting from the cold compaction process taking place involving microfracture of the grains when being pressed together.

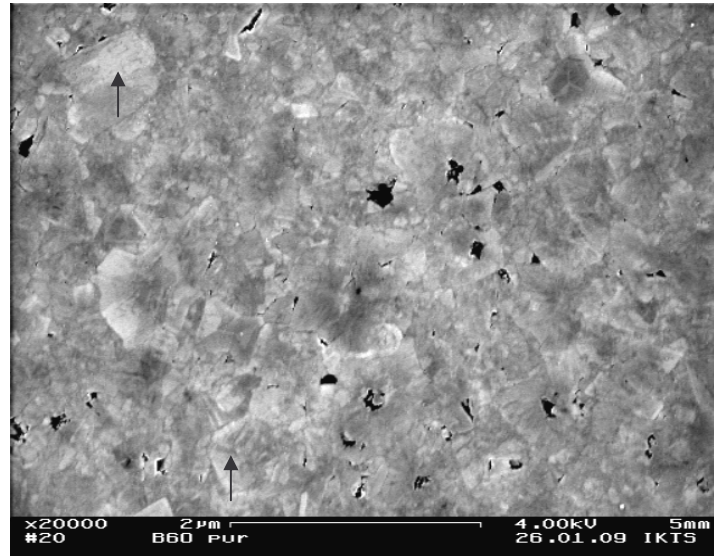


Figure 4.5: In-lens detector SEM image of the pure B₆O ultra high pressure sintered compact. Black areas indicate porosity and the grain structure of the ceramic is clearly visible.

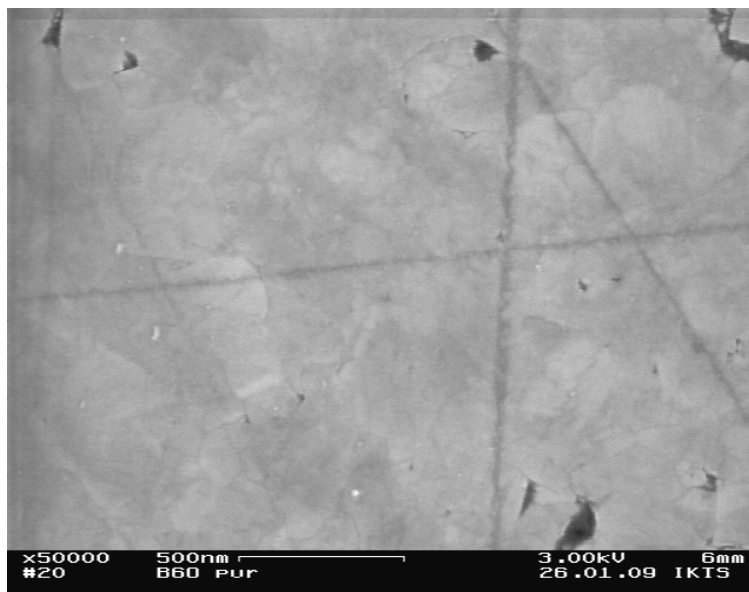


Figure 4.6: Very high magnification SEM image (with in-lens detector) showing fine details in the grain structure of pure B₆O sintered at ultrahigh pressure.

It appears from figures 4.5 and 4.6 as if improper sintering occurred with some plastic deformation of the grains that subsequently relaxed. There appears to be remaining porosity which looks as if sintering was not achieved in the usual manner but rather

that the starting powder was forced together under pressure. B_2O_3 could have allowed some sliding, lubrication and some rearrangement to occur under the applied pressure. Proper sintering by diffusion or through a liquid phase has not taken place. The temperature of 1500°C being below the optimum sintering temperature may have resulted in some healing of some fractures but the sample was not subjected to sufficient time (only ten minutes) for this to occur to any large extent. Some of the lighter and darker features observed may be due to the effect of different grain orientations; this is especially visible in figure 4.5. It can be seen from the particle size analysis results that the starting grain size of the B_6O powder before compaction was under one micron in diameter. Typically, the starting milled powder possessed a size distribution ranging from 0.1 to just over 1 micron (in the extreme cases) yet the grain size of the pure B_6O compact at ultrahigh pressure shows very small grain sizes that are generally less than one micron with a few that are larger than the others (figure 4.5). This seems to indicate that minimal grain growth occurred, but rather that the particles were forced together under immense pressure. It thus appears that grain growth from the original starting powder was negligible. The primary driving force for the densification of the material in this case can thus be said to be the immense pressure. The XRD scan of the material showed only the B_6O peaks.

$B_6O + CoO$

As described in the methodology, cobalt oxide was added to B_6O and sintered under ultrahigh pressure. The resulting micrographs were taken at the IKTS in Dresden Germany, using an in-lens detector arrangement.

The micrographs in figure 4.7 show how inhomogeneously the additive materials were dispersed within the bulk B_6O material. Porosity appears to be higher than the pure material possibly due to pullout of softer secondary phases.

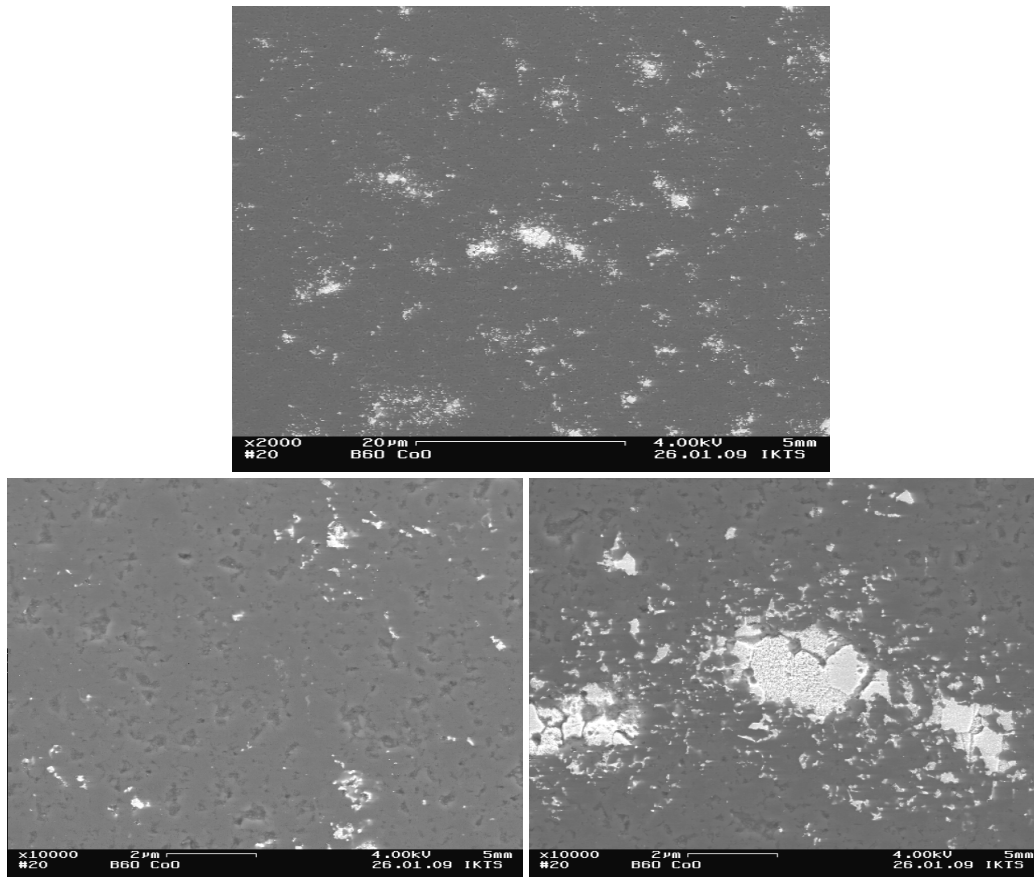


Figure 4.7: Top: SEM micrograph showing distribution of additive material, bottom left: SEM image showing how some areas possessed a very low volume fraction of additive; bottom right: other regions comprised high volume fractions of additive illustrating an inhomogeneous distribution of additive.

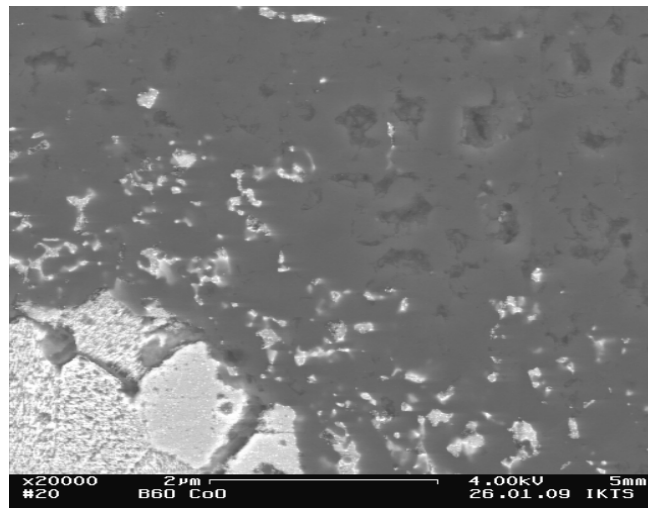


Figure 4.8: High magnification SEM micrograph showing an agglomerate of additive material that appears to have begun to disintegrate and diffuse into the B_6O bulk.

It can be seen from figure 4.7 that the formation of the borides starts from the large agglomerates of the CoO and progresses into the B₆O bulk from there. Porosity can again be seen to be high, perhaps due to pullout of some of the soft B₂O₃ phase during polishing. The in-lens detector image in figure 4.8 also shows extensive porosity to be present. Again, the starting size of the B₆O and additive particles is of importance in understanding these results. From figure 4.9, it again appears that the grain size of the B₆O material is small, within the size distribution range of the starting powder. The CoO additive possessed an average grain size of approximately 5 microns. It can be seen from figures 4.7 and 4.8 that the size of the white phase (CoO originally that became borides after sintering) is approximately 5 microns, leading to the deduction that insufficient time for the full diffusion of the additive particles into the B₆O matrix has been allowed for. The result can be seen in figure 4.8 which shows the transformation and mobility of cobalt borides away from the agglomerate. The low magnification image at the top of figure 4.7 appears to show a similar size distribution of additive colonies around the 5 micron diameter range. Figure 4.9 shows the large amount of open porosity in some regions and figure 4.10 shows the corresponding XRD pattern of the material with the expected B₆O and CoB phase and some Co₃B and B₂Co₃ in smaller amounts.

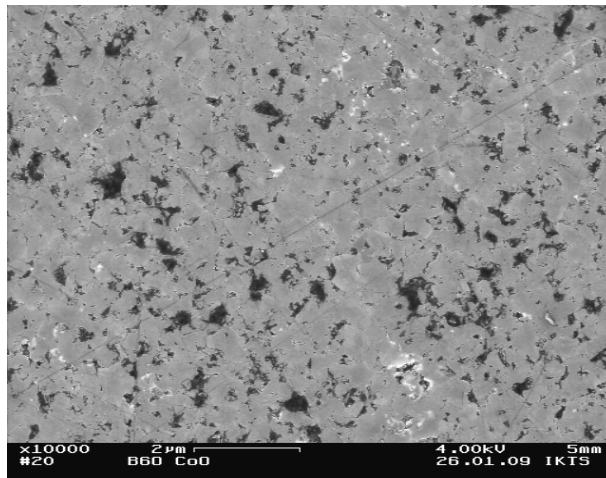


Figure 4.9: Extensive open porosity and inhomogeneity is visible on the UHP B₆O/CoO sample.

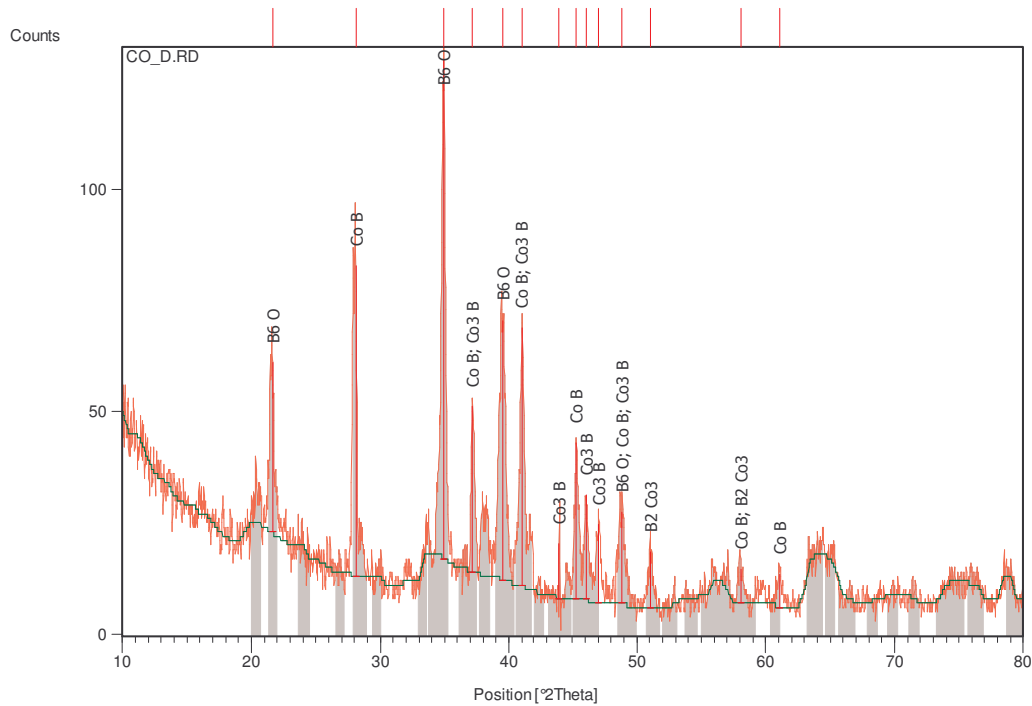


Figure 4.10: XRD scan of the UHP B₆O/CoO material showing the expected CoB phase as well as along with B₆O.

B₆O + Co:

The SEM micrographs of the Co additive proved to be very informative in that they show that the size distribution of the Co additive is very close to that of the agglomerates visible in the SEM images again. It can be seen from figures 4.11 and 4.12 that the diameter of the additive particles appears to be around 30 microns. The average value of the particle size analysis conducted on the starting additive powder was 34 microns in this case. The white spheres in the SEM images, though referred to as cobalt additive, are actually cobalt borides as verified by XRD. The extensive cracking seen in figure 4.13 may be the result of a mismatch in thermal expansion coefficients and elastic constants of the agglomerate and the surrounding B₆O, the softer material (CoB agglomerate) likely has a higher expansion coefficient than B₆O resulting in cracking due to contraction when cooling down (thermal contraction).

The 'halo effect' seen in figures 4.12 and 4.13 corresponds again with diffusion of the cobalt boride phases into the B₆O matrix from the agglomerate as with the CoO

sample, except that the effect is extremely clear in this case due to the large particle size of the agglomerate phase.

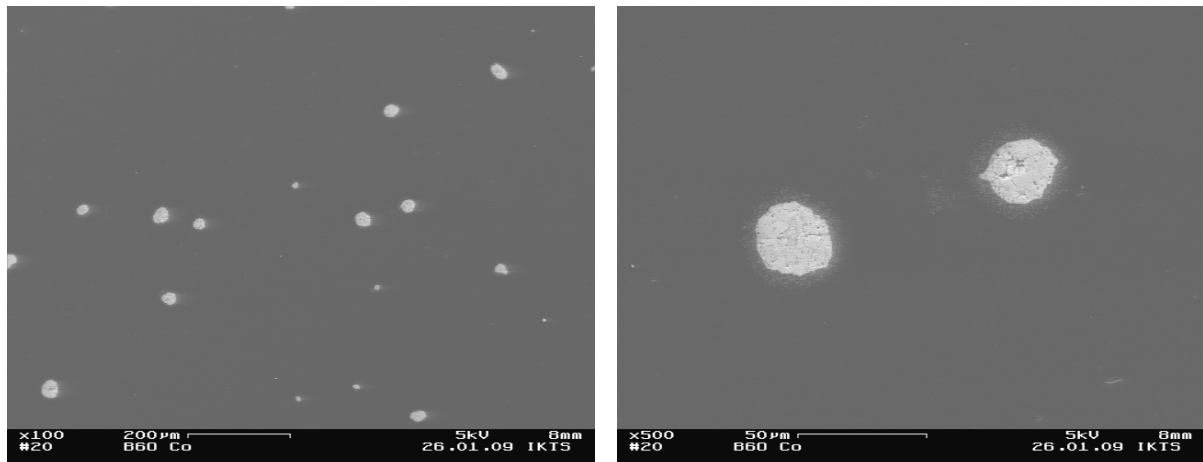


Figure 4.11: Left: Low magnification (100x) SEM image showing the distribution of cobalt additive in the B_6O bulk. Right: Higher magnification (500x) SEM micrograph showing two Co additives in the B_6O bulk.

The grain size distribution in figure 4.14 can be seen to be much the same as the previously described high pressure materials, with poor homogeneity in the distribution of the secondary phase. Regions of almost pure B_6O can be seen that are free from additive phases which is not desirable for the best composite material to result.

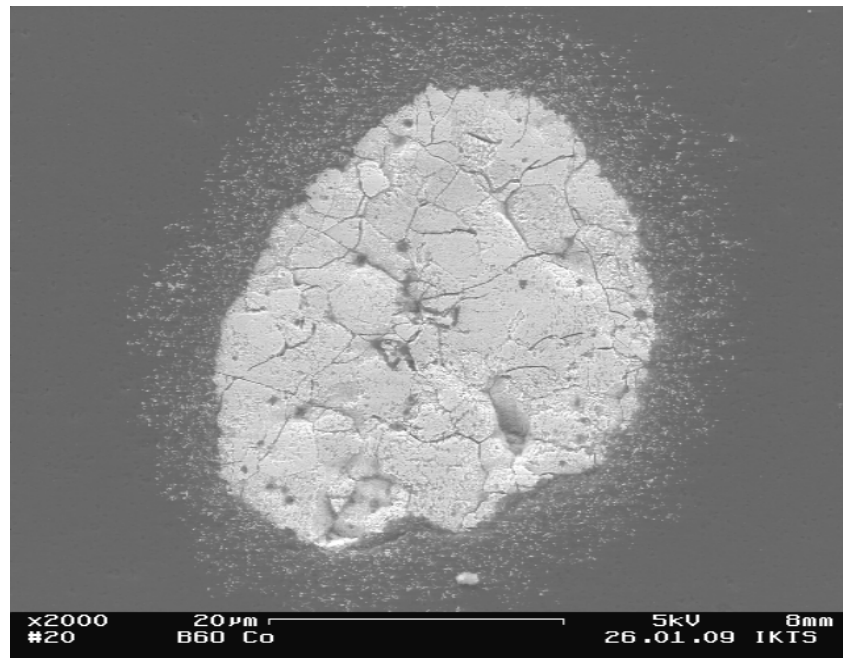


Figure 4.12: SEM micrograph of a Co additive and it's associated 'halo effect' showing boride diffusion into the B₆O matrix.

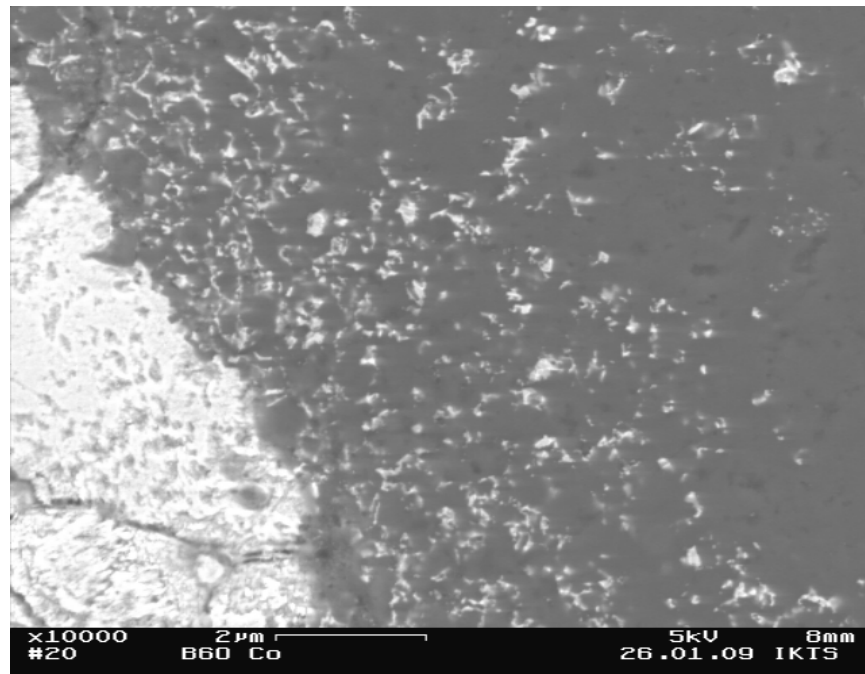


Figure 4.13: SEM micrograph showing the diffusion of cobalt borides from the agglomerate into the B₆O bulk in the UHP B₆O/Co sample.

4.3 Static interaction diffusion couples

Static interaction diffusion couple studies were performed in order to investigate the diffusion properties of the workpiece material (CGI) when in contact with B_6O (the cutting tool material) in order to determine what chemical reactions could occur and what products result. This would allow us to understand and predict possible chemical wear mechanisms that could occur during metal cutting operations.

The static interaction diffusion couple experiments (as described in the methodology) were conducted at 10MPa of pressure for one hour at temperatures of 700, 900, 1100 and 1300 °C with polished surfaces of B_6O and CGI in contact with each other for one hour under an argon atmosphere.

4.3.1 Starting microstructures and compositions

Compacted graphite cast iron:

Compacted graphite cast iron exhibits a vermicular (worm like) morphology of graphite flakes embedded within a pearlite matrix. Optical microscopy and scanning electron microscopy on starting, polished pieces of CGI were conducted in order to act as a basis for comparison between the initial and resulting microstructures post heat and pressure treatment.

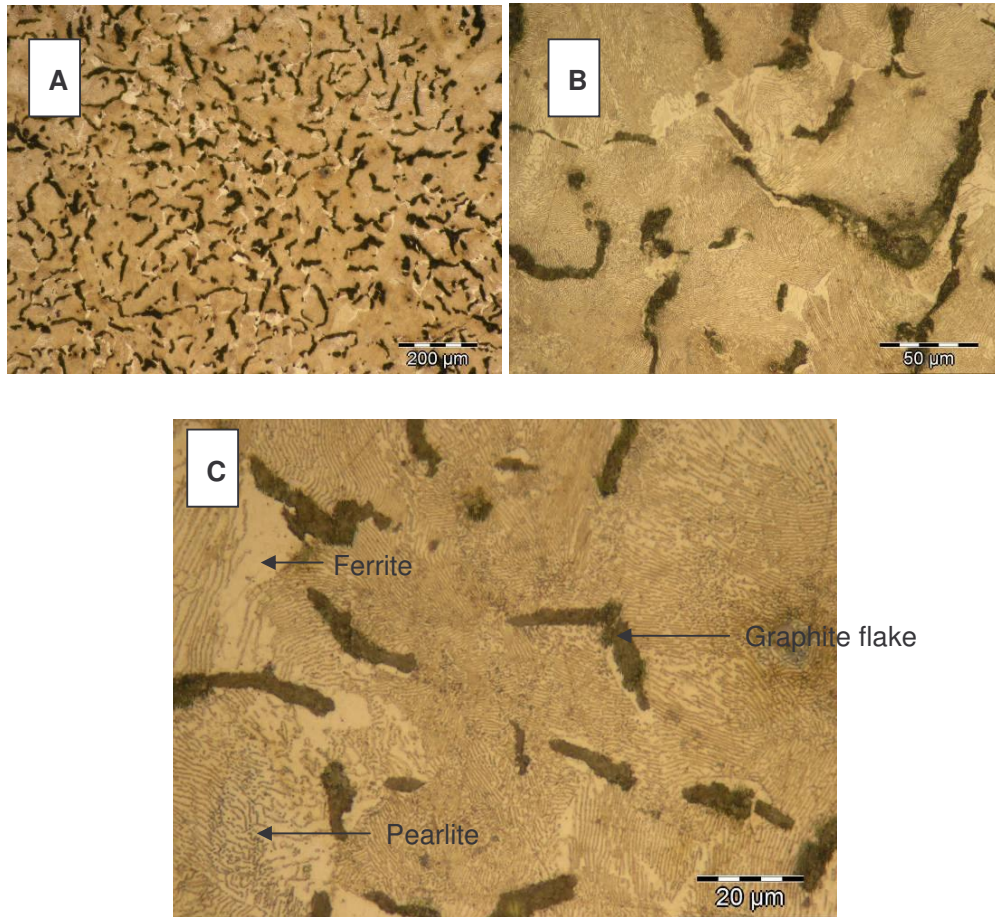


Figure 4.16: A: Low magnification of polished CGI microstructure showing the abundance of vermicular graphite, B: Higher magnification image showing graphite flakes clearly and some pearlite, C: Very high magnification image showing the very fine pearlite (layered) morphology that is typical in this class of cast irons.

X-ray diffraction (figure 4.17) was performed in order to verify the composition of the polished surfaces of CGI before the diffusion couple experiment commenced. The purpose of this being that new phases that evolve during the heat treatment can be attributed to a result of the heat treatment and not the starting composition of the iron. For the same reason, EDS scans using the SEM unit were performed on the same sample in order to quantify the elements present on the surface of the sample and to get some idea of their abundance as shown in figure 4.18.

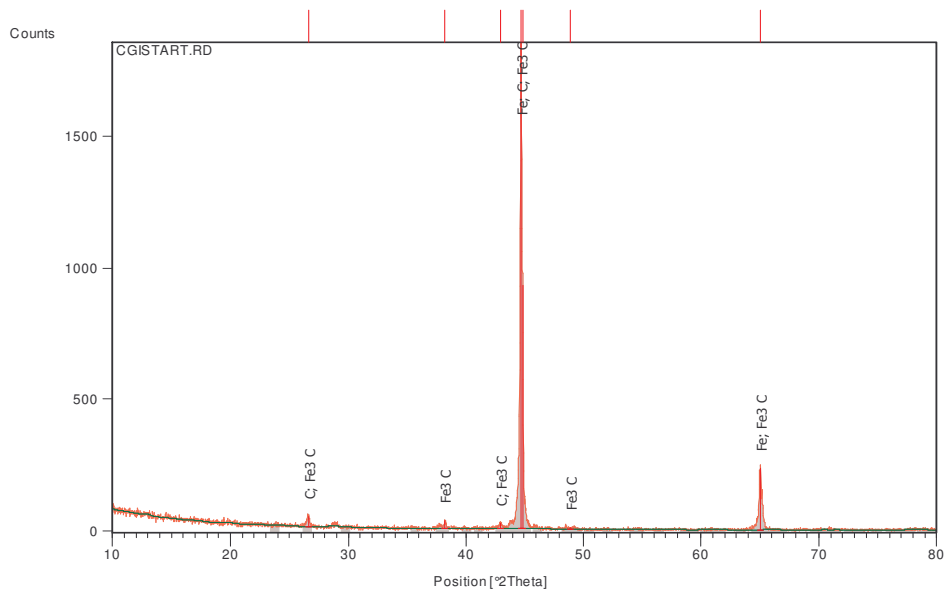


Figure 4.17: XRD trace of the polished surface of a compacted graphite cast iron pill used for static interaction diffusion couple experiments. Note that only carbon (graphite) and iron carbide (pearlite morphology) are detected along with iron as expected.

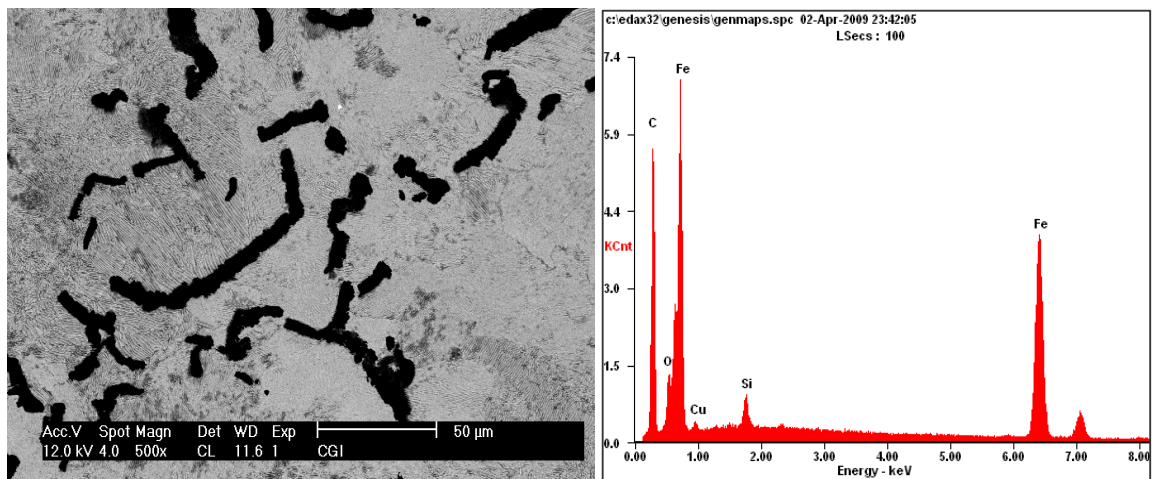


Figure 4.18: Scanning electron micrograph and corresponding EDS analysis of the surface composition of polished CGI.

It can be seen from the XRD trace that the starting composition of polished CGI is, as expected, comprised of iron, carbon and iron carbides. The EDS scan shows an abundance of carbon and some oxygen present on the surface of the CGI pill as well as iron, silicon and some copper (impurity) which is hardly surprising considering the

starting composition of this material (methodology) comprises a number of impurity elements. The reason this EDS trace was taken is because it was necessary to identify if some oxygen was present on the iron surface, which is the case.

Boron suboxide:

Optical microscopy was performed before the couple experiments were performed, but the microstructure of the pure B_6O is unremarkable in such instances. Without a known etchant, it is difficult to observe grain structure without electron microscopy, but the samples were all polished as well as possible in order to ensure good contact surfaces during the experiments. As can be seen below, the sample has been polished (a few scratches remain, but are difficult to remove due to extreme hardness of the material) and some open porosity is visible. All samples were polished in this way, but for brevity, micrographs of these samples are not shown because the image below is representative of the group microstructure.

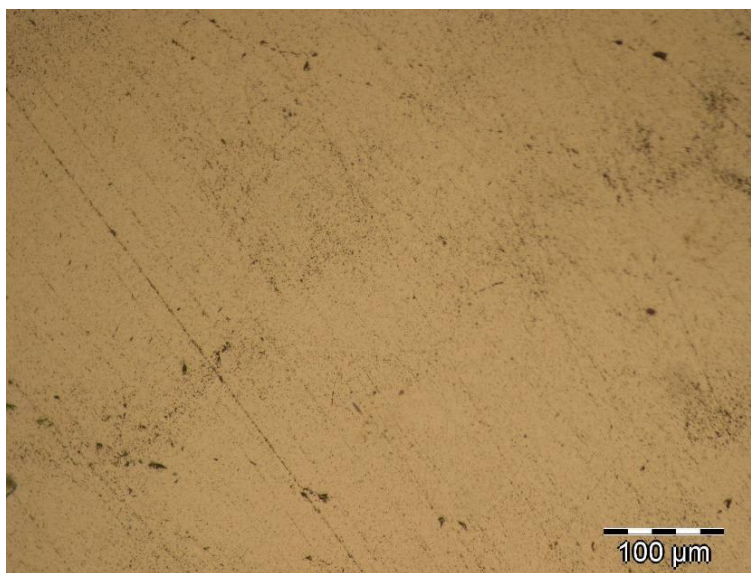


Figure 4.19: Optical micrograph of pure B_6O with polished surface to be in contact with CGI during the couple experiments.

In order to verify that the sintered compacts were indeed boron suboxide as expected, XRD scans were performed on each sample before it was used for couple

experiments. Each pattern produced the same result i.e. pure B_6O diffraction patterns.

4.3.2 Diffusion couple analysis - introduction

The couples separated from one another after the heat treatment process had been completed. The 700 °C couple separated completely and easily without any obvious interaction between the two materials while higher temperatures resulted in localized sticking and pullout of the ceramic material that adhered to the iron. The detailed observations made for each couple in order of increasing temperature is laid out below. Optical microscopy was performed after each heat treatment on the separated surfaces in order to view any significant microstructural changes or visible effects of the heat and pressure treatment.

Scanning electron microscopy and energy dispersive x-ray spectrometry were performed in order to determine the surface morphologies and compositions of the separated couples after their heat and pressure treatment at their respective temperatures. X-ray diffraction studies of the surfaces were also performed as well as cross sectional diffusion profiles and SEM studies of sliced couples using SEM and EDS.

4.3.3 The 700 °C diffusion couple

- **Optical microscopy of the separated couple**

The 700 °C couple separated upon removal from the hBN pot that housed the experiment. Some small blackening was noted on the CGI pill's contact surface with B_6O , but this effect was not particularly remarkable. The sandwiched B_6O pill remained fully intact as did the CGI pills. A side view of the couple is shown in figure 4.20.

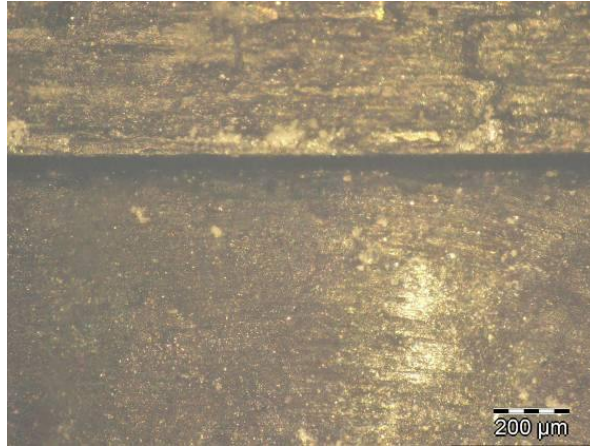


Figure 4.20: Optical micrograph at low magnification showing the B₆O (bottom) and CGI (top) pills as seen from the side. A gap exists between the pills despite the heat and pressure treatment they underwent.

Optical microscopy was also performed on the contact surfaces in order to better characterise the behaviour of the materials in contact. The B₆O showed a persistent shadow effect (figure 4.21) that strongly resembled the graphite flakes of the CGI, possible due to carbon diffusion being active at 700°C already, more so than the other atoms present which allows it to adhere to the B₆O or diffuse into it. The characteristic B₂O₃ film may also have pulled the surface layers of the flakes off the CGI during cooling as it (B₂O₃) solidified. The CGI showed no remarkable distinction from its starting microstructure at low magnification, but at high magnification it could be seen that the pearlite morphology had been damaged by the experiment and it appeared less continuous, with more 'breaks' or interruptions in what were previously parallel lamellae.

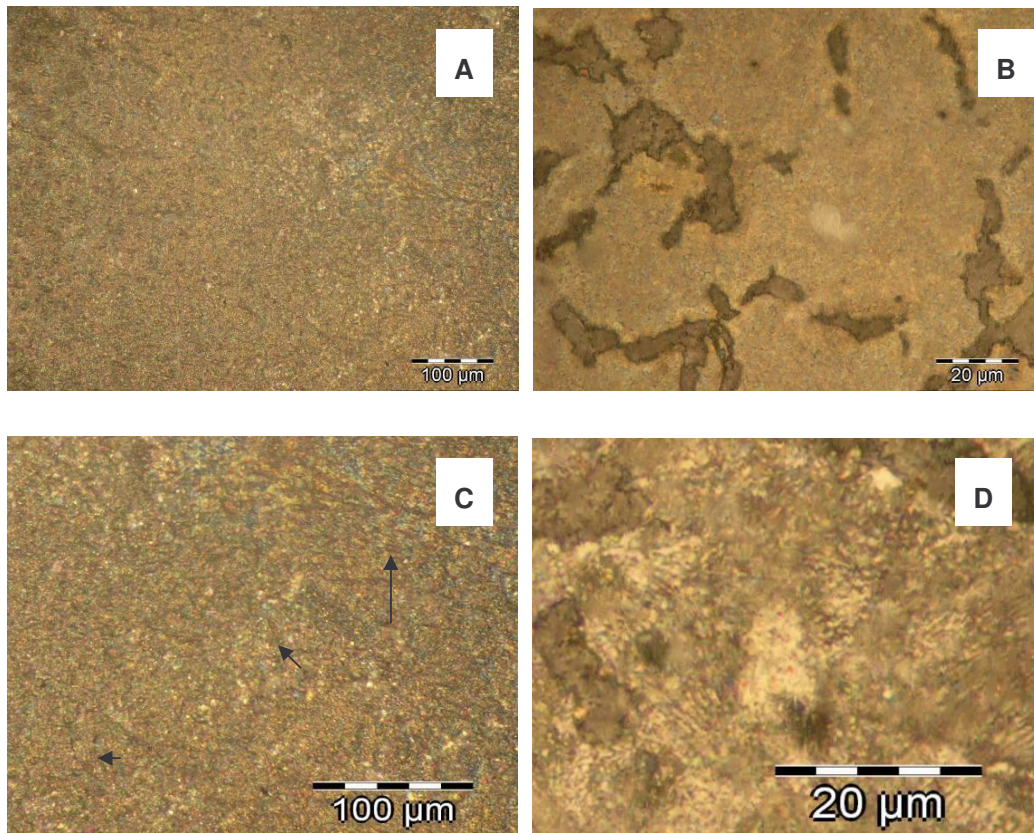


Figure 4.21: A: B₆O surface after the 700 °C treatment; small ‘shadows’ or ‘imprints’ of graphite flakes were clearly visible as indicated by the arrows in C (enlarged image). **B:** CGI surface as seen at high magnification, almost no change was observed except for the destruction of some of the lamellae of the pearlite regions (as seen in D), the lamellae, while still present, appeared less continuous and more chaotic than the starting microstructure.

- **Surface investigation using SEM**

The surface of the CGI pill was seen to be unremarkably changed except for its pearlite morphology appearing slightly less ‘parallel’ with the lamellae appearing to be disjointed and disorganised relative to their original state before the heat treatment. The effect of the heat treatment is more clearly visible on the SEM image below than on the optical micrographs displayed earlier. It can be seen that the pearlite lamellae have been disrupted (possibly even compressed) by the heat and pressure they were subjected to. The EDS pattern of the entire region in the micrograph shows the expected composition of iron and carbon (ferrite and iron carbide phases) as well as some silicon and perhaps a trace of copper.

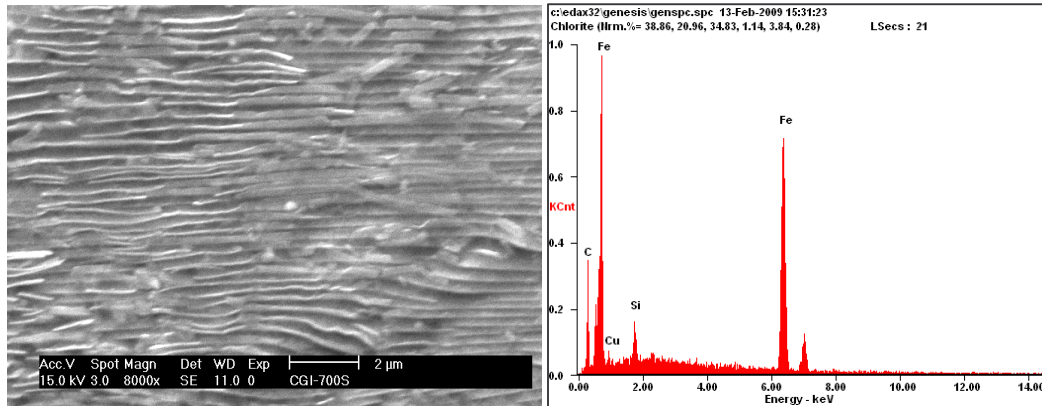


Figure 4.22: Left: SEM micrograph showing the pearlite morphology that resulted after the 700°C experiment; right: the elemental composition of this region displays the expected iron and carbon constituents as well as some silicon and copper impurities.

Figure 4.22 indicates the appearance of the pearlite morphology after the couple experiment at 700 °C. The expected elements were detected in this region with no sign of boron or oxygen.

SEM of a representative region on the surface was performed as seen in figure 4.23. The EDS for this region indicates a slightly higher abundance of silicon, revealing that silicon diffusion is prevalent towards the Fe-B₆O interface even at 700 °C. An almost negligible amount of boron and some oxygen were also detected, along with the expected carbon and iron signals.

The appearance of the 700 °C CGI surface was remarkably unchanged from the starting microstructure and composition and a slightly higher silicon and carbon count which likely indicates that these atoms start to diffuse at this temperature.

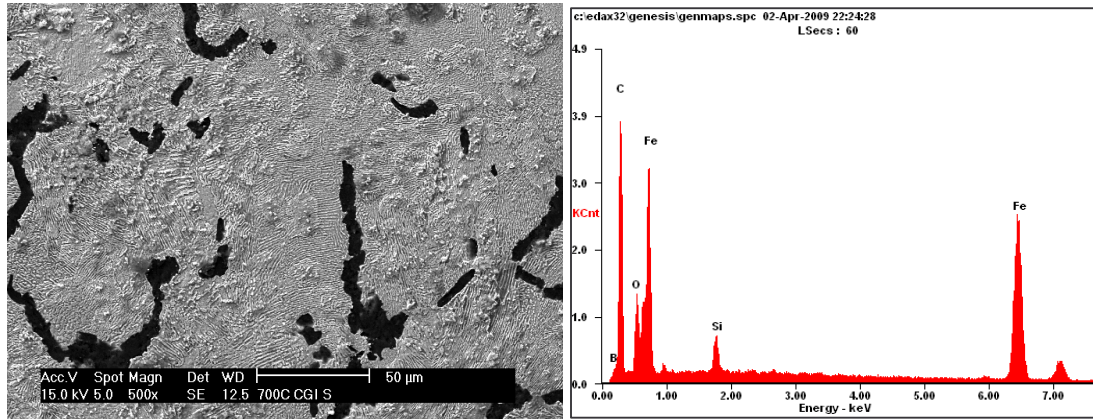


Figure 4.23: SEM image and corresponding EDS trace for the iron surface at 700°C. The EDS trace for the entire image can be seen to the right.

SEM images of the B_6O surface and their corresponding EDS scans were taken and can be seen in figure 4.24. Small white spotted regions were clearly visible on the B_6O surface while they were not visible under optical microscopy. The EDS scan of the micrograph of the general area of the surface shows that B, O, Si, Fe and C are present on the surface of the ceramic. Boron and oxygen of course result from the ceramic material itself; while silicon, iron and carbon originated from the CGI pill. In order to clarify the appearance white regions, a higher magnification image was taken. They indicate that the whitened regions are rich in iron and carbon.

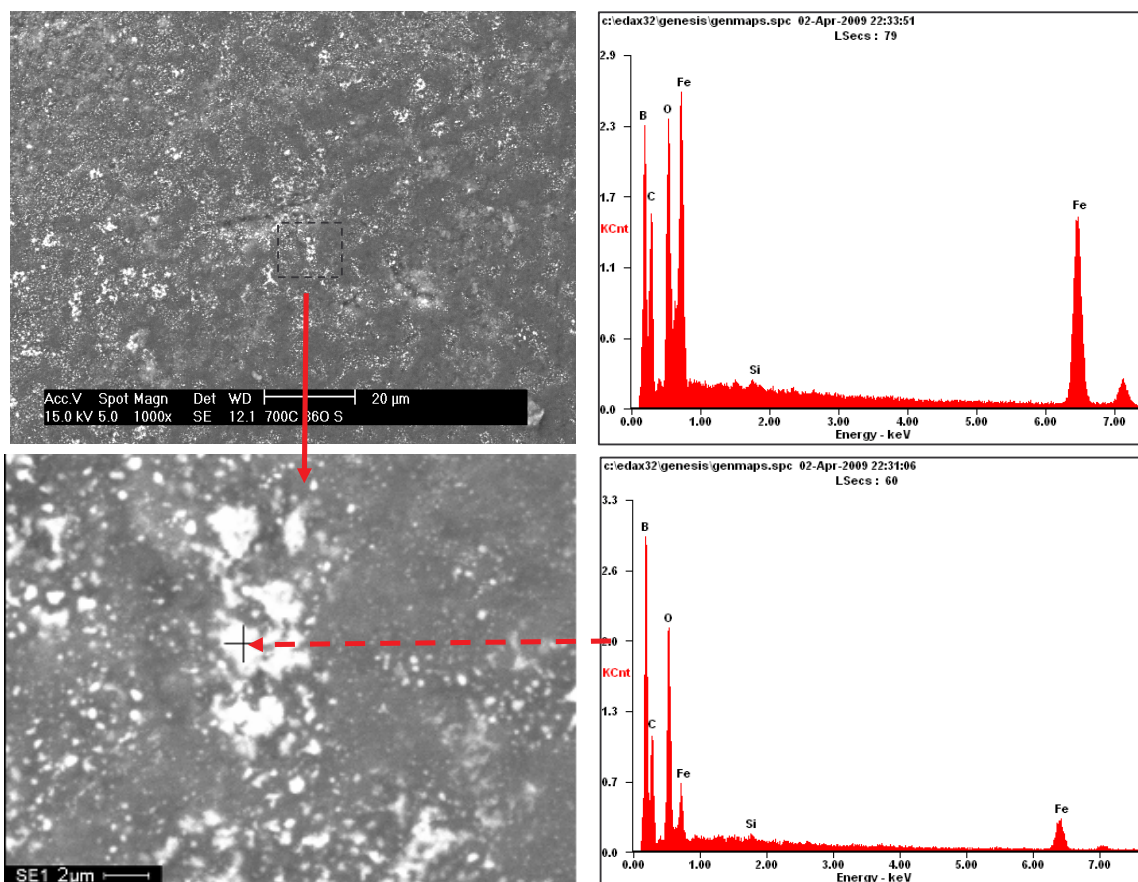


Figure 4.24: SEM micrograph and EDS scan of the entire photographed region of the B_6O side of the 700 °C diffusion couple (top) and micrograph and EDS scan of the targeted white region (bottom).

In figure 4.25, high magnification images of the white spots can be seen. It is likely that the iron adhered preferentially to this region of the sample due to this being a roughened area of the B_6O sample. Some diffusion may have occurred, but very little due to the low temperature and iron being a large atom, which would thus experience difficulty diffusing into the B_6O crystal matrix. Liquid B_2O_3 formation may have aided in some adherence by reacting with the iron or iron oxides and subsequently adhering to those areas even after cooling. The pore likely amplified the effect, because iron adherence was only seen in regions that displayed apparent porosity. A similar (thin) white layer was seen to surround pores as can be seen in figure 4.24.

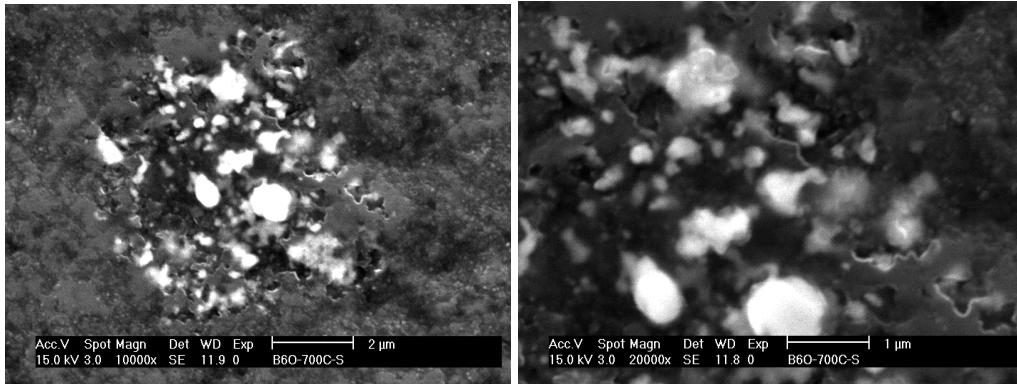


Figure 4.25: Higher magnification SEM micrographs of the white spotted region of the B_6O surface. The iron rich regions (white) appear to be embedded within flake-like layers within what was probably a surface pore in the B_6O sample.

- **XRD of the separated 700 °C couple**

As mentioned above, the diffusion couple separated effortlessly upon removal from the hBN pot. The contact surfaces were subjected to XRD scans in order to determine the phases present. A summary of the detected phases can be seen in table 4-8.

Table 4-8: Table of detected phases on either side of the 700 °C diffusion couple in order of abundance.

Phases detected on the B_6O side	Phases detected on the CGI side
B_6O	Fe
C	SiO_2
FeO	Fe_3C
Fe_3O_4	-

It was seen from the XRD pattern (in the appendix) that silicon dioxide (SiO_2), iron carbide (Fe_3C) and perhaps a little B_2O appear to be present at or near the surface of the pill. Iron is, of course, present but its XRD pattern closely resembles that of iron carbide and there is significant peak overlap, so it is not always clearly visible on

such an image. The largest independent (non-iron or carbon related) peak could be seen to be that corresponding to silicon dioxide, indicating silicon diffusion is definitely present at this temperature.

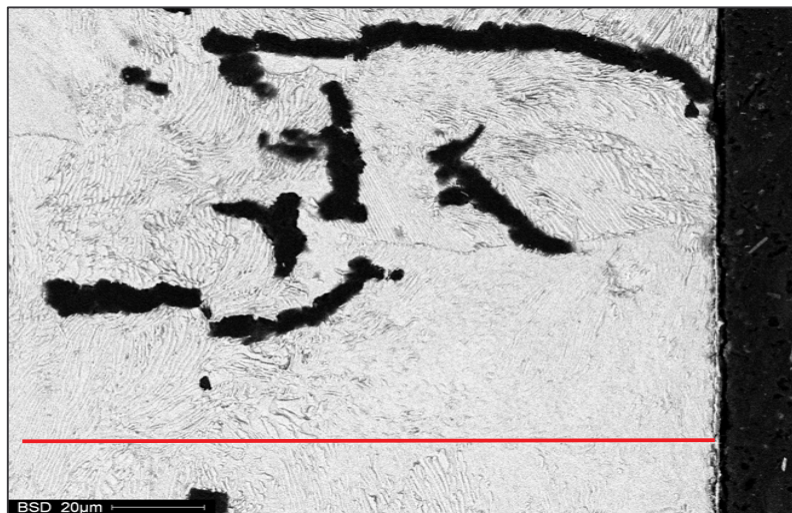
The B₆O side of the couple possessed peaks corresponding to B₆O (of course) as well as iron oxides namely Fe₃O₄ and FeO as well as carbon (from the graphite most likely – possibly the ‘shadow’ effect described above) No silicon was detected on the scanned region. Some very small peaks can be seen that could not be reliably assigned that could correspond to another phase being present, but at the margin of the detection limit of the XRD apparatus.

An investigation into the cross section of the interfacial and near-interfacial regions of the static interaction diffusion couples was performed in order to determine if diffusion was active between the two materials, and the degree of penetration that diffusing atoms may have achieved within the bulk material near the interface over the time period of the heat and pressure treatment. The SEM images have been shown for each side of the diffusion couple as well as the diffusion profile obtained by separate EDS scans on each of the halves of the diffusion couples

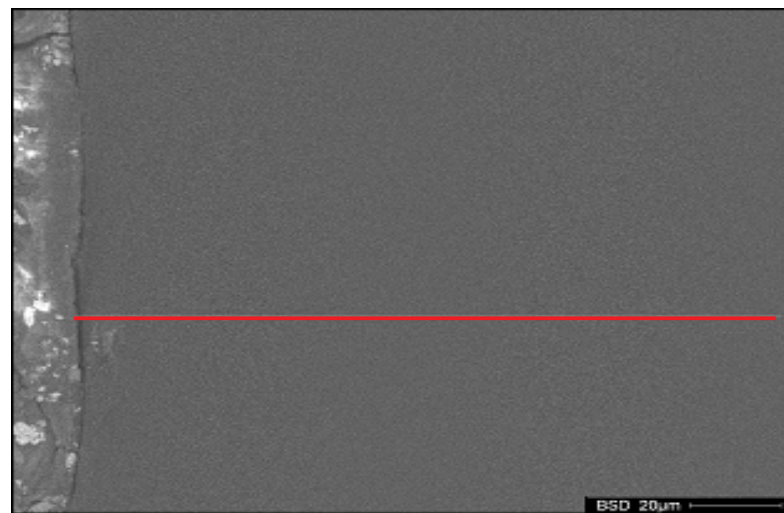
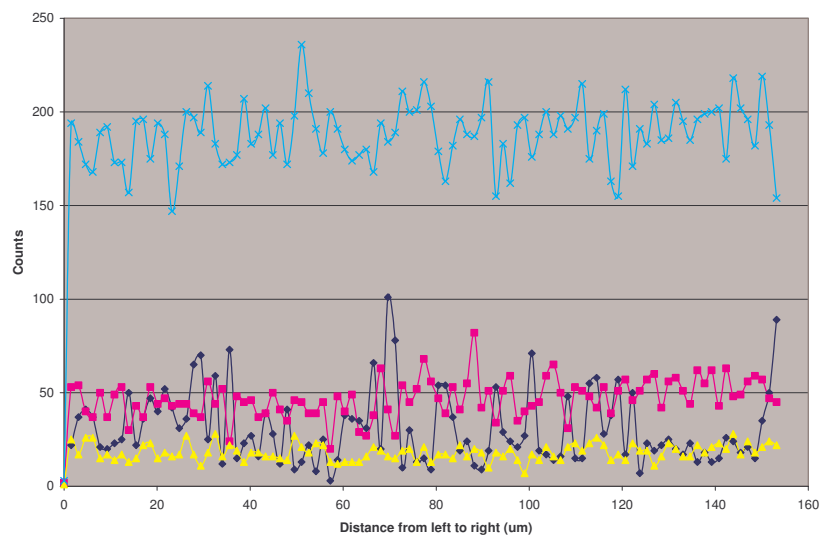
- **SEM investigation of 700 °C diffusion couple cross sections**

The cross sectional EDS trace of the CGI/B₆O diffusion couple at 700 °C (figure 4.26) shows iron concentration to remain fairly consistent through the scan as it proceeds from left to right. Note that the images and scans have been presented so that the reader can read the data and compare this with the location that the scan was taken from on the image as one moves one’s eye across the indicated line scan region from left to right.

The biggest fluctuation occurs in terms of carbon content across the interface, but the reliability of this should be questioned due to the presence of carbon-containing bakelite. The boron content fluctuates notably as does the oxygen content near the interface. The silicon content seems to rise marginally towards the interface.



EDS compositional profile of various detected atoms on the Fe (CGI) side of the interface at 700°C



EDS compositional profile of various detected atoms on the B₂O side of the interface at 700°C

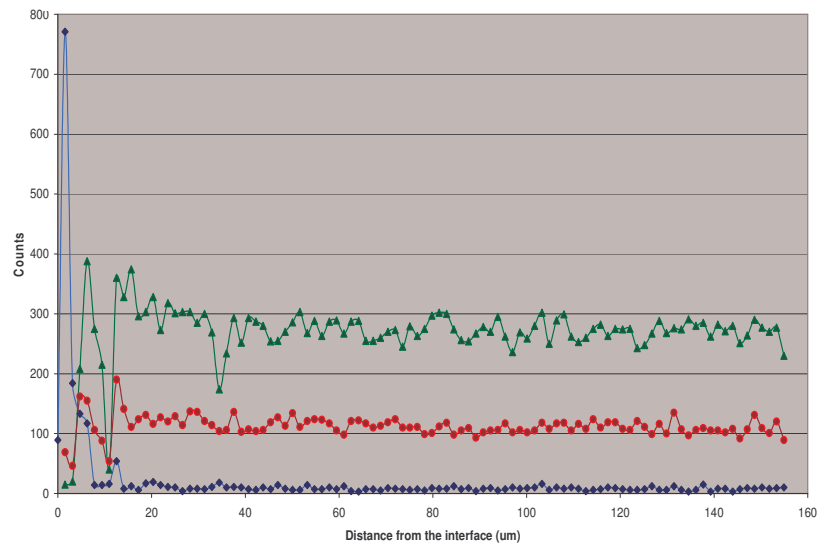


Figure 4.26: EDS line scans and corresponding scanned regions on the images shown and plot of the diffusion profile for the constituent elements.

4.3.4 The 900 °C diffusion couple

- **Observations and optical microscopy**

The interaction at 900 °C resulted in some pullout of the B_6O material which adhered to the CGI pills. While the couple was still separated (the couples simply fell apart) small black areas of adherent B_6O on the CGI were immediately apparent as well as corresponding voids (holes) in the B_6O pill corresponding to the pulled out material. The B_6O surface shows very definite graphite flake shadow effects as described for the 700 °C couple, but are more pronounced. The surface also appeared greyish, not black any longer; possibly due to adherent iron material. The CGI surface appeared to lose its lamellae (pearlite) while the graphite flakes persisted. The surface was most noted for its adherent B_6O , but it too changed colour and appeared quite dull and grey, a definite change from the polished surface that it started out as being.

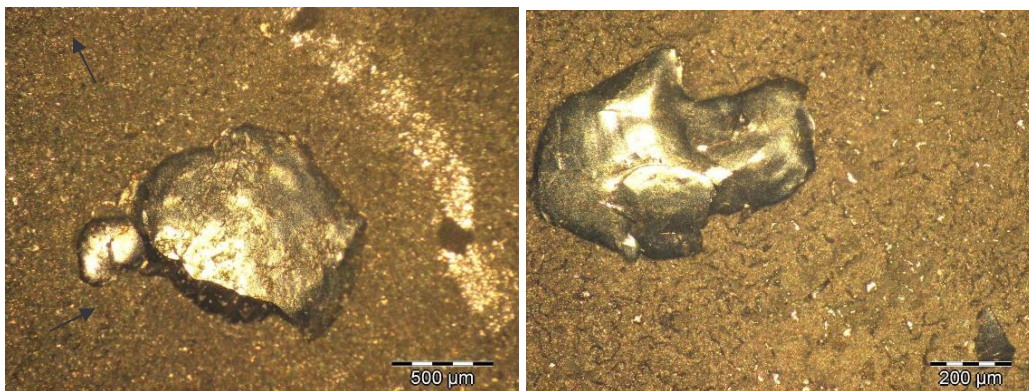


Figure 4.27: Left: B_6O surface resulting from the 900 °C diffusion couple treatment. The clear black regions that look vermicular strongly resemble the graphite flakes of the CGI (marked by the arrows) while the large hole left behind by pullout is very clear. Right: the pulled out B_6O has adhered to the CGI, vermicular graphite flakes are still visible.

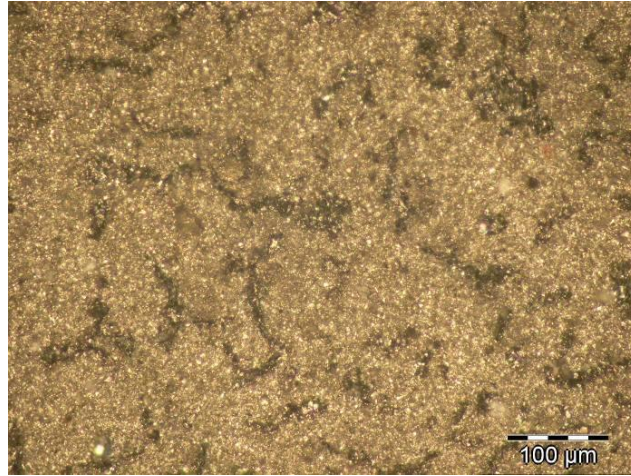


Figure 4.28: Micrograph showing the change in the iron microstructure as a result of the heat treatment at 900 °C. While graphite flakes remain, pearlite lamellae have been lost.

- **Surface investigation using SEM**

The most significant area of interest on the B_6O /CGI diffusion couple surfaces was a piece of adherent B_6O to the CGI surface. The presence of this piece of ceramic allows for a more detailed observation of the interface of B_6O and the CGI.

As can be seen from figure 4.29 this material remains adherent to the CGI half of the couple even after cooling and removal from the pot. The B_6O material still remains intact.

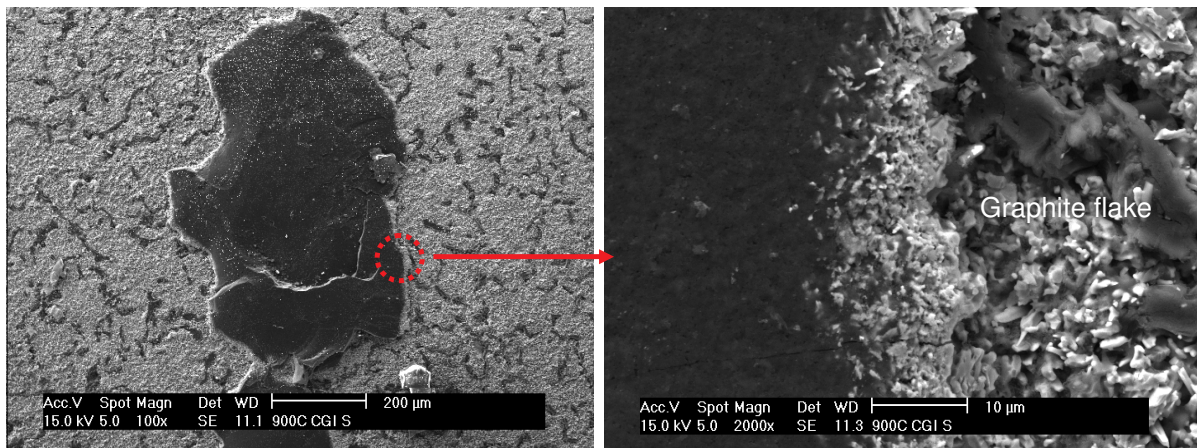


Figure 4.29: The surface of the CGI pill after the diffusion couple experiment at 900 °C. A piece of adherent B_6O is clearly visible. Notice the carbon flakes (vermicular shapes) are still persistent with other interaction products (non-faceted crystals) also present.

The surface of the CGI can also be seen to have changed substantially as it appears more rippled and featured than the 700 °C couple. This is expected due to the higher temperature accelerating the diffusion and interaction reactions and products forming. The graphite flakes appear relatively unchanged. Figure 4.29 shows a higher magnification image of the adherent B₆O and the CGI. There is clearly an interfacial area where iron or iron-boron products adhere to the B₆O or vice versa. The materials may be adhering to surface defects on the B₆O as they did with the 700 °C couple but to a larger extent due to the higher temperature.

The surface of the B₆O half of the diffusion couple was unremarkable and was virtually identical to the surface described with the 700 °C couple, with some colonies of adherent iron products (as before but more of them than before), but mostly pure B₆O. Furthermore, the formations visible in figure 4.29 were investigated in detail for the 1100 °C couple as the same behaviour occurred at that temperature but to a greater and clearer extent. Special attention was paid to the 1100 °C couple due to it being at the expected upper limit of machining temperatures.

- **XRD of the 900 °C diffusion couple surfaces**

The XRD scans of the separated 900 °C diffusion couples detected an increase in the amount of iron products present, demonstrating that a more significant interfacial region resulted with more reactions taking place due to the elevated temperature. Table 4-9 shows the detected phases in order of abundance on either side of the interface detected by XRD. Fe₂B was by far the most abundant product on the CGI side. Silicon dioxide was also readily detected, due to the very active silicon diffusion even at these temperatures. The XRD traces can be viewed in the appendix.

Table 4-9: Table of detected phases on either side of the 900 °C diffusion couple in order of abundance.

Phases detected on the B ₆ O side	Phases detected on the CGI side
B ₆ O	Fe ₂ B
Fe ₂ B	Fe
SiO ₂	B ₆ O (pullout)
BN (contaminant from pot)	SiO ₂
-	C
-	Fe ₃ C

It can be seen from table 4-9 that predominantly B₆O was present on the B₆O side of the diffusion couple interface, but Fe₂B products were abundant with smaller amounts of SiO₂ present. Note that some BN contamination was detected probably due to contamination from the hBN pot that was used to house the experiment.

- **SEM investigation of 900 °C diffusion couple cross sections**

The 900 °C diffusion couple displays marked increases in compositional fluctuations, which is to be expected due to the higher temperature allowing for more reactions and diffusion to take place in the holding time of one hour.

SEM micrographs of the interfaces and near interfacial region of the 900 °C diffusion couple show a thin interfacial region approximately twenty microns thick on the CGI side while the B₆O side shows no interfacial reaction or change, as can be seen in figure 4.30. The light feature seen on the B₆O is not believed to be a feature related to diffusion, but rather, when investigated, was shown to be a porous area that picked up bakelite resin and other stray material during polishing.

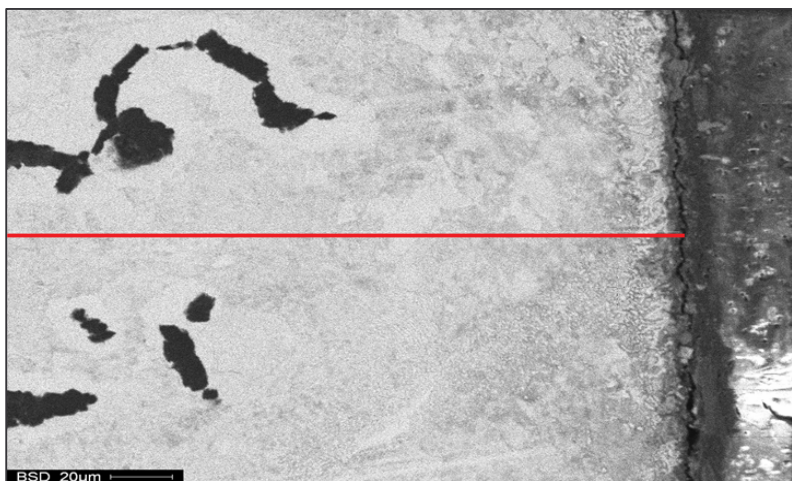
In this particular instance, the polishing of the B₆O seemed to result in some slightly more porous regions of the ceramic being occupied by bakelite resin and other impurity materials as indicated by the high carbon content when the EDS scan was

performed on that area. These phenomena are not related to the heat treatment, because the line scan did not detect a gradual decline in carbon content as one moves further into the B_6O bulk. Rather, the carbon content of the bakelite resin was seen to be high (as expected) and the greyish areas in the bulk also contained high carbon content leading to the deduction that they are a by-product of polishing. They could have been due to impurities in the starting material, but the polishing is a more likely explanation as the XRD traces before the couple experiments showed all the B_6O pieces to be 'pure'.

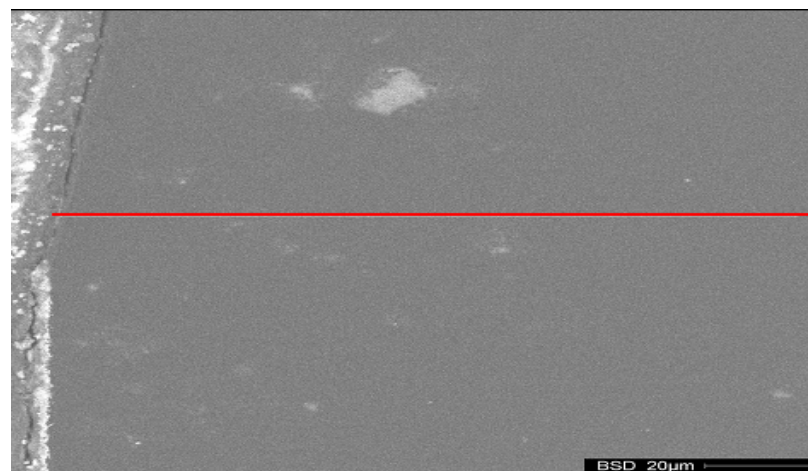
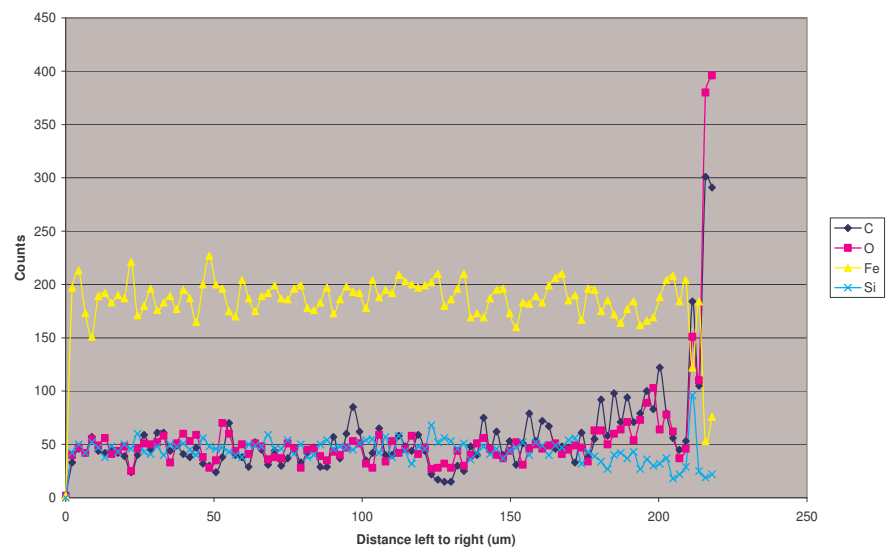
The CGI side of the couple displays an interfacial interaction effect that can be approximated at 10 to 20 microns thick. The B_6O side of the couple again, did not display any noticeable interface, aside from the pulled out B_6O that remained embedded in the iron as described earlier.

The diffusion profile shows significant boron fluctuations near the interface, possibly the result of B_6O decomposing into B_2O_3 and reacting to form borides at the interface. Silicon is seen to spike significantly as well at a specific point, but this is probably a polishing contaminant due to the lack of any kind of nearby silicon gradient.

Oxygen and carbon again fluctuate, most likely significantly due to the bakelite presence, but not exclusively this, the oxide layer on the iron probably contributes some oxygen to this as well as the potential reactions that could occur with oxygen in the interface. The iron content remains consistent and suddenly drops due to the line scan straying slightly into the bakelite resin, i.e. it can be said that iron diffusion into B_6O is minimal at this temperature, but grain boundary diffusion is still possible, but probably not extremely prevalent. Diffusion in general is active however, due to the indicator atoms such as silicon, showing significant changes as one moves towards the interface as seen on the CGI side of the couple.



EDS compositional profile of various detected atoms on the Fe side of the interface at 900 °C



EDS compositional profile of various detected atoms on the B₂O side of the interface at 900 °C

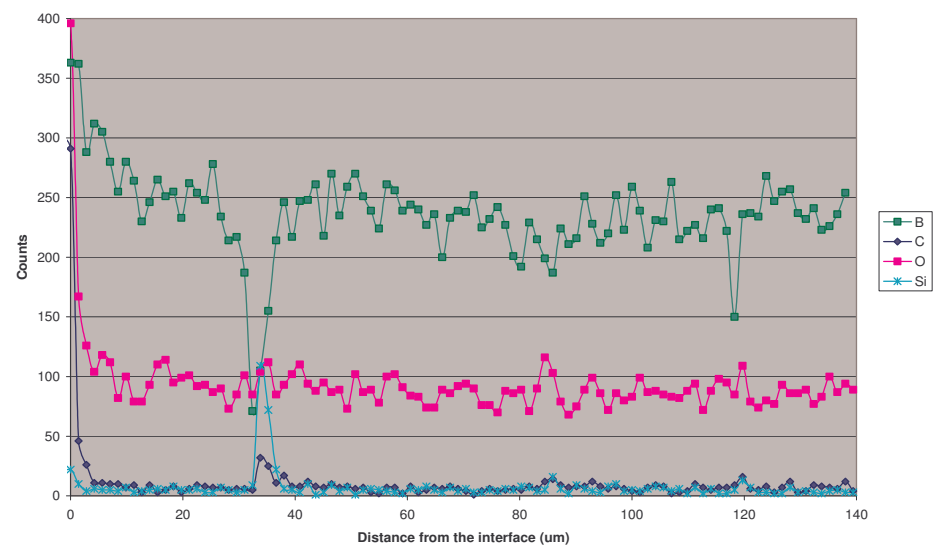


Figure 4.30: Line scan images and corresponding EDS plot of the various detected elements across the 900°C diffusion couple interface.

4.3.5 The 1100 °C diffusion couple

- **Observations and optical microscopy**

The diffusion couple at 1100 °C displayed a marked change as a result of the heat treatment. Firstly, the first reaction couple tested at this temperature cracked while cooling, resulting in only fragments of B_6O . Fortunately the second, while fracturing in places, still produced surfaces that were easy to characterise. The couple still separated, but this time the amount of adherent B_6O on the iron was far greater than at 900 °C. Significant portions of the B_6O surface pulled out and remained embedded in the CGI. Both surfaces were the same colour and appeared almost indistinguishable from one another under light microscopy, most likely due to very active diffusion at these temperatures. The graphite flakes of the CGI seemed to disappear almost completely, but darkened regions, possibly carbon rich, could be indications of where the flakes existed, but the carbon has mostly diffused away.

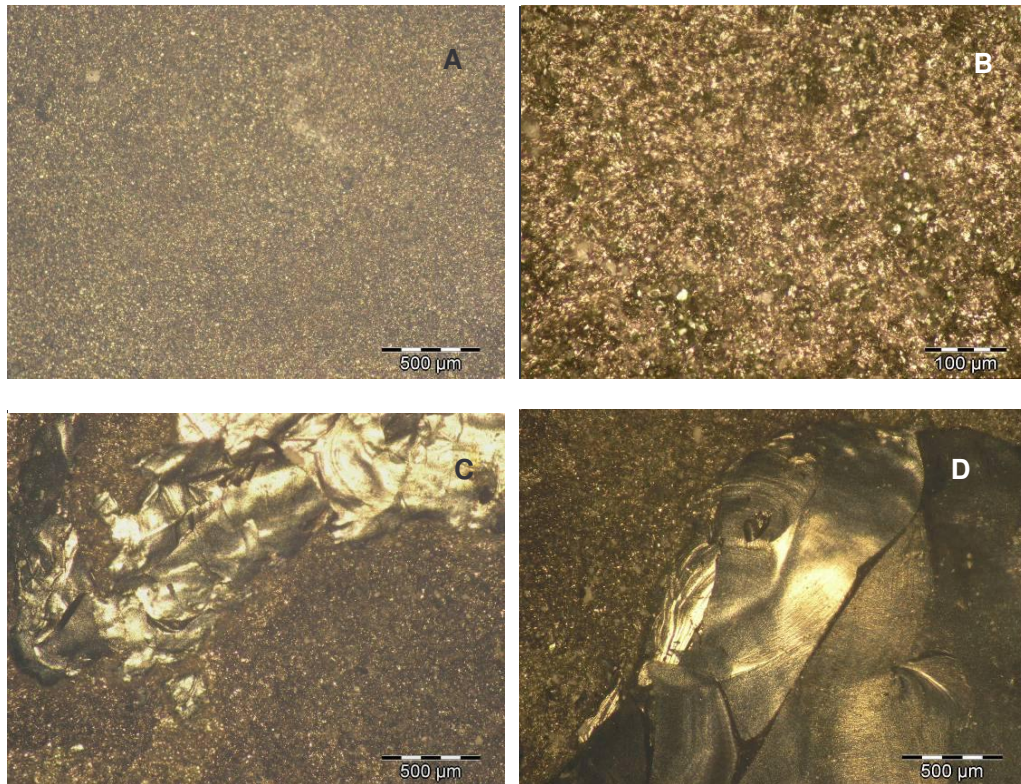


Figure 4.31: A: B_6O surface showing no remarkable features after the 1100 °C couple experiment. B: CGI surface showing no evidence of graphite flakes, but darker regions could indicate their prior presence. C and D: large B_6O adherent islands embedded in the CGI pills.

- **Surface investigation using SEM**

The features shown above in the optical micrographs were further analysed using SEM. The surface of the CGI pill became greyish and pitted with a very rough surface texture, indicating a great deal of interaction between the couple materials at this temperature and pressure. It is also important to note that the iron would plastically deform under a load at this temperature as the temperature is nearing the melting point temperature of these materials of around 1300 °C. Roughening due to applied load is thus expected. The graphite flakes were completely invisible in the resulting CGI pill after the couple experiment.

In figure 4.32, small rounded regions almost resembling globules or crystallized areas can be seen to adhere to the B₆O. The EDS of this region shows an abundance of iron with very significant amounts of boron, oxygen and carbon, and amounts of silicon indicating that diffusion of iron and its constituents is very active at these temperatures. It is unlikely that iron diffuses into the B₆O itself.

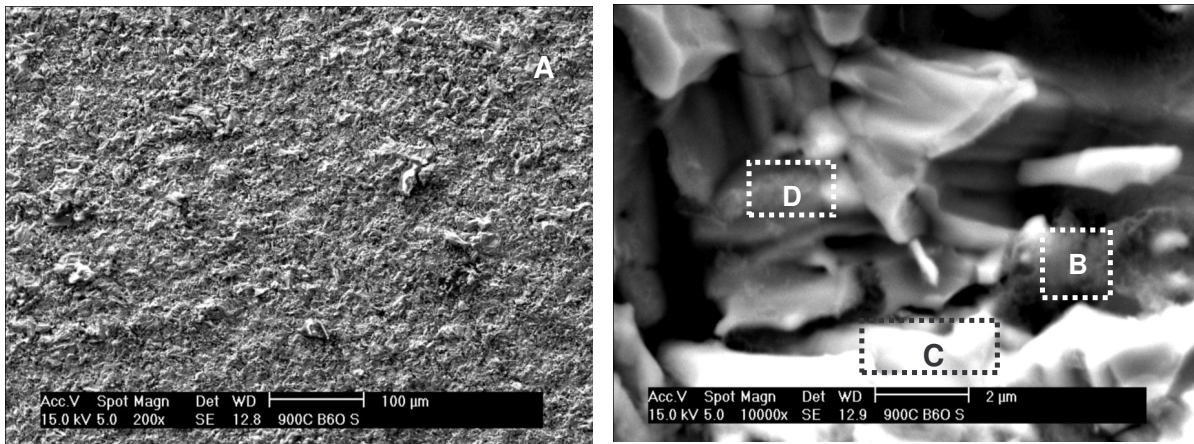


Figure 4.32: SEM micrograph of the B₆O side of the 1100 °C diffusion couple. This particular area was covered in iron and other materials quite extensively.

Table 4-10: Summary of the atomic percentages reported by EDS scans of the B₆O surface of the 1100 °C diffusion couple.

Region	B (at. %)	C (at. %)	O (at. %)	Si (at. %)	Fe (at. %)
A (whole image)	46.00	24.86	5.76	1.06	22.33
B	32.96	42.85	11.41	2.94	9.84
C	61.75	23.44	2.97	0.43	11.42
D	52.84	26.13	4.00	0.084	16.19

Although one has to be careful when comparing EDS values in a quantitative manner, the relative atomic percentages can be considered ‘semi-quantitative’ as they give an idea of where a particular atom is more or less abundant relative to the next region. This is particularly true of polished sections, but regions with porosity need to be treated more carefully. This is because EDS responds differently to the detection of lighter elements than it does to heavy elements, and light element ‘counts’ possess a larger error than heavier ones due to fewer electrons in their electron clouds (i.e. fewer possible x-ray interactions) and thus less accurate determination of atomic or weight percentages of lighter atoms.

Table 4-10 shows that boron is present in all of the areas, as expected on the B₆O surface, but region B is clearly richest in carbon (looks like a piece of adherent graphite flake) and Si, while iron is richest in region D. The region could correspond to a region of iron oxide on top of carbon (graphite).

Figure 4.33 shows a lower magnification image of the surface of the CGI half of the 1100 °C couple with the EDS trace of the entire region shown as well as a higher magnification image showing the remnant of a graphite flake and the surrounding surface features. Table 4-11 shows that region A is definitely carbon (graphite) rich and that the surrounding area contains diffusion products of all the other atoms listed. Boron can be seen to be present, but the atomic percentage (at. %) of the reading is unexpectedly high, probably due to EDS exaggerating the boron signal with significant errors.

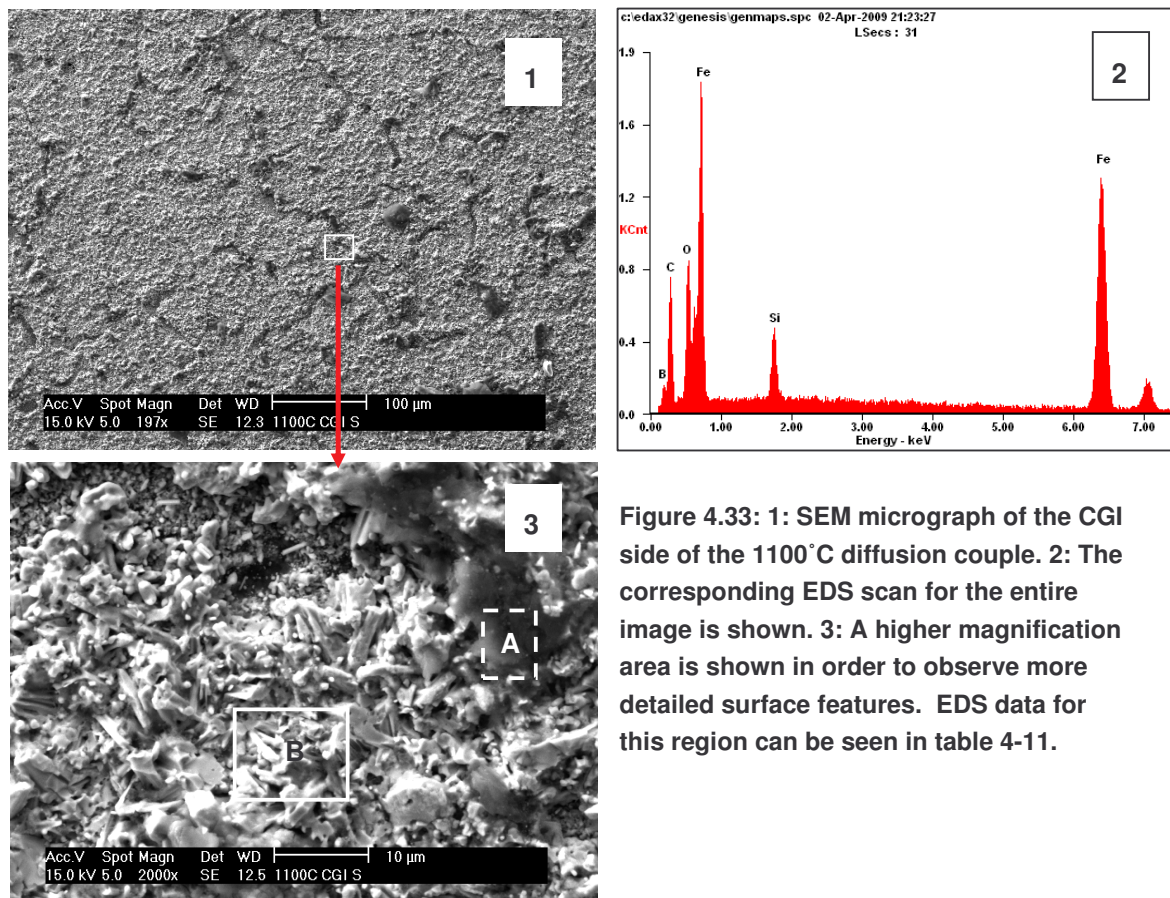


Table 4-11: Summary of the atomic percentages reported by EDS scans of the CGI surface (higher magnification region) of figure 4.33 of the 1100 °C diffusion couple.

Region	B (at. %)	C (at. %)	O (at. %)	Si (at. %)	Fe (at. %)
A	0.00	95.07	3.42	0.39	1.12
B	49.56	22.54	6.66	1.26	19.98

The flake like appearance of the B_6O and CGI surfaces could be the result of rapid diffusion of all the constituent atoms and the 'rounding off' of edges or flakes or even crystal-like formations of the reaction products that formed, resulting in the appearance that we see here. Figure 4.34 is a 'flow diagram' showing adherent B_6O on the CGI side of the 1100°C diffusion couple that shows increasing magnifications of the areas of interest. EDS traces of labelled 'boxed in' areas are shown below the micrographs and are labelled accordingly.

The SEM investigation of the pulled out B_6O piece of the 1100°C diffusion couple shows a clear interfacial region where CGI products diffuse into the B_6O and vice versa. It is clear from the EDS traces that no other atoms aside from boron and oxygen are present in the bulk of the B_6O piece, but closer to the interface, the diffusion products can be seen (Fe, Si, C, B and O). The white spots entering the B_6O appear to be mostly iron, possibly indicating grain boundary diffusion of iron into the B_6O . Silicon and carbon are also present in these regions.

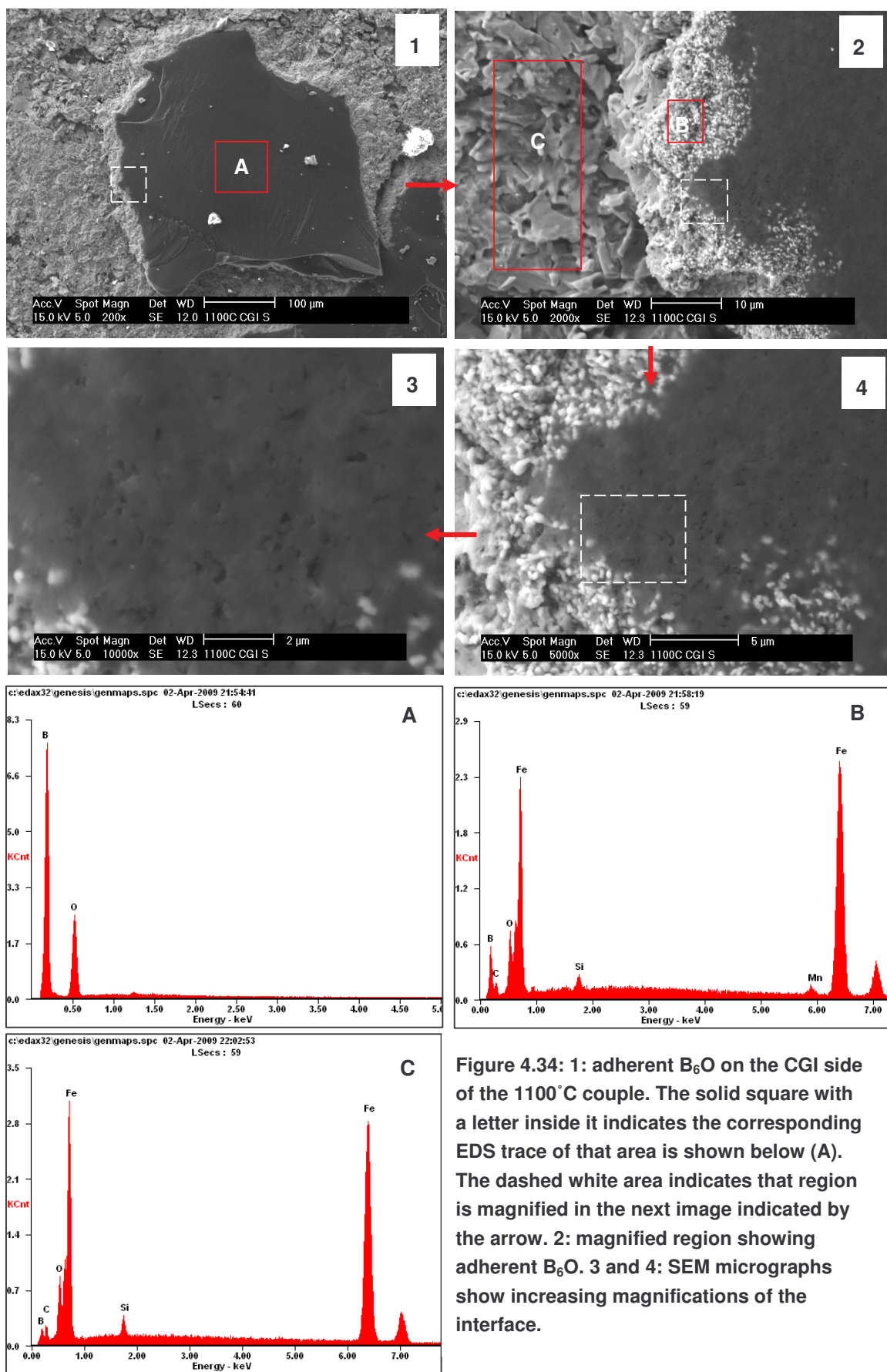


Figure 4.34: 1: adherent B_6O on the CGI side of the 1100°C couple. The solid square with a letter inside it indicates the corresponding EDS trace of that area is shown below (A). The dashed white area indicates that region is magnified in the next image indicated by the arrow. 2: magnified region showing adherent B_6O . 3 and 4: SEM micrographs show increasing magnifications of the interface.

- **XRD of the 1100 °C diffusion couple surfaces**

XRD scans of the separated couple surfaces have revealed a number of secondary phases that evolved as a result of the heat treatment. The separated CGI half of the couple shows plenty of iron boride (Fe_2B) to be present with a very good peak fit with this phase and a fit with FeB peaks as well. The carbon main peak (in the graphite XRD library pattern) clearly corresponds with a significant peak in the XRD and the major peak of B_4C corresponds with a small unassigned peak in the XRD trace, leading it to be classified as a possible by-product but if it is present, it has low abundance. Peaks corresponding to iron were also assigned.

In the case of the B_6O half of the diffusion couple, the dominant phase is very clearly Fe_2B . Again, graphite was found to be present, indicating that carbon adheres to the B_6O . B_6O , FeB and Fe_3O_4 all achieved similar ‘scores’ with respect to peak matches. It is of course known that B_6O was the substrate material, so its presence is expected. FeB and Fe_3O_4 are likely products of the interfacial interaction. Peaks corresponding with SiO_2 were easily matched, and a ternary phase $\text{B}_{0.13}\text{Fe}_{0.82}\text{Si}_{0.05}$ seems to match some of the smaller unassigned peaks, suggesting that it, or a similar phase may be present but this is not known for certain.

Table 4-12: Table of detected phases on either side of the 1100 °C diffusion couple ranked according to abundance

Phases detected on the B_6O side	Phases detected on the CGI side
Fe_2B	Fe_2B
SiO_2	C
B_6O	Fe
FeB	B_4C
Fe_3O_4	FeB

- **SEM investigation of 1100°C diffusion couple cross sections**

The 1100°C couple provided a useful means for studying the CGI/B₆O interface directly in the form of adherent B₆O on the CGI pills. One of these adherent pieces was carefully cross sectioned and polished to reveal the interfacial features as shown below.

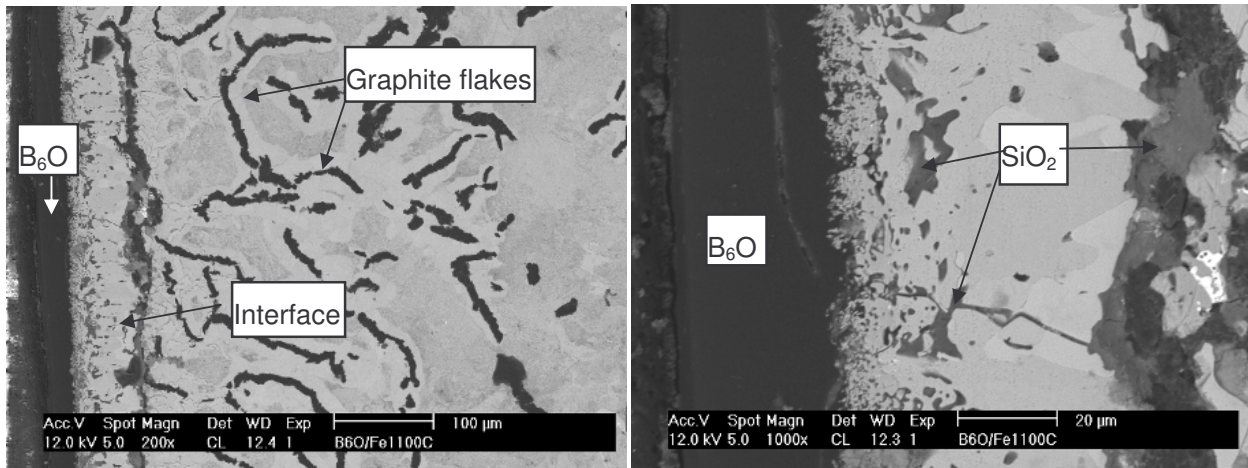


Figure 4.35: Left: low magnification image of the B₆O/CGI interface, right: higher magnification image showing interfacial detail.

It can be seen from the images in figure 4.35 that the interfacial region on the CGI side of the couple is quite thick, approximately 80 to 100 microns thick which is substantially more than that of the 900°C couple. The B₆O appears to have reacted with the CGI material and distinct regions can be observed near the interface. Figure 4.36 with its associated labelled regions and EDS traces shows a significant degree of segregation when the CGI material is in contact with B₆O. Figure 4.36 shows a summary of detected phases across the interface. The adherent piece of ceramic shows only boron and oxygen presence corresponding to a region of pure B₆O. The lighter grey region shows almost pure iron peaks with a small amount of carbon presence. The dark regions near the interface show that silicon and oxygen occur in great abundance while silicon and oxygen contaminated with small amounts of other atoms occurs further from the interface near the remnants of graphite flakes.

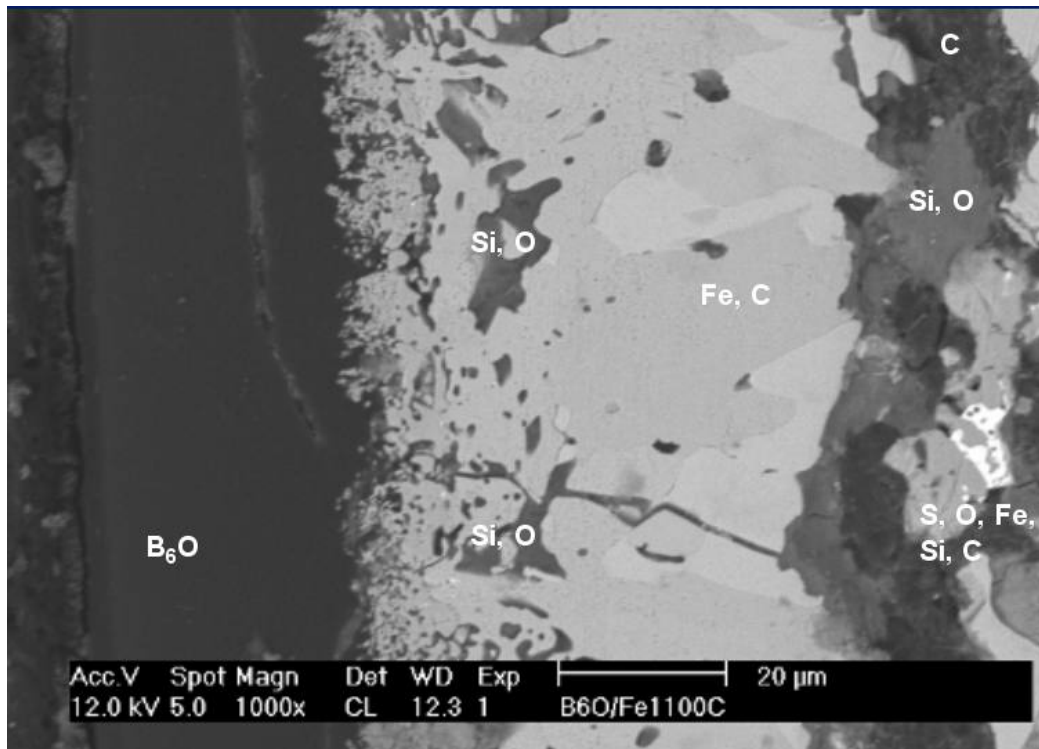


Figure 4.36: Cross section of the interfacial area of the adherent B_6O on the CGI half of the couple showing elements detected by EDS in each region.

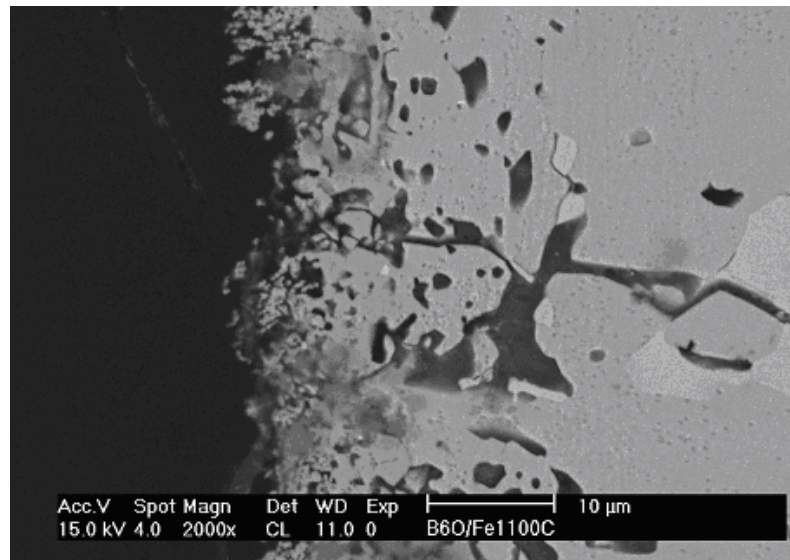


Figure 4.37: SEM micrograph showing detail of the interface between iron and B_6O , notice how the materials appear to interact with one another.

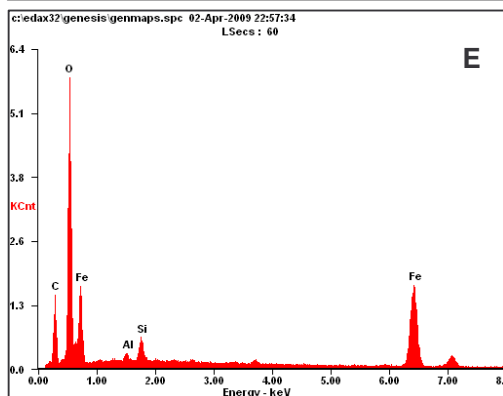
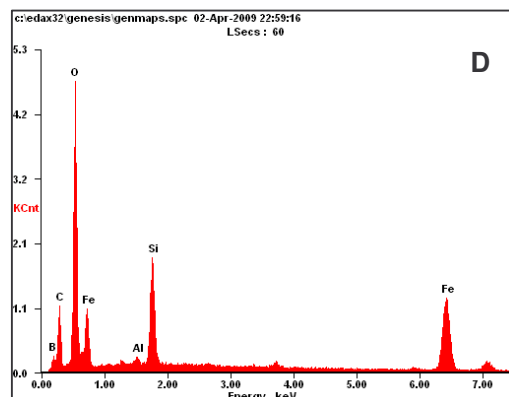
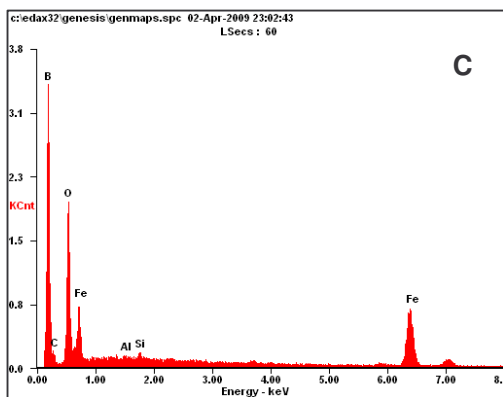
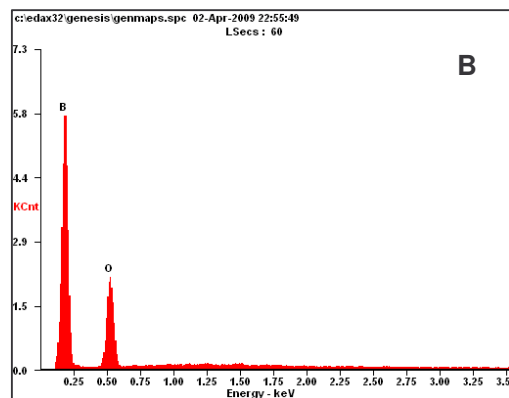
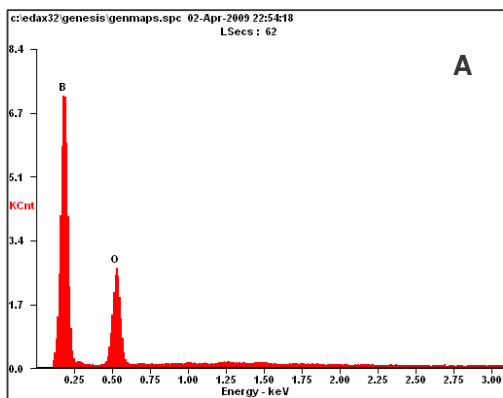
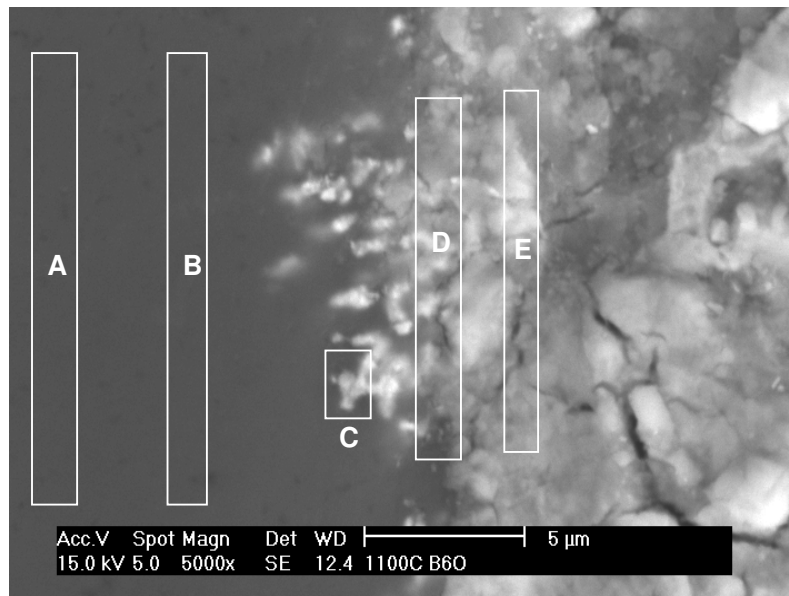


Figure 4.38: High magnification SEM micrograph of the interface between B_6O and CGI showing protrusions of iron into the B_6O ceramic material. Each EDS corresponds to a specific region indicated.

The EDS traces of the regions shown in figure 4.38 illustrate that carbon, silicon, and iron (region C) are present at an iron protuberance which indicates that these atoms react at the interface. The light grey area (D and E) shows an abundance of boron, carbon and oxygen with less iron than expected and some silicon, more silicon appears in D closer to the interface, indicating its tendency to diffuse towards B_6O . This implies that boron, carbon, oxygen and some silicon most likely interact here more than iron does.

Figure 4.39 shows a region in which sulphur is abundant within the white inclusion observed adjacent to the interface. The white area also comprises some C, O, Mn and Fe.

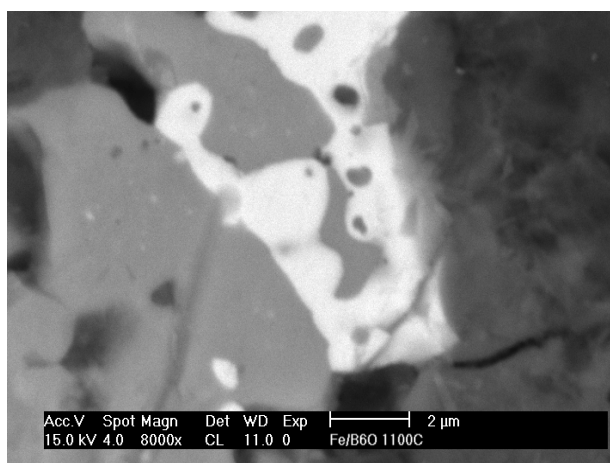
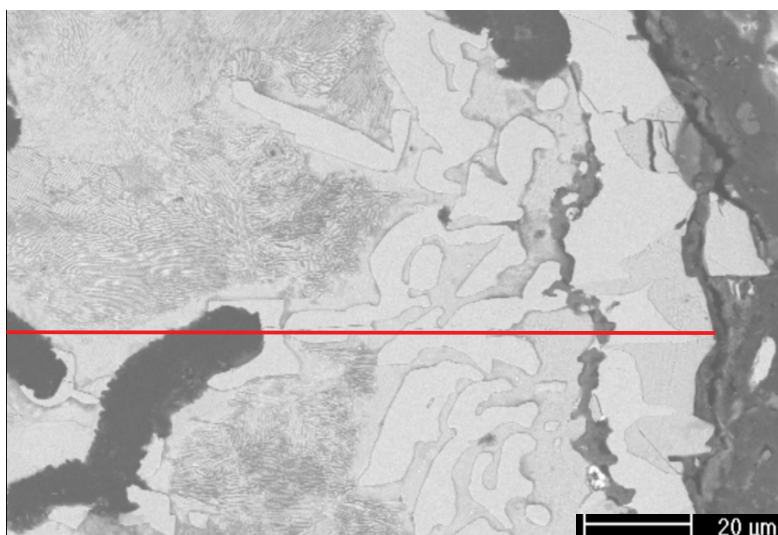
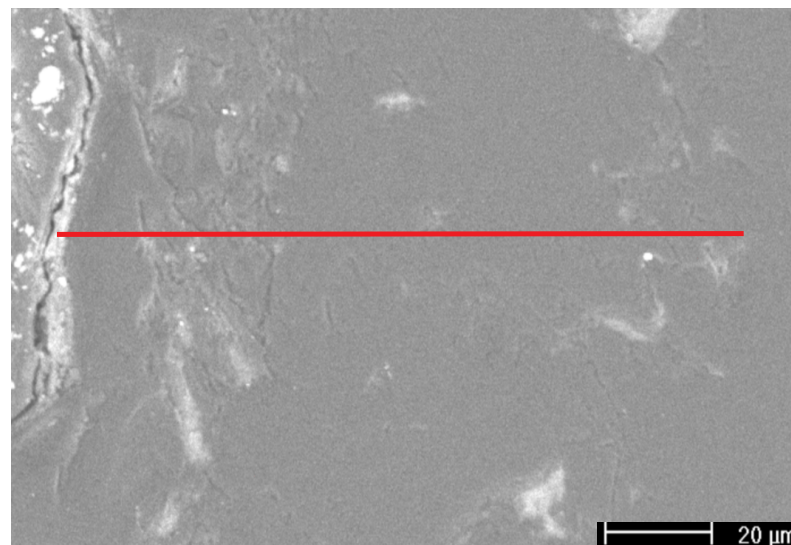
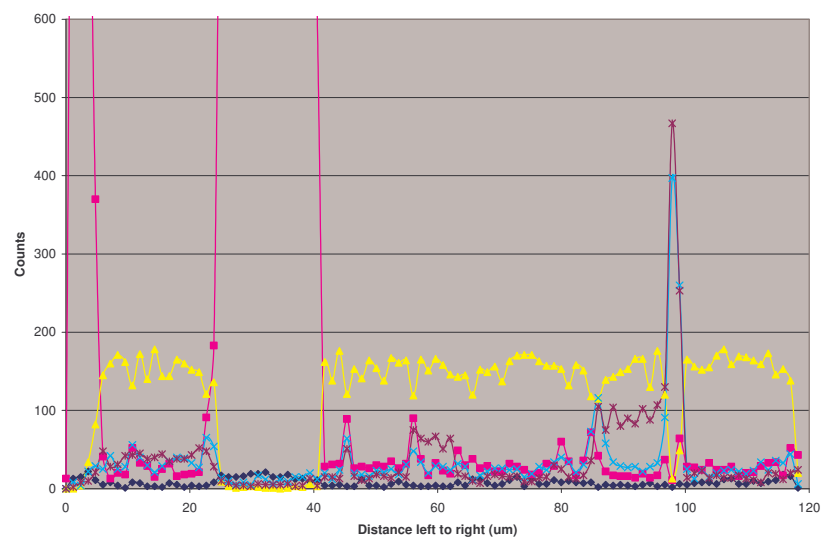


Figure 4.39: High magnification SEM micrograph of the white region noticed near the interface of the 1100°C CGI/ B_6O diffusion couple.

The diffusion couple line scan profile (figure 4.40) shows how the line scan detects relative amounts of elements. The iron concentration remains fairly consistent (other than inside the graphite flakes) and the carbon concentration does not appear to spike significantly at any point. In this case, the line scan did not stray into the bakelite resin. Virtually no boron abundance was detected in the iron side of the couple, but both oxygen and boron contents were seen to increase and then drop as one moves from the bulk of the B_6O towards the interface. The most significant observation is again the formation of a silicon rich layer approximately 20 microns from the interface.



Line scan across the interface of the iron side of the diffusion couple at 1100°C



Line scan across the interface of the B_6O side of the diffusion couple at 1100°C

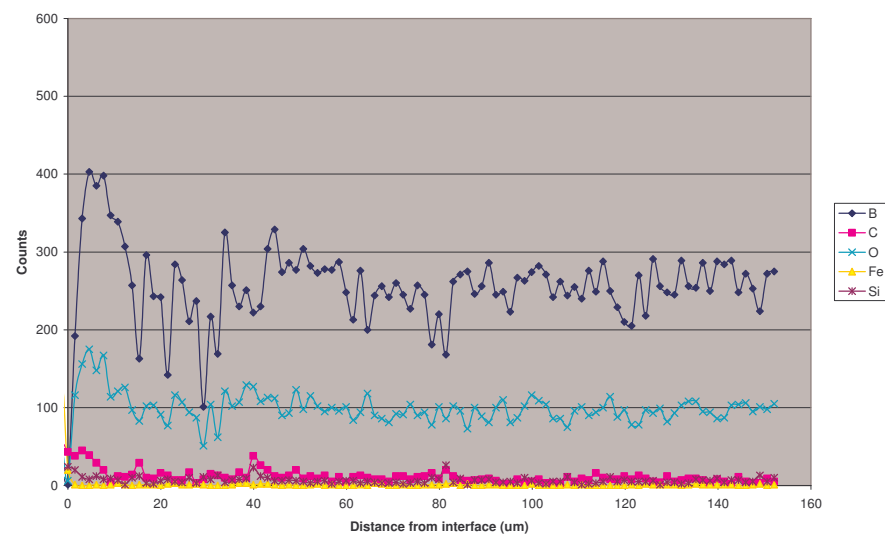


Figure 4.40: Cross sectional diffusion profiles showing the relative abundances of elements at or near the CGI/ B_6O 1100°C diffusion couple interface.

- **1300°C couple**

The couple in this instance remained intact and did not separate upon cooling. The CGI underwent melting and the B₆O pill became retained or embedded in the solidifying CGI as the materials were cooled. No optical microscopy of the separated surfaces was possible due to the couple remaining intact. SEM was used to characterise the appearance of these surfaces as shown in figure 4.41 A to C. During cutting, the sample separated into two halves, but due to the iron having melted, it was unclear as to where the actual interface was located, as such a reliable investigation into the interfacial region is difficult. At best, an appreciation of reaction products can be gained.

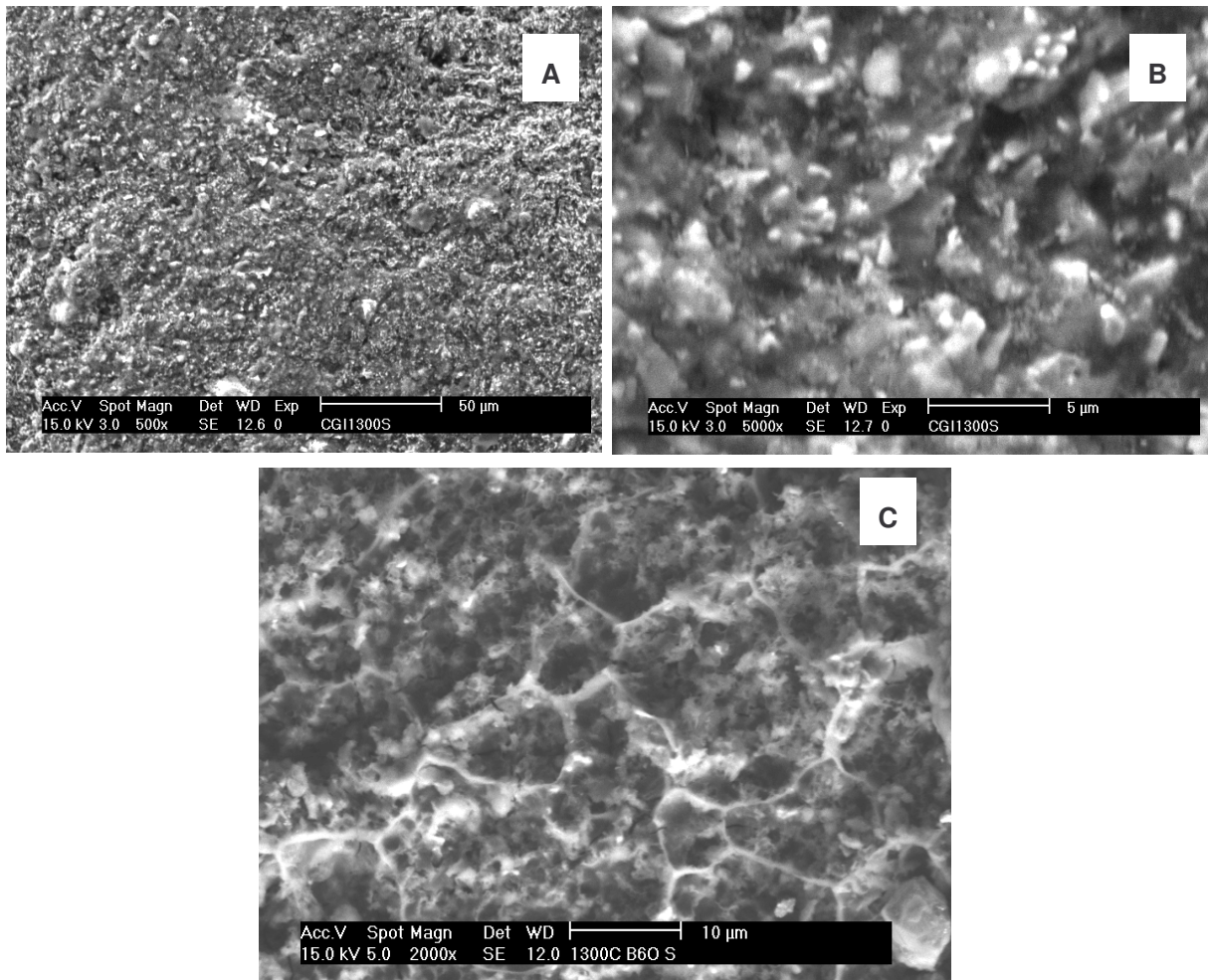


Figure 4.41: The separated 1300°C diffusion couple showing similar features on both sides of the couple.

- **XRD of the 1300 °C couple**

The 1300 °C couple separated naturally when the entire intermelted mass was cross sectioned. XRD was performed across the separated surfaces and table 4-13 shows a summary of the results. Although this should not be used to distinguish either side of the interface, an appreciation of potential reaction products can be gained if the tool and workpiece reach this temperature.

Table 4-13: Table of detected phases on either side of the 1300 °C separated diffusion couple ranked according to abundance

Phases detected on the separated half of the couple closer to the B ₆ O side	Phases detected on the separated half of the couple closer to the CGI side
B ₆ O	Fe ₂ B
Fe	SiO ₂
C	Fe ₃ B
Si	Si
B ₄ C	FeB

It was seen from the XRD pattern of the diffusion couple that Fe₂B peaks correspond with the peak list and that B₆O itself survives for this time at temperature. Some silicon and silicon oxide peaks can also be seen. The highest correlation of the patterns with the database is for the Fe₂B and B₆O phases, followed by Fe, SiO₂, Fe₃B, C, Si, and finally B₄C and FeB with only some degree of matching, suggesting that they may be present, but are not certainly there and are not abundant reaction products.

- **SEM investigation of 1300 °C diffusion couple cross sections**

The diffusion couple carried out at this temperature did not separate upon removal from the hBN pot, rather, the iron melted to form a large mass surrounding the B₆O pill. This mass was cross sectioned and polished together and examined using SEM.

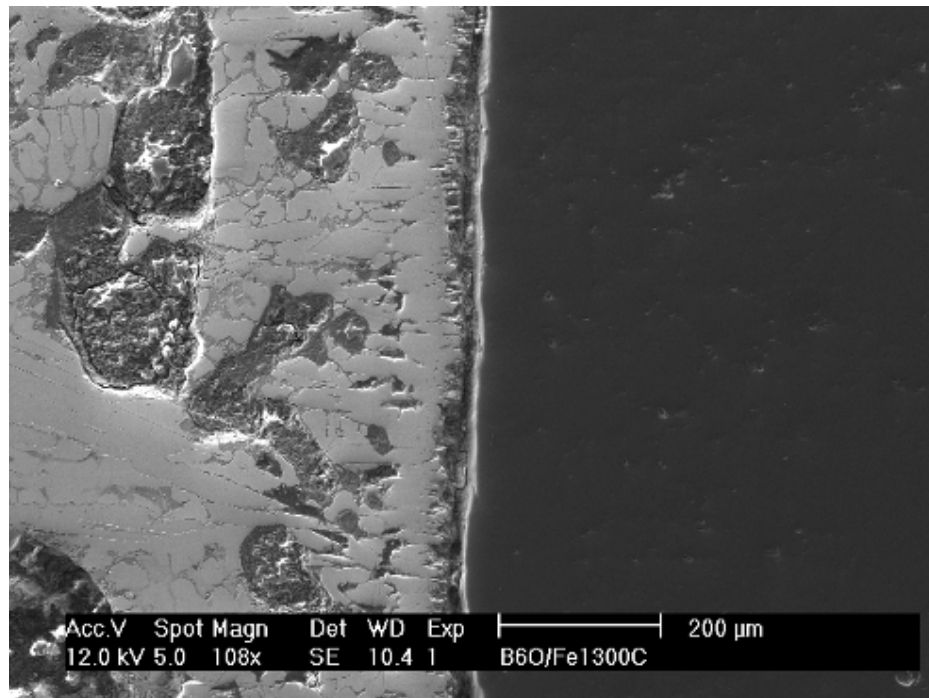


Figure 4.42: Low magnification SEM micrograph showing the unusual features accompanying the CGI/B₆O diffusion couple at 1300°C. The ceramic can be seen to remain stable (right hand side) while the iron melted and then solidified on cooling.

Several images and EDS scans were taken during this investigation that demonstrated boron presence on the iron side of the diffusion couple. Figure 4.42 shows an SEM micrograph of the cross section at low magnification.

Silica formations were once again detected close to the interface (approximately 50 microns away for the smaller features and up to 200 microns away or more for the larger features), but this time they lacked the linear effect that previous couples exhibited in the form of a silicon layer almost equidistant from the interface on the CGI side (20 microns inwards from the interface usually as with the 1100°C couple) in most regions. In this case, the silica colonies appear to be globular, most likely due to the melting of the cast iron resulting in more mobility for the silicon and a tendency to accumulate and react with oxygen. Unfortunately, it appears that a softer phase may have been polished out of the interface as can be seen in figure 4.43, but the XRD results and EDS of the separated surfaces indicate this was likely silicon dioxide and Fe₂B predominantly.

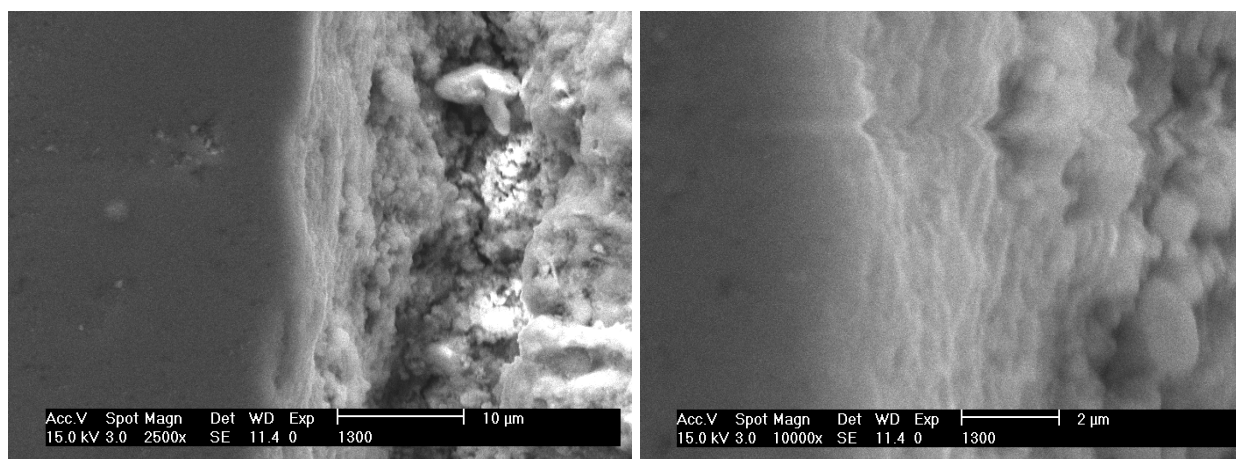


Figure 4.43: High magnification SEM images of the interfacial region of the 1300°C couple showing a crevice that likely corresponds to removed soft phases as the result of polishing.

Silicon oxide, carbon and iron were also detected in the interface by XRD in the near interfacial region. The presence of an abundance of carbon here could explain the detected B_4C phase in the XRD scans shown earlier in this section. Diffusion likely occurred towards the interface resulting in a 'melting pot' of various elements that react with each other to form a number of possible products, some of which were identified by XRD earlier in this section.

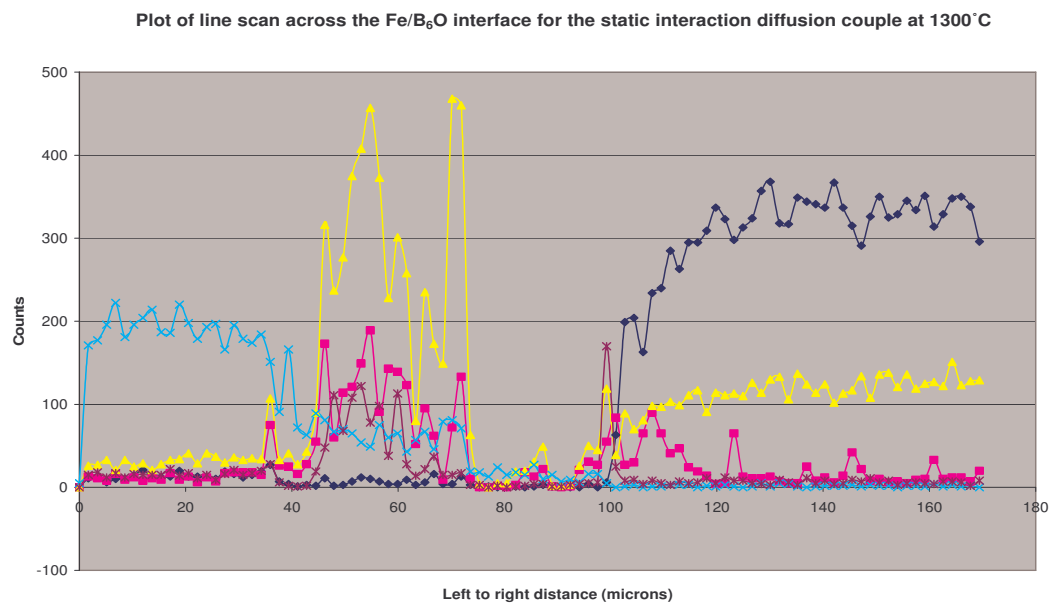
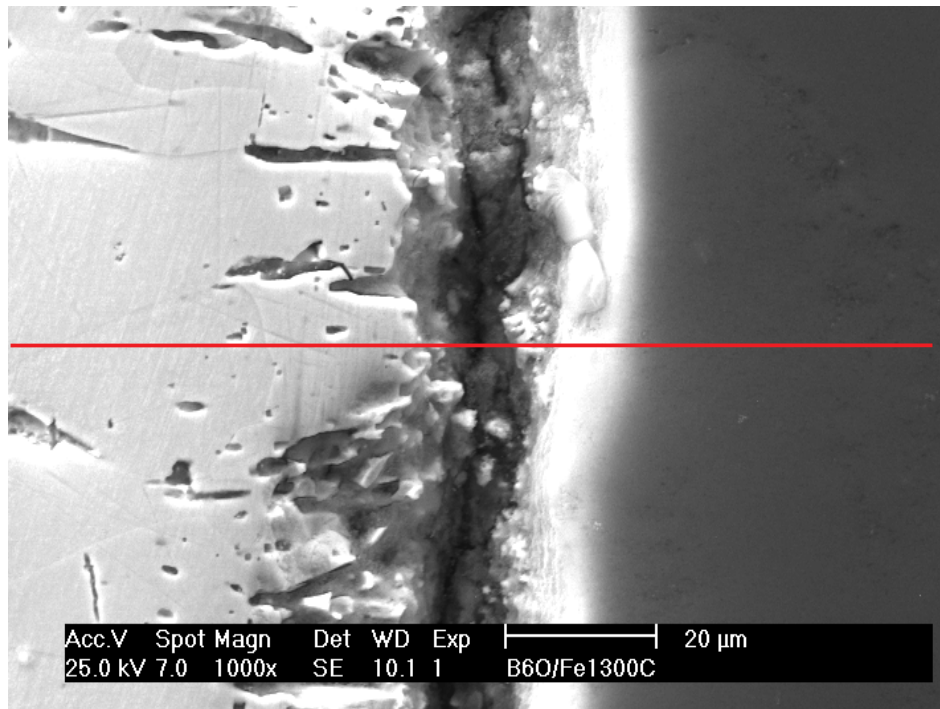


Figure 4.44: EDS line scan showing the region scanned on the SEM micrograph (red line left to right) and the corresponding plot of the scan results of the 1300°C diffusion couple experiment between CGI and B₆O. The interface is between 80 and 100 on the x axis of the plot, due to the scale being micron measurements from left to right along the red line indicated in the micrograph.

Please note that the sample used for this cross sectional examination did not separate in the way the other half of the mass did when cutting. To clarify, cutting created two halves of the pill which comprised both B_6O and CGI layers fused together, one half of which separated near the interface and was used for XRD analysis to identify some reaction products, the other (intact half) was polished and used for the cross sectional examination described here.

The line scan (figure 4.44) of the 1300 °C couple shows a great deal of fluctuation in terms of abundance of compositional atoms. The iron concentration can be seen to drop as the scan progresses from left to right towards the interface. A corresponding increase in oxygen concentration can be seen as along with carbon and silicon spikes. Only a small amount of iron was detected adjacent to the interface in the B_6O material indicating that the iron reacts at the interface to produce FeB_x or FeO_x (where x is a positive number). The iron could also possibly flow or diffuse with molten B_2O_3 . The oxides could be the result of previously oxidized CGI after sample preparation as described earlier but that does not explain the drop in oxygen abundance on the B_6O side of the interface compared to the B_6O bulk. Carbon diffusion into B_6O could result as mentioned earlier in the formation of B_4C as detected by the XRD scans. Furthermore it can be seen that carbon does not have a problem diffusing as far as 70 microns (and further) into the B_6O material.

The silicon spike is significant because it can be seen to occur on the B_6O side of the couple as well as on the iron side. Boron and silicon have an affinity for forming borosilicates and the fact that silicon diffuses so easily towards B_6O and remains there could be an indication of borosilicate glassy phase formation. The fact that boron diffusion into the CGI has been confirmed, further adds to the possibility that borosilicates could form on the CGI side of the couple.

It would appear; however, that polishing of the couple (B_6O and CGI adhering to each other) resulted in pullout or removal of soft interfacial phases that formed in the visible gap between the CGI and B_6O couples. While this is unfortunate, the XRD scans of the interfaces combined with SEM and EDS still give valuable insight into the phases present in the interfacial region.

4.4 Oxidation Resistance

Two sample types were used for oxidation resistance testing as described in the methodology namely hot pressed pure B_6O cut into rectangular blocks and similarly $B_6O/Y_2O_3/Al_2O_3$ SPS sintered material produced from the IKTS and of identical composition to the cutting tools made for this project.

4.4.1 Characterization of the starting materials

Tables 4-2 and 4-3 show the measured densities and open porosities as well as sintering profiles of the materials used during all oxidation tests. Additionally, previously measured hardness and fracture toughness values for these materials have been reported but the measurement thereof did not form part of this project and has been referenced accordingly.

As mentioned above, two different oxidation resistance runs were performed. The first involved a method using XRD to monitor phase changes that occurred after each heat treatment and the second used optical microscopy and mass change measurements with XRD performed before the first treatment and again only after the final heat treatment profile in order to avoid mass changes due to the XRD mounting resin adhering to the material. Also, the results of the phase change monitoring runs showed boron nitride as a major phase, which was thought to be an impurity. The second set of runs was undertaken in order to monitor microstructural changes using optical microscopy and to avoid the large errors observed in mass changes associated with mounting the sample on a polymer for XRD which distorted the mass readings. The second set of runs were also undertaken in order to verify that boron nitride was a contaminant that resulted from inadequate grinding off of the hBN pot material in the first set of runs as it was felt it was highly unlikely that boron nitride could have evolved from the heat treatment regimen.

4.4.1.1 X-ray diffraction

X-ray diffraction of the starting materials was performed for each and every sample used in the oxidation testing. The sample names are presented as phase monitoring 1, 2 and 3 for the pure B_6O samples used to monitor phase changes and pure B_6O

oxidation resistance 1, 2 and 3 for the pure B_6O samples used to measure mass change effects. The $B_6O/Y_2O_3/Al_2O_3$ samples form part of the mass change and microstructural monitoring of the second set of experiments and are labelled as $B_6O/Y_2O_3/Al_2O_3$ #1, #2 and #3 accordingly. The naming of the samples was not arbitrarily chosen as any sample with the number 1 designates it was the largest sample with 2 and 3 following in succession, due to the difficulty in cutting exact sized pieces of these very hard materials.

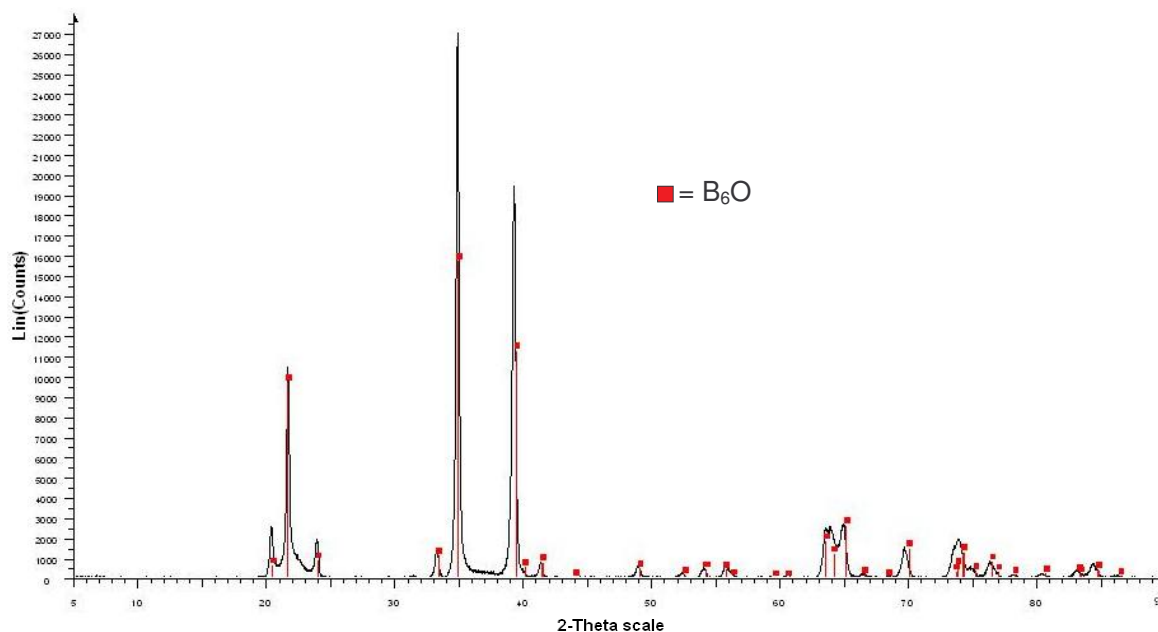


Figure 4.45: XRD pattern corresponding to the (pure B_6O) phase monitoring sample 1.

It can be clearly seen that the peaks of the first run of oxidation resistance samples used for phase monitoring all show the expected peaks. The scan was performed between 5 and 90 degrees 2-theta as opposed to 10 to 80 degrees as used by most of the other scans due to these scans being performed on a high resolution XRD machine. The scans on the other two samples produced identical results.

The XRD pattern that best fitted these B_6O peaks was 01-087-1143 and is much the same as the pattern used to interpret the lower resolution scans.

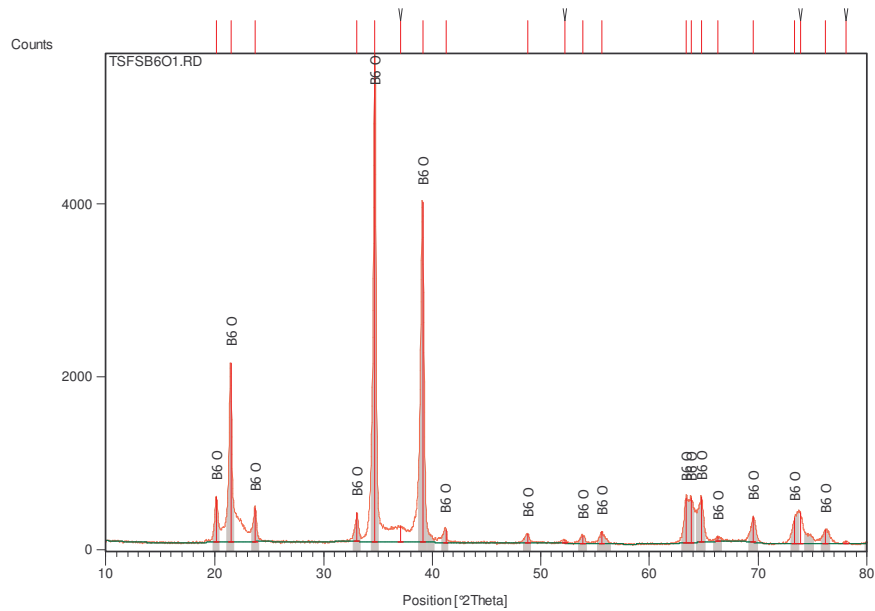


Figure 4.46: XRD pattern corresponding to the pure B_6O oxidation resistance sample 1 showing only the expected pure B_6O fingerprint.

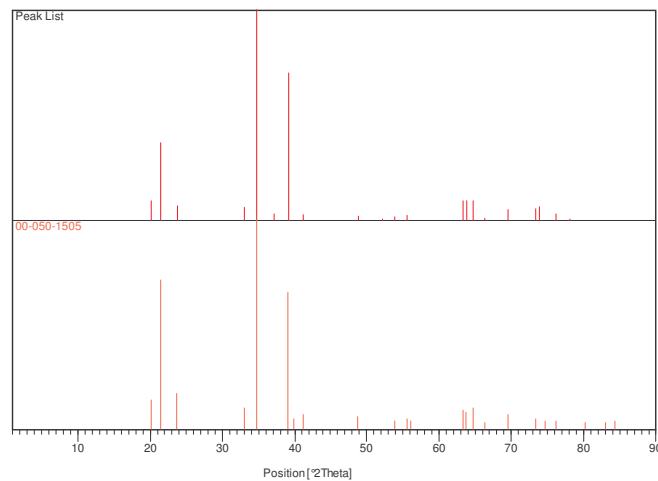


Figure 4.47: Peak list showing the correspondence of the measured B_6O peaks compared to the database 00-050-1505 code corresponding to that of B_6O , the peak list and database peaks match extremely well.

The remaining pure B_6O samples display much the same peak list correspondence as figure 4.47 and the same appearance as figure 4.46 and as such, the peak list and XRD patterns are not included for each sample. It can be seen that all of the starting oxidation resistance samples used to monitor microstructural changes and

mass changes primarily, show the expected composition and corresponding peaks to the expected pattern. The difference in counts is due to the use of a lower resolution x-ray diffractometer than in the phase composition analysis work. The yttria alumina x-ray diffraction pattern is visible in figure 4.48 and shows only B_6O peaks.

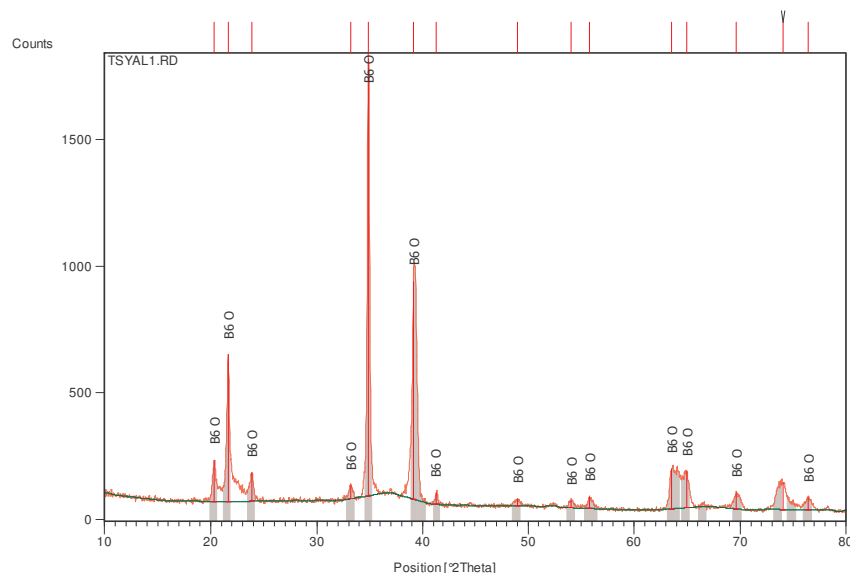


Figure 4.48: XRD pattern of the $B_6O/Y_2O_3/Al_2O_3$ oxidation resistance sample 1.

Interestingly, the yttria alumina phases were not detected in the XRD patterns that resulted from the scans of the said samples due to these phases being amorphous.

4.4.2 Mass change observations

The starting mass of each of the samples as well as the mass following each heat treatment process was measured to 0.01mg accuracy. The surfaces of the samples appeared to degrade significantly which worsened after each heat treatment. The formation of the glassy oxide layer on all of the sample surfaces also resulted in difficulty in removing the samples from the support without the risk of knocking off some of the white (almost transparent) crystals. A mass loss was observed on all of the samples after each heat treatment was complete. It can be seen from figure 4.49 that the samples appear to drop in mass with heating time. The mass change per unit surface area indicates that pure B_6O and yttria alumina doped B_6O behave similarly

in terms of mass loss initially, with the most significant difference appearing after 50 hours at 1000 °C.

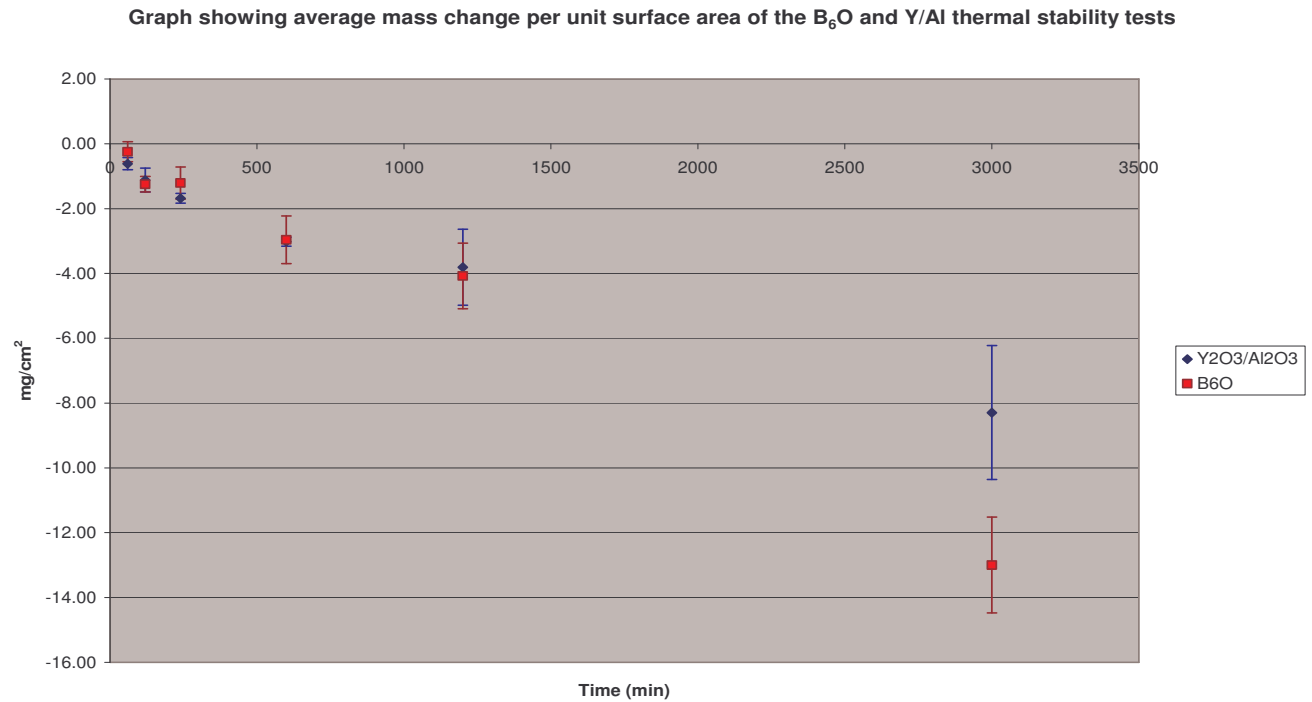


Figure 4.49: Time dependence of the average mass loss per unit surface area of the samples. The two materials behave similarly initially with a significant overall mass loss of the pure B₆O material after 3000 minutes (50 hours) at 1000 °C.

4.4.2.1 Optical microscopy

Optical microscopy was used extensively to compare microstructural changes post heat treatment with the starting microstructures.

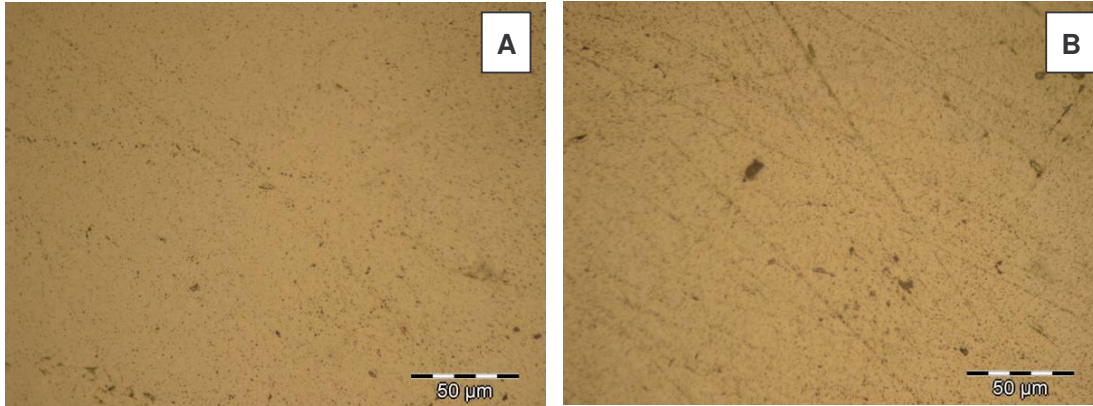


Figure 4.50: A: The starting microstructure of pure B₆O oxidation resistance sample 1 after polishing. **B:** The starting microstructure of pure B₆O oxidation resistance sample 3 after polishing. Sample 2 is omitted because the images are not perceptibly different.

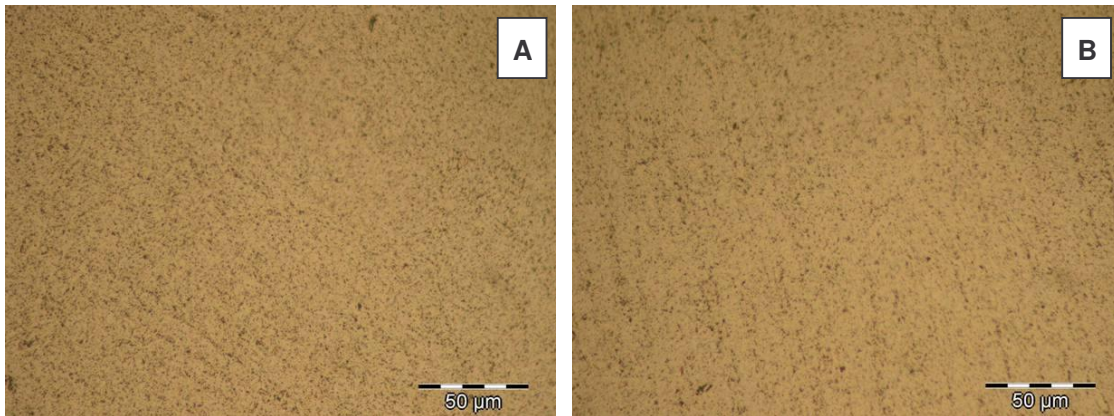


Figure 4.51: A: The starting microstructure of the B₆O/Y₂O₃/Al₂O₃ oxidation resistance sample 1 after polishing. **B:** The starting microstructure the B₆O/Y₂O₃/Al₂O₃ oxidation resistance sample 2 after polishing. Sample 3 is omitted because the images are not perceptibly different.

It is clear from the optical micrographs (figures 4.50 and 4.51) of the polished starting materials that the polishing was reasonably good because of the presence of few severe scratches and little porosity (small black spots). The hot pressed B₆O samples show more defects to be present than the SPS produced material.

4.4.3 Characterization of post heat treatment surface changes using optical microscopy

Microstructural changes were observed to result from the heat treatment regimens undertaken at 1000 °C for increasing amounts of time. The following sections document those changes. Not all micrographs are shown, but those selected are representative of the observed features. Scanning electron microscopy was also attempted but it simply melted and degraded the sample surfaces and was thus avoided initially. The samples were subsequently washed in ethanol to dissolve the B_2O_3 (which is believed to have melted under SEM) and the crystals were successfully micrographed.

4.4.3.1 1 hour at temperature

Pure B_6O samples:

After one hour at 1000 °C, surface colourations were observed all over the surface of the samples as seen in figure 4.52. Very small crystallites started to form at preferred locations on the sample surfaces. Evidence of liquid flow lines resulted that appeared as if the surface had solidified.

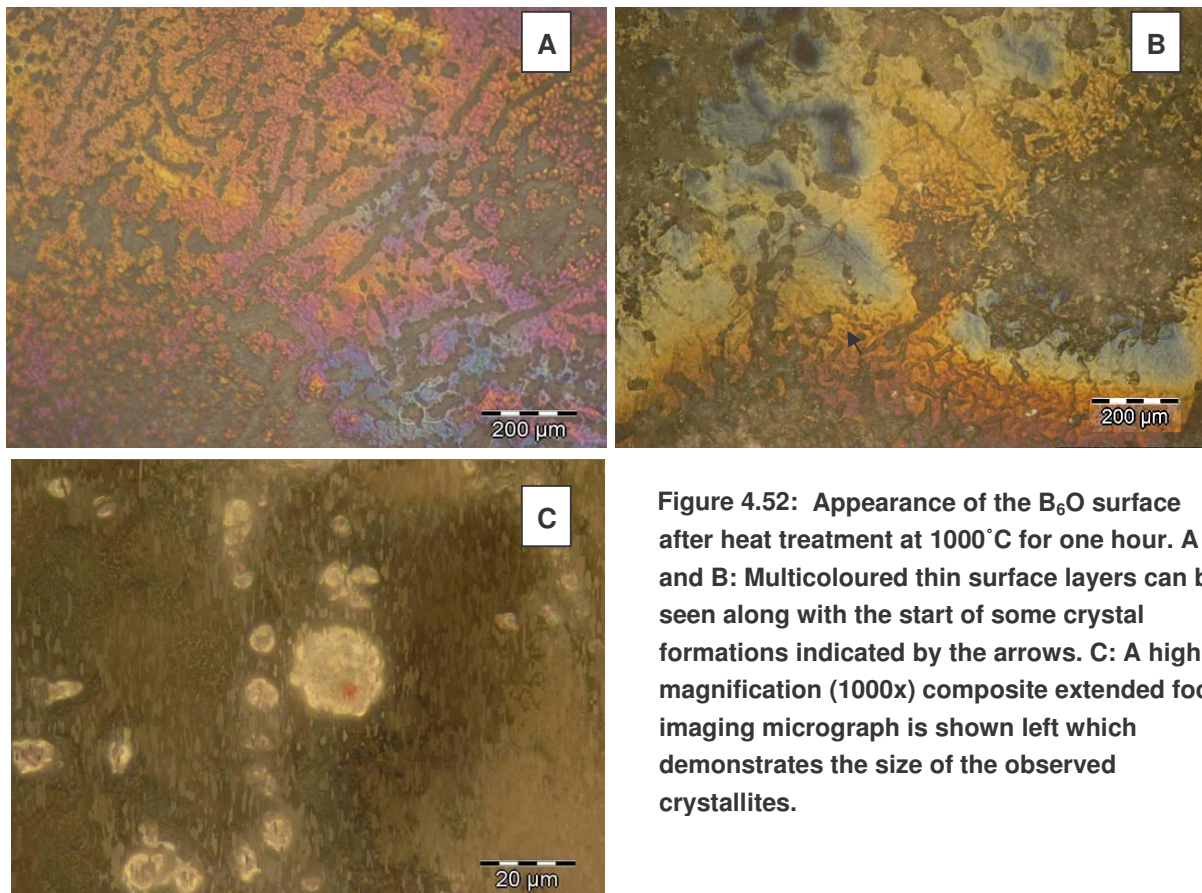


Figure 4.52: Appearance of the B_6O surface after heat treatment at 1000 °C for one hour. A and B: Multicoloured thin surface layers can be seen along with the start of some crystal formations indicated by the arrows. C: A high magnification (1000x) composite extended focal imaging micrograph is shown left which demonstrates the size of the observed crystallites.

$B_6O/Y_2O_3/Al_2O_3$ samples:

These samples displayed a remarkable change after even one hour at temperature as shown in figure 4.53. The surface became covered in crystal formations. The sample appeared white when removed from the furnace. The crystal formations were observed to begin to form 'snowflake' like formations and displayed a tendency to cluster. Melt flow effects were also observed, but few thin surface layer multicoloured regions were observed.

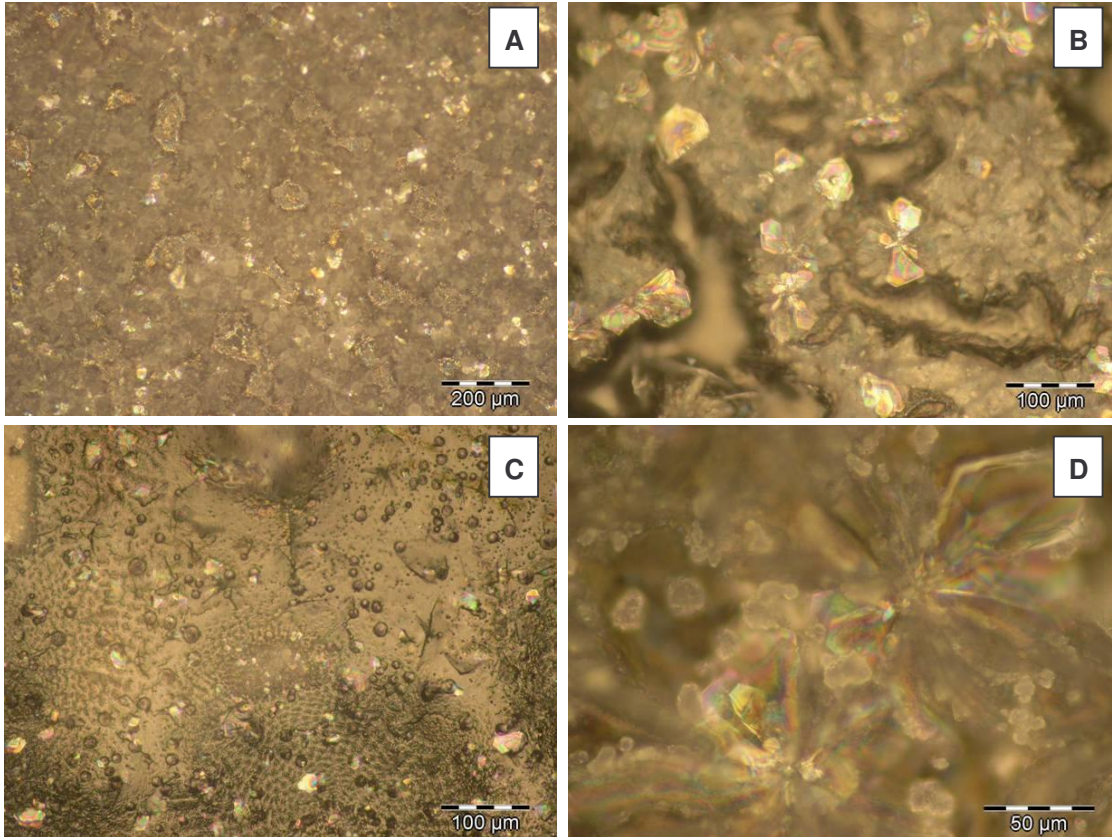


Figure 4.53: Various micrographs of the $B_6O/Y_2O_3/Al_2O_3$ samples heat treated in air at 1000°C for one hour.

4.4.3.2 2 hours at temperature

Pure B_6O samples:

The two hour heat treatment produced larger crystal formations than the one hour treatment as can be seen in figure 4.54. It is interesting to note how two distinct types of crystal appeared to form. Small spherical crystals and larger crystal formations beginning to resemble 'snowflake' like structures. Thin surface layer (brightly coloured) areas were still clearly visible on all the sample surfaces (figure 4.54 B).

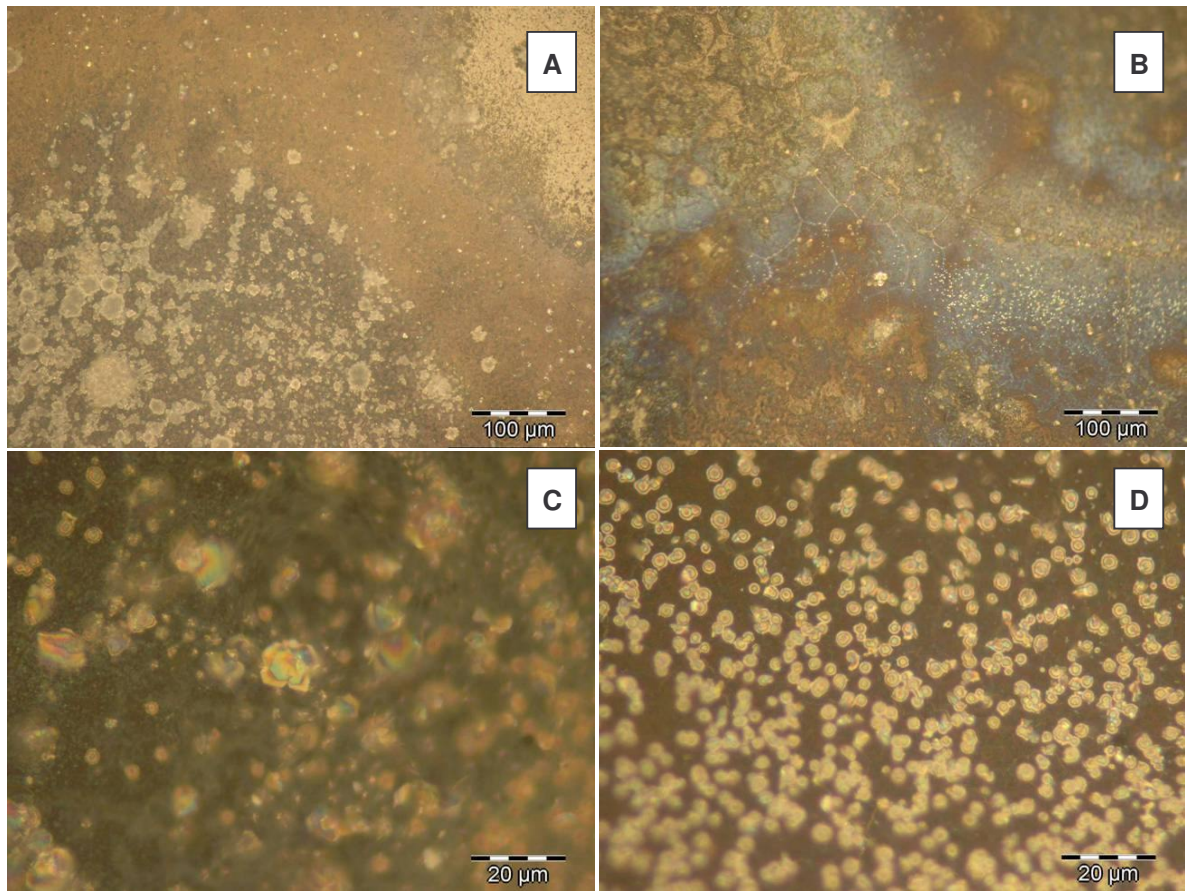


Figure 4.54: A and B: relatively low magnification images showing the significant changes in surface features after the 2 hour heat treatment of the pure B_6O samples. C and D: High magnification images of the crystals formed all over the sample surfaces.

$B_6O/Y_2O_3/Al_2O_3$ samples:

After the two hour heat treatment regimen, the size of the crystal formations increased on the yttria alumina samples as seen in figure 4.55 A to D. Crystal formations in excess of one hundred microns were observed, especially on sample numbers 2 and 3. Sample 1 also produced extensive crystalline features, but in this sample, the crystals appeared to form crystalline islands with less definition as the other samples in terms of individual crystal clarity. Some geometrically shaped crystals were also observed with a small amount of amorphous material, but very much less than the pure B_6O counterparts.

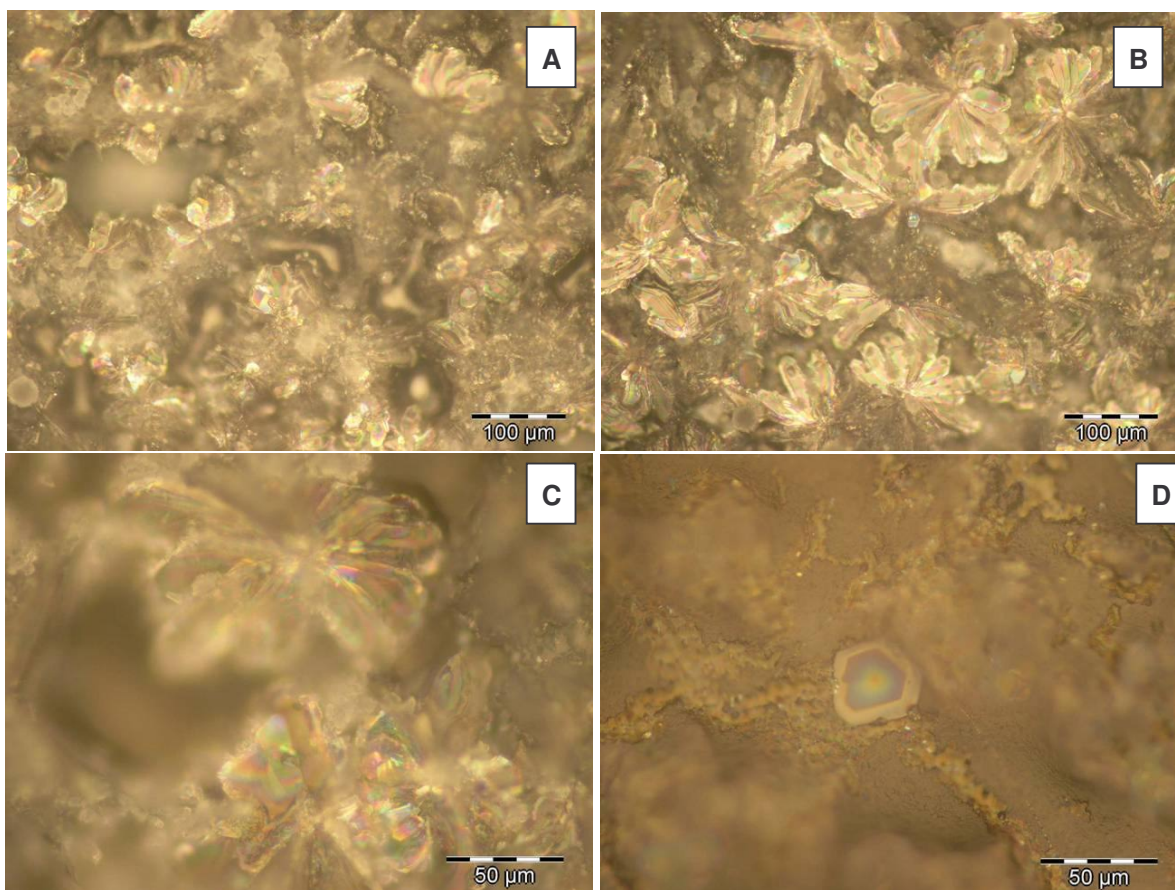


Figure 4.55: Optical micrographs that are representative of the observations made during the $B_6O/Y_2O_3/Al_2O_3$ oxidation resistance investigation after heating at $1000^\circ C$ for two hours in air.

4.4.3.3 4 hours at temperature

Pure B_6O samples:

The most significant feature that was noted after the four hour heat treatment was completed and the samples examined was the formation of large collections or groups of very small, round crystals. Many small crystals appeared to clump together to form a large polycrystalline mass or 'island' surrounded by the thin surface layered material that appeared multicoloured under reflected light. The size of the individual crystallites was imperceptibly different compared to the B_6O samples heat treated for two hours. Most notably, needle shaped crystals, believed to be single crystals, were observed that had not appeared after prior heat treatments. The reason single crystal formation is suspected is because the needle shaped crystals reflected light perfectly of the same visible wavelength uniformly across the crystal i.e. the entire crystal

would appear uniformly green or blue if angled correctly with respect to the incoming reflected light. The sample surfaces can be seen in figure 4.56.

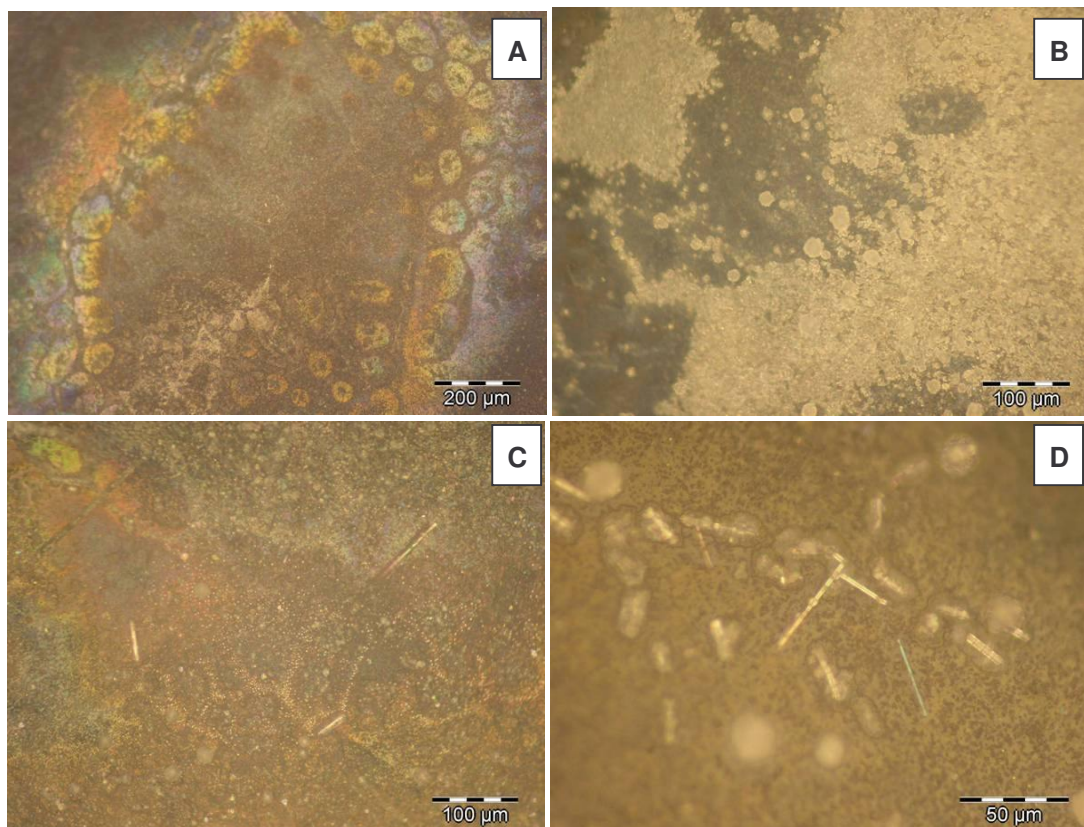


Figure 4.56: Representative optical micrographs of the pure B_6O heat treated samples at 1000°C for four hours in air. A: multicoloured thin surface layer effect is visible surrounding a crystal 'island' mass. B: a polycrystalline mass at higher magnification. C and D: Needle-like single crystals formed in response to this heat treatment along with the regular spheroid crystals.

$B_6O/Y_2O_3/Al_2O_3$ samples:

After heat treating for four hours, the size of the crystal formations appeared to reach a maximum with diameters of the 'snowflake' or rosette formations exceeding two hundred microns (0.2mm) so much so that the crystals were visible with the naked eye. The crystals appeared to form in multiple layers which could be focused on with the optical microscope, almost like a crystalline 'cage' surrounded the entire sample with the rosettes appearing at the highest points of the surface. The surface became very porous as a result of this multilayered crystal mass forming around the sample. The micrographs of the surfaces are shown in figure 4.57 A to D.

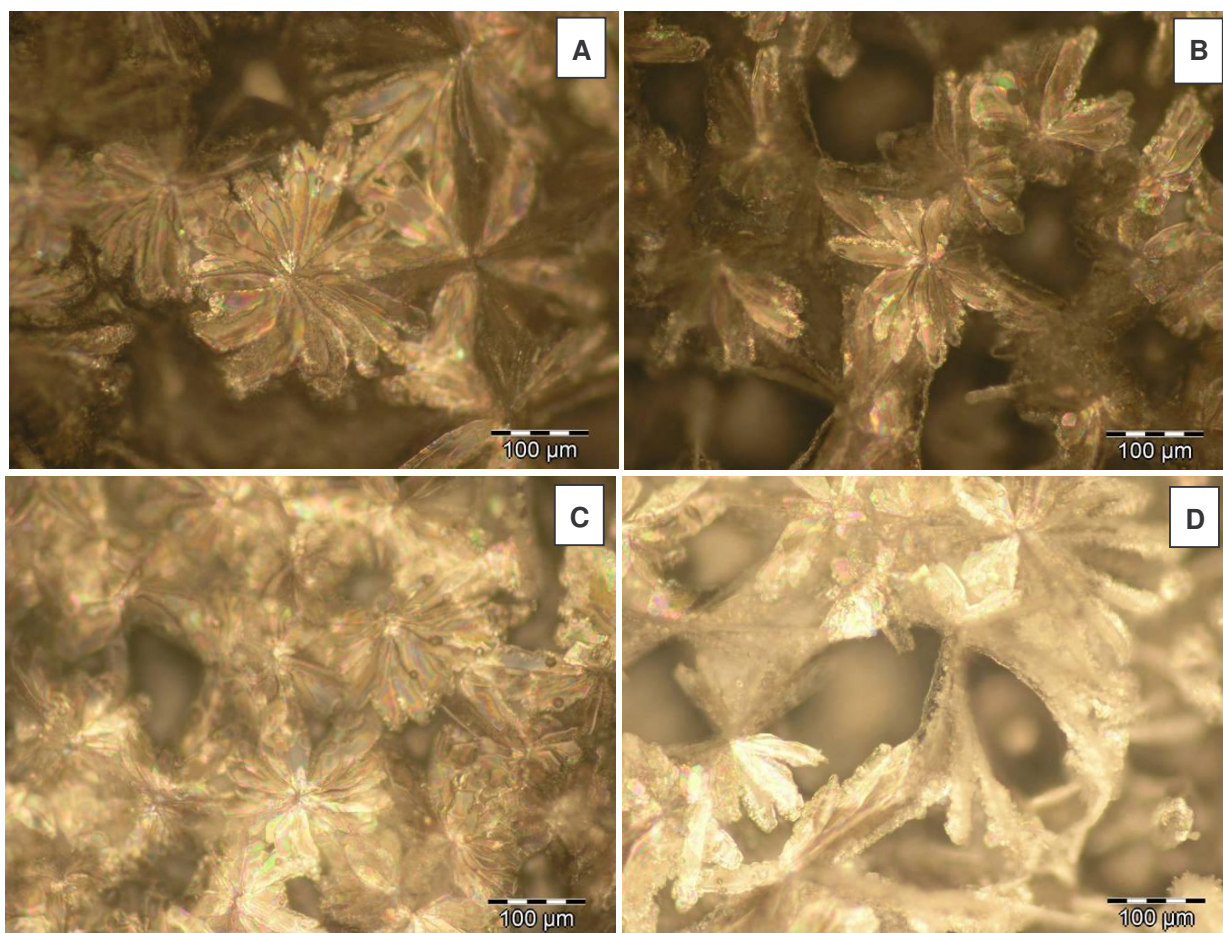


Figure 4.57: Representative optical micrographs of the crystal formations observed on all of the $B_6O/Y_2O_3/Al_2O_3$ samples after heat treating for 4 hours at 1000°C in air. The crystals appear to be in excess of 200 microns in diameter with thickness of about ten microns.

4.4.3.4 10 hours at temperature

Pure B_6O samples:

The ten hour heat treatment produced very long needle shaped crystals in excess of 200 microns. The smaller round crystals did not appear any larger than previous heat treatments, possibly due to them melting each time they were reheated and then crystallizing to a similar size under the same cooling rate. A multifaceted pseudo-grain structure appeared along the surface of the sample within the multicoloured surface formations that can be seen in figure 4.58.

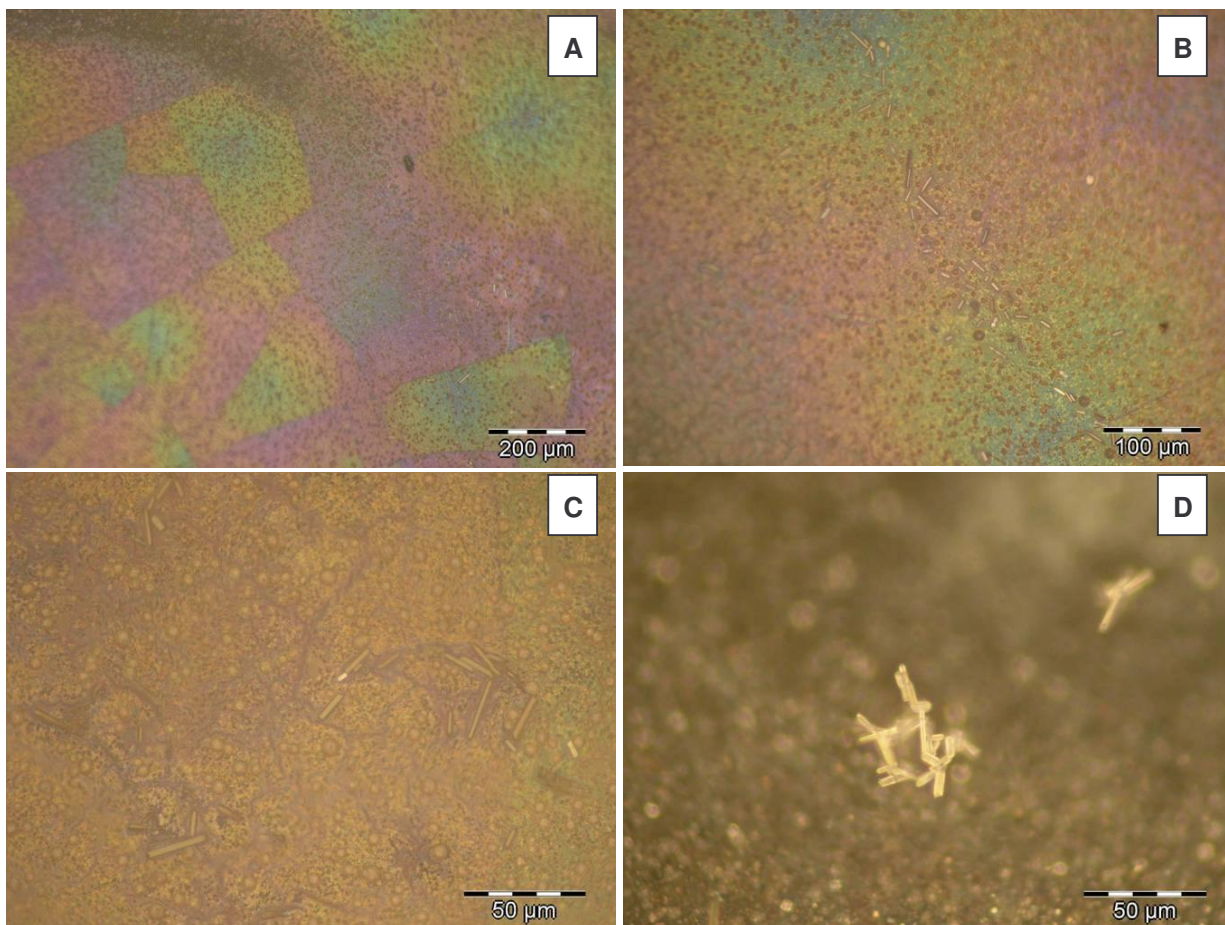


Figure 4.58: Representative micrographs of the resulting pure B_6O sample surfaces after the ten hour heat treatment in air at 1000°C. Top left: multifaceted surface with small crystallites (spots). Top right and bottom right: single crystals visible. Bottom right: a collection of needle shaped crystals protruding from the surface.

$B_6O/Y_2O_3/Al_2O_3$ samples:

The heat treatment resulted in visible degradation of the type of crystalline cage that formed around the samples in the four hour treatment as seen in figure 4.59. The surfaces appeared similar to the four hour heat treatment results although the surface appears to be giving way to a darker material that does not crystallize in the same way previously observed, possibly due to the evaporation of material from the surface resulting in less suitable material for forming the crystals seen before.

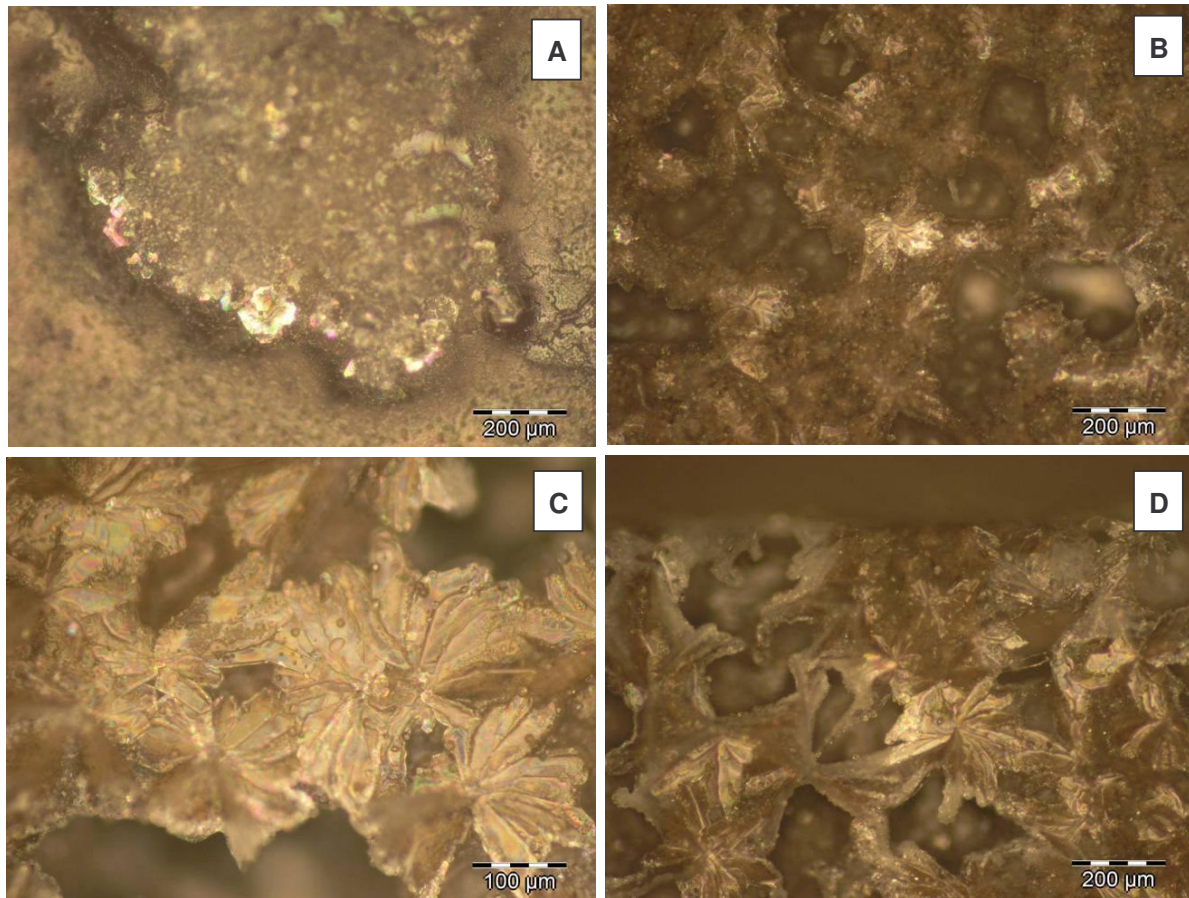


Figure 4.59: Optical micrographs resulting from the ten hour heat treatment at 1000 °C in air. The surface appears to give way to larger ‘islands’ of crystals in certain areas (as in A) with a visibly degraded or inferior crystalline layer surrounding the sample compared to the four hour heat treatment (B and D).

4.4.3.5 20 hours at temperature

Pure B₆O samples:

After twenty hours of heat treatment the samples displayed much the same features to the samples heat treated for 10 hours in that similar crystal structures were formed on the surfaces with a mixture of large single crystals (needle shaped) and rounded and a few very small rosette shaped crystals. The micrographs are shown in figure 4.60. A very noticeable feature was that very definite, dense colonies of spherical crystals formed in preferential areas (figure 4.60 B and D), possible regions which had previously cracked and possessed a high surface area as can be seen in the

following figure. Perhaps later crystal formations formed on earlier ones leading to crystal 'veins' and colonies along the surface.

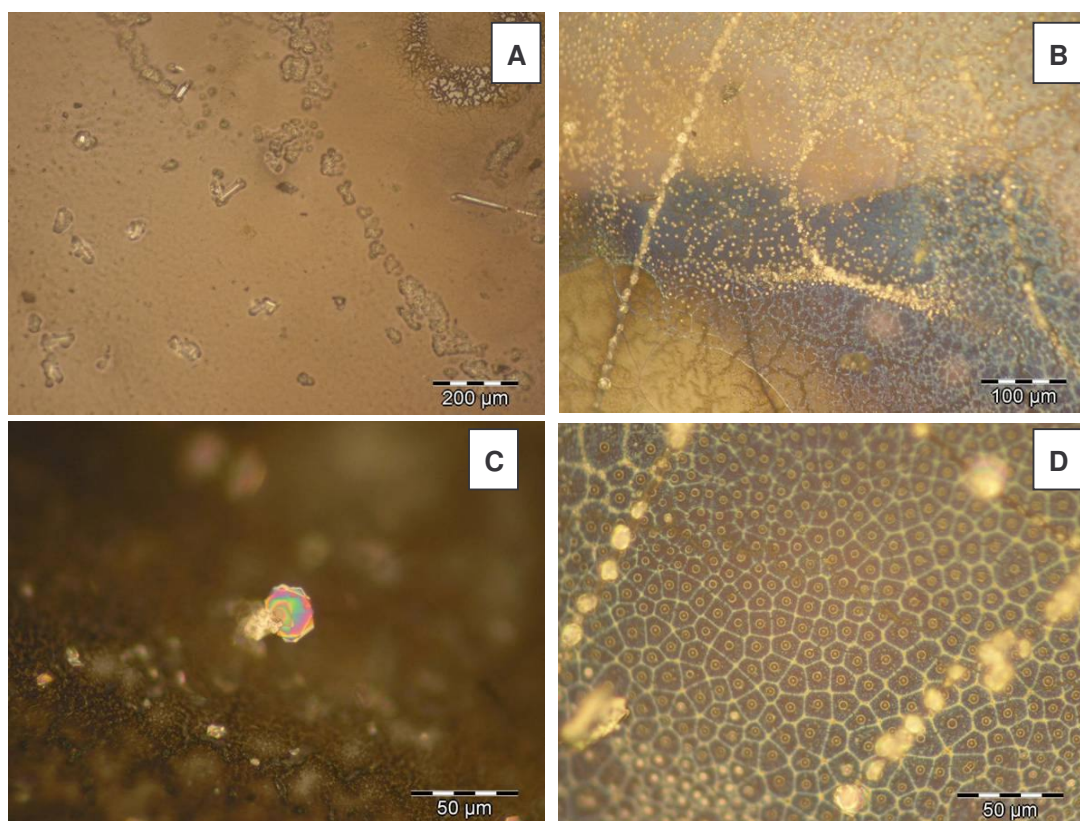


Figure 4.60: Representative micrographs depicting the surface features and microstructure of the pure B_6O samples heat treated at 1000 °C for 20 hours in air.

$B_6O/Y_2O_3/Al_2O_3$ samples:

The heat treated $B_6O/Y_2O_3/Al_2O_3$ samples displayed large crystal formations primarily across the surfaces with some areas with similar rosette shaped formations as found before, but primarily the crystals formed large crystalline masses as can be seen in figure 4.61.

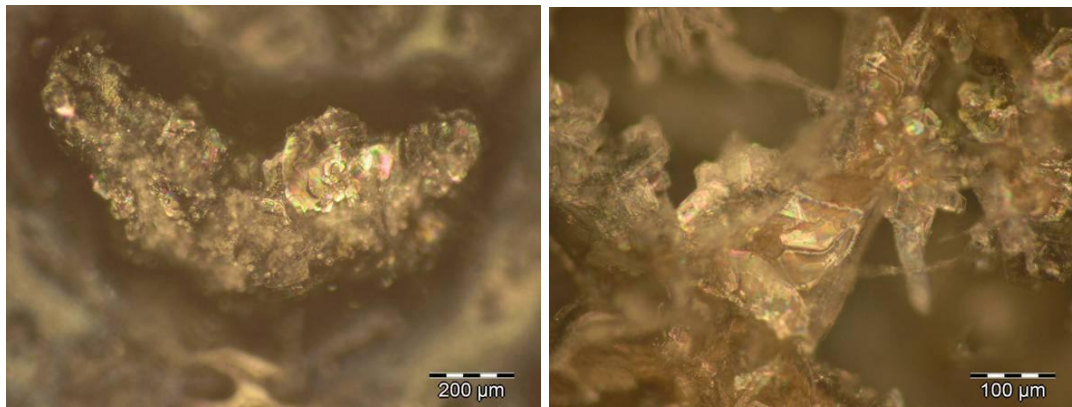


Figure 4.61: Representative optical micrographs of the crystal formations observed on all of the $B_6O/Y_2O_3/Al_2O_3$ samples after heat treating for 20 hours at 1000°C in air. The crystals appear to be in excess of 200 microns in diameter but large agglomerations of crystals form on parts of the surfaces.

4.4.3.6 50 hours at temperature

Pure B_6O samples:

A very noticeable difference was observed between the surfaces of the 20 and 50 hour heat treatments. Some areas of the surfaces displayed glassy phase effects as described earlier and characterised by strong variations in colour due to the variations in thickness of the layer. The surface changed in that it no longer showed small white spherical crystals as it did before. Very long needle like crystal formations were observed in a number of regions on the surface. The surface features can be seen in the micrographs shown in figure 4.62 B.

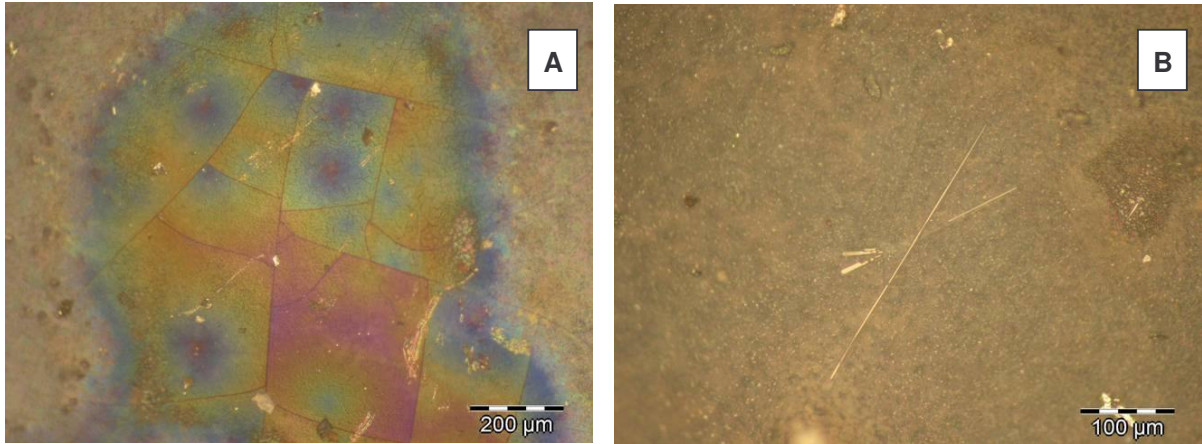


Figure 4.62: Micrographs of the surfaces showing glassy phase and large single crystals on the pure B_6O surfaces after 50 hours at 1000 °C.

$B_6O/Y_2O_3/Al_2O_3$ samples:

After the 50 hour heat treatment, the samples showed little distinction from the observations made after twenty hours at temperature as can be seen in figure 4.63 A and B. Much the same morphology was observed with combinations of crystalline agglomerates as well as regions with rosette shaped crystals and an abundance of darker material.

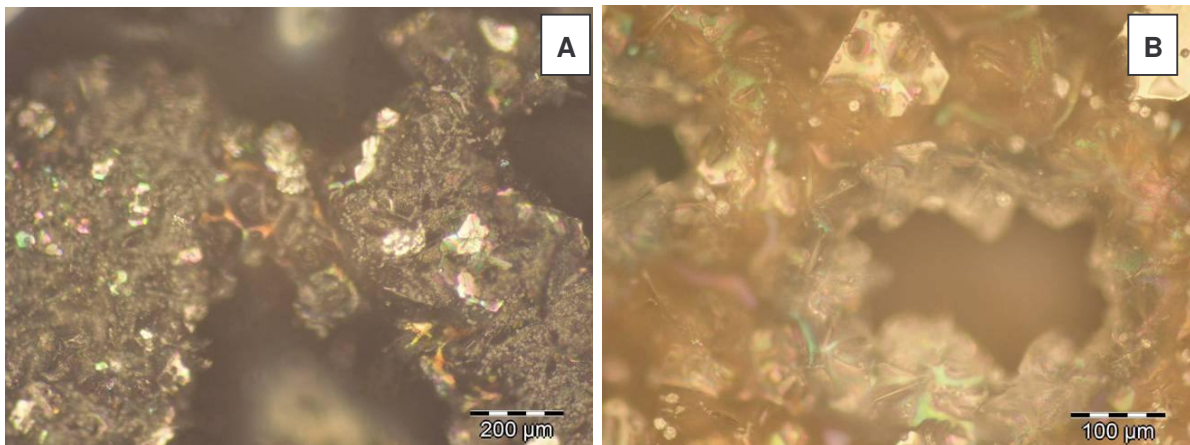


Figure 4.63: Unremarkable different features observed on the 50 hour surfaces as compared to the twenty hour surfaces. Similar crystal agglomerates and a diminished number of rosette formations were observed.

4.4.4 X-ray diffraction of the oxidised samples

X-ray diffraction was performed on both sets of thermal stability experiments, with the major difference being that the phase monitoring experiments had scans performed after each heat treatment time, while the mass change experiments were only scanned before and after heat treatment to prevent mass changes resulting from sample preparation. The starting XRD traces were described earlier in this chapter, the following sections describe the x-ray diffraction results taken during or after the respective sets of experiments.

4.4.4.1 Runs to monitor phase changes

The XRD scans performed during this part of the experiment became an extensive volume of work and the full results can be viewed in the appendix. Only two new phases were observed after heat treatments that were undertaken and those phases are boron nitride (BN) and B_2O_3 / H_3BO_3 . The heat treatments during this part of the work were undertaken for 1, 2, 3 4 and 5 hours at 1000 °C. Only the combined traces of samples 2 and three are shown because of clarity of the signals. Sample 1 showed a strangely large boron nitride peak presumed to be a contaminant. All the BN detected is believed to be residual contamination with only the B_2O_3 (or H_3BO_3) peak formation resulting from sample oxidation or atmospheric moisture effects.

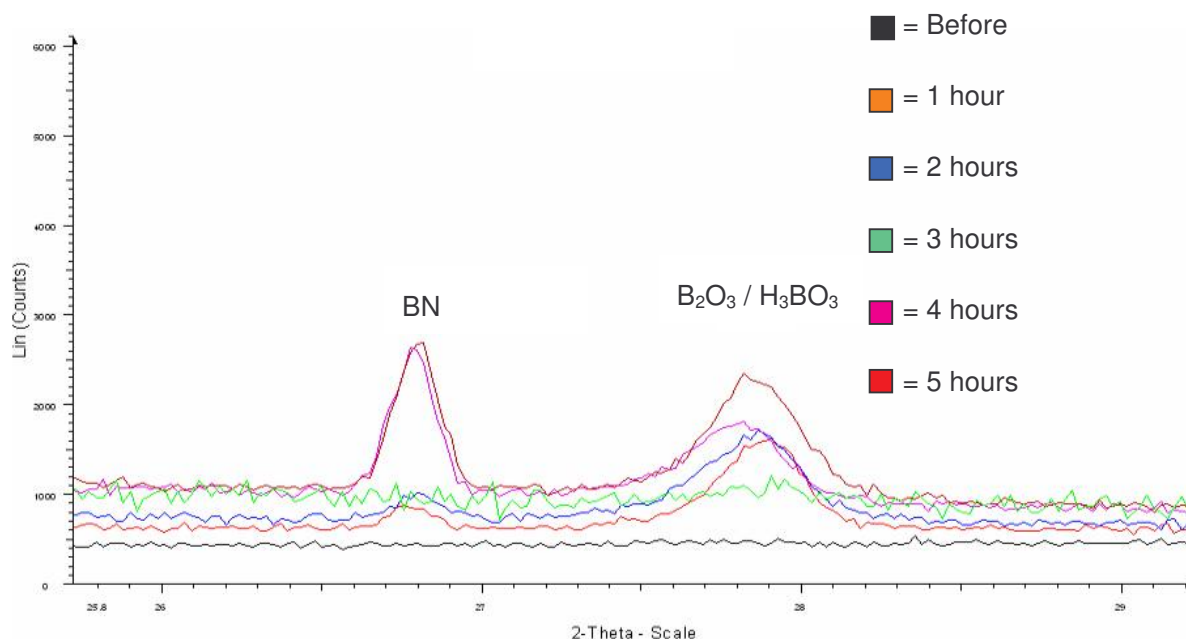


Figure 4.64: Overlaid peak evolution after the successive heat treatment and subsequent XRD scan of the pure B_6O sample 3 heat treated at 1000 °C in air.

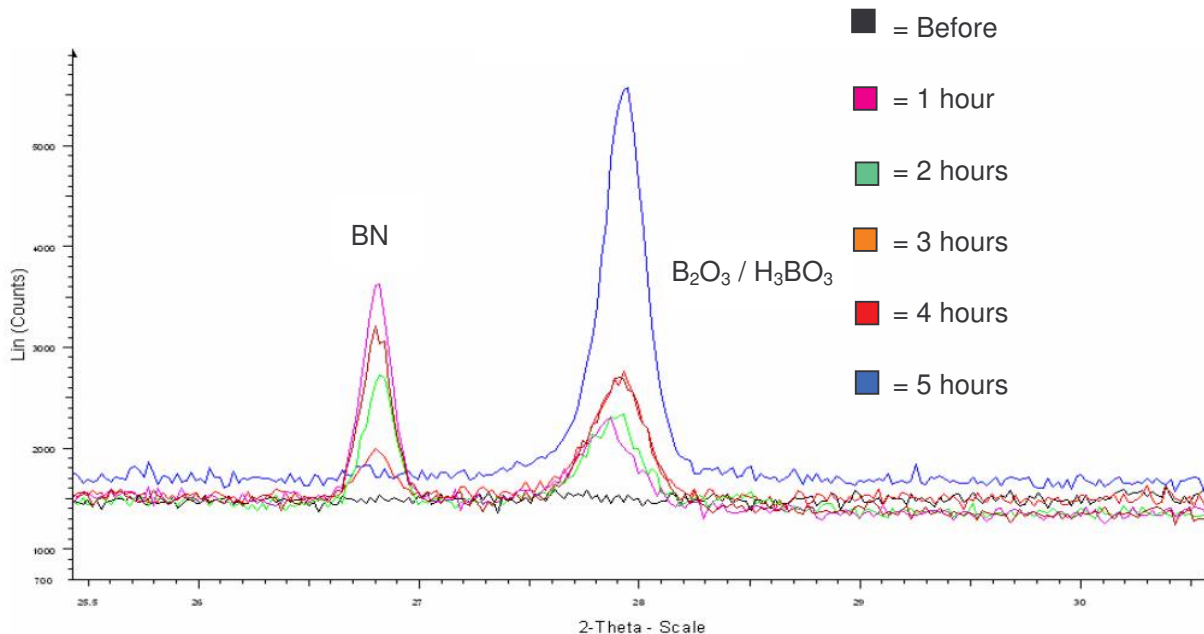


Figure 4.65: Overlaid peak evolution after the successive heat treatment and subsequent XRD scan of the pure B_6O sample 2 heat treated at 1000 °C in air.

It can be seen from the above figure that B_2O_3 (or H_3BO_3) content greatly increases over time. However the BN peaks also seem to become more prevalent over time. BN contamination resulted from inadequate grinding off of the hBN pot that contaminates the surfaces of B_6O pills that have been hot pressed. The ' B_2O_3 ' peak shown in figures 4.64 and 4.65 does not correspond to HBO_2 but can correspond with H_3BO_3 ; unfortunately H_3BO_3 and B_2O_3 have an overlapping primary and secondary peak, making them difficult to tell apart. The smaller peak corresponds to BN contaminant. It is believed that the evaporation or removal of decomposition products from the surface could have resulted in a concentration effect of the BN contaminant which would not evaporate or decompose at such a temperature, resulting in the illusion that BN is evolving, when it is actually a concentrating impurity on the surface.

4.4.4.2 Runs to monitor mass changes

The x-ray diffraction patterns produced after the 50 hour heat treatments on both samples proved very insightful in explaining the presence of the surface features and mass changes observed. Figure 4.66 shows the pattern corresponding to the pure B_6O sample. It shows that $B(OH)_3$ formed on the surface. The only place the hydrogen could have originated from is the water vapour in the atmosphere. The humidity on the days in question when the experiments were run was recorded as between 70 and 80 percent relative humidity (rainy season on the South African highveld). The effect of humidity on the phases generated during heat treatment is explained in detail in the discussion.

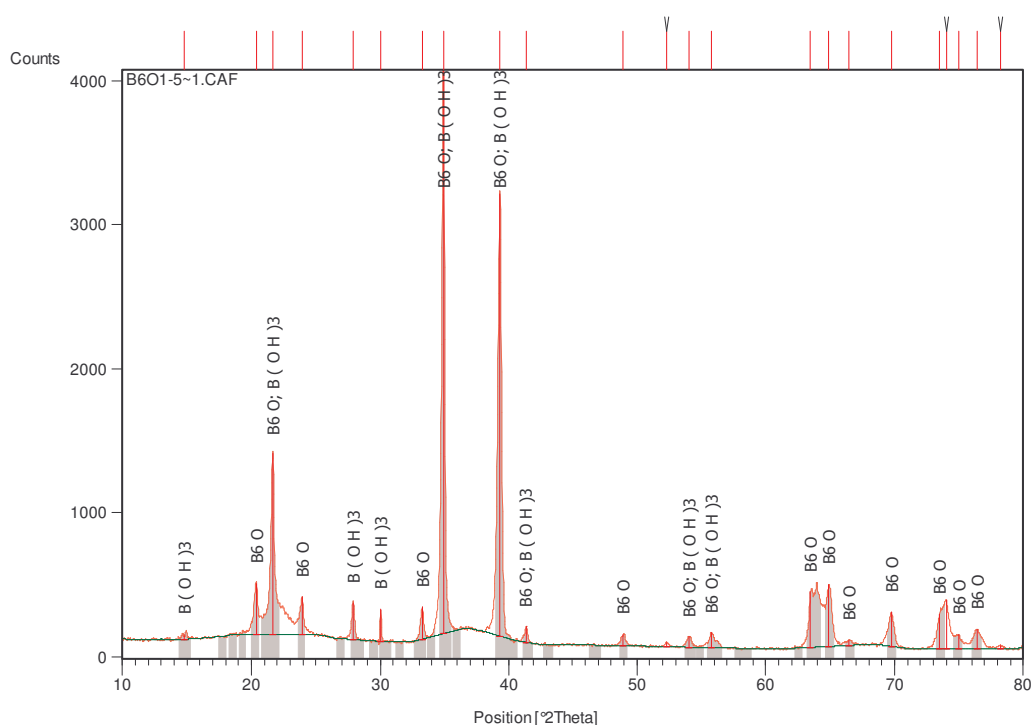


Figure 4.66: XRD pattern showing the detected phases found on the pure B_6O sample after the 50 hour heat treatment.

Figure 4.67 shows the XRD pattern from the $B_6O/Y_2O_3/Al_2O_3$ sample. The peaks clearly show a presence of hydroxides and boric acid (HBO_2). Table 4-14 shows the detected phases on the sample in decreasing order of abundance.



Compound name	Chemical formula
Boron suboxide	B ₆ O
Yttrium borate	Y ₂ B ₂ O ₆
Yttrium borate	YBO ₃
Boron carbide	B ₁₀ C
Metaborite (boroc acid)	HBO ₂
Aluminium yttrium oxide	AlYO ₃
Boric acid	B(OH) ₃

4.4.4.3 SEM of oxidation tested surfaces after 50 hours of heat treatment

After washing the samples in ethanol to dissolve the B_2O_3 and other possible soluble products, the samples were again taken for SEM studies in the hope that the dissolved products were the culprits in terms of obscuring the microscopy by means of melting under the electron beam. Fortunately, the hypothesis was correct, and SEM was indeed successful.

- Pure B_2O_3 surfaces

The pure B_2O_3 sample surface showed bright white regions that seem to correspond with crystal colonies observed under optical microscopy. Figure 4.68 shows the micrographs and EDS traces of the labelled regions.

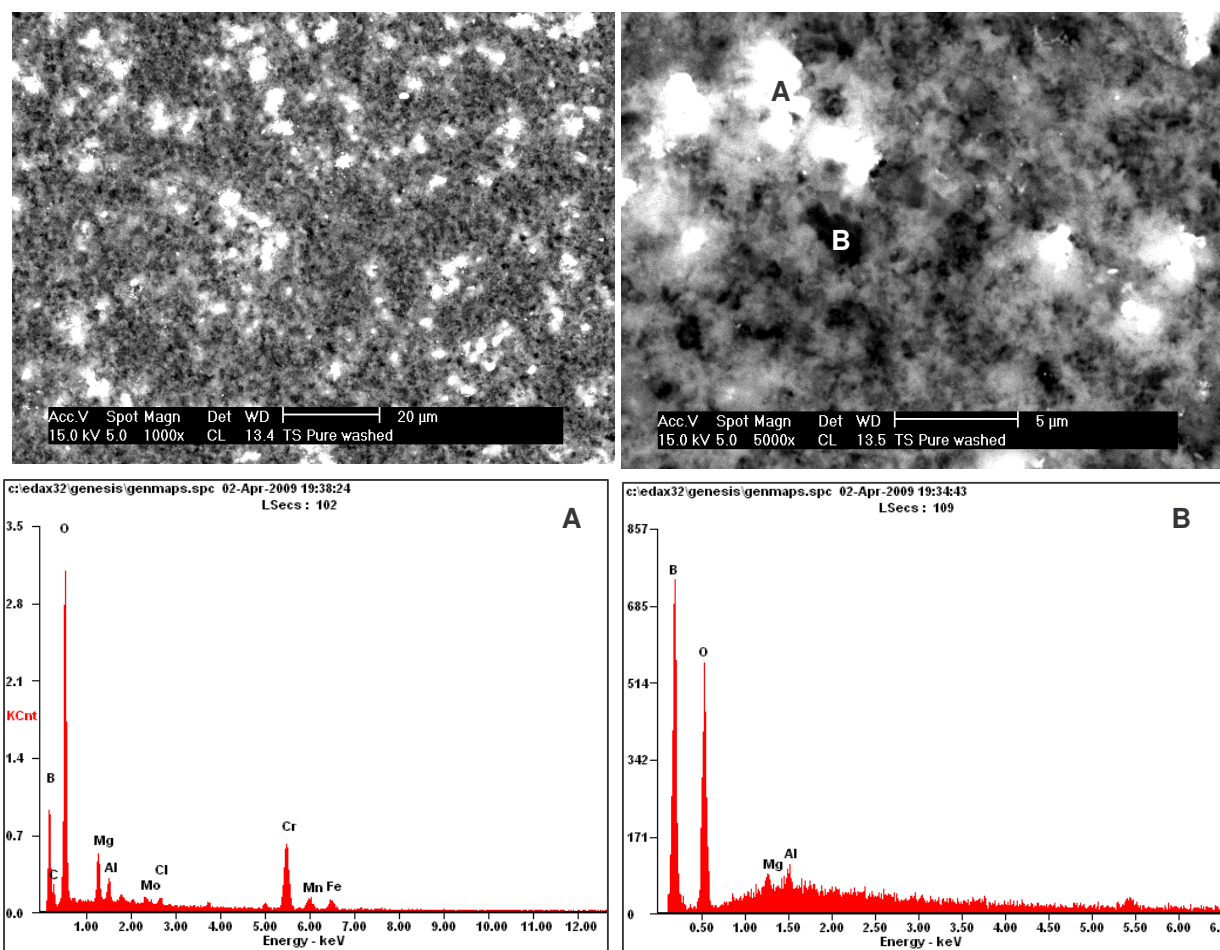


Figure 4.68: SEM micrographs and EDS traces of the regions A and B showing elements present in each region.

Region A appears to be rich in oxygen compared to region B with significant amounts of Al, Mg and Cr impurities. The other indicated elements are most likely impurities. Region B appears to be almost exclusively B and O with some Al and Mg. A few single crystals were seen to survive the washing and were investigated in terms of SEM and EDS. Figure 4.69 shows one of these crystal formations. The EDS scan (taken directly on the crystal) shows that it is composed primarily of boron and oxygen with magnesium, Al and Cr (probably from the nichrome wire) present also, with a small amount of C.

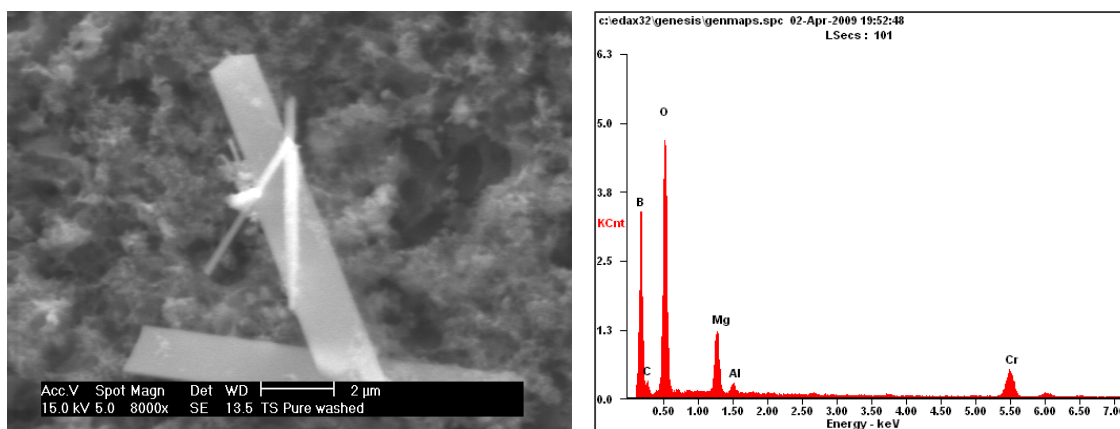


Figure 4.69: Single crystal formation and EDS trace of the crystal itself showing its elemental composition.

- $B_6O/Y_2O_3/Al_2O_3$ samples

The heat treated yttria alumina doped samples were washed in ethanol in the same way as the pure B_6O samples. The crystalline formations were successfully micrographed although some charging of the surface regions was clear and was challenging to compensate for.

EDS traces of the indicated regions of the SEM micrographs in figure 4.70 show that the crystals themselves are composed primarily of O, Al and Y with some silicon (impurity) present. Small peaks corresponding to boron, carbon and magnesium were seen. Some powder dislodged after washing and was collected in order to observe its composition. The crystal structures can be seen to be the same type of formation as those already investigated, but another observed surface feature was scanned using EDS and reveals primarily Y, Al and O peaks with other impurities present.

The characteristic rosette shape of the crystals is clearly visible in figure 4.70 and corresponds very nicely with the optical microscopy results. It would appear that such crystals comprise Al, Y and O elements primarily and are likely one or more of the phases detected with XRD.

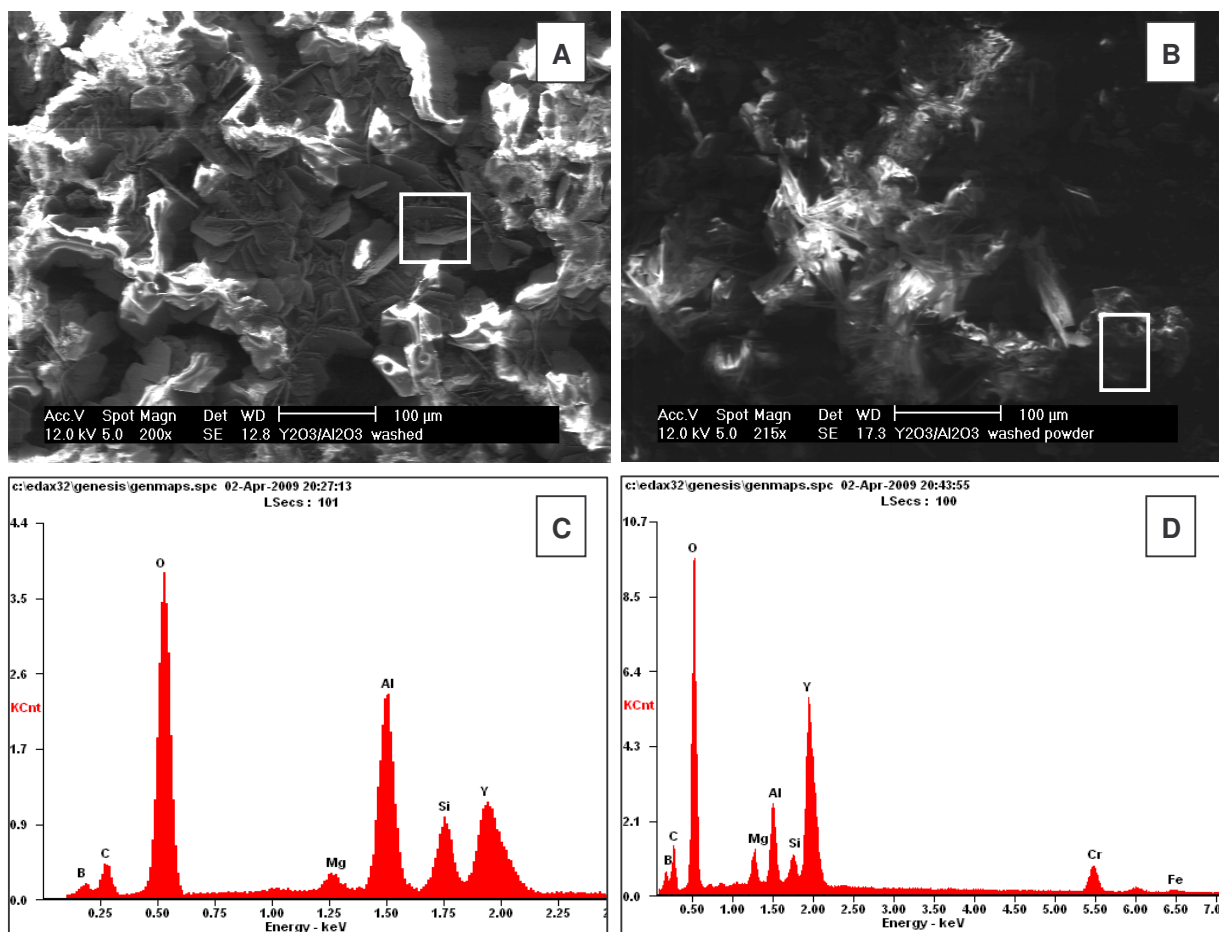


Figure 4.70: A: SEM micrograph showing the layered rosette shaped crystals that were observed on the yttria alumina samples. B: The EDS trace of the region shown in the micrograph (A) can be seen below it in C. B: SEM micrograph of some removed powder from the sample surface with EDS of the indicated region is shown below (D).

4.5 Machining and wear studies

4.5.1 Cutting tool fabrication results

Although cutting tools were successfully made from the $B_6O/Y_2O_3/Al_2O_3$ material, laser cutting trials to produce blanks of the cutting tools revealed a molten surface that formed as well as edge chipping and brittle behaviour of the material when clamped for the cutting, chamfering and honing operations. Because this melt layer was observed, oxidation testing become essential for this material in order to understand what may be happening in response to heating during cutting and tool fabrication. Micrographs shown in figure 4.71 illustrate the laser cut blanks that were subsequently chamfered and honed to produce the first set of B_6O based cutting tools known to exist.

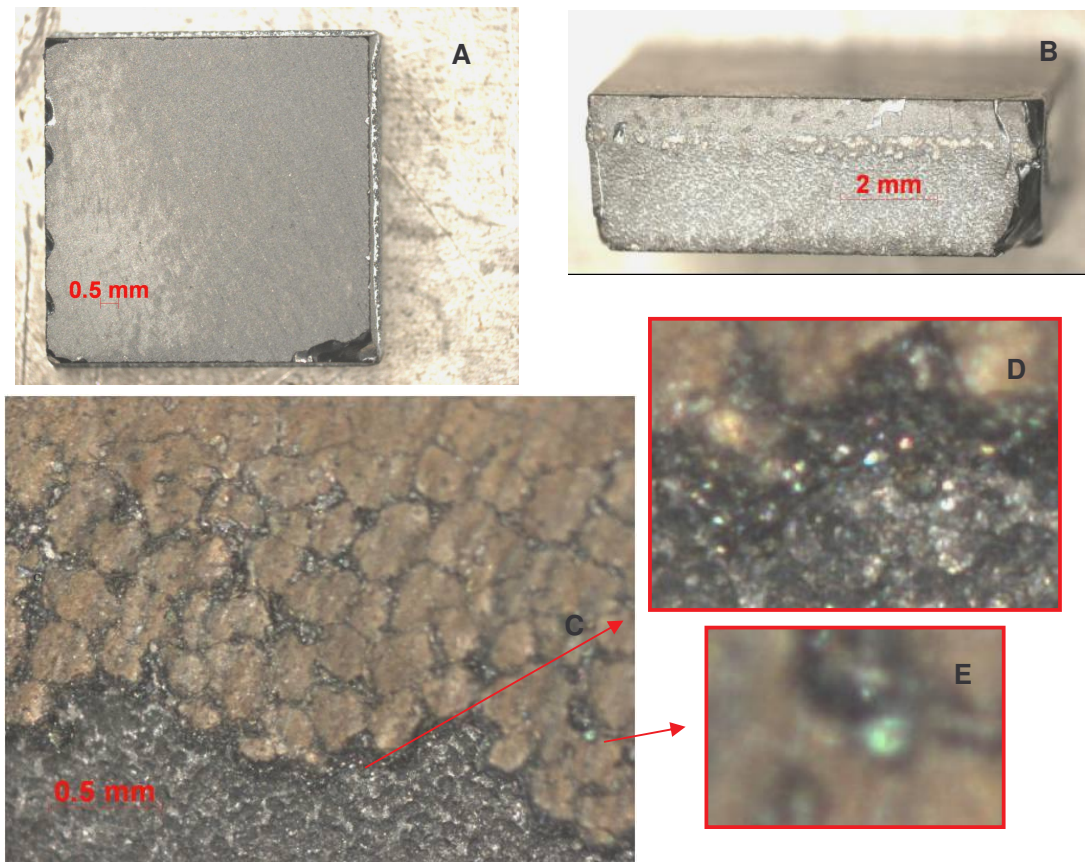


Figure 4.71: A: Laser cut blank viewed from above showing edge chipping and brittle fracture, B: the same blank showing the melt layer similar to that observed in the thermal stability tests, C: close up image of the melt layer that strongly resembles thermal stability testing results, D and E: zoomed in images of the regions indicated by the arrows showing crystallite formation, as was observed in thermal stability testing.

The images of the molten layer and the crystallite formation link very closely with observations of the oxidized samples. In spite of the difficulties associated with laser cutting, cutting tools were still produced from the laser cut blanks but some were noted to possess fractured edges, most likely a result of a lack of optimization of cutting the new material. After all B_6O has never been fabricated into a tool before and it is unrealistic to expect perfect results on the first attempt in work such as this.

The cutting edges were examined prior to cutting operations (figure 4.72) commencing on both the DBC50 and B_6O cutting tools. It was found that while DBC50 possessed a very well finished surface, the B_6O material appeared porous and with many surface imperfections including scratches and a great deal of open porosity.

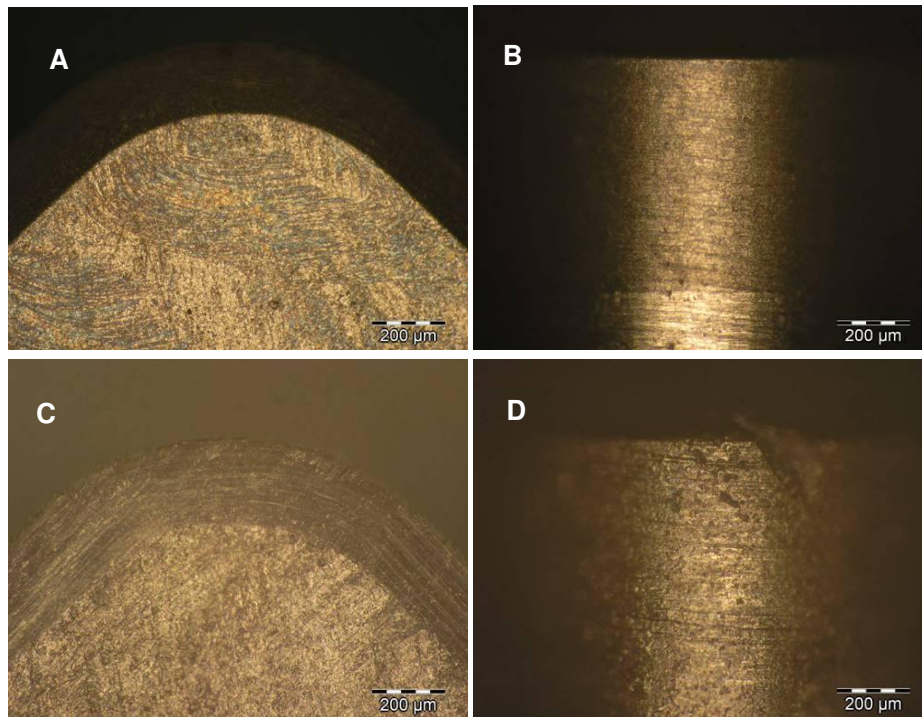


Figure 4.72: A and B: DBC50 rake face and flank respectively showing good chamfering and honing with insignificant surface imperfections. C and D: $B_6O/Y_2O_3/Al_2O_3$ rake face and flank respectively showing a high degree of deep surface scratching and porosity.

Porosity and scratches on a tool surface can be extremely detrimental if workpiece material can build up within them and increase pressure from within these crevices and open a crack that could lead to fracture and tool failure, especially if there are mismatching thermal expansion coefficients between tool and workpiece.

4.5.1.1 X-ray diffraction studies of laser cut surface

X-ray diffraction was performed on a laser cut section of the yttria alumina boron suboxide composite in order to verify the composition of the 'melt layer' observed after laser cutting. Only one foreign peak was detected, namely B_2O_3 .

XRD trace of the laser cut surface taken over the largest surface area of the sample

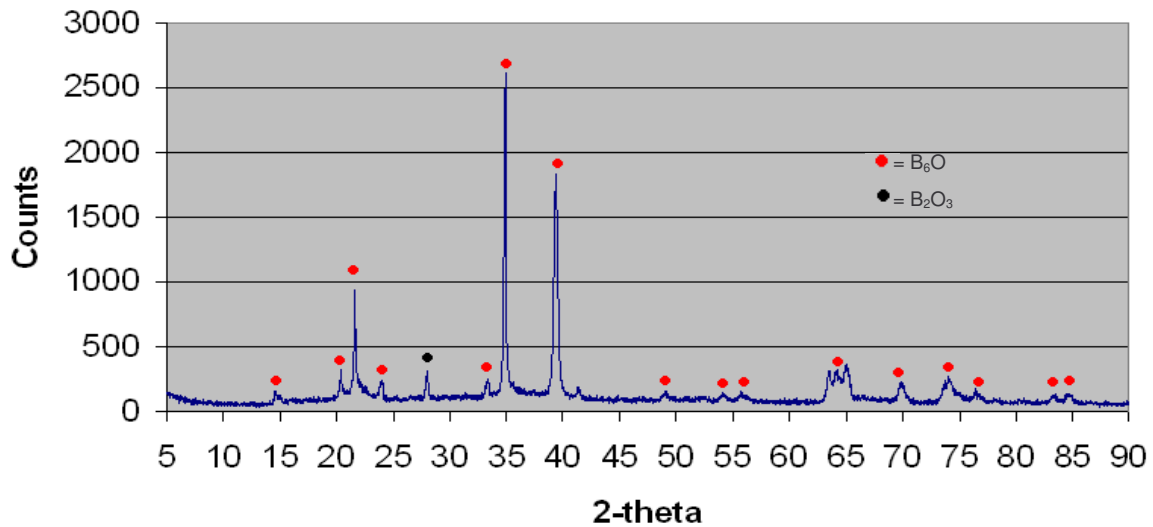


Figure 4.73: XRD trace of the laser cut melt surface of a blank, showing B_2O_3 as a product phase.

4.5.2 Turning test results

In order to gauge the cutting performance of the B₆O cutting tools, it was necessary to compare them to a well known and used tool, DBC50 of the same geometry. Cutting operations (turning tests on CGI) were conducted on both tool materials in an identical way. After a particular cutting time and length, the tool was examined for flank wear scars and the width of such scars was measured. The average of ten flank wear measurements was taken in each case and a graph of flank wear scar magnitude against cutting time was plotted.

4.5.2.1 50m/min cutting speed

The graph of the flank wear scar magnitude of B₆O and DBC50 cutting tools against CGI at 50 metres per minute cutting speed is shown in figure 4.74. The depth of cut was taken as 0.25mm and the feed rate was set to 0.1mm per revolution. The cutting tool inserts were secured onto a tool holder with the combination of tool holder and cutting tool insert resulting in a rake angle of -6°, a clearance angle of 6° and a lead angle of 45° as described in the methodology.

The B₆O tools were seen to provide an excellent surface finish to the CGI workpiece compared to the DBC50 tools in the sense that the CGI workpiece appeared and felt smooth compared to cutting with DBC50. Unfortunately, the B₆O tools tended to undergo a loss of the nose radius after cutting for some time.

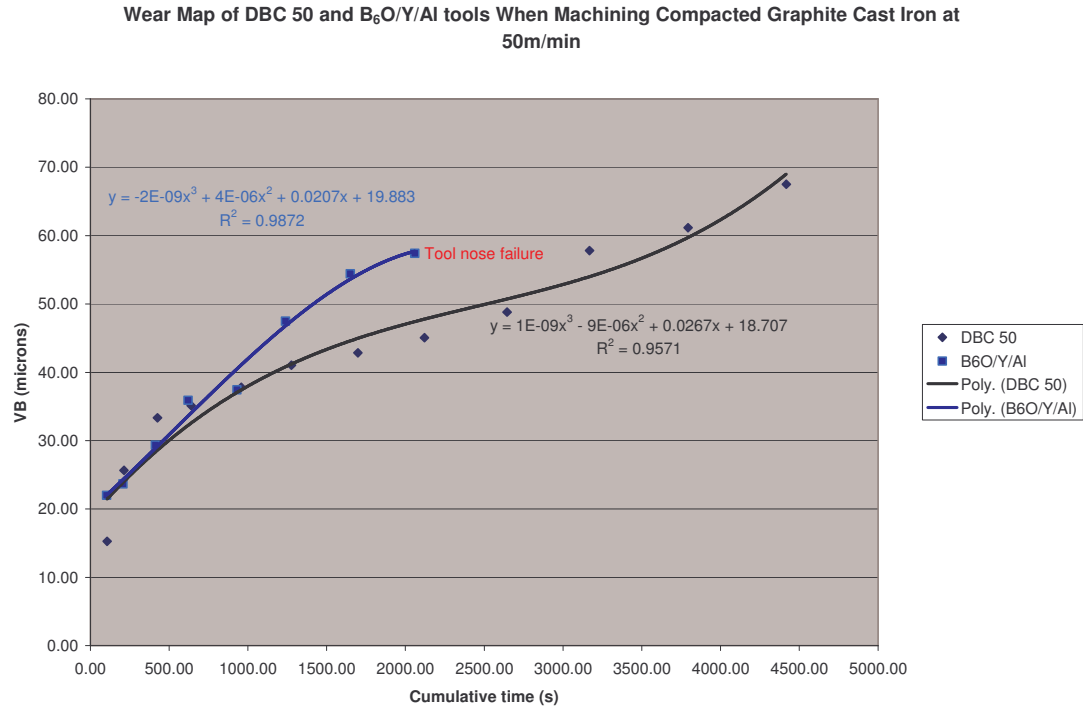


Figure 4.74: Flank wear scar magnitude of DBC50 vs. B₆O machining time for 50m/min, depth of cut 0.25mm and feed rate of 0.1mm per revolution.

The B₆O tool appears to perform similarly to DBC50 initially, but the loss of the nose radius resulted in catastrophic failure of the tool and the experiment ceased at this point. Other attempts to cut with the B₆O tools to acquire a better result than the one displayed in the flank wear scar magnitude vs. cutting time graph resulted in an earlier loss of the nose radius than what occurred in the displayed results.

4.5.2.2 100m/min cutting speed

At this higher cutting speed, the abrasive and chemical wear effects would be expected to be higher and thus more difficult for the cutting tools to withstand. Several attempts at cutting CGI were made at this speed, some with loss of nose radius as before. The only successful test resulted in rapid progression of the flank wear scar past the flank wear failure criterion of 300 microns in 426 seconds of cutting time. In an attempt to prevent tool nose failure, the best cutting tool was selected by using optical microscopy to select the finest finished flank and chamfer on all the remaining tools. This tool was then subjected to the cutting test and did not

lose the nose radius, but did wear very quickly as can be seen in figure 4.75 A to D. The same depth of cut and feed as before were used.

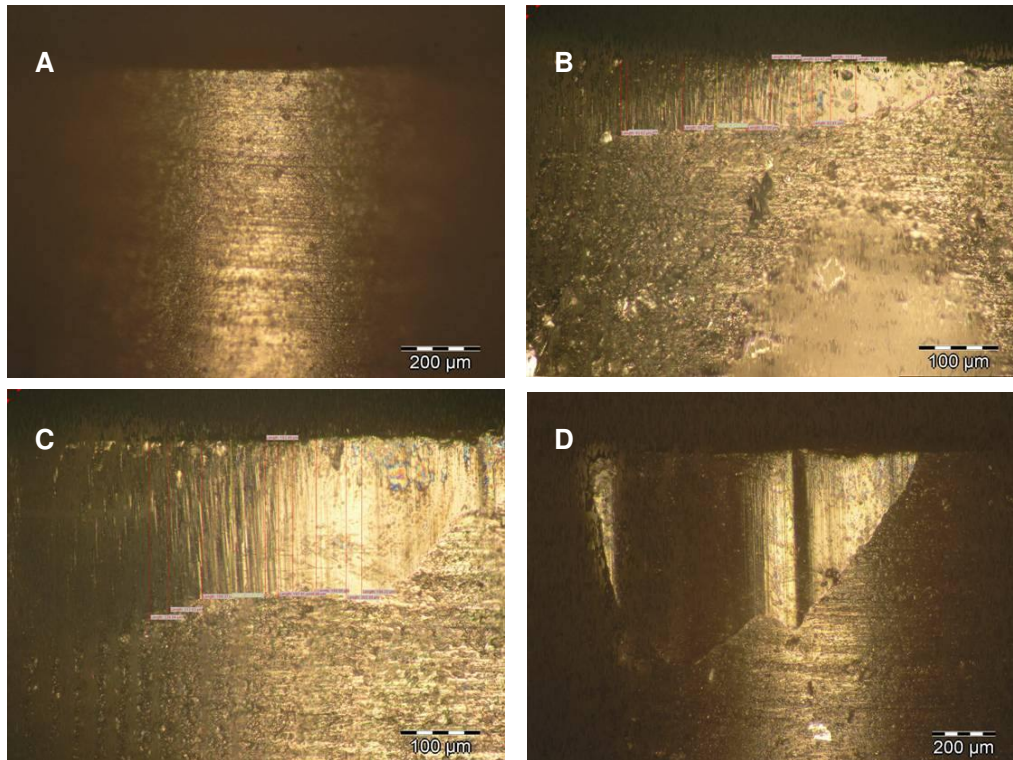


Figure 4.75: A: The best flank of the tool selected for 100m/min cutting trials. B: after a cutting time of 106.50 seconds, a flank wear scar in excess of 100µm resulted. C: after a cutting time of 213.00 seconds, a flank wear scar in excess of 250µm resulted, D: after 426.00 seconds the flank wear failure criterion (300µm) was exceeded.

4.5.3 Tool failure analysis

In an attempt to explain the tool nose failure that was observed when cutting CGI with the B₆O tools, a closer look at the wear scar progression revealed an interesting development. The apparent open porosity of the tools and the poor surface finish of the flank resulted in constructive progression of the pores and flaws as the scar progresses. The image progression in figure 4.76 demonstrates how the porosity exacerbates the formation of the wear scar and ultimately leads to failure.

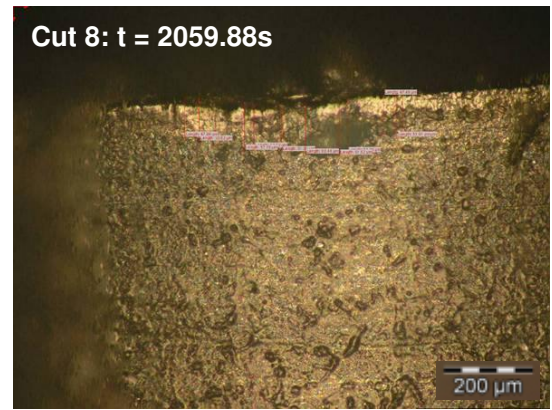
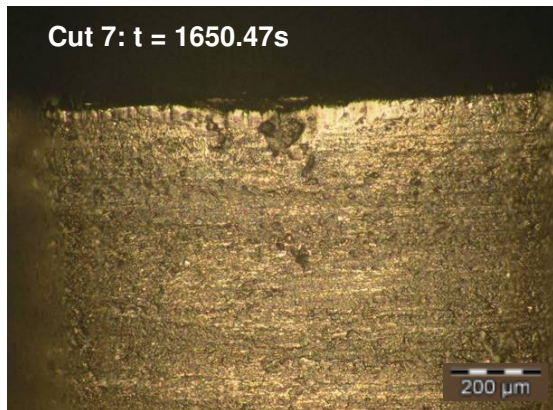
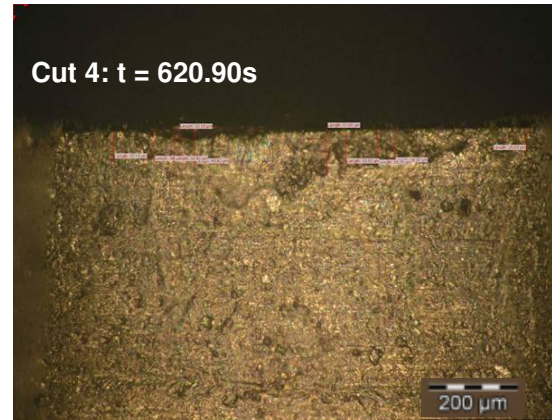
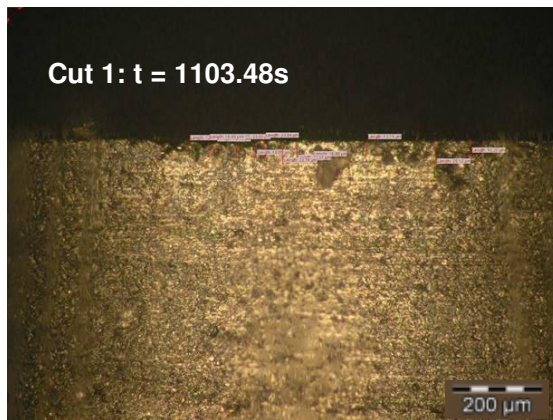


Figure 4.76: Progression of cuts showing the development of the wear scar, exacerbated by surface imperfections. The time for each cut is shown next to the label of each cutting operation. Cut 9 does not have a measured time because the cutting operation was stopped when the tool nose failed and the surface finish of the workpiece was compromised.

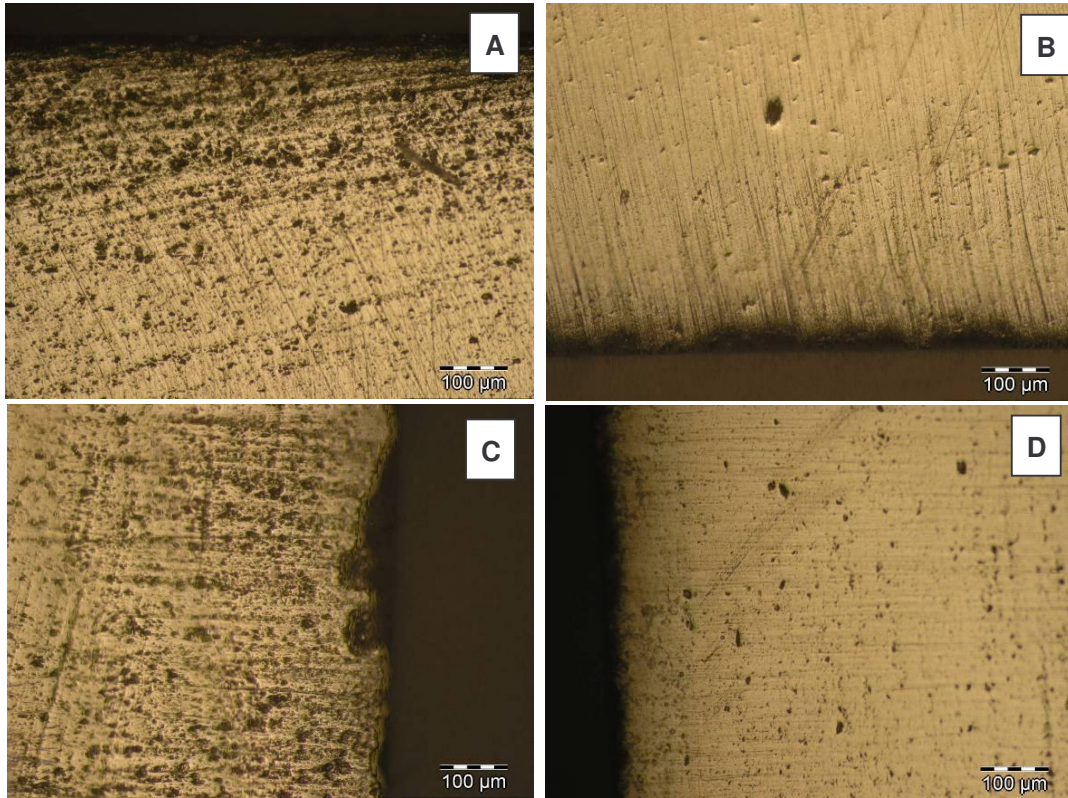


Figure 4.77: A: laser cut side of the material. B: uncut (normal) side of the material. The sample in question has been designated sample 1. C: laser cut side of the material. D: uncut (normal) side of the material. The sample in question has been designated sample 2.

It is very clear that the laser cut side of the material (figure 4.77 A and C) has suffered increased porosity as a symptom of what is believed to be a heat affected zone most likely resulting from the laser cutting operation. The thickness of this porosity layer or heat affected zone is substantial. It is obvious that the layer with higher porosity extends inwards from the surface in excess of half a millimetre! If this indeed the case then the cutting edge, chamfer etc could all be sitting in a heat affected zone with elevated porosity which is certain to detrimentally affect the performance of the cutting edge. The porosity of the cutting tools is clearly visible on preceding micrographs and is a very detrimental effect for a cutting tool surface.

4.5.3.1 Optical microscopy of surface effects

The surfaces of the cutting tools were observed for microstructural features that could indicate flaws that result in the poor tool performance and can be viewed in figure 4.78. Features very similar to that seen in the oxidation experiments were

observed, but with less distinct clarity. Figure 4.78 A and B also indicate a height profile of the surfaces, indicating a lack of smoothness, which could also prove problematic as heightened regions above the chamfer or cutting region could shear off and severely impair the cutting tool performance.

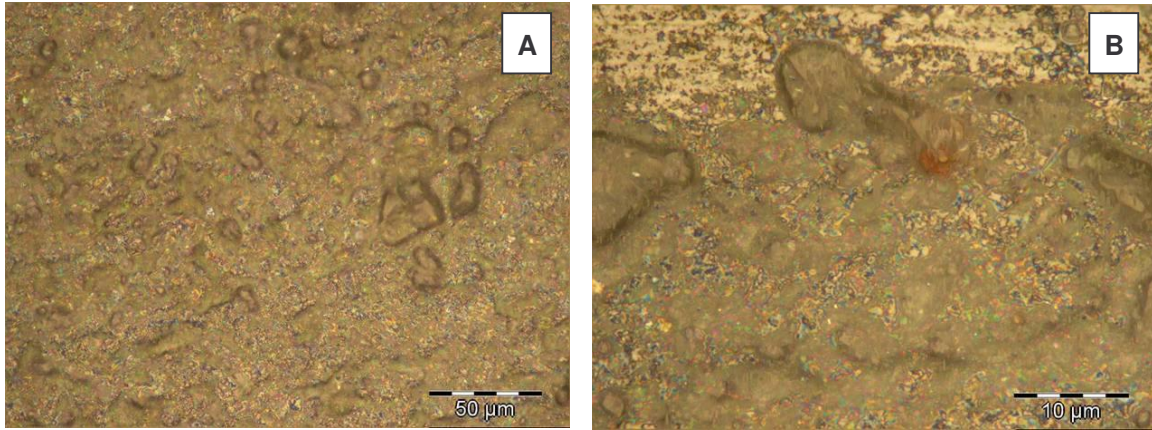


Figure 4.78: A: high magnification optical micrograph of a B₆O cutting tool surface in the as-produced state i.e. prior to turning. Similarly, B shows the same effect on another, separate tool.

4.5.3.2 Scanning electron microscopy investigation of chamfer and surface finish

The surface finish of the cutting tools was investigated with SEM and can be seen in figure 4.79. The chamfer itself appears to be nicely honed, but the surface of the cutting tool material appears highly porous with many surface imperfections that could lead to fracture.

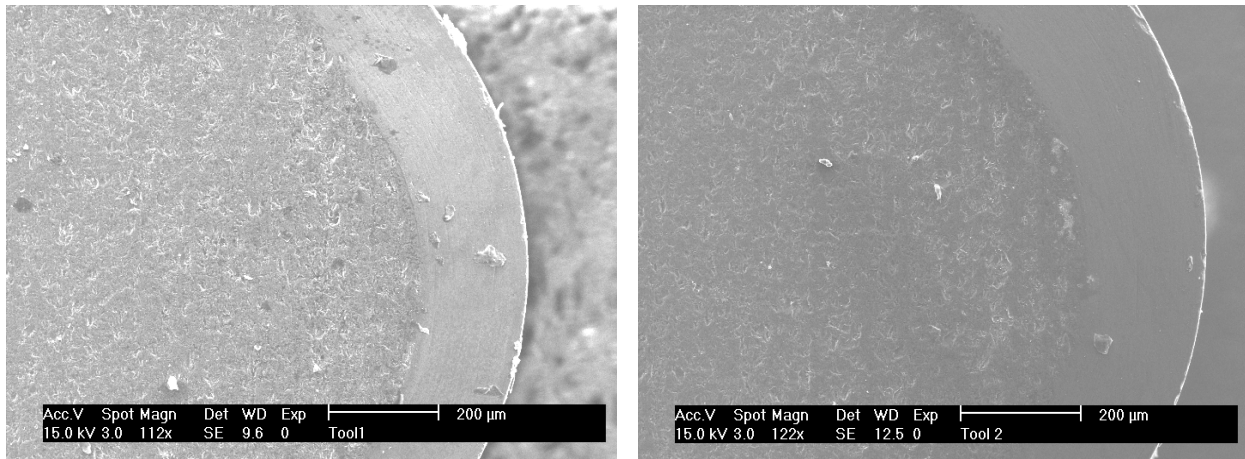


Figure 4.79: SEM micrographs of the chamfer and rake faces of two $B_6O/Y_2O_3/Al_2O_3$ cutting tools showing surface porosity.

An EDS of the surface of the cutting tools was performed in order to determine the elemental composition. The EDS trace is shown in figure 4.80 and shows the expected B, O, Al and Y phases but with many impurities especially carbon. These atoms likely were introduced during the tool making process. It is doubtful that so much carbon was present in the starting material, thus it can be attributed to the tool making process almost certainly or dirt on the surface.

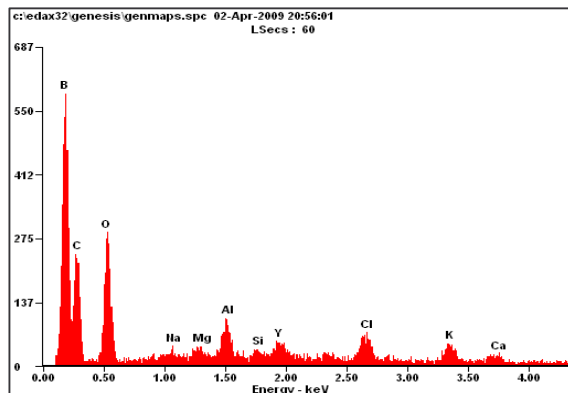


Figure 4.80 EDS trace taken over the surface of the $B_6O/Y_2O_3/Al_2O_3$ cutting tool surface in order to verify elemental composition.

4.5.3.3 SEM investigation of wear scars

In order to provide some insight into the conditions occurring at the cutting edge at the machining speeds of 50 and 100m/min, a brief turning operation was undertaken to produce a wear scar. The cutting time at each speed was only one minute in order to prevent the tool nose failure problem. The tool was then removed from the holder and SEM studies performed.

- 100m/min

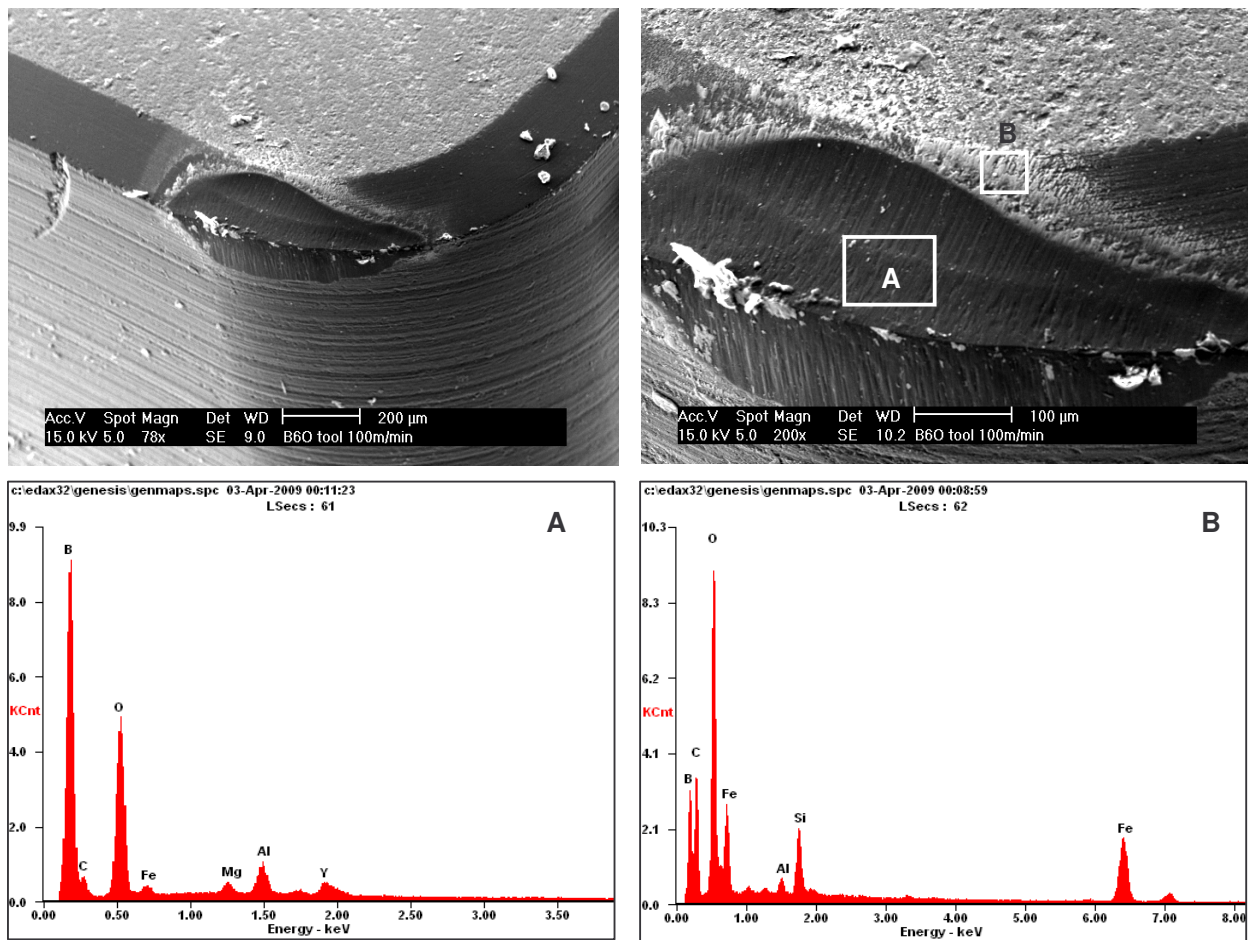


Figure 4.81: Top left: SEM micrograph of the 100m/min after 1 minute of cutting time against CGI. Top right: magnified image of the wear scar. Labelled areas correspond to EDS traces shown below the micrographs.

It is clear from figure 4.81 that the wear scar produced after 100m/min of cutting for one minute is very substantial. Primarily abrasive wear is evident with no crater evident on the rake face but rather a severe wear scar on the chamfer itself. The EDS traces of region A shows the expected composition of the tool with some impurities, but region B shows a substantial amount of SiO_2 even after 1 minute of machining time, which verifies that silicon has an affinity for B_6O as seen by the diffusion couples experiments. Iron has adhered to the rake face and the boron signal has strongly diminished.

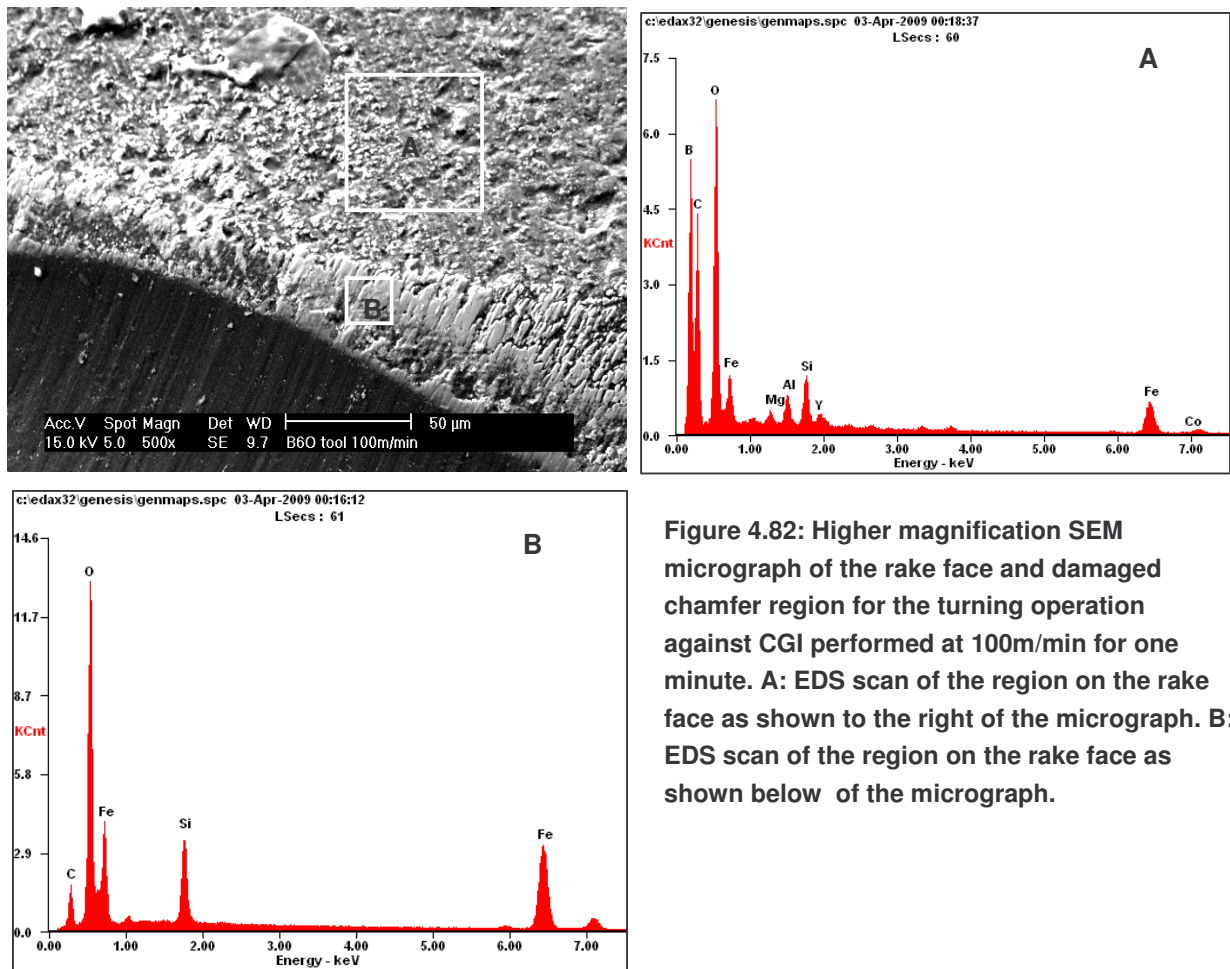


Figure 4.82: Higher magnification SEM micrograph of the rake face and damaged chamfer region for the turning operation against CGI performed at 100m/min for one minute. A: EDS scan of the region on the rake face as shown to the right of the micrograph. B: EDS scan of the region on the rake face as shown below of the micrograph.

Figure 4.82 shows a higher magnification image of the rake face and damaged chamfer region resulting from the one minute of turning against CGI. Region A shows an abundance of carbon with some silicon presence and some iron, likely resulting from the CGI. Region B however shows a substantial amount of silicon to be present with no boron detected there at all, possibly due to the thickness of the iron and oxygen containing layer obscuring the signal. Iron oxides and silicon oxides could perhaps have formed here.

- 50 m/min

Far less significant wear scarring was observed for the 50 m/min turning test for one minute than the 100m/min test.

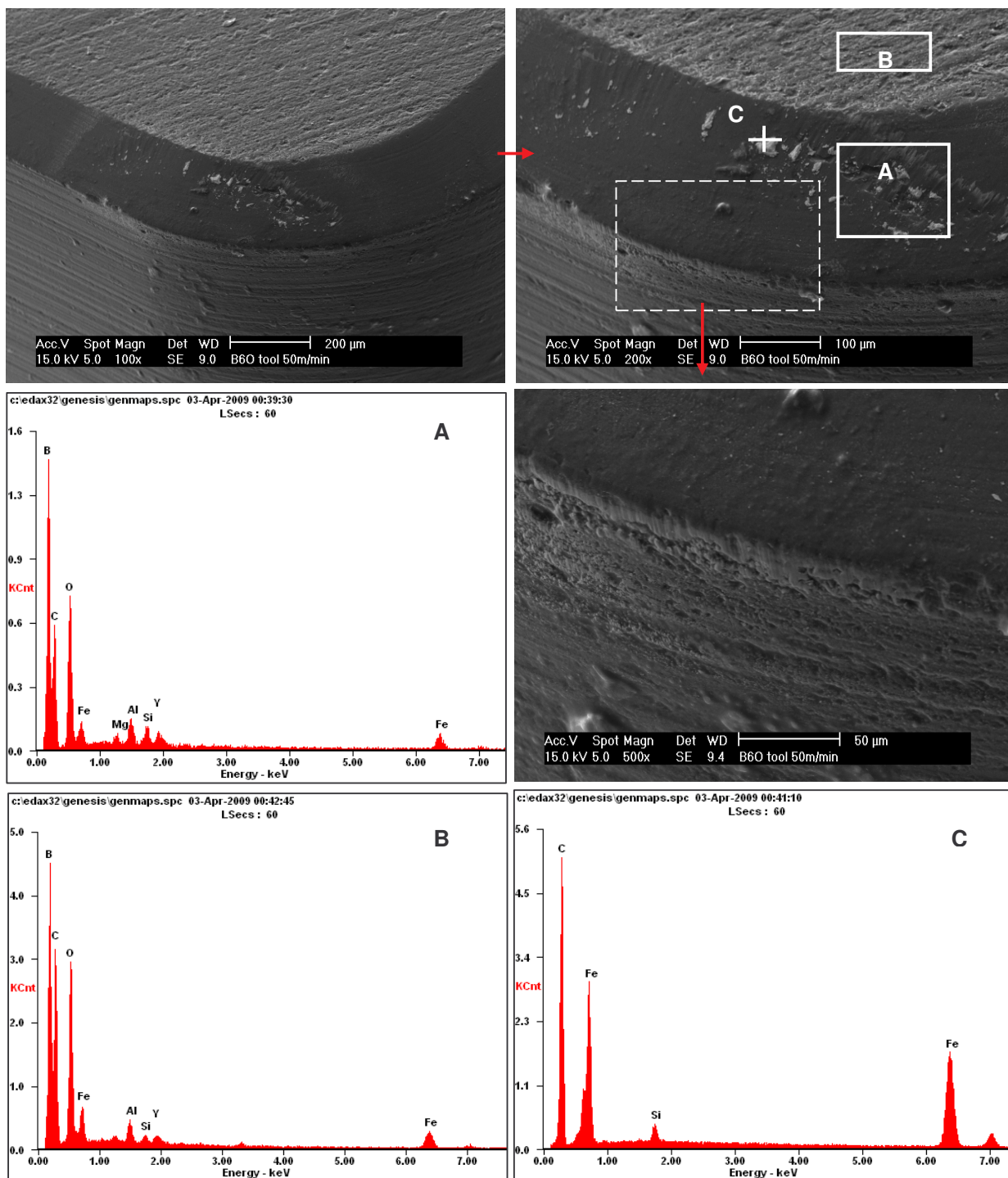


Figure 4.83: 50m/min wear scar (1 minute machining time) and corresponding EDS traces.

It can be seen from figure 4.83 that the wear scar produced by 50m/min is insignificant after only one minute of machining, which can also be predicted from graph of the flank wear scar size shown earlier in this report. The box (broken lines) indicates the region magnified in the lower micrograph of figure 4.83. Region A, on the chamfer itself, shows only a small amount of iron relative to the other peaks. The unexpectedly large carbon signal could be a combination of carbon contamination from the chamfering process combined with carbon diffusion into or adherence onto the B_6O during the machining process. Region B also shows a high carbon content relative to the other peaks. The targeted region C is a piece of adherent iron from the machining process which also contains a lot of carbon. A high magnification micrograph of the flank wear scar is shown (lower SEM image in figure 4.83) and indicates that the wear scar is still quite small (as expected) after such a short cutting time.

5 DISCUSSION

5.1 Powder preparation

5.1.1 Pure B₆O powders

Powder batch 1 was seen to consist of a particle size of less than 0.64μm for 50% of the particles and that 90% of the particles fell below the 1.31μm size. It can thus be inferred that milling was carried out successfully and reduced the particle size to an acceptable size range for sintering. Iron and chromium contamination were 0.052 and 0.054 wt. % respectively which is sufficiently low indicating that the washing procedure was carried out successfully. Good results were obtained for batches 2 and 3 in terms of iron and chromium contamination (table 4-3) and none of the batches displayed more than 0.06wt. % contamination of the elements. Batch 2 displayed a pre-milling particle size distribution of between ≈0.2 and 30μm, however this was reduced to an average of less than one micron after 20 hours of milling at 400rpm and thus it can be deduced that the milling operation was a success. Batch 3 however, exhibited a poor pre-milling powder distribution (figure 4.3 page 89) of approximately 0.1 to 110μm which is a very broad range. It is possible that the ultrasonic agitation on the particle size analyzer was unable to break up some agglomerates within the pre-milled powder that came about during storage. Fortunately, the milled powder possessed a good distribution comparable to those mentioned for batches 1 and 2 and thus the milling operation reduced the broad particle size distribution to an acceptable level.

5.1.2 Co and CoO additive powders

The starting size distribution of the additives used in the ultrahigh pressure experiments (table 4-2) can be seen to be 5μm and 34μm for the Co and CoO powders respectively. Compared to the pure B₆O powder, such particle sizes are too large to allow for homogeneous distribution of the secondary phases during sintering. The problem with this is that the properties of the resulting compact cannot possibly be optimum without a homogeneous distribution of the second phase. Hence, it can be deduced that such large particle sizes should be reduced in future work by milling or some other means in order to allow for a better distribution of the additive phase and a better size ratio between the additive and the bulk powders.

5.2 Properties of the sintered materials

5.2.1 Lower pressure samples

All of the hot pressed pure B_6O compacts fell within the approximate range of density and open porosity as shown in table 4-4 on page 92. All of the compacts shown in table 4-4 achieved a density greater than 96.4% of the theoretical density of B_6O , taken as 2.55 g/cm^3 from previous studies⁴. Pure B_6O does not typically densify easily to the same level as the compacts with additive phases hence the open porosity is higher additionally as described by previous authors^{3, 4, and 5}. The spark plasma sintered (IKTS) samples show excellent properties in terms of density and open porosity indicating the superior sintering technology that exists relative to hot pressing techniques, higher density is however expected due to the presence of the Al_2O_3/Y_2O_3 additive phases, but the difference in open porosity is especially evident. Comparisons between polished samples of these materials also reveals a clear visual difference in terms of open porosity as can be seen by comparing figures 4.50 and 4.51 (page 145) taken prior to oxidation experiments. The yttria-alumina samples clearly display very small pores compared to hot pressed materials. The XRD data also detected only the B_6O phase to be present in all of these materials indicating a high level of purity, however, the yttria alumina phases cannot be quantified by XRD due to their amorphous nature.

5.2.2 Ultrahigh pressure sintered compacts

The density and open porosity of the ultrahigh pressure sintered compacts is excellent compared to all of the other materials shown in this project (table 4-6) but unfortunately error analysis was not performed by the experimentalist⁵¹ and thus reliability of the data cannot be obtained from this information. Nevertheless the hardness values were performed by the IKTS team (table 4-7) and can be seen to be 35 to 36GPa under a 400g load. These values are similar to the hardness values obtained for SPS samples but are higher than some of the previously measured hot pressed samples. The hardness of the compacts is less than the single crystal microhardness values reported in literature of 45GPa¹⁶. It was noted by He and Zhao¹⁶ that Vickers hardness tends to decrease with increasing load and a wide variety of hardness values have so far been reported for boron suboxide, ranging from 32 to 38 GPa, which places the sintered compacts from this project directly in the expected range.

The small grain size for the ultrahigh pressure (UHP) compacts is approximately the same as the starting powder which indicates that a true sintering process did not

occur due to insufficient time and temperature and thus the compaction process under enormous pressures is believed to be what is holding the grains together primarily. This implies that cutting tool performance of the tools produced from these materials is unlikely to be optimised because sintering did not occur in the proper manner. Despite possessing excellent density and open porosity as well as hardness, a proper sintering process strengthens the bonds between the grains and thus should result in improved wear performance. Additionally, the poor distribution of the additive phases is unlikely to bode well for the performance of the cutting tools, because the toughening effects intended to be imparted to the tool from the additive phases, are not homogeneously distributed within the material as indicated by the SEM micrographs (figures 4.5 to 4.9 on pages 95 to 98 and 4.11 to 4.13 on pages 100 and 101). In order to optimize the performance of these materials, it would be best to refine the microstructure so that the additive phases are evenly distributed within the material which would require smaller additive particles as well as higher temperatures or longer holding times to allow for a typical sintering (diffusion controlled) process to occur.

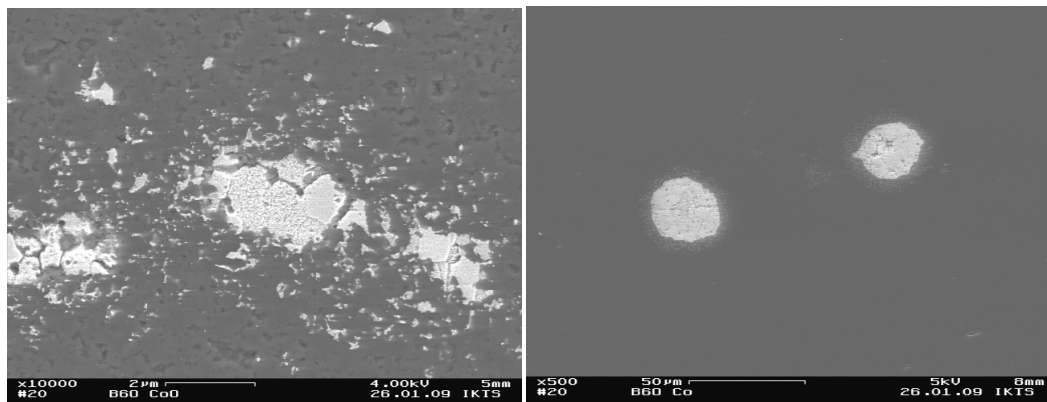


Figure 5.1: Left: SEM micrograph of the B_6O/Co sintered compact, the size of the formed cobalt boride phase (white) can be seen to be approximately 4 to 5 microns: the same approximate size as the starting powder (5 microns). Right: B_6O/CoO material with CoB phases approximately 30 microns in size: the starting powder possessed an average particle size of 34 microns.

The approximate size of the secondary boride phases in the microstructure can be seen to be approximately the same as the average particle size of the Co and CoO starting powders as shown comparatively in figure 5.1, although some diffusion appears to have taken place with a 'halo' effect of broken off pieces of the agglomerate moving into the bulk of the ceramic. The XRD data indicates that the Co and CoO give way to cobalt borides which clearly indicates that chemical reactions and diffusion have occurred at the sintering temperature of 1500 °C, but the size of the additive phases means that much more time would be required to diffuse the boride agglomerate into the bulk ceramic material, which is undesirable as more time usually implies grain growth which can reduce strength. It can thus be deduced that a poor starting powder distribution results in a poor quality sintered compact. It can be seen from figures 4.12 and 4.13 (page 101) the boride secondary phase is able to mix with the B₆O, but that it would take too much time for this process to occur with large additive particle sizes. Kosolapova⁵⁰ reports that CoB possesses a thermal expansion coefficient of $7.24 \times 10^{-6} / ^\circ\text{C}^{-1}$ compared to that of B₆O with $5.5 \times 10^{-6} / ^\circ\text{C}^{-1}$ which helps to explain the cracking of the cobalt boride agglomerates as visible in figures 4.8, 4.12 and 4.13 (pages 97 and 101). The cobalt boride agglomerate (composed primarily of CoB but with some other cobalt borides detected by XRD), possessing a higher thermal expansion coefficient, expands and contracts at a higher rate than the boron suboxide during increasing and decreasing temperatures respectively. The result of the mismatch in expansion rate implies that residual stresses can build up between the bulk and additive phases, possibly resulting in cracking, especially during heating or cooling cycles. The possibility of cracking of the secondary phase during polishing cannot be ignored however, but thermal expansion coefficient mismatch is a significant observation. It can be seen from figure 5.1 that the CoB phase becomes molten at 1460 °C (ambient conditions), implying that the primary detected phase (CoB) by XRD was either liquid during the 1500 °C ultrahigh pressure run or close to the solid-liquid transition temperature because of the ultrahigh pressure. Pressure typically increases the melting point of the materials in the sample, it is possible then, that the CoB phase was below its melting point under pressure at 1500 °C, nevertheless diffusion would be very active at such temperatures.

The other primary detected phase was Co₃B which can be seen to be liquid at these temperatures. B₂Co₃ was also detected to a lesser extent. It can thus be deduced that the addition of cobalt was appropriate in terms of using it as a liquid phase sintering aid. It can be seen from the cobalt / oxygen phase diagram in figure 5.3 that

CoO only melts at 1813°C and thus this phase could only have produced the observed borides from a diffusion controlled process i.e. a solid state reaction between B₂O₃ and cobalt oxide to form cobalt borides and B₂O₃.

These boride phases could then melt because the sintering temperature was above their melting point, but the cobalt oxide phase itself would not melt. This is not necessarily unfavourable however, as long as the additive phase possesses a sufficiently small particle size to allow for adequate interaction (and homogeneous diffusion) with the ceramic bulk in order to optimize properties.

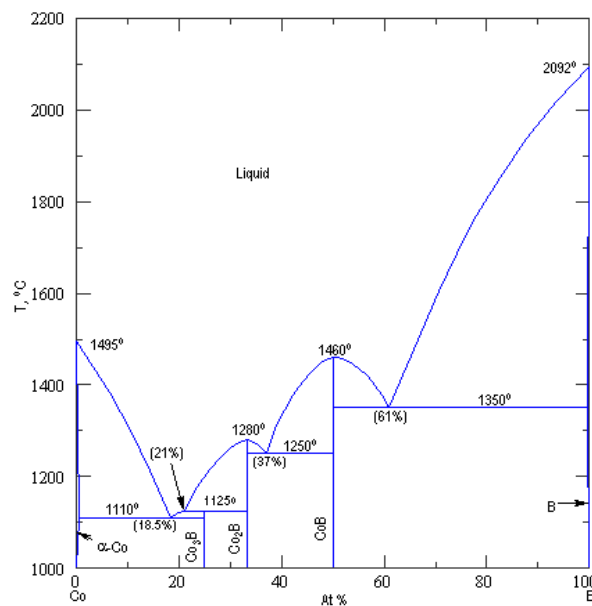


Figure 5.2: The cobalt-boron phase diagram⁴⁹ showing that the CoB phase is molten above 1460°C at 50at. % of cobalt and boron (at ambient pressure).

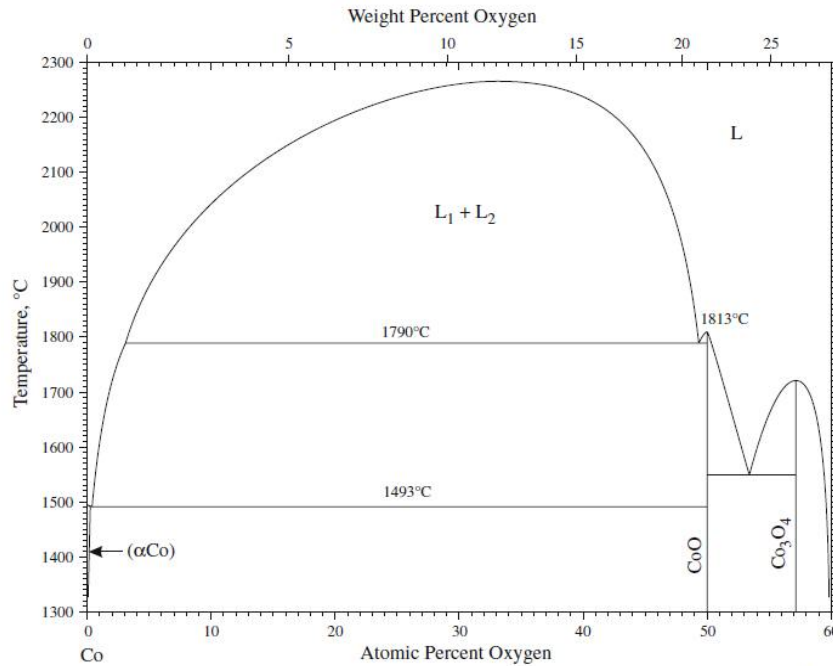


Figure 5.3: Cobalt-oxygen phase diagram up to 60at. % oxygen⁵¹.

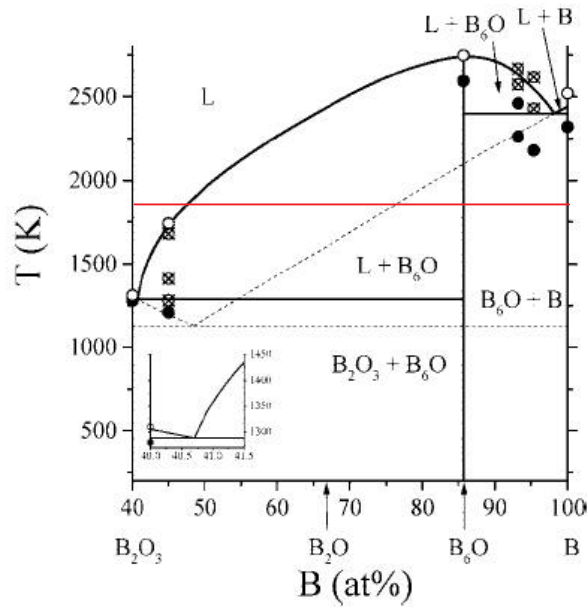


Figure 5.4: Phase diagram of the B-B₂O₃ system at 5 GPa. The black circles correspond to the solid state of the system, the crossed circles correspond to the coexistence of a liquid phase with a solid, and the open circles correspond to the completely molten samples. Solid lines show the equilibrium phase diagram, while dashed lines represent the metastable diagram⁵². The red line corresponds to $\approx 1500^\circ\text{C}$.

Solozhenko et al⁵² have published a phase diagram of the B-B₂O₃ system at 5GPa as shown in figure 5.3. Although the ultrahigh pressure sintering was performed at 7GPa for the samples produced during this project, the 5GPa phase diagram can still give valuable insight into what phases to expect at pressures close to those used on the UHP B₆O compacts. Figure 5.3 shows the sintering temperature used in this work i.e. 1500 °C (1773K) as indicated by the horizontal red line. At 1500 °C the phase diagram shows that some liquid phase B₂O₃ should be formed at this pressure at equilibrium. Under ambient conditions B₂O₃ melts at approximately 450 °C whereas at 5GPa the liquid phase can be seen to exist only at much higher temperatures. Insufficient diffusion time and time for accommodation of the grains took place to form a fully sintered compact; instead, grains were forced together under ultrahigh pressure as discussed above.

5.3 Static Interaction diffusion couples

5.3.1 The 700 °C couple demonstrated minimal interaction

As described in section 4.3.3, the 700 °C diffusion couple showed very little interaction after 1 hour at temperature under an argon atmosphere and 10MPa pressure. The couple separated without any observed pullout, unlike the higher temperature couples, and this is because the temperature was too low to cause significant interaction other than the adherence of the CGI material around porous regions of the B₆O. XRD did not detect iron boride phases but rather detected carbon (possibly from the bakelite resin) and iron oxides on the B₆O side of the interface and some silica on the CGI side in addition to iron (of course). The indication from this is that insufficient time at temperature was allowed for equilibrium phases to result. The Fe-O-B ternary phase diagram generated during the course of this project (using Factsage) shows that FeB would be the only boride phase expected to exist at equilibrium with B₆O (which could take a very long time to reach) and that Fe₂B will form in equilibrium with FeB and B₂O₃ at higher iron mole fractions i.e. closer to the iron rich side of the interface or reaction couple. At a mole fraction of 50% iron, B₆O will cease to exist at equilibrium and will give way to a combination of iron borides and B₂O₃. Of course, the time taken to reach such equilibrium is clearly far in excess of an hour because the interaction couple at 700 °C did not reveal any boride phases to be present and the B₆O remained intact. What is useful from this phase diagram however is that B₂O₃ (liquid) formation is expected to be present in this system and is likely to be easily removed from the tool surface as it is formed during machining.

Furthermore iron borides (and B_2O_3) result from the reaction of B_6O with Fe, which indicates that chemical wear is possible at 700 °C.

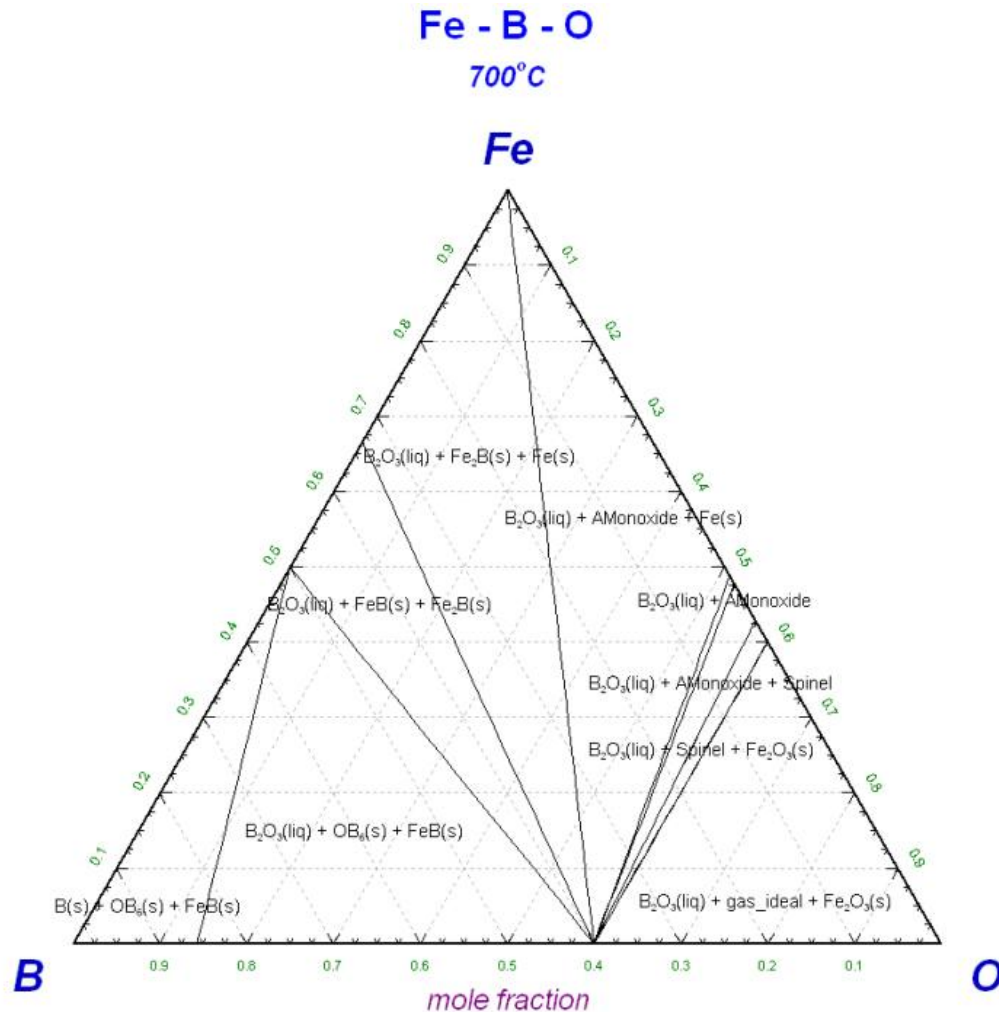


Figure 5.5: Fe-O-B ternary phase diagram generated for a temperature of 700 °C.

The line scan plots of either side of the diffusion couple at 700 °C shows limited interaction to have occurred as a result of the heat treatment. The most notable feature on the B_6O side of the couple is the carbon spike at the interface, but this is clearly the result of the line scan straying slightly into the bakelite mounting resin. The CGI side also shows a similar carbon spike for the same reason and no boron present at all. It can be deduced that the interaction between the tool material (CGI) and work piece material (B_6O) would be minimal at this temperature.

5.3.2 Interaction was observed at 900 °C

Interaction at 900 °C was clearly evident by the separated surfaces of the diffusion couple. Pullout likely occurred because of good wetting experienced between B₆O and Fe as temperature increases. Evidence of this has been found by Kharlamov et al⁵² who found the wetting angles between B₆O (B₁₃O₂) and several metals (including iron shown in table 5-1) at different temperatures. Iron can be seen to possess a low (acute) wetting angle at 1200 °C and a very low angle at 1300 °C indicating that wetting angle improves with increasing temperature i.e. the materials wet each other better at higher temperatures. It is thus possible, that wetting occurred at 900 °C which led to pullout of the B₆O and adherence to the CGI upon cooling of the couple.

Table 5-1: Wetting of hot-pressed boron suboxide samples⁵³

<i>T</i> , °C	<i>θ</i> , deg
Iron	
1200	50
1250	30
1300	18

The piece of adherent B₆O also shows reaction products on the outline of the fractured piece indicating that wetting indeed does occur at these temperatures. The most informative results were obtained from the XRD scans of the separated couple, showing Fe₂B as the dominant phase on the iron side of the couple and as the second most dominant phase on the B₆O side, after B₆O itself. SiO₂ was again observed on both sides of the couple indicating that it is a reaction and diffusion product and can be expected to be detected during machining operations.

Since Fe₂B was detected as the most dominant iron boride phase even on the B₆O side of the diffusion couple, the expected layering of iron borides (as shown in figure 5.6) appears not to have taken place. Since the different layers were not clearly evident, but rather Fe₂B was dominant, it follows that Fe diffusion in Fe₂B is more rapid than boron diffusion in FeB.

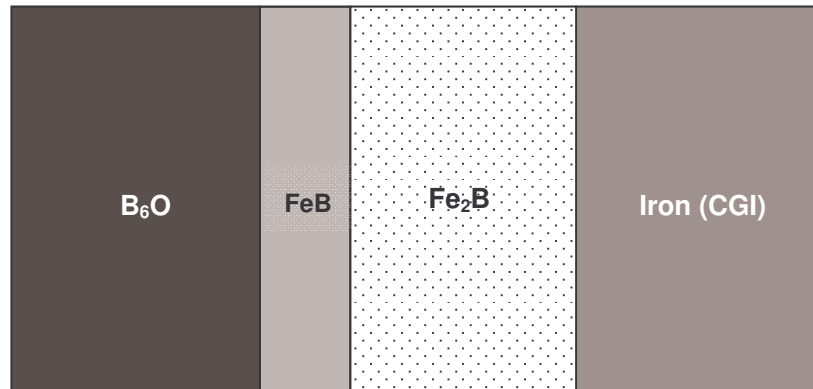


Figure 5.6: Diagram showing expected FeB, Fe₂B layering, the FeB (boron rich) would be expected to form on the B₆O side of the diffusion couple, with Fe₂B on the iron rich side primarily.

The line scan data of the CGI side of the diffusion couple showed no remarkable indications of changes in terms of composition until one moves very close to the interface, in fact, the only true evidence of an interaction layer is the one that can be seen on the micrograph corresponding to the line scan that is 10-20 microns thick. The presence of this layer indicates that the CGI materials have begun to react at and near the interface at this temperature, but not very significantly as yet. There is a slight increase in carbon and oxygen counts as the scan moves through the near-interfacial layer, but it is so close to the interface that it is difficult to attribute this to carbon and oxygen diffusion exclusively, it could be the result of proximity to the bakelite resin (e.g. polishing could have promoted some material 'smudging'). There is however, a substantial silicon and oxygen spike within 10 microns from the interface, demonstrating that SiO₂ is forming close to the interface on the CGI side.

The line scans appear to indicate a very low level of interaction between B₆O and CGI at this temperature which implies that B₆O could be relatively chemically resistant against CGI when machining at this temperature.

The binary phase diagram and solvus curves (figures 5.7 and 5.8) show that boron is barely soluble in iron. Regions of FeB and Fe₂B can be seen to exist stably at equilibrium. It is thus clear that the line scans would not reveal significant boron present in the iron bulk due to its poor solubility in iron. Iron boride phases would be expected to form at an interface as described above, with Fe₂B being the more abundant phase present in iron rich environments.

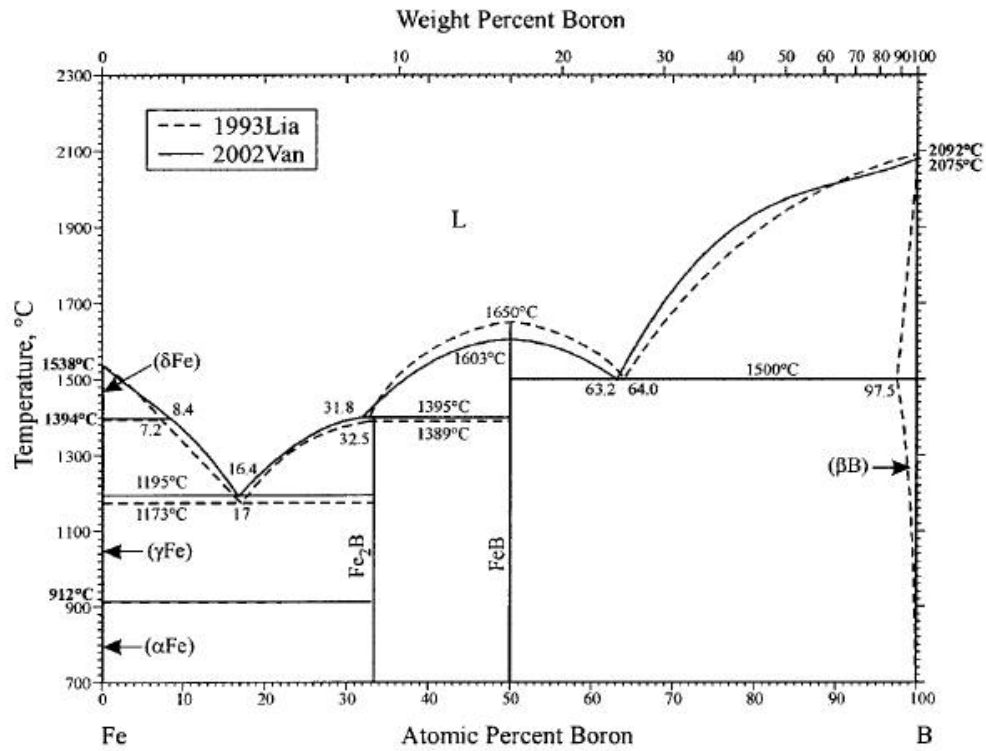


Figure 5.7: Fe-B phase diagram⁵⁴

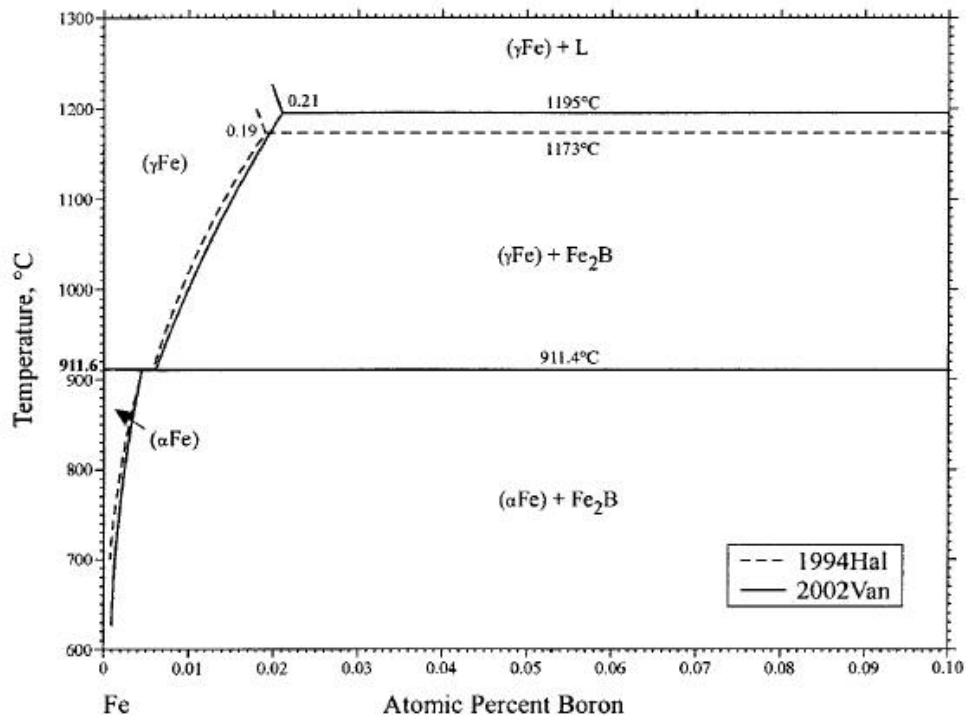


Figure 5.8: γ Fe and α Fe solvus curves⁵⁴

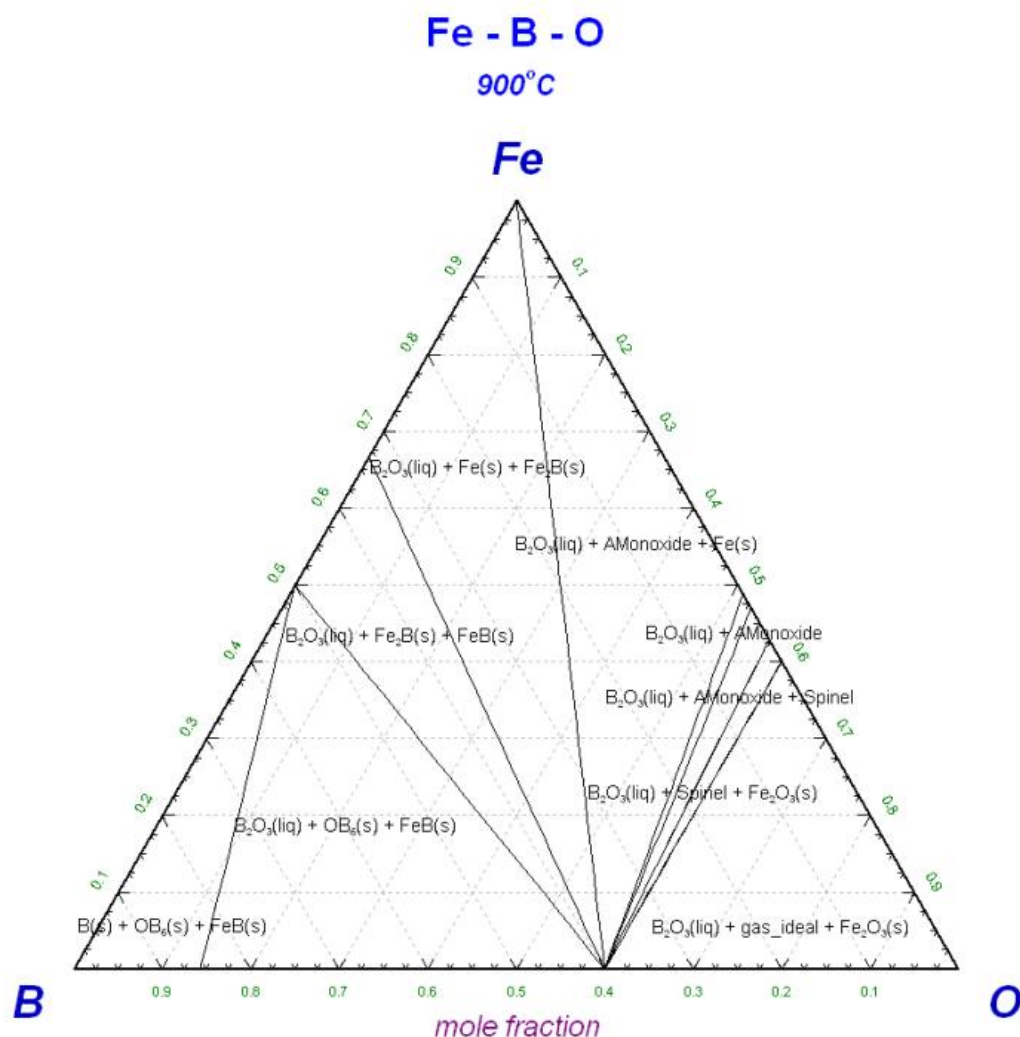


Figure 5.9: Fe-O-B ternary phase diagram generated for a temperature of 900°C.

The ternary phase diagram between Fe, B and O in figure 5.9 can be seen to be very similar to that generated for 700 °C with insignificant differences between them in terms of the composition regions in which B_6O survives. Again, FeB and Fe_2B are expected phases resulting from exposure of B_6O to iron at 900 °C for sufficient time. The expected phase (Fe_2B) was detected by XRD especially towards the iron rich side of the couple, which is indicative of a good correlation between the experimental results and the predictions made by the phase diagrams. FeB was again not detected at anywhere near the abundance of Fe_2B across the interface, indicating as mentioned above, that again Fe diffusion in Fe_2B is rapid compared to boron diffusion in FeB, hence the abundance of Fe_2B detected by XRD.

5.3.3 Substantial interaction took place at 1100°C

Stronger interaction was observed between the two halves of the diffusion couple at 1100°C as indicated by the optical microscopy results as well as the SEM micrographs that were taken. Pullout of B₆O was seen to increase in that significantly more B₆O material pulled out from the ceramic pill and adhered to the CGI pill during cooling. The contact surfaces appeared virtually indistinguishable from one another (except for pullout effects) indicating interaction had taken place. SEM micrographs and corresponding EDS scanned regions of the B₆O side of the couple showed that iron and boron were present in all scanned regions, indicative of a great deal of diffusion and interaction taking place at this temperature. Significant amounts of carbon were detected but this is not surprising giving the composition of CGI. However, the abundance near the interface of carbon indicates that it is an active diffusing species at 1100°C and could react with other available elements to form various reaction products. Carbon, because it is soft, could also have been deposited across the surface of the sample during polishing however, and this effect cannot be ignored. Nevertheless, carbon is known to diffuse in ferrous metals at these temperatures. Carbon rich areas on the CGI surface were seen to survive the heat treatment which implies that graphite flakes may act as a significant abrasive during machining operations up to temperatures as high as 1100°C because of their large size not allowing for quick enough reactions to remove all the carbon from its graphite form.

As mentioned above, the wetting angle of iron and B₆O has been demonstrated to decrease for increasing temperature and this can be observed when viewing the micrographs of the adherent B₆O material on CGI. There is a distinct interfacial region where iron and boron products appear to have interacted (figure 4.34 page 127) and EDS scans of such areas demonstrate predominantly iron with significant amounts of boron and some carbon, probably the detected Fe₂B phase as determined by XRD of the surfaces. The clearly dominant phase on both sides of the couple investigated by XRD was Fe₂B with SiO₂, B₆O, FeB and Fe₂O₃ also detected on the B₆O side and C, Fe, B₄C and FeB detected on the CGI side. The presence of Fe₂B as the dominant phase is not surprising as it is a predicted thermodynamically stable iron-boron phase in iron rich environments as indicated by the Fe-O-B ternary phase diagram shown in figure 5.10.

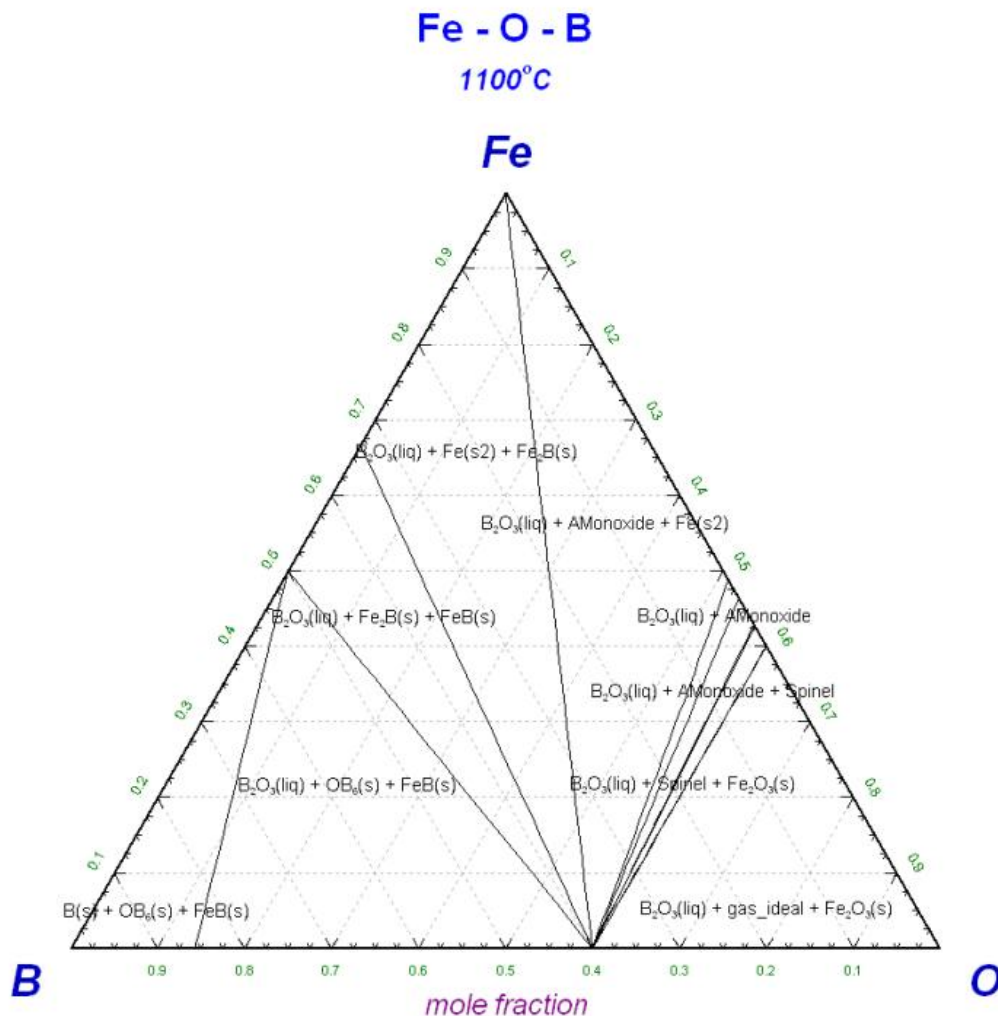


Figure 5.10: Fe-O-B ternary phase diagram generated for a temperature of 1100°C.

Again the phase diagram shows that B_6O is expected to survive at equilibrium with iron for mole fractions of less than 50% Fe, after which, the B_6O gives way to iron borides and B_2O_3 and iron oxide in oxygen rich environments.

Again the graphite flakes were seen to survive the heat treatment at 1100°C which again indicates that they are likely to perform a significant role in abrasive wear when machining this material. The most significant discovery from this work was the formation of the SiO_2 layers adjacent to the interface on the CGI side of the couple. The dominant SiO_2 layer can be seen approximately 100µm away from the interface (into the CGI side) with smaller collections of SiO_2 closer to the B_6O half (figure 4.35 page 129). There appear to be protrusions of CGI products into the B_6O when higher

magnification SEM images were taken (Figure 4.38 page 131) and the EDS scans of these regions show that iron is not present approximately 5 microns into the B_6O from the nearest iron protuberance. This fact indicates that iron cannot easily diffuse into the B_6O lattice and thus iron diffusion into B_6O can be concluded to be negligible during machining operations. Figure 4.38 (page 131) also shows that silicon is a significant constituent across the interface of the materials and thus can be expected to play a role in terms of chemical interactions while machining at or near 1100°C.

As mentioned in the results section, the line scan data across the interface displays a clear silicon spike 20 microns away from the interface (on the CGI side of the couple). Marked changes in microstructure can be seen adjacent to the interface on the CGI side of the couple which can be used to identify some of the diffusion processes taking place.

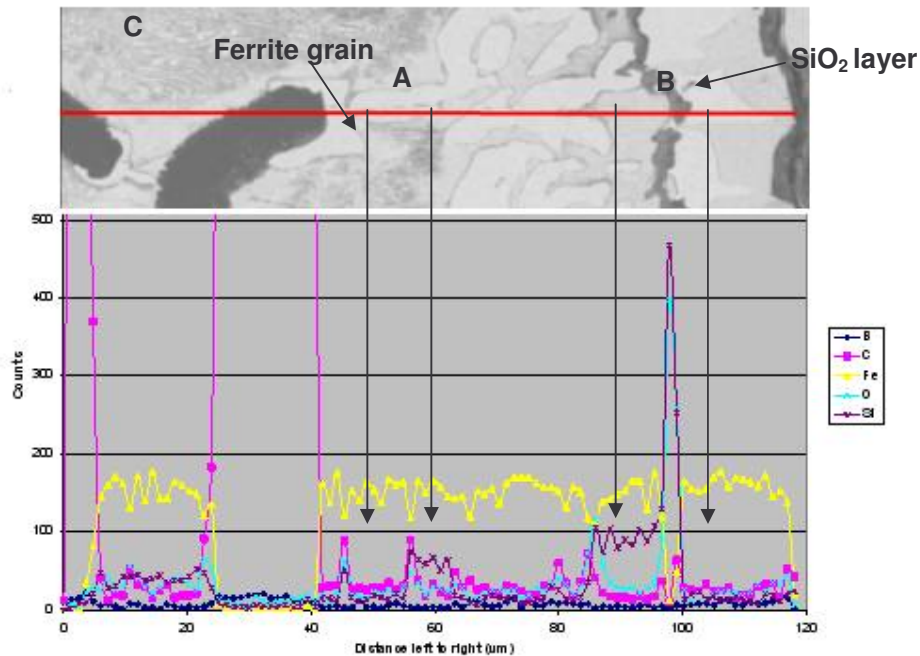


Figure 5.11: Line scan of the 1100°C diffusion couple on the CGI side showing regions and features of interest. The B_6O half of the couple was present on the right hand side of this image.

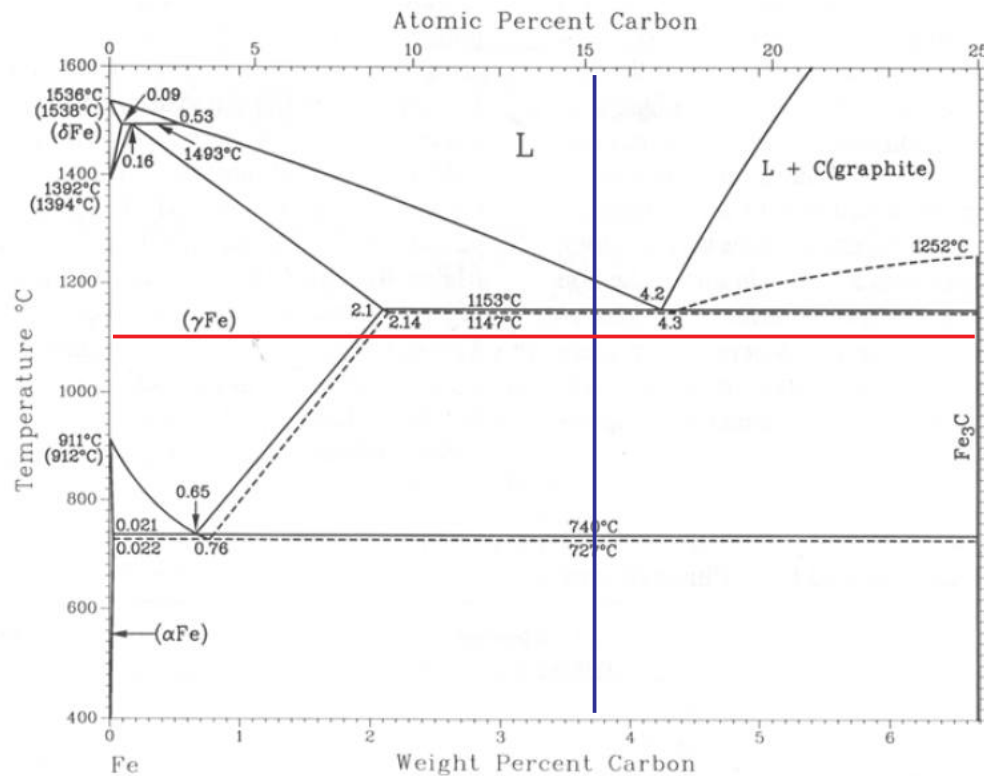


Figure 5.12: Binary phase diagram⁵⁵ of the C-Fe system showing the composition of the CGI used in this project (vertical line) and the temperature of 1100°C as the horizontal line indicated. The intersection of the two lines indicates the point corresponding to the temperature the composition was held at for one hour.

Figure 5.11 shows a correspondence between the CGI microstructural features and the results of the line scan. It can be seen from figure 5.12, which shows the C-Fe binary phase diagram, that the intersection of the indicated lines corresponds to the temperature that the composition was held at during the experiment. The point exists in the austenitic and Fe₃C region. Holding at this temperature would thus result in these two phases in the microstructure. Upon cooling, the austenite can be expected to form ferrite and iron carbide as indicated below approximately 727°C as shown by the zero phase fraction line at that temperature. It can thus be expected theoretically that the microstructure would contain regions of ferrite and iron carbide.

Region C (figure 5.11) is a pearlite rich region and can be identified by the lamellar structures of ferrite and iron carbide. Ferrite grains (light grey) have formed adjacent to the graphite flakes in the micrograph. These areas of ferrite show higher concentrations (counts) of silicon than the average background silicon content,

silicon is a ferrite forming element i.e. it assists in the formation of ferritic regions. The ferrite grains in question also reject carbides into the grain boundaries as can be seen by the sudden spike in carbon content indicated by the arrows adjacent to regions A and B. Darker ferritic grains appear to contain increased amounts of silicon as can be seen with the scan corresponding to the grain labelled B. There is a clear separation (grain boundary containing carbides) between the silicon rich and carbon rich grains, as expected due to silicon being a ferrite forming element. Since ferrite has a limit as to the amount of carbon that can exist in solid solution, silicon rich grains reject substantial amounts of carbon into the grain boundaries upon cooling. This is why regions rich in silicon show a lower carbon content simultaneously as indicated in the line scan. It can be argued that the silicon diffusion towards the interface through the CGI bulk leads to regions richer in silicon than others, and upon cooling, these regions preferentially form ferrite which rejects excess carbon into the grain boundaries (explaining the carbon spike observed as indicated by the arrows in figure 5.11) Regions with lower silicon content proceed through the formation of ferrite and iron carbide from austenite upon cooling and can be observed as pearlitic regions. The interfacial region seen in the 900°C and 1100°C can thus be largely attributed to the diffusion of silicon towards the interface of B₆O and CGI resulting in a higher than usual silicon content in the material towards the interface. Silicon, being a ferrite forming element, assists in formation of ferrite grains which are evident adjacent to the interface and is clearly visible in figures 4.36 and 4.40 on pages 130 and 133 respectively.

Silicon diffusion towards and build up at the interface of the CGI/B₆O couple is clear when comparing the background silicon content of starting CGI material taken by EDS (figure 4.23 page 111) with figure 4.38 D (page 131). The silicon count is less than 1 in the starting CGI material whereas it increases to approximately 2 kilocounts at the interface of the 1100 °C diffusion couple.

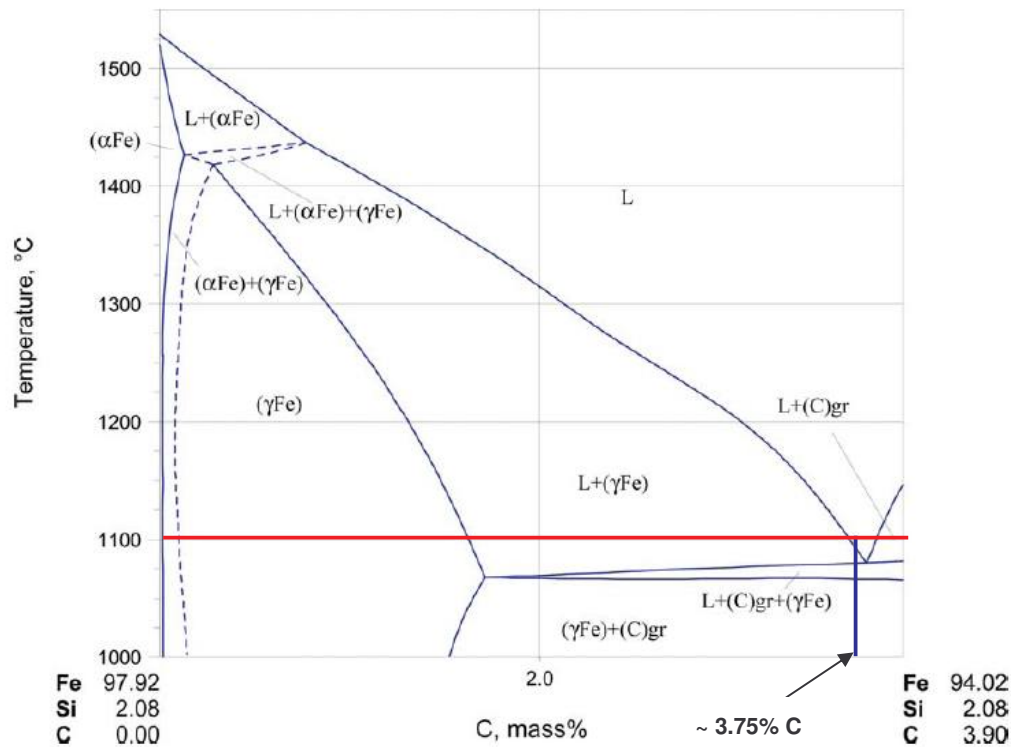


Figure 5.13: C-Fe-Si phase diagram: stable vertical section at 2.08 mass percent silicon⁵⁶.

Figure 5.13 shows the C-Fe-Si stable vertical section phase diagram. This is the closest ternary composition of C-Fe-Si that could be found from literature that closely matches the composition of these elements in the CGI used in this project. The only difference is 0.11 mass percent Si, i.e. this diagram represents 2.08 mass % silicon, while the CGI used in this work possesses approximately 2.11 mass % silicon. Nevertheless, this diagram gives a close approximation of what to expect at 1100 °C for this approximate composition. Cooling from the temperature (1100 °C) and composition (3.75 mass percent C corresponding to that of the CGI) indicated reveals that the austenitic iron phase will result, along with graphite. The austenite can be expected to transform into ferrite and iron carbide at the low cooling rate used (20 °C per minute), which corresponds with the micrographs and line scans discussed above. It would be expected that the amount of formed ferrite would be more than in a silicon deficient environment due to silicon being a ferrite stabilizer.

The boron and oxygen counts on the B₆O side of the line scan fluctuate very significantly close to the interface. The fluctuations could be an indicator of B₂O₃ formation between the grains closer to the interface, but the lack of an appropriate etchant for B₆O makes it difficult to appreciate what is happening in this region. The main point of interest is that the B₆O was seen to survive the treatment, with minimal

carbon content detected in the bulk, indicating that diffusion into B_6O for the elements from CGI is difficult which bodes well for machining, because any chemical reactions taking place would probably occur as the result of B_2O_3 formation at the interface first, followed by reaction of B_2O_3 with other elements, affirming that B_2O_3 formation is the rate determining step in terms of chemical interactions.

5.3.4 The 1300 °C couple can only reveal limited useful information

Because the 1300 °C couple melted and fused together into a large mass, it is difficult to obtain solid state diffusion data from the results. The only results that can be gleaned from the experiment is whether or not B_6O survives in contact with molten CGI for prolonged periods and what chemical products result from the interaction. The B_6O was seen to survive the experiment after an hour at temperature, which is a good indicator that B_6O is not rapidly consumed by the workpiece material even at high temperatures (higher than expected machining temperatures which typically do not exceed 1100 °C). The thermodynamic predictions of equilibrium phases as seen in the phase diagram in figure 5.14 are similar to those obtained by the predictions of lower temperature interactions, except that at higher oxygen concentrations, new oxide and spinel phases become possible which was not predicted for lower temperatures. The survivability of B_6O is again predicted in a similar way, and at equilibrium, B_6O would cease to exist at high iron concentrations. The 1300 °C couple indicates however, that even after an hour at this temperature, B_6O remains intact, showing that the equilibrium predicted in the ternary phase diagram is far from being reached and would require far more than one hour at temperature to be reached. The importance of this is that it can be deduced that the rate of B_6O degradation is low and thus it is likely to survive machining, at least chemically, for appreciable periods of time.

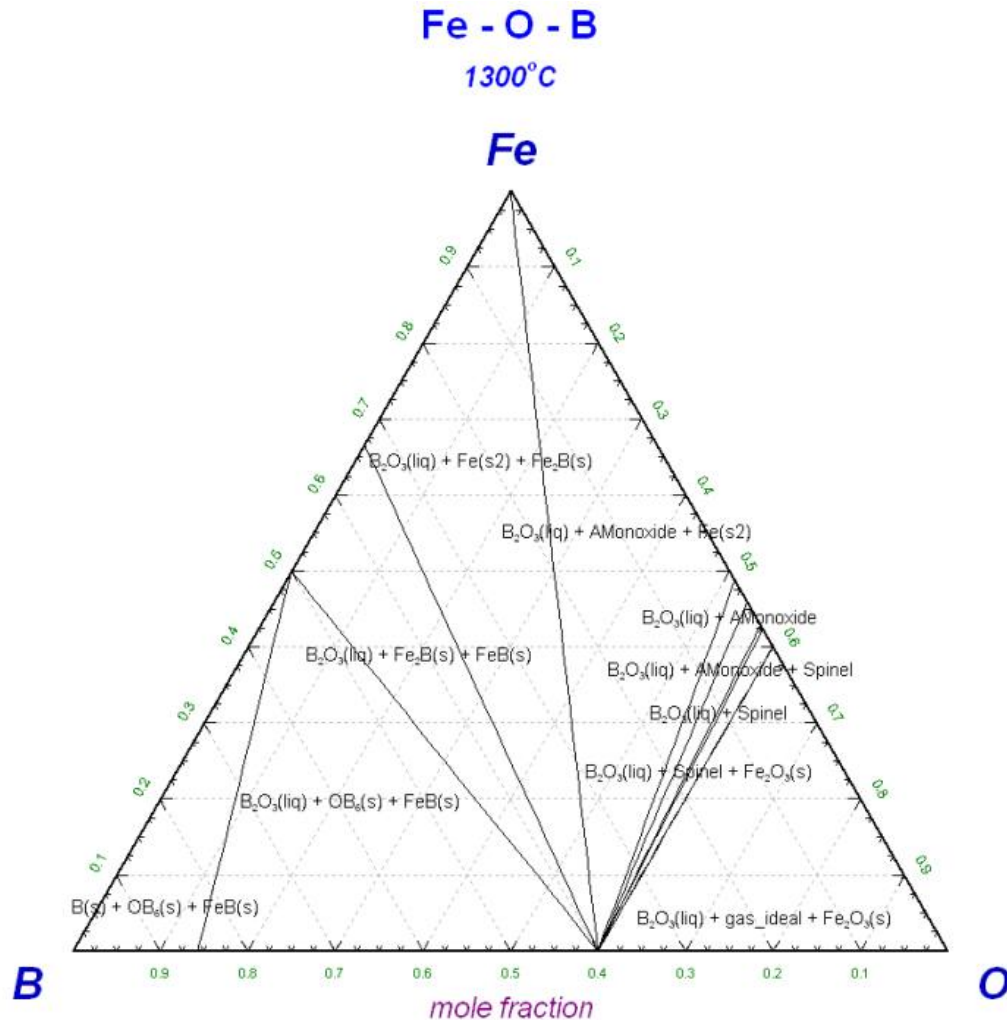


Figure 5.14: Fe-O-B ternary phase diagram predicted for 1300°C.

Figures 4.42 and 4.44 on pages 136 and 138 respectively show that the ferritic iron grains can again be observed as the result of silicon content as with the 1100°C couple, but the line scan indicates that some boron was able to enter the iron. Due to melting however, it is likely that the boron was introduced as iron borides or borosilicates from reactions of the molten iron and silicon with B_2O_3 and which then became trapped in the solidifying iron matrix. Silicon rich regions were detected on the CGI side of the diffusion couple and more importantly, on the B_6O side, which did not occur in the 1100°C couple. Silicon does possess an affinity for oxygen as can be appreciated from the existence and abundance of silica in the environment, thus the silicon likely begins to react with oxides at the interface.

The XRD of the separated couple has to be scrutinized and questioned because it is possible that the couple separated along a crack on the B_6O side of the interface and

that the XRD traces of each half may not be a true representation of the 'B₆O' and 'CGI' sides of the couple. What can be appreciated is what phases exist in proximity to the interface and the XRD data shows these. B₆O, Fe₂B and SiO₂ were detected, showing that the same phases as the 1100 °C couple produced occur in the 1300 °C couple. The most important information that can be used from this data is that B₆O is confirmed to survive and that Fe₂B is the next most abundant phase detected, and is expected in iron rich environments as shown by the phase diagram.

5.4 Oxidation resistance

Both the pure B₆O and B₆O/Y₂O₃/Al₂O₃ samples showed consistent mass losses after each heat treatment. Figure 4.49 (page 144) shows the mass loss per unit surface area for the samples as a function of time. The increasing error bars associated with longer holding times occurred because sample surfaces degraded (became roughened, brittle and crystalline) and this worsened after each heat treatment. The surface layer also became brittle, making the sample difficult to remove from the sample holder without loss of a small amount of the formed crystallites, thus exaggerating the error. Figure 2.27 (page 60) of the literature review indicates how previous TGA/DTA work has been performed on B₆O, and this shows a marginal decline in mass of the B₆O sample when cooling from 1000 °C. The effect seen in the figure however, appears less profound than that observed in the results of this project. In order to explain the observations, factors other than the reaction of B₆O with atmospheric oxygen had to be considered. At the time of the experiment (January 2009) the atmospheric conditions in Johannesburg were particularly humid. On the days in question, the relative humidity was recorded at 70 to 80% due to heavy rains at the time. It was thus considered that atmospheric moisture could be responsible not only for the mass loss, but also, the crystalline features observed on the sample surfaces. In order to obtain useful predictions of the order of magnitude of the mass loss possible as the result of atmospheric moisture, steam or humidity tables were required in order to approximate the amount of water present in the atmosphere at the time. A suitable approximation was obtained for 80% relative humidity at ambient conditions (20 °C) from a humidity table⁵⁷ and a psychrometric chart⁵⁸. The table and chart are shown in appendix E. The mass of water vapour in air at 80% relative humidity is given as 13.8 g/m³ (approximately 14g/m³) Using this information, the number of moles present per unit volume of air can be approximated as follows:

Assuming ideal gas behaviour, 1 mole of air possesses a volume of 22.4 dm³. Thus one cubic metre of comprises 44.6 moles of air. In the correct oxygen / nitrogen

volumetric ratio present in air there are thus 35.2 moles of N₂ and 9.4 moles of O₂ to be present per m³ of air. From the humidity table for 20 °C and 80% humidity, approximately 14g/m³ of water vapour is assumed to be present which equates to approximately 0.77 moles of water vapour per cubic metre of air (7.7x10⁻⁴ mol/dm³). Finally, ten moles of B₂O₃ are assumed to be present in the system, since B₂O₃ is the first decomposition product of B₆O in air when heating.

Inputting the appropriate amounts of B₂O₃, N₂, O₂ and H₂O and using Factsage, the partial pressure curves of the product gases as a function of temperature can be plotted. The partial pressure curve is shown in figure 5.15 and clearly demonstrates that the partial pressure of HBO₂ becomes high near 1000 °C but that (HBO₂)₃ and H₃BO₃ are higher at lower temperatures. The dotted lines on the graph indicate that B₂O₃ and BO₂ partial pressures in the absence of water vapour are the same as when water vapour is present. The addition of water vapour into the system has a significant effect as indicated by the new gaseous phase partial pressures shown in figure 5.15 (shown by the solid lines). Since the partial pressure of HBO₂ becomes high at the experimental temperature of 1000 °C, it is expected to form on the surface of the B₆O and to evaporate. Evaporation is also significant at lower temperatures as can be seen from figure 5.15.

The mass loss experienced can thus be explained by the increased partial pressure of HBO₂, and (HBO₂)₃ gas (and H₃BO₃ to a lesser extent) which evaporates from the sample surface, hence reducing the mass of the sample. Not all of the HBO₂ evaporates, and the remaining material crystallizes as H₃BO₃ and can be seen in the optical micrographs after each heat treatment shown in section 4.4.3.

The following chemical reactions occurred:



In other words, HBO₂ is stable as a solid phase up to 218 °C. B₂O₃ is a liquid above 450 °C.

Predicted partial pressure curves when heating boron suboxide in air



FactSage™

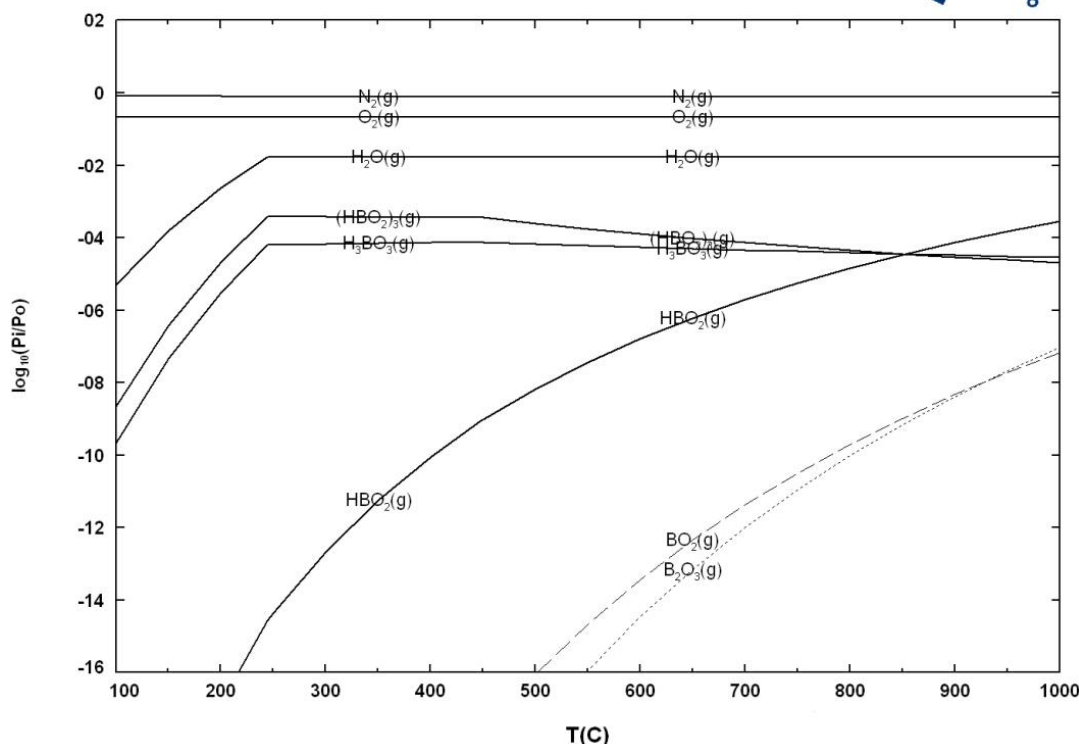


Figure 5.15: Partial pressure vs. temperature curves of the gaseous phases predicted to exist at 80% relative humidity. The mole ratios of the molecules are indicated above the diagram and the amount of water present corresponds with 80% relative humidity as given by the humidity table.

XRD was performed before the experiment (on each sample) and revealed the expected B_6O pattern, and again after the full 50 hour heat treatment time. The pure B_6O sample post heat treatment XRD (figure 4.66 page 159) shows $\text{B}(\text{OH})_3$ as the phase detected on the surface other than B_6O itself. The hydrogen present in on the sample surface could only have come from atmospheric moisture in the lab at the time of the experiment. The yttria-alumina XRD trace (figure 4.67 page 160) shows many additional phases to have formed as the result of the heat treatment. Most notably HBO_2 , $\text{B}(\text{OH})_3$ – from the atmospheric moisture again, and other boride and oxide phases of aluminium and yttrium. It is likely that the differently shaped crystal formations seen of these samples resulted from the reactions involving the additive phases (i.e. alumina and yttria) with atmospheric moisture and boron and oxygen e.g. $\text{Y}_2\text{B}_2\text{O}_6$ and HBO_2 etc. It is possible that the yttria-alumina samples showed a lower mass loss than the pure B_6O samples due to borate formation and thus less availability of boron to form boric acids i.e. the boron was ‘tied up’ as borates rather than forming boric acids.

SEM was performed on the crystals on the surfaces, however hydrogen is not detectable by EDS, thus only a partial idea of composition of the crystals can be identified this way. Predominantly O, Al, Y and small amounts of B and C (contaminant) were seen to comprise the rosette shaped crystals on the $B_6O/Y_2O_3/Al_2O_3$ samples. The presence of some silicon is believed to be a contaminant e.g. dust from the experiment or handling and moving of the samples and is not likely representative of the composition. It would appear that the rosette crystals are composed of $Y_2B_2O_6$, YBO_3 or $AlYO_3$ because the EDS detected primarily these constituent atoms and these are also the phases detected by XRD corresponding to a similar composition of elements as those detected in EDS. Since the surface was almost covered in rosette crystals, it can be argued that the strongest XRD pattern corresponds to the most abundant crystal type observed on the surface. In the case of the $B_6O/Y_2O_3/Al_2O_3$ samples, this was clearly the rosette shaped crystals, which are thus most likely $Y_2B_2O_6$ crystals because it was the strongest peak detected by XRD.

Since XRD of the pure B_6O surfaces yielded only one crystalline pattern other than B_6O , it can be concluded that the crystals observed in that instance are $B(OH)_3$.

5.5 Machining and wear studies

The micrographs of the blanks used to produce the cutting tools show indications of crystal formations, very much like those micrographed during the oxidation resistance experiments. Figure 4.71 (page 164) shows the crystals. The crystals formed as a result of laser cutting of the material. The process was performed at Element 6 Ireland, most likely in an atmosphere possessing appreciable natural humidity. The crystals did not grow as seen in the oxidation resistance experiments because the cooling rate of the laser cut blank was more rapid than the 10°C per minute cooling rate allowed for the oxidation resistance experiments, thus the fast cooling rate experienced by the laser cut blank resulted in less time for crystal growth.

Porosity and surface defects were also observed on the surfaces of the chamfered and honed cutting tools. The porosity resulted from the laser cutting of the material creating a heat affected zone where B_2O_3 and other products could have formed, which is softer and hence easily removed during the chamfering and honing process. Furthermore and most importantly, the increase in volume fraction of softer phase material close to the surface weakens the cutting tool. Comparing the DBC50 (PcBN) cutting tool's chamfer and flank with those of the B_6O tool, the effects of the heat affected zone (HAZ) can be appreciated as the B_6O tool clearly possesses an inferior tool finish as seen in figure 4.72 (page 165). The laser cutting and tool production techniques will have to be improved in future work in order to prevent destroying the

tool material and hampering tool performance. Laser cutting in a water vapour rich atmosphere would increase the amount of HBO_2 and other hydrogen borates produced which would expend the excess heat associated with the laser beam in their evaporation (and formation) accelerating the cutting operation and possibly reducing the heat affected zone.

The turning test results are summarized in the graph produced for the 50m/min cutting operation (figure 4.74 page 168) and show that B_6O tools perform comparably with the DBC50 tools, at least for the first 2000 seconds (≈ 33 minutes) of turning against compacted graphite cast iron. The only reason the experiment terminated is because of the loss of the nose radius of the cutting tool, due to the HAZ (laser cutting) causing porosity that results in the shearing off of the cutting material. The graph appears to indicate that, had the porosity not caused the tool to fail, that the cutting operation may have proceeded for a long time, comparably to DBC50, without reaching the flank wear failure criterion of a 300 micron flank wear scar.

It is also possible that the graph (of flank wear scar magnitude against cutting time) under-represents the performance of B_6O tools because the porosity effect is the result of soft secondary phases forming in the HAZ. A porous microstructure results from the polishing (or honing) of the material that pulls out these softer phases. These phases must have been present in the tool from the beginning and during the first 33 minutes of cutting before the tool failed, likely exaggerating the wear scar beyond what it would have been had the HAZ been absent. It is thus vital that the HAZ be eliminated in future work should an accurate determination of the actual performance of B_6O tools be desired.

Further evidence of the effect of the softer phases and porosity leading to tool failure can be seen in the sequence of cuts illustrated in figure 4.76 page 170. From the progression, it is clear that what starts out as relatively small pores (but still too large for good tool performance), which grow as the cutting operation proceeds.

The cutting performance of the B_6O tools was poor for the turning tests conducted at 100 m/min. Wear scars rapidly developed, so quickly in fact, that after several short cutting operations described in section 4.5.2.2, the flank wear passed the flank wear failure criterion. The failure criterion was exceeded in 426 seconds (approximately 7 minutes) which is inadequate cutting time if the material was to have a viable industrial application as a cutting tool. Several turning tests were attempted and most resulted in rapid loss of the tool nose radius, the results shown in figure 4.75 (page 169) are those of the only cutting tool tested at 100m/min that did not rapidly fracture. Because of the inability to reproduce results or even produce more than six data

values, a graph of the flank wear scar magnitude of B₆O tools at 100m/min against cutting time could not be produced. Again, the HAZ introduced by laser cutting is almost certainly to blame. The faster cutting speed would exaggerate the wear rate between tool and workpiece, hence increasing the shear stress experienced at the cutting tip resulting in either tool failure or rapid wear.

5.5.1 SEM tool investigation

5.5.1.1 100m/min wear scar forms quickly

Figure 4.82 (page 175) demonstrates the rapid development of flank wear and damage to the chamfer after only one minute of cutting time at 100m/min. The flank wear scar is around 100 microns in length and the chamfer has undergone severe abrasive wear. As predicted by the static interaction diffusion couples, silicon (probably SiO₂) displays an affinity for adhering to B₆O and is detected in the built up edge surrounding the wear scars in greater abundance than would be expected in a scan of the CGI itself, the silicon peak shown in the EDS trace is almost as abundant as the iron peak, which indicates that it builds up (and possibly diffuses) rapidly during machining. It can thus be expected in future machining of silicon containing ferrous metals with B₆O that this phenomenon will occur and will play a part in wear processes.

5.5.1.2 50 m/min wear scar minimal after 1min of cutting time

The wear scar resulting from 50 m/min for one minute is no more than 20 microns (consistent with the wear curve) and there is almost no visible damage to the chamfer. In this instance, it can be seen from the EDS scans that iron and silicon again adhere to the cutting tool, but the cutting tool fares the turning test very much better than 100m/min for the same amount of time. This is probably due to the very significant increase in energy transfer to the cutting tool at 100m/min compared to 50m/min and the corresponding increase in shear stresses. Not to mention higher operating temperatures at the cutting tip. If the surface velocity is considered linear at the point of contact between tool and workpiece, then the energy transfer between the tool and workpiece is proportional to v^2 (v = speed) from the kinetic energy relationship. Hence an increase in cutting speed by a factor of two results in an increase in kinetic energy by a factor of four. Because of the heat affected zone and imperfections in the tool properties resulting there from, a factor of four increase in kinetic energy at the cutting tip is likely to push the already weakened tool past its material limitations very quickly and cause failure. This would be worsened by the

effect of interconnecting porosity and soft phase removal at higher rates. The fact that such a substantial difference in wear has been observed between the cutting speeds of 50 and 100m/min supports this argument.

6 CONCLUSIONS

The aim of the project was the evaluation of the wear properties of boron suboxide based cutting tool materials when machining ferrous metals, specifically compacted graphite cast iron, due to the difficulties in machining this metal by other industrial cutting tool materials. A comparison of the wear properties of B_6O with the industrial competitor material (polycrystalline cubic boron nitride DBC 50) was required in order to determine the potential use of B_6O for machining applications in industry. The project undertook the task of determining wear behaviour both in terms of abrasive wear and chemical compatibility (and chemical wear) of the tool and workpiece materials. Oxidation resistance at machining temperatures was also of interest and was investigated.

In order to evaluate the wear properties of the materials, cutting tools were produced from spark plasma sintered $B_6O/Y_2O_3/Al_2O_3$ material by laser cutting 'blanks' that were then chamfered and honed into a square tool geometry. Samples of the identical material used to produce the $B_6O/Y_2O_3/Al_2O_3$ cutting tools as well as hot pressed pure B_6O materials were used for oxidation resistance experiments. Additionally, high pressure experiments with Co and CoO additives were carried out to generate materials without oxide additive phases i.e. with boride secondary phases. The resulting microstructures showed that the high pressure materials were dense, but the distribution of the additives was inhomogeneous due to insufficient mixing of the additive phase with the milled B_6O starting powder. As such, the materials were not used for wear tests. Future work should undertake to improve secondary phase dispersion of potential tool materials as well as sintering time and temperature parameters in order to optimize the material properties.

In order to understand the wear behaviour of the material, different tests were carried out:

- diffusion couples between B_6O materials and cast iron (CGI) in argon to estimate the chemical interaction at temperatures within the expected temperature range typically experienced during machining operations
- oxidation experiments to estimate the influence of oxygen (and the atmosphere) on the material
- turning tests of CGI (the workpiece material) with B_6O cutting tool materials

The diffusion couple experiments showed that at 700 °C and 900 °C the chemical interaction between B_6O and CGI is minimal.

At higher temperatures, Fe_2B and SiO_2 were observed at the interface. These phases result in some adhering of iron to the B_6O causing some local breaking out of B_6O along the interface. The result of this is B_6O fragments embedded in the iron surface. This phenomenon occurs to a lesser extent at 900 °C and a greater extent at 1100 °C.

No pronounced diffusion of iron into B_6O or boron into iron was observed even at 1100 °C. The Fe_2B layer that was formed is believed to result in passivation of the interface. Ferritic and pearlitic regions within the iron microstructure were observed close to the interface of the 1100 °C diffusion couple. Silicon diffusion from the bulk of the CGI towards the interface is believed to stabilize ferrite and result in the ferritic regions within the observed iron microstructure near the interface. Machining at 1100 °C is thus likely to result in chemical wear mechanisms playing a role in tool wear in terms of the formation of iron borides, which will easily be removed from the tool-workpiece interface (after formation or diffusion at the interface) by abrasion of the two surfaces in relative motion.

The implications of chemical wear mechanisms being present at temperatures in excess of 900 °C are significant for tool performance in that the chemical wear mechanisms need to be fully understood if tool performance is to be optimized. The rate of diffusion of the constituent elements as well the rate of formation of the product phases would be useful for understanding chemical wear of the cutting tools.

The ternary phase diagrams generated for each temperature (700, 900, 1100 and 1300 °C) all indicate that iron boride and iron oxide reaction products form along with the formation of B_2O_3 . B_2O_3 , being a liquid phase in excess of ≈ 450 °C in ambient conditions, is rapidly removed (due to abrasion) from the tool surface (by the work piece) as it is formed, resulting in a high probability that the rate of tool degradation (or the rate that the tool approaches the flank wear failure criterion) is closely linked to the rate of B_2O_3 formation and the rate of formation of iron borides on the surface of the tool. Additionally the formation of the other interaction products must also play a part in tool wear and it would be useful to investigate the role of these products in tool wear in the future. It is clear that the contact between the tool and work piece material will involve a quantity of liquid B_2O_3 . The rate of B_2O_3 formation from B_6O is

an important wear process that needs to be better understood in order to fully appreciate the wear mechanisms taking place with this material.

From the phase diagrams, it can be seen that B_6O is expected to deteriorate in equilibrium with iron borides with high mole fractions of iron. After an hour at expected machining temperatures only a thin interlayer is formed in the diffusion couple experiments, even at 1100°C . This layer comprises iron borides primarily, with some iron oxides, with SiO_2 in abundance (due to silicon being present in CGI) and a number of other products resulting from other minor cast iron additive phases.

The oxidation experiments on both pure B_6O samples and $B_6O/Y_2O_3/Al_2O_3$ samples at 1000°C did not result in a mass gain, but rather in a mass loss. The reason for this mass loss was the moisture content in the atmosphere at the time of the experiment. The formed B_2O_3 on the surface therefore evaporates as gaseous boric acid. During the isothermal heat treatment a more or less steady state is formed. With increasing oxidation time different phases start to crystallize on the sample surface.

The B_6O material with oxide additives has a similar behaviour as the additive free materials in terms of mass loss in response to heat treatment. Differences in the phases formed on the surfaces of the tested materials were clearly observed by XRD however, with the $B_6O/Y_2O_3/Al_2O_3$ material forming a number of additional product phases compared to pure B_6O . These phases result from reactions involving the oxide additives during the heat treatment, whereas only boric acid crystals were observed by XRD on the pure B_6O sample surfaces.

The mass loss effect of B_6O based materials would restrict the use of water based (or containing) coolants in machining operations involving B_6O as chemical wear would be enhanced by this chemical reaction at the expense of the tool material and tool surface quality. These processes take place in the similar way for cubic boron nitride tools.

Laser cutting of the spark plasma sintered material into blanks (precursor shapes of cutting tools) resulted in increased porosity within a heat affected zone, reducing the quality of the cutting surface and impeding good performance during turning tests. The turning tests performed during this work were adversely affected by this

phenomenon and thus cannot be reliably used to gauge the best possible performance of B_6O based cutting tools. Future work should focus on first improving the quality of produced cutting edges, optimization of laser cutting and minimization of a heat affected zone (and porosity) in order to produce good quality cutting tools.

In spite of introduced porosity, the 50m/min graph of flank wear scar magnitude against time of B_6O cutting tools performs comparably with PcBN DBC 50 (the primary competitor material). It can thus be concluded that tool performance should improve if preparation can be optimised.

The turning tests performed at 100m/min resulted in rapid loss of the tool nose radius or fracture of the cutting tool, and in the instance when the tool survived; the flank wear failure criterion was achieved very quickly. The higher the cutting speed, the more sensitive the tool becomes to inherent flaws, thus for higher cutting speeds, the material properties of the tool become increasingly important.

7 REFERENCES

- 1) Masuda, M., Sato, T., Kori, T. and Chujo, Y. 1994. 'Cutting performance and wear mechanism of alumina-based ceramic tools when machining austempered ductile iron.' *Wear*, vol. 174 pp147 – 153.
- 2) Heck, M., Ortner, H.M., Flege, S., Reuter, U. and Ensinger, W. 2008. 'Analytical investigations concerning the wear behaviour of cutting tools used for the machining of compacted graphite iron and grey cast iron.' *International Journal of Refractory Metals & Hard Materials*, vol. 26, pp 197 – 206.
- 3) Andrews, A. 2008. 'Development of boron suboxide composites with improved toughness.' PhD Thesis, University of the Witwatersrand.
- 4) Johnson, O.T. 2008. 'Improvement of the mechanical properties of boron suboxide (B_6O) based composites using other compounds as second phase.' MSc Dissertation, University of the Witwatersrand.
- 5) Shabalala, T.C. 2007. 'The preparation and characterisation of boron suboxide (B_6O) based composites.' PhD Thesis, University of the Witwatersrand.
- 6) Lundström, T. 1997. 'Structure and Bulk Modulus of High-Strength Boron Compounds.' *Journal of Solid State Chemistry*, vol. 133, pp 88 – 92.
- 7) Shabalala, T.C., McLachlan, D.S., Sigalas, I. and Herrmann, M. 2008. 'Hard and tough boron suboxide based composites.' *Ceramics International*, vol. 34 issue 7, pp 1713 – 1717.

- 8) Liu, X., Zhao, X., Hou, W. and Su, W. 1995. 'A new route for the synthesis of boron suboxide B_7O .' Journal of Alloys and Compounds, vol. 223, L7 – L9.
- 9) Yu. S., Ji, Y., Li, T., Han, M., Wang, G., Yuan, X., Li, Z. and Chen, P. 2000. 'Nanofilms with clusters of boron suboxide and their infrared absorption.' Solid State Communications, vol. 115, pp 307 – 311.
- 10) Gladkaya, I.S., Dyuzheva, T.I., Ekimov, E.A., Nikolaev, N.A. and Bendeliani, N.A. 2001. 'Crystal growth at high pressure and the problem of characterization of the interstitial phases in the B-C-O system.' Journal of Alloys and Compounds, vol. 329, pp 153 – 156.
- 11) Zhongwu Wang and Yusheng Zhao, 2005. 'In situ pressure Raman spectroscopy and mechanical stability of superhard boron suboxide.' Applied Physics Letters vol. 86, 041911 – 041913.
- 12) Lundström, T. and Andreev, Y.G. 1996. 'Superhard boron-rich borides and studies of the B-C-N system.' Materials Science and Engineering A, vol. 209, pp 16 – 22.
- 13) Kobayashi, M., Higashi, I., Brodhag, C. and Thévenot, F. 1993. 'Structure of B_6O boron-suboxide by Rietveld refinement.' Journal of Materials Science, vol. 28, pp 2129 – 2134.
- 14) Olofsson, M. and Lundström, T. 1997. 'Synthesis and structure of non-stoichiometric B_6O .' J. Alloys and Compounds, vol. 257, pp 91–95.

- 15) Hubert, H., Garvie, L.A.J., Devouard, B., Buseck, P.R., Petuskey, W.T. and McMillan, P.F. 1998. 'High-Pressure, High-Temperature Synthesis and Characterization of Boron Suboxide (B_6O).' American Chemical Society, vol. 10, pp 1530 – 1537.
- 16) Duanwei He, Zhao, Y., Daemen, L., Qian, J., Shen, T.D. and Zerda, T.W. 2002. 'Boron suboxide: As hard as cubic boron nitride.' Applied Physics Letters 81, vol. 4, pp 643 – 645.
- 17) Brookes, C.A. 'Mechanical properties of cubic boron nitride – a perspective. Institute of Phys. Conference Series., Issue 75, pp 207 – 220
- 18) Itoh, H., Maekawa, I. and Iwahara, H. 1998. 'High pressure sintering of B_6O powder and properties of the sintered compact.' J. Soc. Mat. Sci., Vol. 47, pp.1000-1005.
- 19) Zhongwu, W. and Yusheng, Z. 2005. 'In situ Raman spectroscopy and mechanical stability of superhard boron suboxide.' Appl. Phys. Letters., vol. 86, pp 1-3.
- 20) McMillan, P.F., Hubert, H., Chizmeshya, A., Petuskey, W.T., Garvie, L.A.J. and Devouard, B. 1999. 'Nucleation and growth of Icosahedral Boron Suboxide Clusters at High Pressure.' Journal of Solid State Chemistry, vol. 147, pp 281 – 290.
- 21) Veprěk, S. 1999. 'The Search for Novel Super Hard Materials.' American Vacuum Society.

- 22) Andrews, A., Herrmann, M., Shabalala, T.C. and Sigalas, I. 2008. 'Liquid phase assisted hot pressing of boron suboxide materials.' Journal of the European Ceramic Society.
- 23) Ellison-Hayashi, C., Zandi, M., Shetty, D.K., Kuo, P., Yeckley, R. and Csillag, F. 1994. 'Boron suboxide material and method for its preparation.' 5,330,937, US Patent.
- 24) Sasai, R., Fukatsu, H., Kojima, T. and Itoh, H. , 2001. 'High pressure consolidation of B₆O-diamond mixtures', Journal of Materials Science, vol. 36, pp. 5339-5343.
- 25) Kayhan, I.O. and Inal, O.T. 1999. 'Synthesis of aluminium infiltrated boron suboxide drag cutters and drill bits.' Journal of Materials Science, vol. 34, pp 4105 – 4120.
- 26) Liu, Y.R., Liu, J. J., Zhu, B.L., Zhou, Z.R., Vincent, L. and Kapsa, P. 1997. 'Wear Maps of Si₃N₄ Ceramic Cutting Tool.' Journal of Materials Engineering and Performance, vol. 6(5), October edition.
- 27) Like, Q., Xikun, L., Guanming, Q., Weimin, M., Yanbin, S. and Huadong, Y. 2007. 'Study on Toughness Mechanism of Ceramic Cutting Tools.' Journal of Rare Earths, vol. 25, pp 309, June edition.
- 28) Lim, S.C. 1996. 'Wear Maps for some Uncoated Cutting Tools.' Tribotest Journal 3, vol. 1, September edition.
- 29) Trent E.M, Wright P.K., 2000. 'Metal Cutting', 4th Edition, Butterworth.

- 30) Liew, W.Y.H., Ngoi, B.K.A. and Lu, Y.G. 2003. 'Wear characteristics of PcBN tools in the ultra –precision machining of stainless steel at low speeds.' *Wear*, vol. 254, pp 265–277.
- 31) Ghani, A.K. 2002. 'Study of tool life, surface roughness and vibration in machining nodular cast iron with ceramic tool.' *Journal of Materials Processing Technology*, vol. 127, pp 17–22.
- 32) Camuşcu, N. 2006. 'Effect of cutting speed on the performance of Al_2O_3 based ceramic cutting tools in turning nodular cast iron.' *Materials and Design*, vol. 27 pp 997 – 1006.
- 33) Mills, B. 1996. 'Recent Developments in Cutting Tool Materials.' *Journal of Materials Processing Technology*, vol. 56, pp 16 – 23.
- 34) Secomax PcBN Technical guide. 2003. Seco Tools, Sweden, pp 41.
- 35) Vleugels, J., Jacobs, P., Kruth, J.P., Vanherck, P., Du Mong, W. and Van Der Biest, O. 1995. 'Machining of steel with sialon ceramics: influence of ceramic and workpiece composition on tool wear.' *Wear*, vol.189, pp 32–34.
- 36) Vleugels, J. and Van Der Biest, O. 1999. 'Chemical wear mechanisms of innovative ceramic cutting tools in the machining of steel.' *Wear*, vol. 225-229, pp 285–294.
- 37) Giménez, S., Van der Biest, O. and Vleugels, J. 2007. 'The role of chemical wear in machining iron based materials by PCD and PcBN and super-hard tool materials.' *Diamond and Related Materials*, vol. 16, pp 435 –445.

38) Gastel, M., Konetschny, C., Reuter, U., Fasel, C., Schulz, H., Riedel, R. and Ortner, H.M. 2000. 'Investigation of the wear mechanism of cubic boron nitride tools used for the machining of compacted graphite iron and grey cast iron.' International Journal of Refractory Metals & Hard Materials, vol. 18, pp 287 – 296.

39) Katak, K. Private communication, School of Process and Materials Engineering, University of the Witwatersrand, Johannesburg

40) Dlamini, P. Private communication, School of Process and Materials Engineering, University of the Witwatersrand, Johannesburg

41) Davis, J.R. (Ed). 1996. 'ASM Speciality Handbook - Cast Irons', ASM International.

42) Pretorius, N. and Toomey, T. 2007. 'Evaluation of different cutting tool materials for the interrupted machining of compacted graphite cast iron.' Industrial Diamond Review, vol. 4.

43) Pretorius, N., Howard, T.P., Bowler, J.J. and Toomey, T. 2006. 'Evaluation of different cutting tool materials for the interrupted machining of compacted graphite cast iron.' Industrial Diamond Review, vol. 2.

44) Makarov, V.S. and Ugai, Y. 1986. 'Thermochemical study of boron suboxide B_6O '. Journal of the Less-Common Metals., Vol. 117, pp. 277-281.

{Thermodynamic data and formula used as basis for Andrews's database}

45) Tsagareishvili, G.V., Tsagareishvili, D.S., Tushishvili, M.Ch., Omiadze, I.S., Naumov, V.N. and Tagaev, A.B. 1991. 'Enthalpy and heat capacity of boron suboxide in the temperature range of 298.15-781.8K.' Inst. Metall., Vol. 231, pp 384-391.

46) Fraunhofer Institute, http://www.ifam-dd.fraunhofer.de/fhg/ifam_dd/EN/labor/sps/index.jsp, 4 February 2009.

47) Pavel, R. Marinescu, I and Pillar, J. 2005. 'Effect of tool wear on surface finish for a case of continuous and interrupted hard turning.' Journal of Materials Processing Technology, vol. 170, pp341 – 349.

48) Ofunguyiwa, E. Private communication, School of Process and Materials Engineering, University of the Witwatersrand, Johannesburg

49) Moropeng, M.D. 2008. 'Sintering of boron suboxide composite ultrahard materials at ultra high pressures.' Fourth year final project report, University of the Witwatersrand.

50) Kosolapova, T., Ja. Svoistva. 1986. 'Poluschenie I Primenenie Tugoplavkikh Soedinenii', Metallurgija, Moscow.

51) Okamoto, H. 2008. 'Co-O (cobalt-oxygen).' Journal of Phase Equilibria and Diffusion, vol. 29 No. 6, pp 548.

52) Solozhenko, V.L., Kurakevych, O., Turkevich, V. and Turkevich, D. 2008. 'Phase diagram of the B–B₂O₃ system at 5GPa: experimental and theoretical studies.' J. Phys. Chem. B. Vol. 112, pp 6683–6687.

- 53) Kharlamov, A.I. and Kirillova, N.V. 2002. 'Properties of boron suboxide B₁₃O₂.' Powder Metallurgy and Metal Ceramics, Vol. 41, No. 1-2, pp 97–106.
- 54) Okamoto, H. 2004. 'B-Fe (Boron Iron)', Journal of Phase Equilibria and Diffusion, Vol. 25 No. 3, pp 297.
- 55) Okamoto, H. 1992. 'The C-Fe (Carbon-Iron) System.' Journal of Phase Equilibria, Vol. 13 No. 5, pp 543–565.
- 56) Lebrun, N. 2008. 'Iron Systems, Part 2', Landolt-Börnstein - Group IV Physical Chemistry, Vol. 11D2, Carbon–Iron–Silicon.
- 57) Climate / Humidity Table, TIS, German Transport Information Services, http://www.tis-gdv.de/tis_e/misc/klima.htm, March 2009.
- 58) Perry, R. Green, D. 1999. 'Perry's Chemical Engineers' Handbook', Seventh Edition, McGraw-Hill, pp 12-28.

APPENDIX

Appendix A

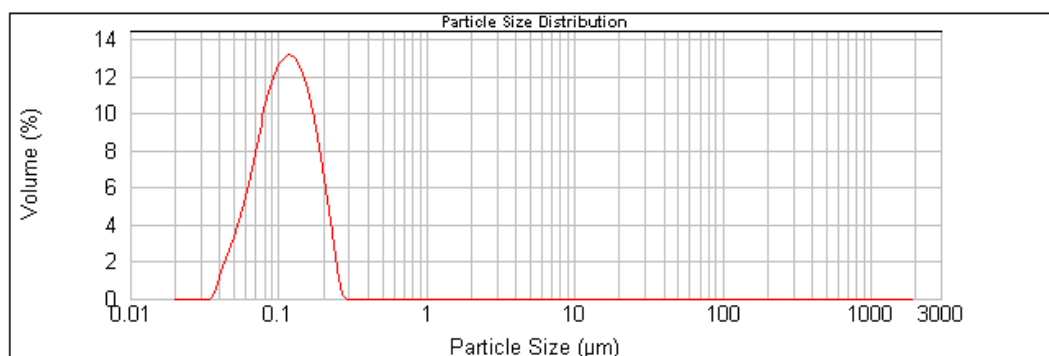
Weight percentages of additives used in the selection process for cutting tools

<i>Sample name</i>	<i>Hot pressing conditions</i>	<i>Density (g/cm³)</i>	<i>Open Porosity (%)</i>	<i>Vickers hardness (GPa)</i>	<i>Fracture Toughness (MPa.m.^{0.5})</i>
Pure B ₆ O	1900°C, 50 MPa, 20 min.	2.46	3.7	30.2 ± 1.0 (1 kg)	brittle
B ₆ O+1.17wt% Fe	1850°C, 50 MPa, 20 min.	2.53	1.1	27.4 ± 1.5 (5Kg)	3.2 ± 0.8
B ₆ O+1.07wt% Cr	1850°C, 50 MPa, 20 min.	2.57	0.7	29.4±2.9 (5Kg)	5.5 ± 0.4
B ₆ O+1.33wt% Co	1850°C, 50 MPa, 20 min.	2.53	1.2	33.9±2.2 (5Kg)	5.3 ± 0.8
B ₆ O+1.50wt% FeO	1850°C, 50 MPa, 20 min.	2.51	0.9	28.4 ± 1.4 (5Kg)	3.1 ± 0.2

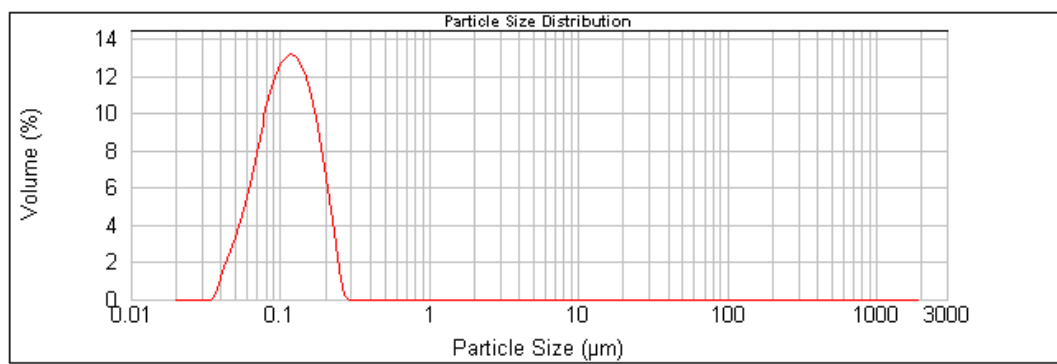
B ₆ O+2.06wt% CrO ₃	1850°C, 50 MPa, 20 min.	2.53	1.2	30.4±2.6 (5Kg)	4.8 ± 0.3
B ₆ O+1.40wt% FeB	1850°C, 50 MPa, 20 min.	2.56	0.4	30.8±2.6 (1 kg) 27.2±2.2 (5Kg)	7.6 ± 1.1
B ₆ O+1.50wt% Sc ₂ O ₃	1850°C, 50 MPa, 20 min.	2.48	1.6	31.6±0.9 (5Kg)	5.6±0.2
B ₆ O+2.50wt% La ₂ O ₃	1850°C, 80 MPa, 20 min.	2.47	2.1	31.0±1.8 (5Kg)	5.6 ±0.8
B ₆ O+1.50wt% Yb ₂ O ₃	1850°C, 80 MPa, 20 min.	2.51	0.9	30.5±1.7 (5Kg)	3.9±0.8

Appendix B

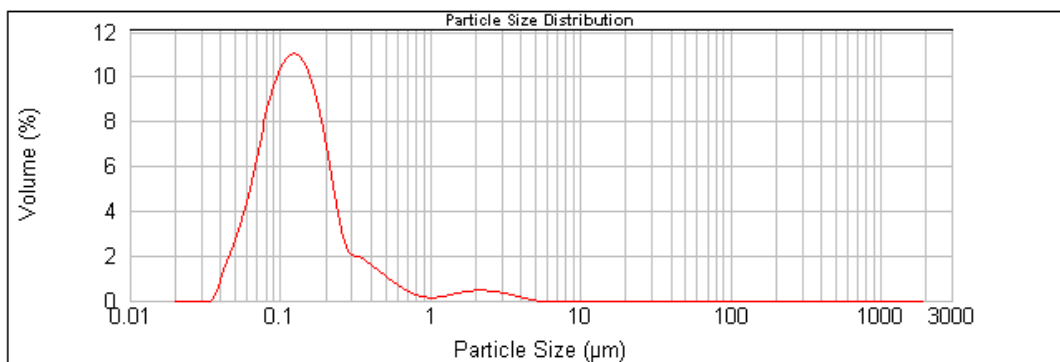
Powder Batch 3, progressive investigation into milling efficiency:



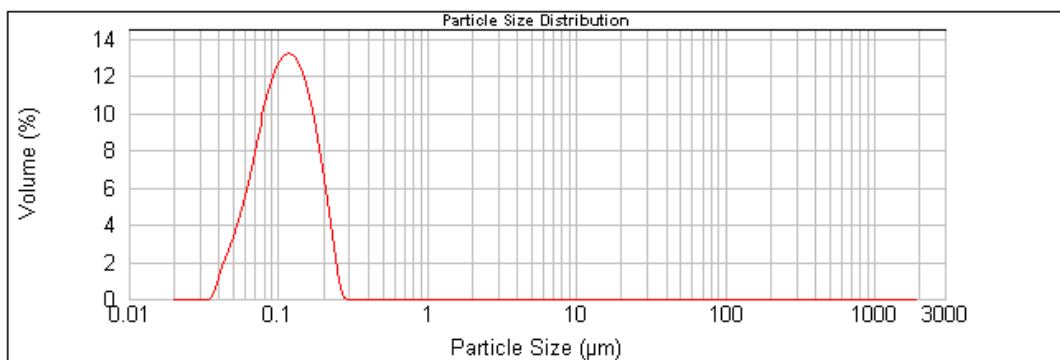
Particle size distribution of the B_6O powder after 5hrs of milling at 200rpm, particle $d_{50} = 0.112\mu m$.



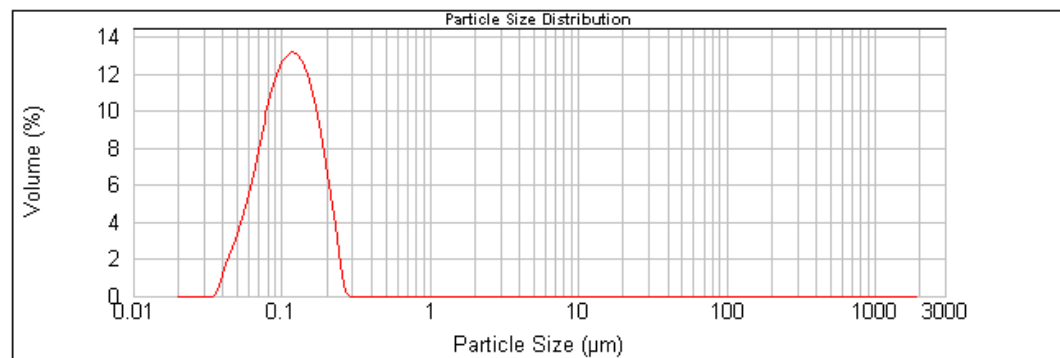
Particle size distribution of the B_6O powder after 10hrs of milling at 200rpm, particle $d_{50} = 0.112\mu m$.



Particle size distribution of the B_6O powder after 15hrs of milling at 200rpm, particle $d_{50} = 0.128\mu m$



Particle size distribution of the B_6O powder after 20hrs of milling at 200rpm, particle $d_{50} = 0.112\mu m$



Particle size distribution of the B_6O powder after 25hrs of milling at 200rpm, particle $d_{50} = 0.113\mu m$

Appendix C

Formulae for weight, volume percent and theoretical density calculations:

- Wt. % of additive A in bulk material B = Mass A / (Mass A + Mass B) x 100%

- $$Vol_i \% = \left(\frac{m_i / \rho_i}{m_i / \rho_i + m_b / \rho_b} \right) \times 100\%$$

Where 'i' is the introduced phase (additive) and 'b' is the bulk phase (B₆O in this project)

- Theoretical density:

$$\rho_{Theoretical} = \left(\frac{x_1}{\rho_1} + \frac{x_2}{\rho_2} \right)^{-1}$$

Where :

x_1 = The mass fraction of component 1 in the mixture

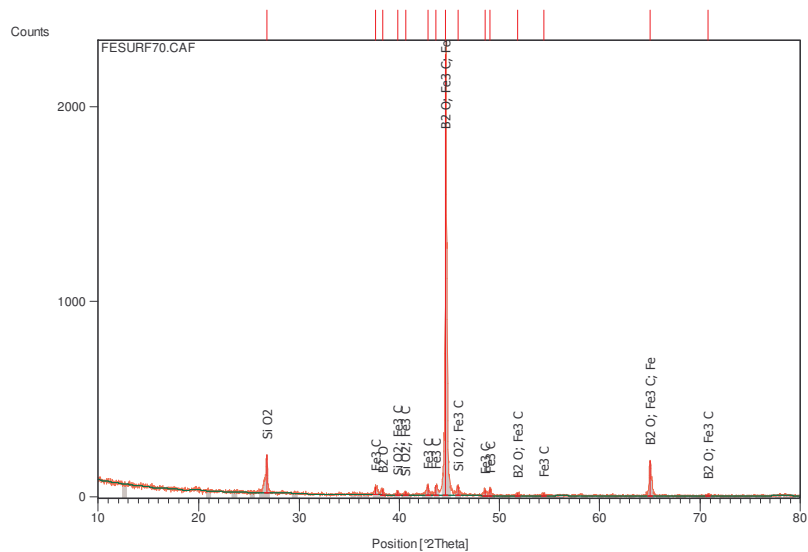
x_2 = The mass fraction of component 2 in the mixture

ρ_1 = The specific gravity of component 1

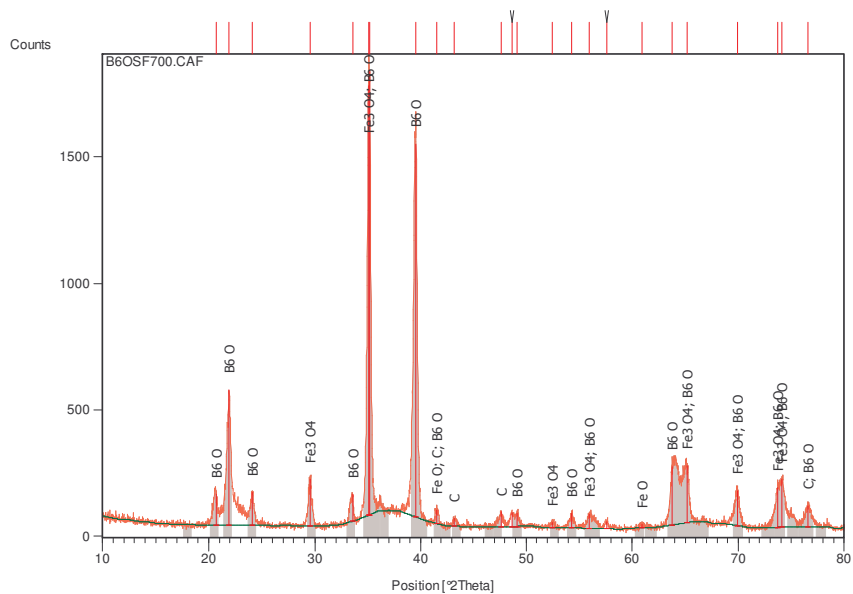
ρ_2 = The specific gravity of component 2

Appendix D

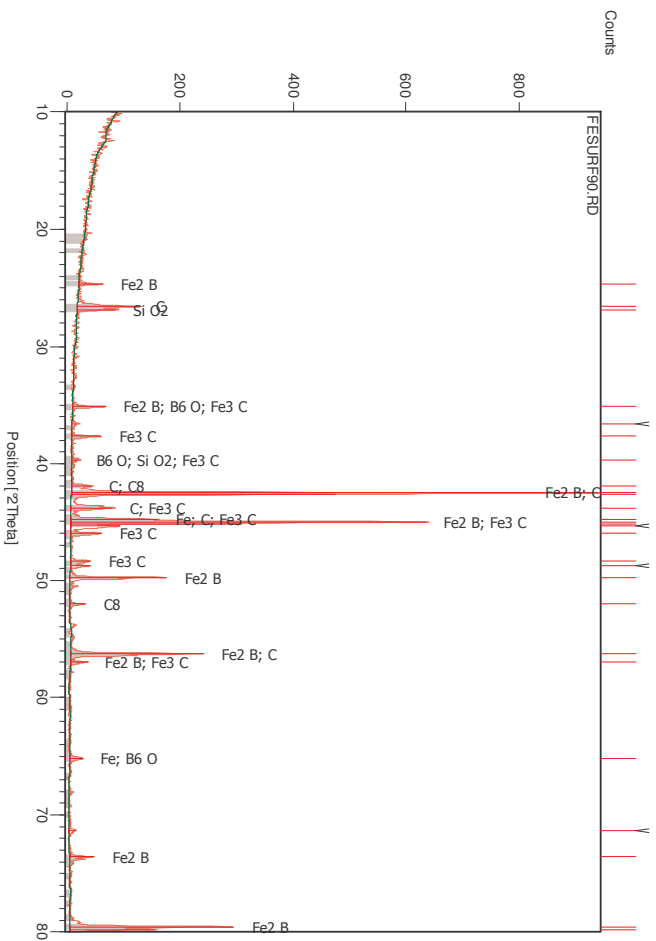
XRD traces



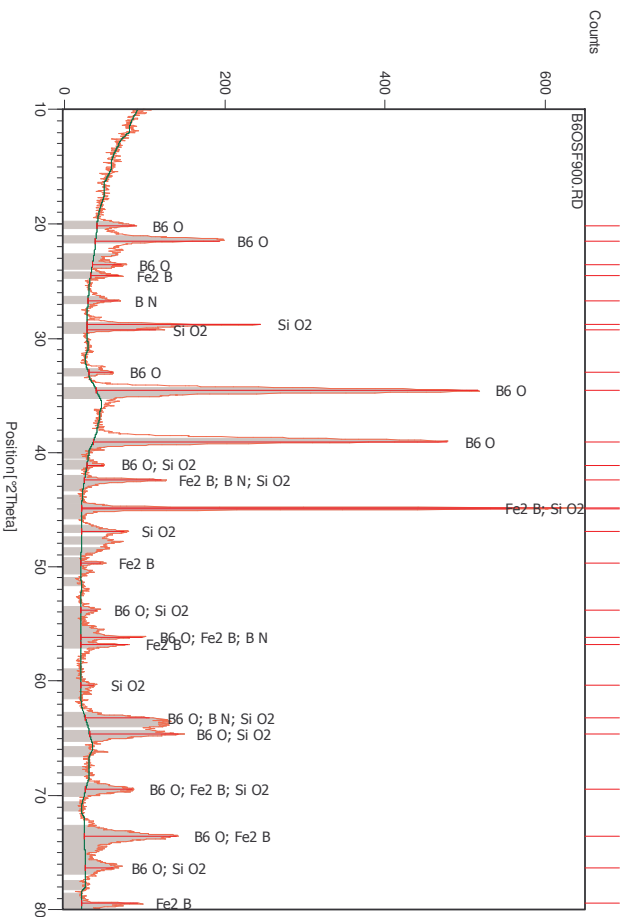
XRD pattern of the surface of CGI after contact with B_2O_3 in the 700°C diffusion couple experiment.



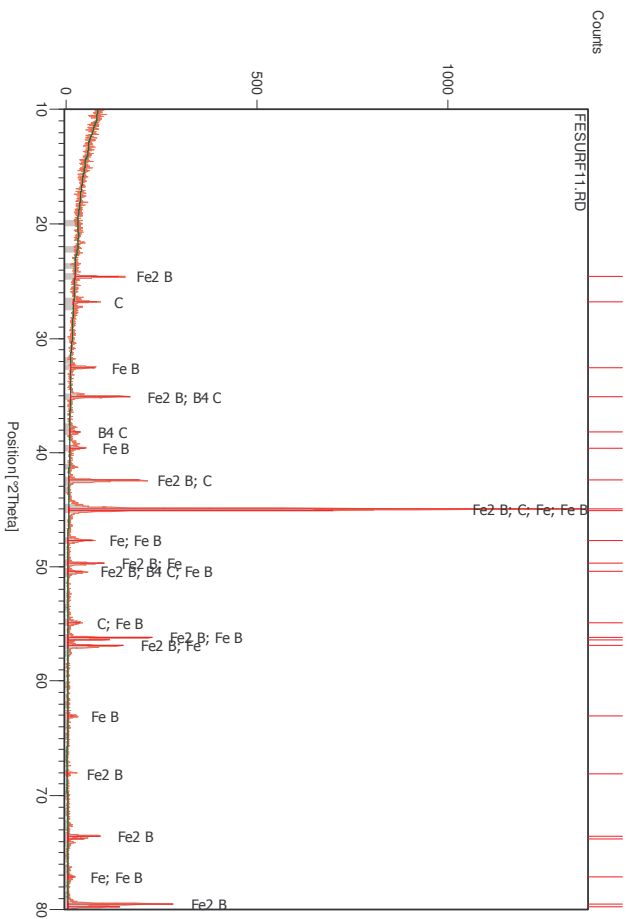
XRD pattern of the B_2O_3 surface after contact with CGI in the 700°C diffusion couple experiment.



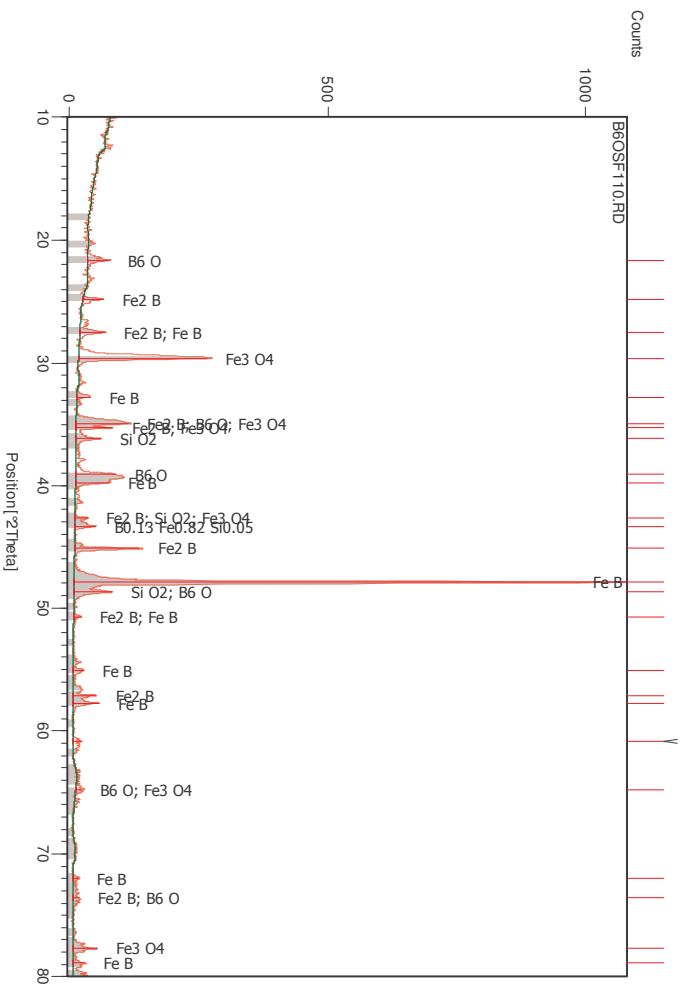
XRD trace of the CGI side of the 900 °C diffusion couple.



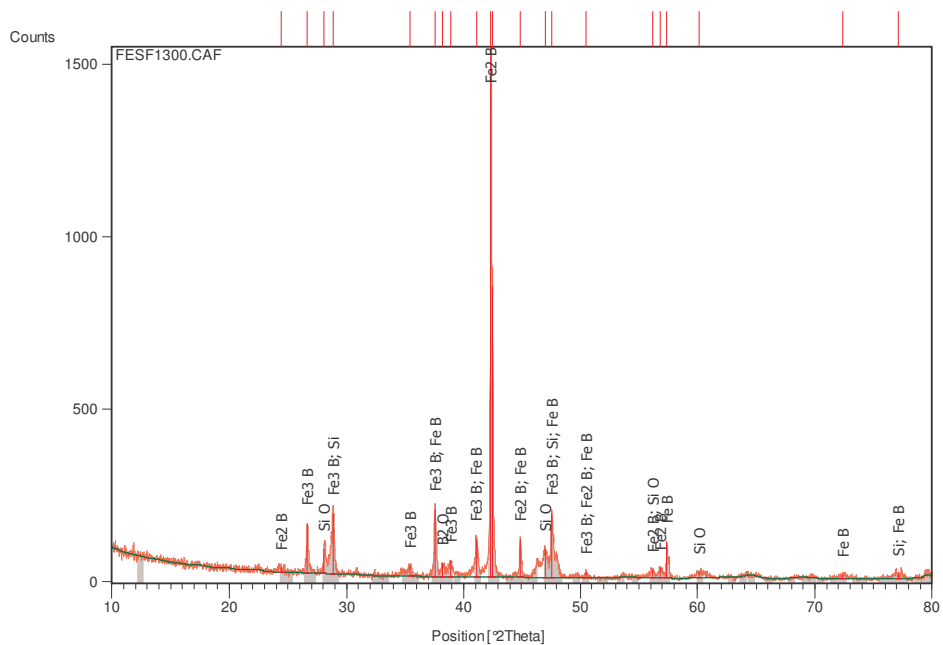
XRD trace of the B₆O side of the 900 °C diffusion couple.



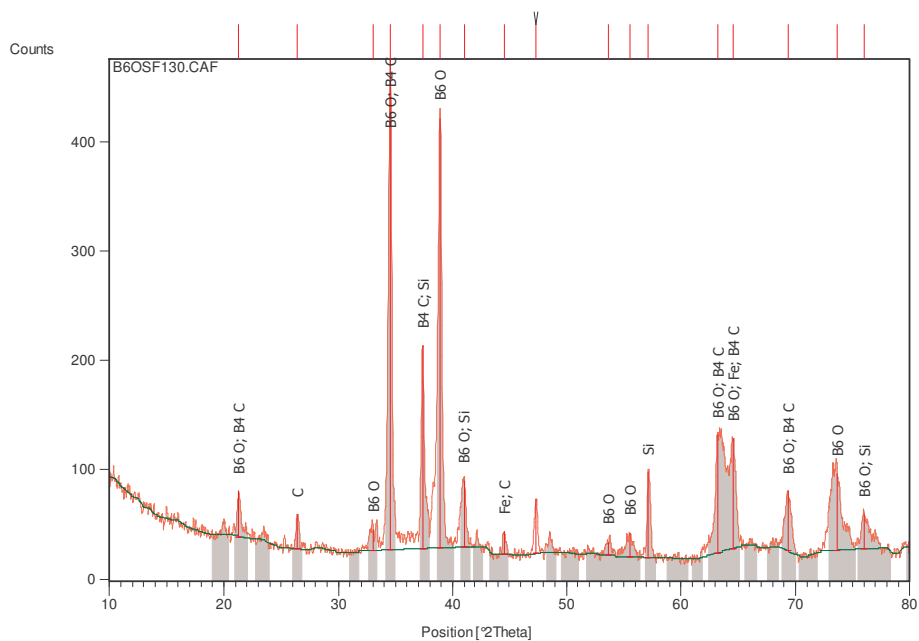
XRD trace of the CGI half of the 1100°C diffusion couple.



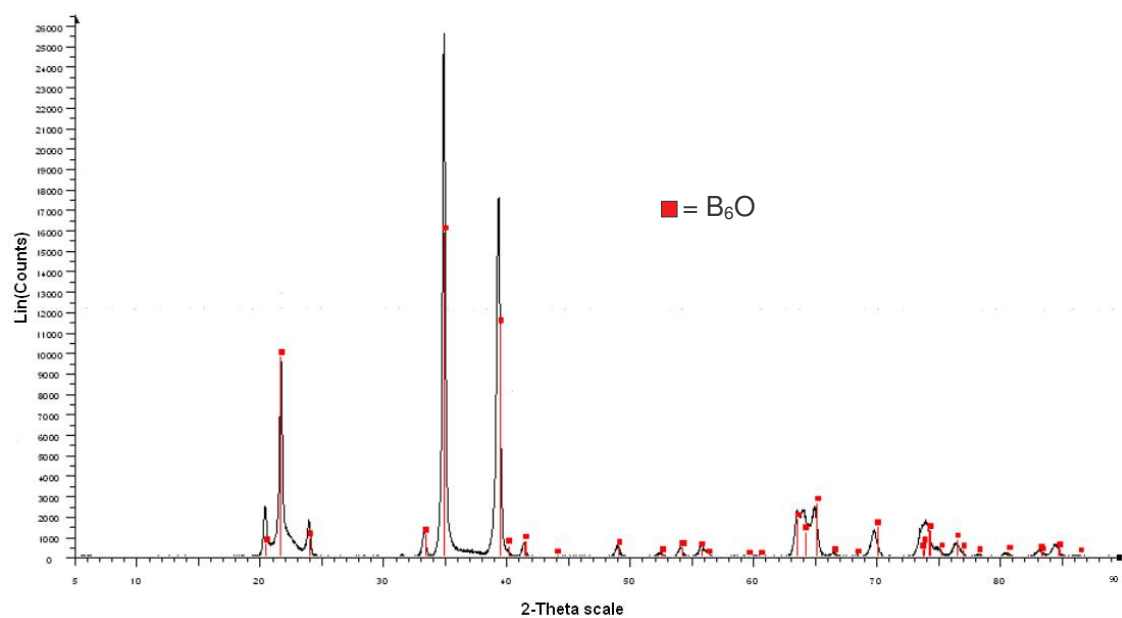
XRD trace of the B₆O half of the 1100°C diffusion couple.



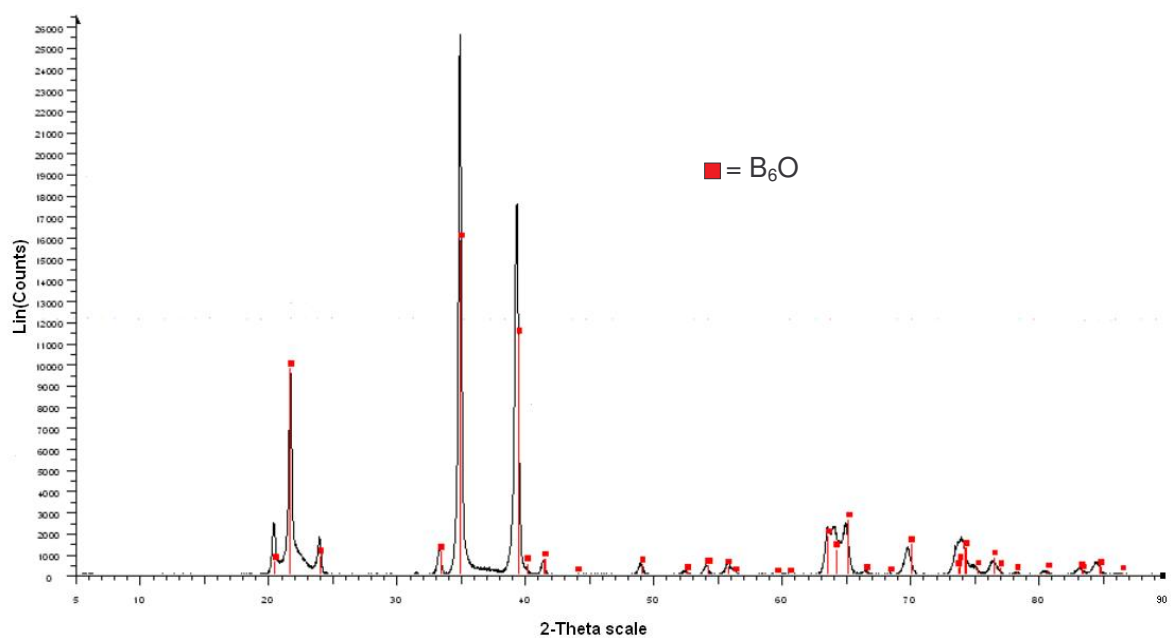
XRD trace of the iron side of the 1300°C diffusion couple.



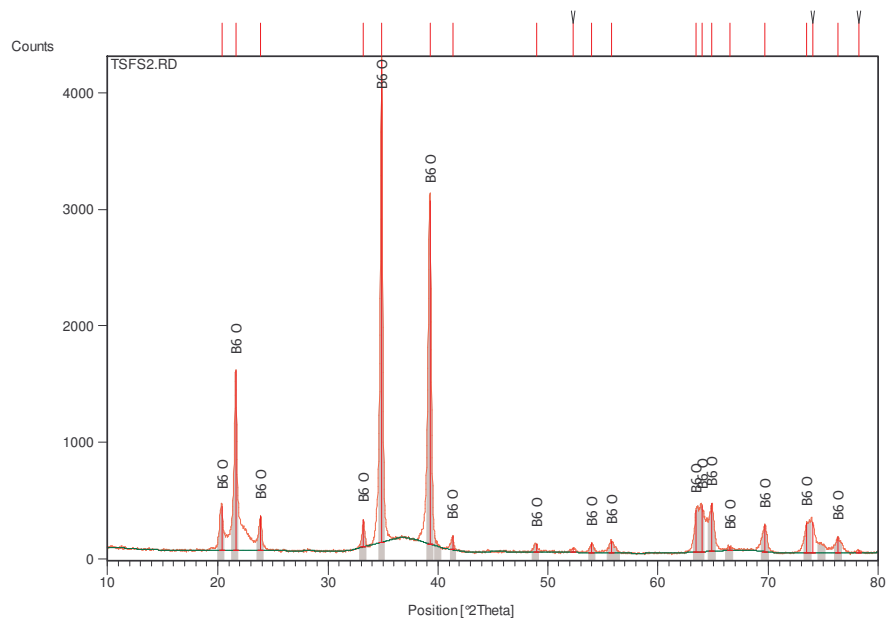
XRD pattern of the B₆O side of the 1300°C diffusion couple.



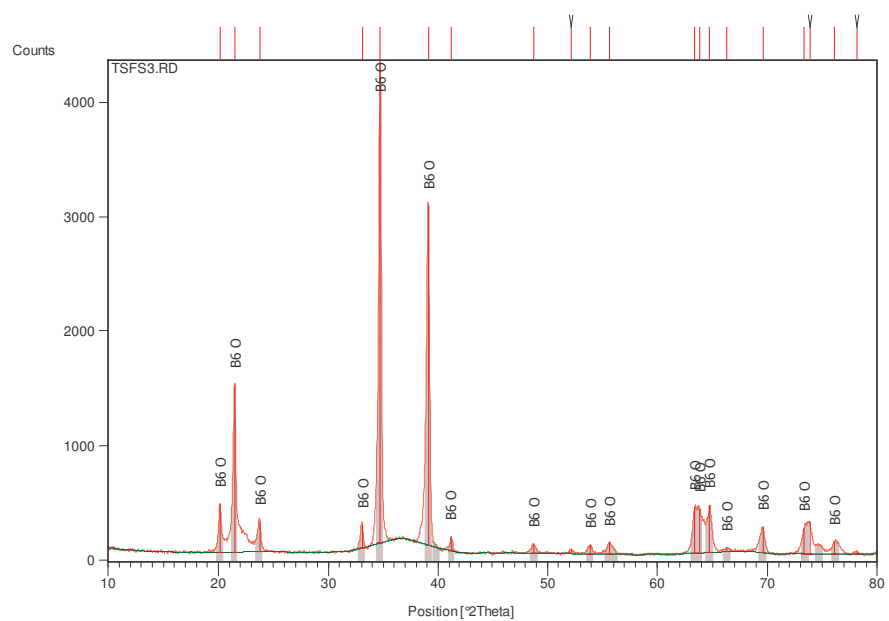
XRD pattern corresponding to the (pure B_6O) phase monitoring sample 2.



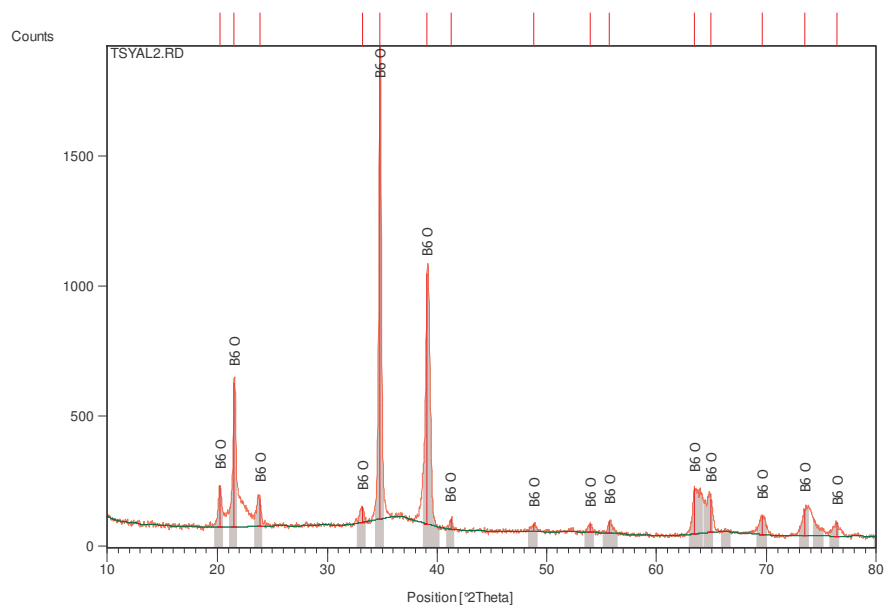
XRD pattern corresponding to the (pure B_6O) phase monitoring sample 3.



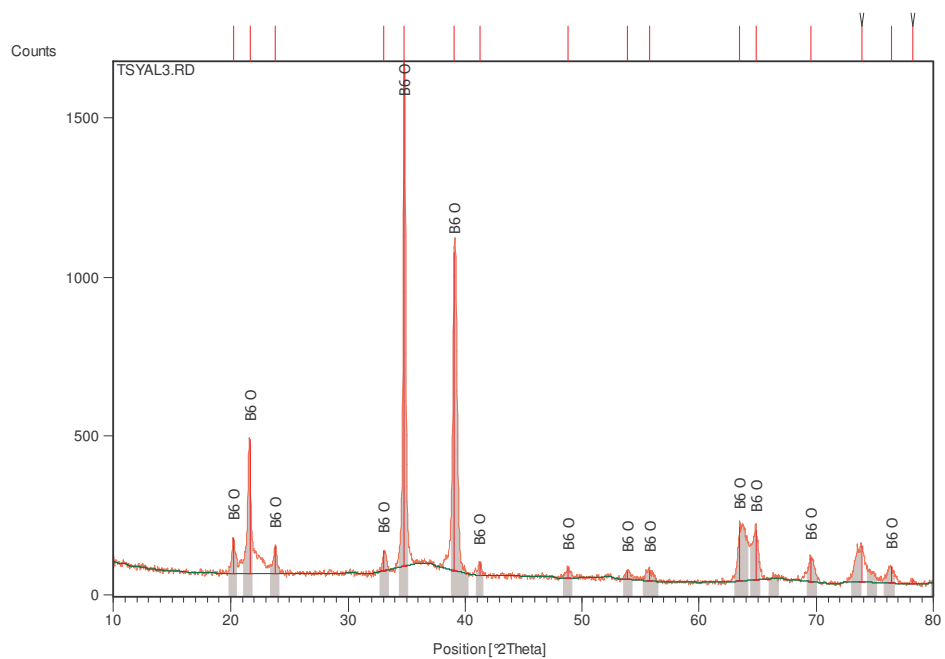
XRD pattern corresponding to the pure B₆O oxidation resistance sample 2.



XRD pattern corresponding to the pure B₆O oxidation resistance sample 3.



XRD pattern of the $B_6O/Y_2O_3/Al_2O_3$ oxidation resistance sample 2.



XRD pattern of the $B_6O/Y_2O_3/Al_2O_3$ oxidation resistance sample 2.

Appendix E

Climate / Humidity Table⁵⁹:

The table shows the "absolute humidity" in g/m³ (upper line) and the "dew point temperature" of the air in °C (lower line) for certain air temperatures as a function of "relative humidity".

Example: At an air temperature of 50°C and a relative humidity of 70%, the absolute humidity is 58.1 g/m³ and the dew point temperature is 43°C.

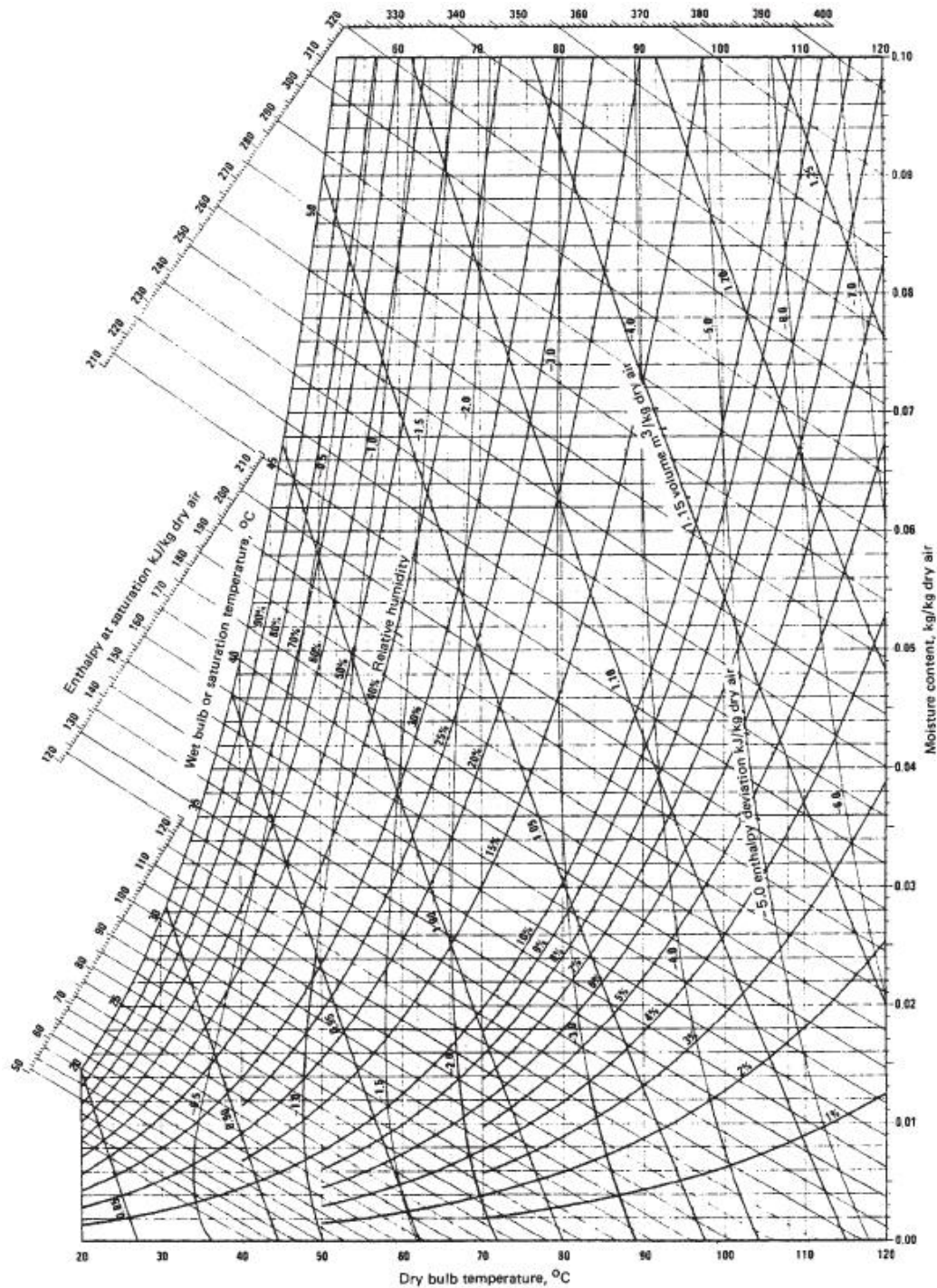
Relative humidity	10%	20%	30%	40%	50%	60%	70%	80%	90%	100%
Air temperature [°C]										
+50	8.3	16.6	24.9	33.2	41.5	49.8	58.1	66.4	74.7	83.0
	+8	+19	+26	+32	+36	+40	+43	+45	+48	+50
+45	6.5	13.1	19.6	26.2	32.7	39.3	45.8	52.4	58.9	65.4
	+4	+15	+22	+27	+32	+36	+38	+41	+43	+45
+40	5.1	10.2	15.3	20.5	25.6	30.7	35.8	40.9	46.0	51.1
	+1	+11	+18	+23	+27	+30	+33	+36	+38	+40
+35	4.0	7.9	11.9	15.8	19.8	23.8	27.7	31.7	35.6	39.6
	-2	+8	+14	+18	+21	+25	+28	+31	+33	+35

+30	3.0	6.1	9.1	12.1	15.2	18.2	21.3	24.3	27.3	30.4
	-6	+3	+10	+14	+18	+21	+24	+26	+28	+30
+25	2.3	4.6	6.9	9.2	11.5	13.8	16.1	18.4	20.7	23.0
	-8	0	+5	+10	+13	+16	+19	+21	+23	+25
+20	1.7	3.5	5.2	6.9	8.7	10.4	12.1	13.8	15.6	17.3
	-12	-4	+1	+5	+9	+12	+14	+16	+18	+20
+15	1.3	2.6	3.9	5.1	6.4	7.7	9.0	10.3	11.5	12.8
	-16	-7	-3	+1	+4	+7	+9	+11	+13	+15
+10	0.9	1.9	2.8	3.8	4.7	5.6	6.6	7.5	8.5	9.4
	-19	-11	-7	-3	0	+1	+4	+6	+8	+10
+5	0.7	1.4	2.0	2.7	3.4	4.1	4.8	5.4	6.1	6.8
	-23	-15	-11	-7	-5	-2	0	+2	+3	+5
0	0.5	1.0	1.5	1.9	2.4	2.9	3.4	3.9	4.4	4.8
	-26	-19	-14	-11	-8	-6	-4	-3	-2	0
-5	0.3	0.7	1.0	1.4	1.7	2.1	2.4	2.7	3.1	3.4
	-29	-22	-18	-15	-13	-11	-8	-7	-6	-5
-10	0.2	0.5	0.7	0.9	1.2	1.4	1.6	1.9	2.1	2.3

	-34	-26	-22	-19	-17	-15	-13	-11	-11	-10
-15	0.2	0.3	0.5	0.6	0.8	1.0	1.1	1.3	1.5	1.6
	-37	-30	-26	-23	-21	-19	-17	-16	-15	-15
-20	0.1	0.2	0.3	0.4	0.4	0.5	0.6	0.7	0.8	0.9
	-42	-35	-32	-29	-27	-25	-24	-22	-21	-20
-25	0.1	0.1	0.2	0.2	0.3	0.3	0.4	0.4	0.5	0.6
	-45	-40	-36	-34	-32	-30	-29	-27	-26	-25

*Note that the above table links very closely with the psychrometric chart provided on the next page.

Psychrometric chart extracted from Perry's Chemical Engineer's Handbook,
Seventh Edition⁶⁰



Psychrometric chart: properties of air and water-vapor mixtures from 20 to 120°C. (*Carrier Corp.*)